

Durham E-Theses

The Design, Synthesis and Biological Testing of Potential CCL2 and EBNA1 Therapeutics

ZAWADZKI, ISABELLE,GRACE

How to cite:

ZAWADZKI, ISABELLE,GRACE (2024) *The Design, Synthesis and Biological Testing of Potential CCL2 and EBNA1 Therapeutics*, Durham theses, Durham University. Available at Durham E-Theses Online: <http://etheses.dur.ac.uk/15476/>

Use policy

The full-text may be used and/or reproduced, and given to third parties in any format or medium, without prior permission or charge, for personal research or study, educational, or not-for-profit purposes provided that:

- a full bibliographic reference is made to the original source
- a [link](#) is made to the metadata record in Durham E-Theses
- the full-text is not changed in any way

The full-text must not be sold in any format or medium without the formal permission of the copyright holders.

Please consult the [full Durham E-Theses policy](#) for further details.



The Design, Synthesis and Biological Testing of Potential CCL2 and EBNA1 Therapeutics

*A Thesis Presented for the Degree of Doctor of Philosophy
The Department of Chemistry
Durham University, Ustinov College*

Isabelle Grace Zawadzki

Supervised by Professor Steven Cobb and Professor Simi Ali

2024

Statement of Copyright

The copyright of this thesis rests with the author. No quotation or image from it should be published without the author's prior written consent and information derived from it should be acknowledged.

Author's Declaration

I declare that this thesis is a presentation of original work, and it is the work of the author unless otherwise stated. This work was conducted in the Department of Chemistry at Durham University and collaborative work was mentioned where applicable. The work has not been submitted for a degree in this or other university.

Abstract

Chemokine ligand 1 (CCL2) is an inflammatory protein that induces the chemotaxis of leukocytes to sites of inflammation or infection through binding with its receptor CCR2. Epstein-Barr virus nuclear antigen 1 (EBNA1) is essential for the DNA replication and episome maintenance of the Epstein-Barr virus (EBV) which is estimated to have infected over 90% of the worldwide population. Both CCL2 and EBNA1 are associated with autoimmune diseases and cancer and thus they represent potential therapeutic targets. The emerging field of proteolysis targeting chimeras (PROTACs) presents an alternative therapeutic approach to small molecule drug discovery, with the key benefits of targeting 'undruggable' proteins and transient binding modes with the target of interest. The primary aims of this thesis were to design, synthesise and evaluate the first examples of CCL2 and EBNA1-targeting PROTACs.

2,5-Diketopiperazines (DKPS) have been shown in previous work to inhibit CCL2-mediated chemotaxis, with CCL2 binding as their proposed mode of action. In **Chapter 2** a library of 13 DKPs, that incorporate fluorinated or unnatural amino acids, were synthesised using solid phase or solution phase peptide synthesis. From subsequent Boyden chamber (chemotaxis) assays, an improved chemotaxis inhibitor (**43**) was discovered in which THP-1 migration was reduced to approximately 51% (at 50 μ M). Next, the mode of action in which the DKPs reduced THP-1 chemotaxis was evaluated using CCR2 internalisation assays. In the work presented in **Chapter 2**, it was shown that DKP **43** (at 100 μ M and 50 μ M) and previous lead **27** (100 μ M) were neither agonists for CCR2 internalisation nor were they outcompeting CCL2 for the orthosteric site. The mode of action was further assessed through the analysis of DKP-CCL2 binding in **Chapter 3**. The first step was *hsCCL2* overexpression in *E. coli* which produced moderate amounts of high purity protein. Subsequently, DKP ligand-binding assays with *hsCCL2*, as well as *btnCCL2*, were undertaken using surface plasmon resonance (SPR) with no binding events observed (up to 200 μ M). The work in both **Chapter 2** and **Chapter 3** indicated

that DKPs were not CCR2 orthosteric antagonists or CCL2 binders thus the new proposed mode of action is that DKPs likely act as allosteric CCR2 antagonists. In addition, the CCL2 binding of a group of fluorinated, small molecule fragments was assessed using SPR assays (with *hsCCL2* and *btnCCL2*) with fragment **80** as the most promising binder ($K_D = 89 \mu\text{M}$ for *btnCCL2*). This was an important discovery as few CCL2 small molecule binders are currently known. **Chapter 4** reported the synthesis and biological testing of three potential CCL2-PROTACs **105 - 107** (work undertaken prior to biophysical studies detailed in **Chapter 3**) incorporating hydroxyl-containing DKPs. The reduction of CCL2 levels in response to each PROTAC (100 nM) was determined using a novel CCL2 degradation assay, however a consistent reduction in CCL2 was not observed. Finally, in **Chapter 5**, the synthesis of YFMF-NH₂ incorporating PROTACs, with the potential to degrade EBNA1 via the CRBN, were synthesised. Initial *in vivo* EBNA1-degradation assays indicated **147**, **149** and **153** as potential hits, however this work is still in its infancy and is an ongoing project in the Cobb group.

In summary, the design, synthesis, and biological testing of potential CCL2 and EBNA1 PROTACs was undertaken. Although the PROTACs prepared were unable to degrade CCL2, the newly discovered CCL2 binders and the emerging alternative approaches to targeted protein degradation (e.g. LYTACs) still make CCL2 a viable target. The synthesis of 13 EBNA1-PROTACs was achieved, and their initial biological evaluation has identified some promising leads for further development.

Acknowledgements

Firstly, I would like to thank my supervisor Professor Steven Cobb, for giving me the opportunity to undertake this research project and for providing invaluable advice, guidance, good-humour, and positivity throughout the past few years. I am grateful for his dedication to this project and the scientific expertise he has provided. Additionally, I would like to thank my co-supervisor at Newcastle University, Professor Simi Ali, for her guidance and training in molecular biology. I would also like to thank Professor Ehmke Pohl, for not only assisting me with extra training but for always being so supportive and encouraging. I would also like to thank EPSRC (MoSMed) for funding this research project.

Secondly, I would like to thank those who are not part of the Cobb group but have helped me greatly when working in other labs. A huge thanks goes to Dr Chong Pang, whose seemingly endless knowledge of the biomedical sciences helped guide the path for this project. I am grateful for not just the training, the research ideas, and the many scientific discussions, but for making me feel welcome in the Ali research group. Also, thank you to Ian Edwards in the Pohl group, for the extensive training in protein expression. Additionally, I would like to thank all members of the Pohl group especially Dr Daniel Bruce, Dr Stephanie Pohl, Dr Katy Cornish, Abbey Butler and Dori Gašparíková. I would also like to thank Dr Matthew Martin at the Newcastle CRUK drug discovery unit, for helping me undertake SPR experiments even when incredibly busy!

Thirdly, endless thanks go to the members of the Cobb group (Yazmin Santos, Hirunika Perera, Carissa Llyod, Diana Kolos, Katie Dowell, Eleanor Taylor-Newman) who have helped me so much throughout the past four years and have become my good friends. I would also like to thank Dr William Brittain for his help and guidance with everything organic chemistry related. I would also like to thank the O'Donoghue group, particularly Matthew Smith and Josh Rawlinson, with whom I shared a lab in the final year of my PhD.

You helped make the last year, the best year, and I will greatly miss our 10.30 coffee breaks!

I would like to thank my family for their love and support throughout this time. A special thanks to my mum, who has always been on the other end of the phone when things got tough. And last, but not least, I am most grateful to John, who I met at the very beginning of my time at Durham and has been with me throughout all the highs and lows. Without his endless love and support, good humour and endless positivity and encouragement, I would not have been able to finish this project.

Memorandum

The work within this thesis has been presented by the author at the following meetings:

Poster presentation at the MoSMed Annual Conference (2020)

Poster presentation at the online MoSMed Annual Conference (2021)

Presentation at the MoSMed Annual Conference (2022)

Abbreviations

AA	Amino acid
aq.	Aqueous
AU	Arbitrary unit
bRO5	Beyond rule of 5
Boc	<i>tert</i> -butyloxycarbonyl
BSA	Bovine serum albumin
Btn	Biotin
Cbz (Z)	Benzyloxycarbonyl
CCL2	Chemokine Ligand 2
CCR2	Chemokine Receptor 2
CD	Circular dichroism
CHP	<i>Cis</i> -hydroxyproline
CRBN	Cereblon
CRS1/2	Chemokine receptor binding site 1/2
CNS	Central nervous system
CV	Column volume
dTAG	Degradation tag
DBD	Dimerisation binding domain
DC₅₀	Half maximal degradation concentration
DCM	Dichloromethane
DEL	DNA-encoded library
DIC	N,N-Diisopropylcarbodiimide
DIPEA	N,N-Diisopropylethylamine
DKP	2,5-Diketopiperazine
DMAP	4-Dimethylaminopyridine

DMF	Dimethylformamide
DMSO	Dimethyl sulfoxide
E3	E3 ligase
EBNA1	Epstein-Barr virus nuclear antigen -1
EBV	Epstein-Barr virus
ECL	Extra-cellular loop
EDC	1-Ethyl-3-(3-dimethylaminopropyl)carbodiimide
EDTA	Ethylenediaminetetraacetic acid
ELISA	Enzyme-Linked Immunosorbent Assay
ERK1/2	Extracellular Signal-Regulated Kinase 1/2
ES	Electrospray
EtOAc	Ethyl acetate
EtOH	Ethanol
EV	Elution volume
FACs	Fluorescence activated cell sorting
FBS	Fetal bovine serum
flp	<i>R</i> -4-Fluoroproline
Flp	<i>S</i> -4-Fluoroproline
FPLC	Fast protein liquid chromatography
GFP	Green fluorescent protein
GPCR	G-protein coupled receptor
h	Hour
HATU	Hexafluorophosphate azabenzotriazole tetramethyl uronium
HBA	Hydrogen bond acceptor
HBD	Hydrogen bond donor
HL	High-loading
HOBt	Hydroxybenzotriazole

HPLC	High performance liquid chromatography
HRMS	High resolution mass spectrometry
Hs	His ₆ -tag
HSCs	Hematopoietic stem cells
HTS	High-throughput screening
IC₅₀	Half maximal inhibitory concentration
IMiD	Immunomodulatory drug
IEX	Ion-exchange chromatography
ITC	Isothermal titration calorimetry
IR	Infrared spectroscopy
IMAC	Ion-metal affinity chromatography
K_D	Equilibrium dissociation constant
LCMS	Liquid chromatography mass spectrometry
mAU	Milli absorbance unit
MCP-1	Monocyte chemoattractant protein 1
MeCN	Acetonitrile
MeOH	Methanol
Mep	Methylproline
min	Minute
MG	Molecular glue
MFI	Median Fluorescence Intensity
MHRA	Medicines and Healthcare products Regulatory Agency
MS	Mass spectrometry
mw	Microwave
MW	Molecular weight
Nal	Naphthyl alanine
NCL	Native chemical ligation

NHS	N-Hydroxysuccinimide
NIS	N-iodosuccinate
NMR	Nuclear Magnetic Resonance
NTA	Nitrilotriacetic acid
OD	Optical density
<i>ori-P</i>	Origin replicator protein
OXYMA	Ethyl cyanohydroxyiminoacetate
LL	Low-loading
LYTACs	Lysosome targeting chimeras
PAMPA	Parallel artificial membrane permeability assay
PBS	Phosphate-buffered saline
PCR	Polymerase chain reaction
PEG	Poly-ethylene glycol
PFA	Paraformaldehyde
PFP	Pentafluoropyridine
Pfp	Pentafluorophenol
PI	Propidium iodide
pI	Isoelectric point
POI	Protein of interest
PPI	Protein-protein interaction
PROTAC	Proteolysis targeting chimeras
RA	Rheumatoid arthritis
RIBOTAC	Ribonuclease targeting chimeras
RM	Relative Migration
RO3/5	Rule of 3/5
rpm	Revolutions per minute
rt	Room temperature

RU	Response Unit
SA	Streptavidin
SDS	Sodium dodecyl sulphate
SEC	Size exclusion chromatography
SEM	Standard error mean
SPPS	Solid phase peptide synthesis
SPR	Surface plasmon resonance
TIPS	Triisopropylsilane
TFA	Trifluoroacetic acid
TFE	Trifluoroethanol
TM	Transmembrane
TFP	Tetrafluoropyridine
TNF-α	Tumour necrosis factor
TLC	Thin-layer chromatography
TPD	Targeted protein degradation
uHTS	Ultra-high throughput screening
UPS	Ubiquitin proteasome system
UV	Ultraviolet
VHL	Von-Hippel Lindau
WT	Wild-type

Contents

Statement of Copyright	ii
Authors Declaration	iii
Abstract	iv
Acknowledgements.....	vi
Memorandum	viii
Abbreviations	ix
Contents.....	xiv
1. Introduction.....	1
1.1 The drug discovery process	1
1.2 Hit discovery	2
1.2.1 High-throughput screening (HTS).....	2
1.2.2 DNA-encoded libraries (DELs)	3
1.2.3 Fragment screening	4
1.2.4 Structure-based drug design	5
1.3 Chemical space and the RO5	5
1.4 'Undruggable' protein targets	6
1.5 Targeted degradation	7
1.6 The ubiquitin proteasome system (UPS).....	8
1.7 Proteolysis targeting chimeras (PROTACs).....	9
1.8 Elements of PROTAC design	10
1.8.1 E3 ligands	10
1.8.2 PROTAC linkers.....	11
1.8.3 Ternary complex formation, cooperativity, and the Hook effect.....	13
1.8.4 Beyond the rule of 5 (bRO5)	15
1.9 Molecular glues (MGs)	16
1.10 Lysosome targeting chimeras (LYTACs).....	17
1.11 Ribonuclease targeting chimeras (RIBOTACs).....	18
1.12 Peptide-based PROTACs (p-PROTACs).....	20
1.13 Targeted protein degraders in clinical trials	21
1.14 Project Aims	24
1.15 References	26
2. Inhibitors of CCL2-mediated chemotaxis	30
2.1 An introduction to 2,5-diketopiperazines (DKPs)	30
2.1.1 DKP bioactivity and medicinal properties	31

2.2	An introduction to chemokines	33
2.2.1	Chemokine function	34
2.2.2	Chemokine structure	34
2.2.3	Chemokine therapeutics	36
2.3	An Introduction to CCL2 (MCP-1)	38
2.3.1	Issues targeting CCL2-CCR2	38
2.3.2	DKP based CCL2-CCR2 inhibitors	40
2.3.3	Mode of action for CCL2 chemotaxis inhibition	41
2.3.4	A new library of DKP inhibitors.....	41
2.4	Aims	42
2.4.1	Design of the 2 nd generation DKP library	43
2.5	Synthesis of the 2 nd generation DKP library	46
2.5.1	General DKP SPPS (N-Boc-protected).....	47
2.5.2	SPPS of cyclo(L-Phe-L-Pro) (27).....	48
2.5.3	SPPS of the DKP library (N-Boc).....	50
2.5.4	Modified SPPS of cyclo(L-Nitro-Tyr-L-Pro) (47)	51
2.5.5	Attempted SPPS of cyclo(L-TFP-Tyr-L-Pro) (43) and cyclo(L-TFP-Hyp-L-Pro) (44)53	
2.5.6	SPPS of hydroxyl-containing DKPs (N-Boc protected).....	55
2.5.7	Solution phase DKP synthesis	56
2.5.8	Synthesis of cyclo(L-TFP-Tyr-L-Pro) (43) and cyclo(L-3-Iodo-Tyr-L-Pro) (48) 59	
2.5.9	DKP crystal structures	60
2.6	Molecular Biology	62
2.6.1	Chemotaxis assays	62
2.6.2	CCL2-mediated chemotaxis assay development	63
2.6.3	CCL2-mediated chemotaxis assay – inhibitor testing.....	67
2.6.4	THP-1 apoptosis assays.....	72
2.6.5	CCR2 internalisation assays.....	73
2.6.6	Chapter summary	77
2.7	References	79
3.	Small molecule CCL2 binders.....	83
3.1	CCL2 structure	83
3.2	CCL2-CCR2 binding	84
3.3	CCR2 antagonists	85
3.4	CCL2 binders	88
3.5	CCL2 production.....	90
3.6	Aims	90

3.7	<i>HsCCL2</i> overexpression in <i>E. coli</i>	91
3.7.1	Medium scale <i>hsCCL2</i> preparation	91
3.7.2	Large scale <i>hsCCL2</i> preparation.....	94
3.7.3	Medium scale <i>hsCCL2</i> preparation (SEC purification).....	96
3.7.4	<i>CCL2</i> folding	100
3.8	<i>CCL2</i> -DKP ligand-binding studies	100
3.8.1	Surface plasmon resonance (SPR).....	101
3.8.2	SPR screening of DKPs with <i>hsCCL2</i> and <i>btnCCL2</i>	101
3.9	New <i>CCL2</i> binders	104
3.10	Chapter summary	113
3.11	References	115
4.	<i>CCL2</i>-targeting PROTACs.....	117
4.1	<i>CCL2</i> degradation.....	117
4.2	Aims.....	117
4.2.1	PROTAC design.....	118
4.3	PROTAC synthesis	119
4.3.1	Synthesis of thalidomide-linker conjugates.....	119
4.3.2	PROTAC assembly	121
4.4	<i>CCL2</i> -PROTAC <i>in vitro</i> testing	125
4.4.1	PROTAC toxicity	125
4.4.2	<i>CCL2</i> degradation assays.....	125
4.4.3	Preliminary degradation assay	126
4.4.4	<i>CCL2</i> -PROTAC degradation assay.....	127
4.5	SPR analysis of <i>CCL2</i> -targeting PROTACs.....	129
4.6	Chapter Summary	129
4.7	References	130
5.	EBNA1-targeting PROTACs.....	131
5.1	Introduction to EBV	131
5.2	EBV structure and mode of infection	131
5.3	Introduction to EBNA1.....	132
5.4	Peptide inhibitors of EBNA1 dimerisation	132
5.5	Aims.....	134
5.6	Group 1 EBNA1-PROTAC synthesis.....	135
5.6.1	Synthesis of PROTAC warheads.....	136
5.6.2	Synthesis of lenalidomide-linker conjugates.....	139
5.6.3	Optimisation of PROTAC assembly.....	141
5.6.4	Group 1 EBNA1-PROTACs.....	146

5.7	Group 2 EBNA1-PROTAC synthesis	146
5.7.1	Synthesis of peptide-alkyne conjugates.....	147
5.7.2	Synthesis of lenalidomide-azide conjugates	149
5.7.3	Group 2 EBNA1 PROTAC assembly	150
5.8	EBNA1-targeting PROTACs <i>in vitro</i> testing.....	152
5.8.1	EBNA1 degradation assay design	152
5.8.2	PROTAC PAMPA.....	157
5.9	Chapter Summary	159
5.10	References	161
6.	Conclusions and future work.....	163
6.1	References	176
7.	Experimental.....	177
7.1	General procedures	177
7.1.1	Nuclear Magnetic Resonance (NMR)	177
7.1.2	Mass Spectrometry (MS).....	177
7.1.3	Analytical HPLC.....	178
7.1.4	X-Ray Crystallography.....	178
7.2	General procedures (Chapter 2)	179
7.2.1	Solid phase DKP synthesis.....	179
7.2.2	Solution phase peptide coupling	179
7.2.3	Solution phase DKP formation.....	180
7.2.4	Formation of tetrafluoropyridyl (TFP) ethers	180
7.2.5	Ester hydrolysis	180
7.3	Chemical synthesis (Chapter 2).....	180
7.3.1	Synthesis of 4-(hydroxymethyl)-3-nitrobenzoic acid (50).....	180
7.3.2	Synthesis of activated linker 51	181
7.3.3	Synthesis of Cyclo(L-Phe-L-Pro) (27)	181
7.3.4	Synthesis of Cyclo(L-Trp-L-Pro) (37)	182
7.3.5	Synthesis of Cyclo(L-Dfp-L-Phe) (39)	183
7.3.6	Synthesis of Cyclo(L-Pfp-L-Pro) (41)	184
7.3.7	Synthesis of Cyclo(L-Phe-L-Nal) (48)	185
7.3.8	Synthesis of Cyclo(L-4-Mep-L-Phe) (55).....	185
7.3.9	Synthesis of Cyclo(L-flp-L-Phe) (56).....	186
7.3.10	Synthesis of Cyclo(L-Flp-L-Phe) (57).....	187
7.3.11	Synthesis of Cyclo(d-3F-Phe-L-Pro) (58).....	188
7.3.12	Synthesis of Cyclo(L-Tyr(3-NO ₂)-L-Pro) (47).....	189
7.3.13	Synthesis of Boc-TFP-Tyr-OMe (63).....	190

7.3.14	Synthesis of Boc-TFP-Tyr-OH (65).....	191
7.3.15	Synthesis of Boc-TFP-Hyp-OMe (64).....	192
7.3.16	Synthesis of Boc-TFP-Hyp-OH (66)	193
7.3.17	Synthesis of Cyclo(L-3-Fluoro-Tyr-L-Pro) (42).....	194
7.3.18	Synthesis of Cyclo(L-CHP-L-Phe) (67).....	194
7.3.19	Synthesis of Cbz-L-Hyp-L-Phe-OMe (69).....	195
7.3.20	Synthesis of Cyclo(L-Hyp-L-Phe) (38) and cyclo(D-Hyp-L-Phe) (70).....	196
7.3.21	Synthesis of Cbz-L-Pro-L-Tyr-OMe (73).....	197
7.3.22	Synthesis of Cyclo(L-Pro-L-Tyr) (29).....	198
7.3.23	Characterisation of distereoisomer Cyclo(D-Pro-L-Tyr) (71).....	199
7.3.24	Synthesis of Cyclo(L-TFP-Tyr-L-Pro) (43)	199
7.3.25	Synthesis of Cyclo(L-3-Iodo-Tyr-L-Pro) (47).....	200
7.4	General procedures (Chapter 4).....	201
7.4.1	Microwave synthesis of thalidomide analogues.....	201
7.4.2	Synthesis of thalidomide-linker conjugates.....	201
7.4.3	PROTAC Assembly via a Steglich Esterification.....	201
7.5	Chemical synthesis (Chapter 4)	202
7.5.1	Synthesis of 4-Fluorothalidomide (96).....	202
7.5.2	Synthesis of 4-Hydroxythalidomide (98).....	203
7.5.3	Synthesis of <i>tert</i> -butyl 3-(2-(2-(2-((2-(2,6-dioxopiperidin-3-yl)-1,3-dioxoisindolin-4-yl)amino)ethoxy)ethoxy)ethoxy)propanoate (101).....	204
7.5.4	Synthesis of 3-(2-(2-(2-((2-(2,6-dioxopiperidin-3-yl)-1,3-dioxoisindolin-4-yl)amino)ethoxy)ethoxy)ethoxy)propanoic acid (103)	205
7.5.5	Synthesis of <i>tert</i> -butyl 1-((2-(2,6-dioxopiperidin-3-yl)-1,3-dioxoisindolin-4-yl) amino)-3,6,9,12-tetraoxapentadecan-15-oate (102).....	206
7.5.6	1-((2-(2,6-dioxopiperidin-3-yl)-1,3-dioxoisindolin-4-yl)amino)-3,6,9,12-tetraoxapentadecan-15-oic acid (104).....	207
7.5.7	Synthesis of CCL2-PROTAC 105.....	208
7.5.8	Synthesis of CCL2-PROTAC 106.....	209
7.5.9	Synthesis of PROTAC 107	210
7.6	General procedures (Chapter 5).....	212
7.6.1	EDC mediated solution phase amide coupling	212
7.6.2	<i>tert</i> -butyl deprotection	212
7.6.3	Test cleavage.....	212
7.6.4	Resin cleavage	212
7.6.5	Preparative HPLC	213
7.6.6	Automated solid phase synthesis of peptides.....	213
7.6.7	Automated solid phase functionalised peptide synthesis.....	213

7.6.8	PROTAC assembly (click chemistry)	213
7.7	Chemical synthesis of Group 1 PROTACs (Chapter 5)	214
7.7.1	Synthesis of peptide 115(ON)	214
7.7.2	Synthesis of peptide 116(ON)	215
7.7.3	Synthesis of peptide 117(ON)	215
7.7.4	Synthesis of peptide 118(ON)	216
7.7.5	Synthesis of tert-butyl 3-((2-(2,6-dioxopiperidin-3-yl)-1-oxoisindolin-4-yl)amino)-3-oxopropanoate (126).....	216
7.7.6	Synthesis of 3-((2-(2,6-dioxopiperidin-3-yl)-1-oxoisindolin-4-yl)amino)-3-oxopropanoic acid (128)	217
7.7.7	Synthesis of tert-butyl 4-((2-(2,6-dioxopiperidin-3-yl)-1-oxoisindolin-4-yl)amino)-4-oxobutanoate (127).....	218
7.7.8	Synthesis of 4-((2-(2,6-dioxopiperidin-3-yl)-1-oxoisindolin-4-yl) amino)-4-oxobutanoic acid (129)	219
7.7.9	Synthesis of PROTAC 131.....	220
7.7.10	Synthesis of PROTAC 132.....	221
7.7.11	Synthesis of PROTAC 133.....	222
7.7.12	Synthesis of PROTAC 134.....	223
7.7.13	Synthesis of PROTAC 135.....	224
7.7.14	Synthesis of PROTAC 136.....	225
7.8	Chemical synthesis of Group 2 PROTACs (Chapter 5)	226
7.8.1	Synthesis of peptide 140	226
7.8.2	Synthesis of peptide 141	226
7.8.3	Synthesis of peptide 142	227
7.8.4	Synthesis of peptide 143	227
7.8.5	Synthesis of 4-azido-N-(2-(2,6-dioxopiperidin-3-yl)-1-oxoisindolin-4-yl) butanamide (144)	228
7.8.6	Synthesis of 5-azido-N-(2-(2,6-dioxopiperidin-3-yl)-1-oxoisindolin-4-yl)pentanamide (145).....	229
7.8.7	Synthesis 6-azido-N-(2-(2,6-dioxopiperidin-3-yl)-1-oxoisindolin-4-yl)hexanamide (146).....	230
7.8.8	Synthesis of PROTAC 147.....	231
7.8.9	Synthesis of PROTAC 148.....	232
7.8.10	Synthesis of PROTAC 149.....	233
7.8.11	Synthesis of PROTAC 150.....	234
7.8.12	Synthesis of PROTAC 151.....	235
7.8.13	Synthesis of PROTAC 152.....	236
7.8.14	Synthesis of PROTAC 153.....	237
7.9	Biochemical methods (Chapter 3).....	238

7.9.1	Plasmid Transformation	238
7.9.2	Stock formation	238
7.9.3	Medium-scale protein expression.....	238
7.9.4	Large scale protein expression	238
7.9.5	Immobilised metal ion affinity chromatography (IMAC).....	239
7.9.6	Ion exchange chromatography (IEX).....	240
7.9.7	Size Exclusion Chromatography	240
7.9.8	SDS-PAGE.....	240
7.9.9	Sample preparation (for SDS-PAGE)	241
7.9.10	ES ⁺ TOF MS	241
7.9.11	Trypsin digest MS	241
7.9.12	Circular Dichroism (CD)	241
7.9.13	Surface Plasmon Resonance (SPR)	242
7.9.14	Protein capture (NTA)	242
7.9.15	Protein capture (SA).....	242
7.10	Molecular biology methods (Chapter 2).....	243
7.10.1	THP-1 cell culture	243
7.10.2	THP-1 cell migration (chemotaxis) assays	243
7.10.3	Cell apoptosis assay	244
7.10.4	CCR2 internalisation assay	244
7.11	Molecular biology methods (Chapter 4).....	245
7.11.1	HMEC-1 cell culture	245
7.11.2	Cell viability (HMEC-1 cells).....	245
7.11.3	PROTAC degradation assay	246
7.11.4	Data processing	246
7.12	References	247
8.	Appendices.....	248
8.1	Trypsin digest for <i>hsCCL2</i> (Chapter 3, Section 3.7.1).....	248
8.2	SPR DKP screen (Chapter 3, Section 3.8.2)	248
8.3	SPR fragment screen - <i>hsCCL2</i> (Chapter 3, Section 3.9).....	250
8.4	HMEC-1 viability (Chapter 4).....	253

1. Introduction

1.1 The drug discovery process

Developing a drug and gaining market approval is a long and challenging process that can take 12-15 years to complete.¹ In addition to lengthy development times, the overall success rate is low, with an estimated 90% failure rate from drugs that enter clinical trials.²

From start to finish, the standard process for the development of a drug candidate incorporates four main stages (**Figure 1.1 (A)**). The first stage is early drug discovery, which takes place in both academia and industry. At this stage a series of drug-like molecules are developed for a validated biological target. If successful, the pharmacology and toxicology of the lead molecules are optimised and following this, the drug candidates are assessed in preclinical trials which are carried out in test-tube (*in vitro*), in animals (*in vivo*) or using computer modelling (*in silico*). If at this stage the drug candidate displays promising efficacy and low toxicity, clinical trials on humans can be undertaken. Unfortunately, this is where most drugs will fail and only 10% will be approved to become marketed medicines (by the Medicines and Healthcare products Regulatory Agency (MHRA) in the UK).³

Early drug discovery is an area in which many research scientists in academia are active (**Figure 1.1 (B)**). In this stage, a 'druggable' target must be identified and validated. Following this, hit screening is undertaken to find a drug candidate (or hit) that elucidates the desired biological response. If successful, hit-to-lead screening is undertaken to improve the potency and efficacy of the lead candidates, with these properties further optimised for use in pre-clinical trials.⁴

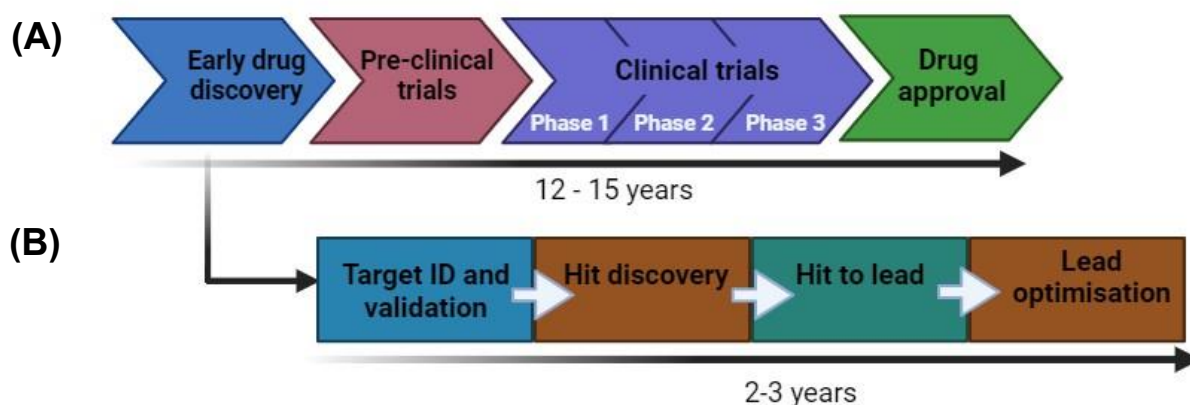


Figure 1.1 (A) The timeline for the overall drug discovery process. **(B)** The timeline for early drug discovery. [Image created using BioRender].

1.2 Hit discovery

Upon validation of a suitable biological target, the hit discovery process is required to identify a lead, or series of lead compounds, that can be further developed into drug-candidates. Methods such as high-throughput screening (HTS), fragment screening and structure-based drug design are commonly used in the hit discovery process.

1.2.1 High-throughput screening (HTS)

One of the most used methods for hit discovery is high-throughput screening (HTS) which enables a large library of compounds, typically made using parallel or combinatorial synthesis, to be screened against a biological target.^{5,6} HTS enables up to 10^3 compounds to be screened in one day with hits typically identified by the readout of an optical measurement (i.e., fluorescence or chemiluminescence).^{7,8}

AlphaScreen is an example HTS technique and is a bead-based assay that produces a chemiluminescent signal when 'donor' and 'acceptor' beads are in close proximity (under 200 nm).⁹ Donor beads contain a photosensitiser (e.g. phthalocyanine) which is irradiated by a laser at 680 nm, generating singlet state oxygen molecules. The oxygen molecules are then transferred to acceptor beads that contain chemiluminescent agents such as

rubrene, resulting in an energy emission that can be detected (between 520 - 620 nm for rubrene) (**Figure 1.2**).¹⁰

Over the past few years, progress in the field of HTS has worked towards its automisation and miniaturisation, speeding up the drug development process and thus reducing the overall costs. The previous example AlphaScreen, incorporates ultra-high throughput screening (uHTS) and can be performed in 1536-well plates.¹¹

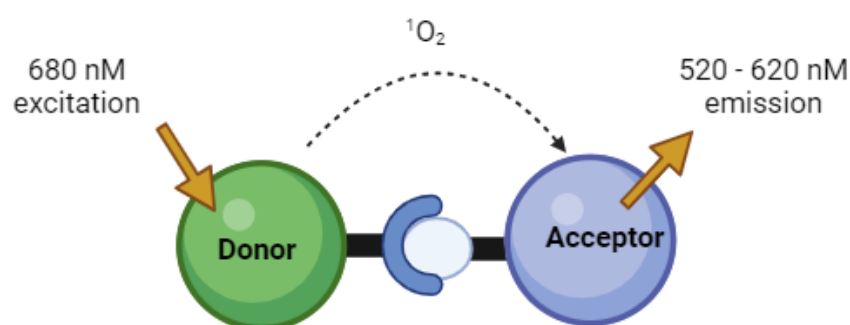


Figure 1.2 Key principles of an AlphaScreen assay. [Image created using BioRender].

1.2.2 DNA-encoded libraries (DELs)

Over the past decade, DNA-encoded libraries (DELs) have emerged as a new tool for both hit discovery and the rapid chemical synthesis of diverse libraries. DELs consist of molecules covalently attached to a specific DNA sequence which acts as a 'barcode' for identification. They are usually synthesised using a 'split and pool' method allowing the synthesis of a large library of molecules with high diversity.¹² Affinity screening can then be used to identify any hits from the DEL against a specific biological target. This typically involves the incubation of DELs with a target protein (often immobilised on a solid phase support), with positive candidates binding to the protein and non-binders being removed in subsequent wash steps. Following this, binders are detached from the protein and the unique DNA barcode is amplified using PCR, enabling the identification of the binders. This method is ultra-high throughput, enabling library sizes of up to 10^9 molecules to be screened using a small quantity of the DNA-tagged molecule.¹³

1.2.3 Fragment screening

Another method of hit discovery is fragment screening, in which compounds with low molecular weights (MW) and low chemical complexity, are screened at high concentrations against a desired biological target.¹⁴ This technique differs to HTS as smaller libraries, often between 500 and 2,000 compounds, are typically screened.¹⁵ In fragment screens, biophysical techniques such as surface plasmon resonance (SPR)¹⁵ and nuclear magnetic resonance (NMR)¹⁶, are often used for hit detection. The ideal fragment falls into a 'sweet spot' in which it is large enough to interact with the biological target but is small enough to limit unfavourable interactions. To achieve this, the rule of 3 (RO3) has been recommended and states that fragments should have a MW \leq 300 Da, hydrogen bond donors (HBD) /acceptors (HBA) \leq 3 and LogP \leq 3.¹⁷ Additionally, fragments should have \leq 20 atoms and should assemble libraries with high chemical diversity. Fragments are typically screened at a high concentration (between μ M and mM) to allow the identification of weak binders. This can provide a starting point to the discovery of the pharmacophore necessary for binding. FragLites are an example fragment-based strategy designed by Wood *et al.*¹⁸ FragLites are defined as molecules containing \leq 13 heavy atoms, a pharmacophoric doublet and a heavy halogen atom (bromine or iodine), enabling successful fragment screens encompassing a large chemical space from fewer molecules. This method enabled the discovery of binders for cyclin-dependant kinase (CDK2) with 9 out of the 31 fragments binding (as determined by X-ray crystallography). Example FragLites **1 - 4**, that displayed CDK2 binding, are shown in **Figure 1.3**.

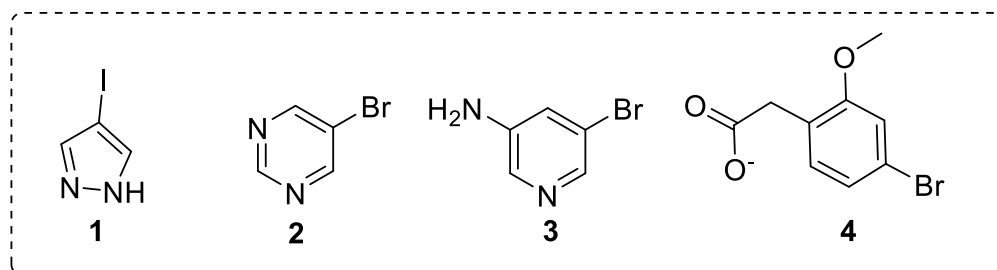


Figure 1.3 Example FragLite chemical structures (**1 – 4**) used in work by Wood *et al.*¹⁸

1.2.4 Structure-based drug design

The aforementioned screening techniques can be time-consuming and costly. Additionally, both HTS, DELs and fragment screening require little knowledge of the hit producing pharmacophore and rely on finding a lead from a large compound library. A more rational approach uses the structure of the biological target to aid molecular design. If 3D structural information e.g. an X-ray crystal structure, is available, then *in silico* screening methods can be used to dock databases of small molecules and fragments into binding sites.¹⁹ Alternatively, *de novo* design, in which chemical structures are designed from potential interactions with binding sites themselves, can be undertaken.²⁰

1.3 Chemical space and the RO5

Traditionally, Lipinski's rule of 5 (RO5) has been viewed as the 'gold standard' rule for producing the optimal oral absorption and cell permeability for small molecule drug-candidates.²¹ This rule stipulates that drug-like compounds should have a MW \leq 500 Da, with \leq 5 HBDs and \leq 10 HBAs, in addition to a LogP \leq 5. Despite the pharmacokinetic advantages of small molecules, they often lack specificity for biological targets. Certain biological processes are controlled by protein-protein interactions (PPIs) which have a large interaction surface, with key 'hot spots' necessary for disruption of affinity. Often larger structures that occupy a greater chemical space, such as peptides or biologics, are required to disrupt these interactions (**Figure 1.4**).¹³ However, due to their larger molecular size ($>$ 500 Da), these can suffer from poor cell permeability and are often used for extracellular rather than intracellular targets. Despite the increasing number of tools available for the generation of hits, many targets remain 'undruggable' and alternative methods are desired.

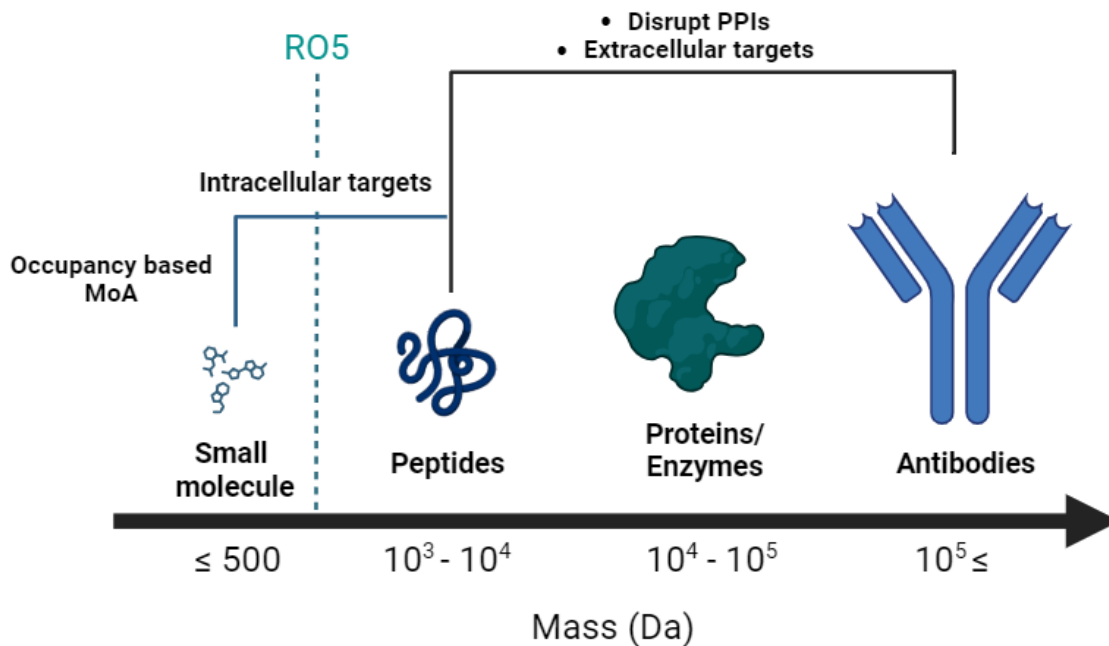


Figure 1.4 Chemical space exploited in drug discovery, from small molecule therapeutics to biologics. [Image created using BioRender].

1.4 'Undruggable' protein targets

'Undruggable' protein targets represent a major hurdle for the development of new and innovative therapeutics. It is estimated that 85% of all human proteins fall into this category and thus discovering solutions to tackle this challenge is a major focus for the pharmaceutical industry.²² Many proteins, such as small GTPases, phosphatases and transcription factors, are deemed 'undruggable' as they possess active sites with broad or shallow pockets that are difficult to target using traditional drug discovery methods (e.g. small molecule ligands).²³ This has led to the development of new strategies, for example, covalent regulators²⁴, allosteric modulators²⁵, PPI inhibitors²⁶ and targeted protein degraders²⁷, that enable 'undruggable' proteins to be therapeutically targeted.

Covalent regulators are small molecules that irreversibly bind to a target protein.²⁴ They typically contain an electrophilic warhead capable of binding to a nucleophilic amino acid (e.g. cysteine or lysine) inducing covalent inhibition that has the potential to be sustained

for a longer time.²⁸ Example warheads that can be incorporated are those containing acrylamide (**5**) which can covalently bind to cysteine residues, or sulfotetrafluorophenyl esters (**6**) that are capable of binding to lysine residues (**Figure 1.5**).^{28,24} Additionally, molecules that bind to allosteric sites have been developed to impact biological processes without competing against endogenous ligands.

Another field that has seen rapid growth over the past decade (particularly since the start of this research project) is the field of targeted protein degradation (TPD). TPD utilizes the body's natural disposal system to specifically destroy target proteins by proteasomal or lysosomal degradation.²⁹

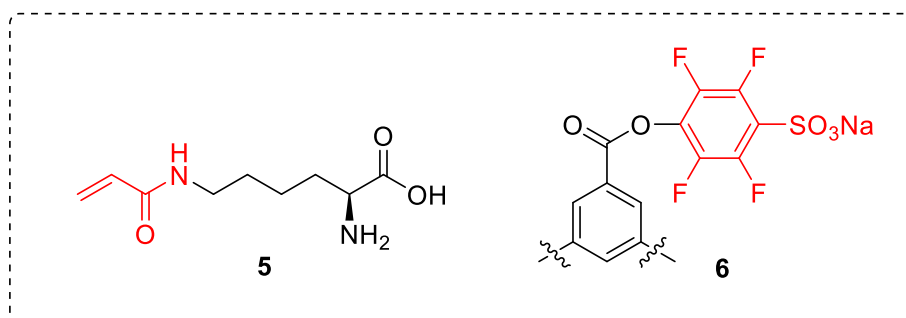


Figure 1.5 Example electrophilic warheads taken from reference 28. Acrylamide warheads (**5**) can be incorporated into proteins containing lysine. Warhead **6** can be incorporated into a peptide to react with a nucleophilic lysine on protein targets.

1.5 Targeted degradation

In eukaryotic cells, soluble short-lived or misfolded proteins are removed by the ubiquitin-proteasome system (UPS) and insoluble protein aggregates or macromolecular compounds are removed via lysosomes by endocytosis, phagocytosis, or autophagy.^{23,29} Many different targeted degraders, such as proteolysis targeting chimeras (PROTACs),³⁰ molecular glues (MGs),³¹ lysosome targeting chimeras (LYTACs)³² and ribonuclease targeting chimeras (RIBOTACs),³³ have been created to utilise these pathways to degrade specific targets.

1.6 The ubiquitin proteasome system (UPS)

By far the most researched targeted protein degraders are PROTACs and MGs; both of which exploit the ubiquitin proteasome system (UPS). The UPS utilises three main enzymes: a ubiquitin-activating enzyme (E1), a ubiquitin-conjugating enzyme (E2) and a ubiquitin ligase (E3). Initially, ubiquitin is attached to E1 through a thioester bond before it is transferred to E2 to form an E2-ubiquitin complex. This complex binds to E3 which mediates multiple transfers of ubiquitin to the target substrate. It is this ubiquitination that results in the recognition and subsequent degradation of the substrate by the proteasome (**Figure 1.6**).³⁴ PROTACs and MGs artificially replicate this process for **targeted** protein degradation.

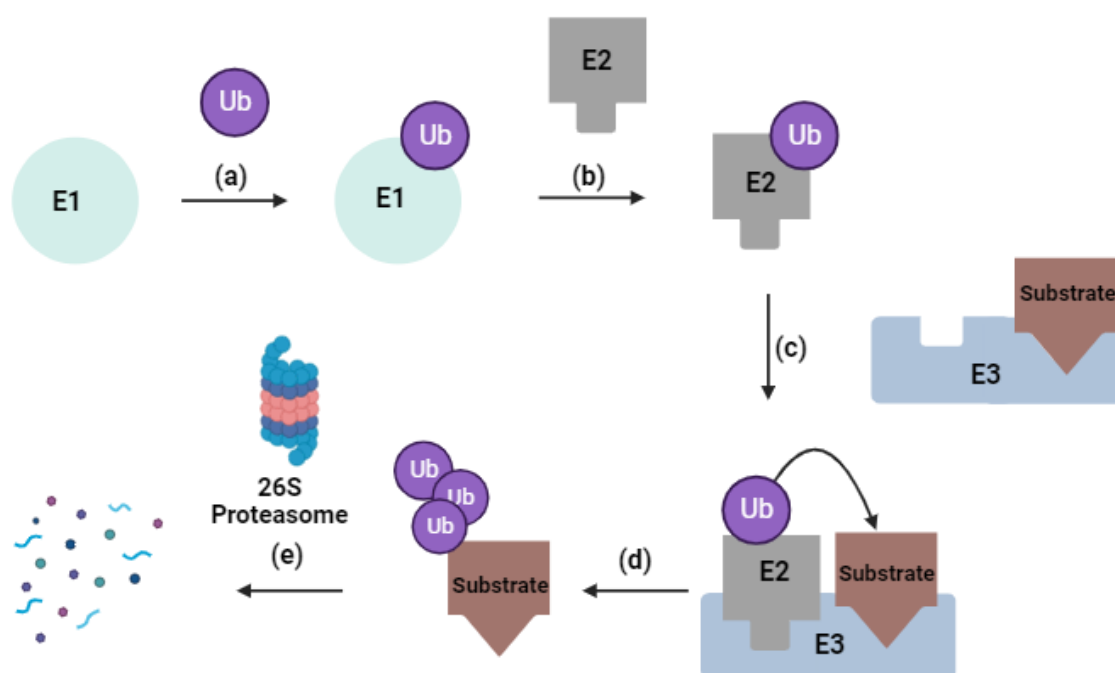


Figure 1.6 The function of the UPS. **(a)** Ubiquitination of E1. **(b)** Ubiquitin is transferred to E2. **(c)** The ternary complex (E2-E3-substrate) is formed. **(d)** Transfer of ubiquitin to the substrate from E2. **(e)** Proteasomal degradation of the polyubiquitinated substrate.[Image created using BioRender].

1.7 Proteolysis targeting chimeras (PROTACs)

PROTACs are heterobifunctional molecules consisting of three main parts; a ligand capable of binding to E3, a protein of interest (POI) warhead and a linker of optimised length and composition that connects them. The bifunctional molecule enables ternary complex formation between itself, the POI and E3. This facilitates the transfer of ubiquitin onto the POI which enables its proteasomal degradation (**Figure 1.7**).

PROTACs can offer several benefits over standard small molecule drug discovery. They have an 'event-driven' binding mode in contrast to the occupancy 'binding' mode of small molecules.³⁵ This enables traditionally 'undruggable' proteins (proteins with shallow, non-enzymatic binding pockets) to be targeted. Additionally, PROTACs can have a catalytic mode of action and thus require sub-stoichiometric doses, which can help to minimise off-target effects.³⁶

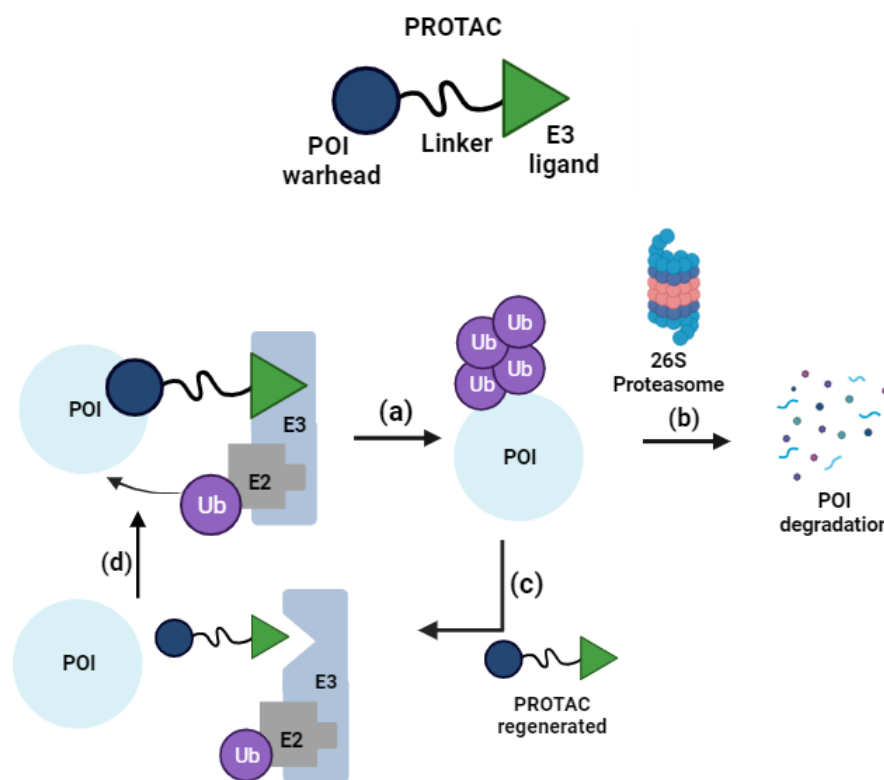


Figure 1.7 Targeted protein degradation using PROTACs. (a) Ubiquitination of the POI. (b) Proteasomal degradation of the POI. (c) PROTAC regeneration. (d) E3-PROTAC-POI ternary complex formation. [Diagram created using BioRender].

1.8 Elements of PROTAC design

1.8.1 E3 ligands

Although there are estimated to be over 600 E3 ligases in the human genome, the vast majority of PROTACs target cereblon (CRBN) or Von-Hippel Lindau (VHL) E3 ligases.³⁷ CRBN-targeting PROTACs typically incorporate analogues of the immunomodulatory drug (IMiD) thalidomide (**7**), such as pomalidomide (**8**) or lenalidomide (**9**), whereas small molecules VH101 (**10**) ($K_D = 185$ nM) and VH032 (**11**) ($K_D = 44$ nM) are typically incorporated into VHL-targeting PROTACs (**Figure 1.8**).^{38,39} In drug discovery, PROTACs that contain the CRBN ligands **7 - 9** are often preferred over VHL ligands **10 - 11**, due to their more favourable physicochemical profile (e.g. lower MWs and fewer HBDs) and an abundance of data regarding their biophysical and structural properties.⁴⁰

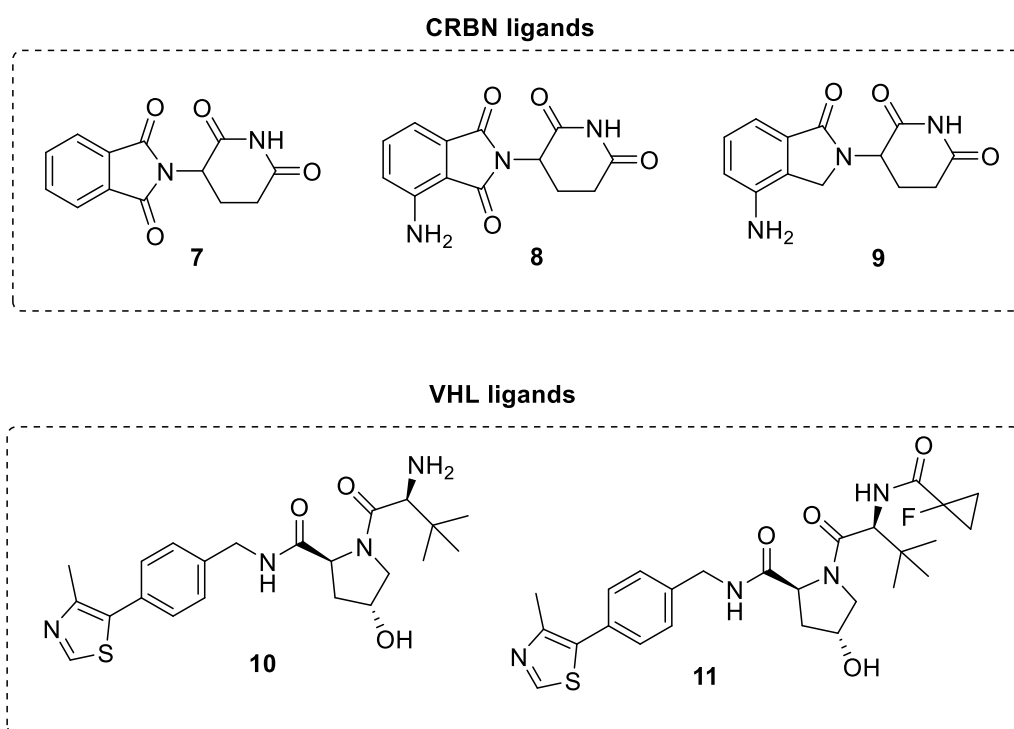


Figure 1.8 Chemical structures of CRBN (**7 - 9**) and VHL (**10 - 11**) small molecule ligands.

1.8.2 PROTAC linkers

Linker composition and length is a fundamental aspect of PROTAC design and is a key determinant for the successful formation of ternary complexes. Flexible linkers composed of ethylene glycol (PEG) or alkyl chains are widely used, with many bi-functionalised chains commercially available for incorporation into PROTACs.⁴¹ These chains are typically coupled to ligands by either amide, ether, ester or C-C bond formation (**Figure 1.9 (A)**). Alternatively, PROTACs can be assembled using a copper(I) catalysed azide-alkyne cycloaddition (click-chemistry); incorporating a 1,2,3-triazole into the PROTAC linker (**Figure 1.9 (B)**).⁴² Once the optimal linker length for the given PROTAC is established, replacement of the flexible PEG or alkyl linkers with more tailored, rigid linkers has been demonstrated to increase the PROTACs' physicochemical properties.⁴³ Typical rigid linkers can incorporate hetero(cycles), alkynes or spirocycles.³⁹ Example PROTACs that incorporate flexible linkers (**12** and **13**), a 1,2,3-triazole (**14**) and a rigid linker (**15**) are shown in **Figure 1.9 (C)**.

Linker design is an iterative process, with no 'hard and fast' rules regarding the optimal length and composition. PROTACs capable of degrading TANK-binding kinase 1 (TBK1) were synthesised in work by Crew *et al.*, where it was found that longer linker lengths improved targeted degradation.⁴⁴ In this work, PROTACs with linkers composed of < 12 atoms displayed no appreciable protein degradation. In contrast, a PROTAC (**12**) containing a linker of 15 atoms had a DC₅₀ⁱ of 12 nM and an even longer PROTAC, with a linker consisting of 29 atoms, was still appreciably active with a DC₅₀ of 292 nM. In contrast, work by Cyrus *et al.*, showed that shorter linker lengths were preferred for their PROTACs that targeted the estrogen receptor ER- α .⁴⁵ In this work, PROTACs with linker lengths > 16 atoms did not induce target degradation (at 25 μ M) but PROTACs with shorter linker lengths of 9, 12 and 16 atoms induced significant degradation at 1 μ M.

ⁱ DC₅₀ refers to the half-maximal degradation concentration.

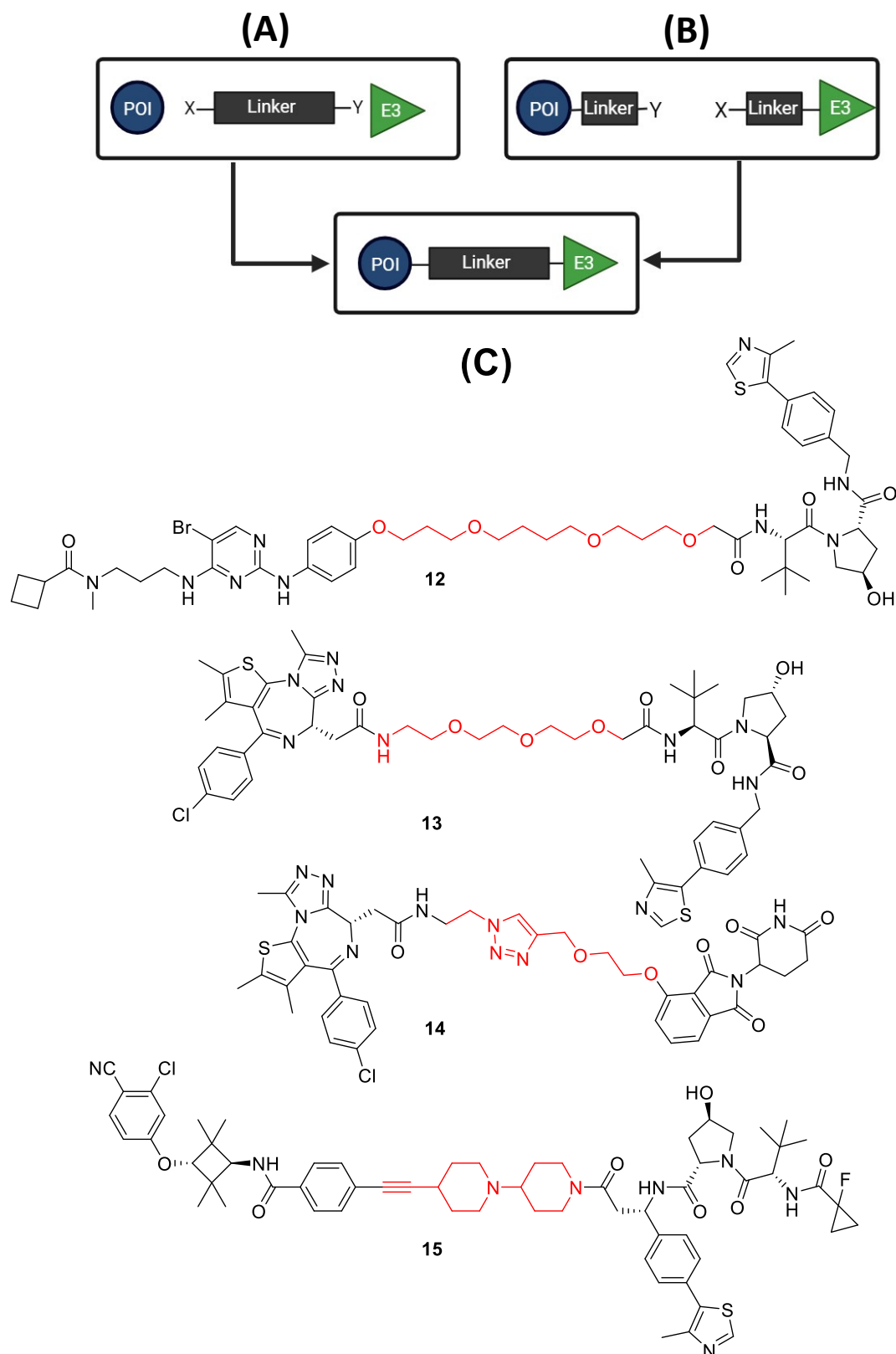


Figure 1.9 (A) Use of a bifunctional linker to bind both E3 and POI ligands. **(B)** Functionalising the POI or E3 (e.g., with alkyne and azide) and coupling the two parts (e.g., using click chemistry to form a 1,2,3-triazole). **(C)** Chemical structures of different PROTACs showing the variety of linker composition and length. Chemical structures of PROTACs **12** and **13** that contain flexible linkers PROTAC **14** which incorporates a 1,2,3-triazole and PROTAC **15** that incorporates a rigid piperidine linker.

In contrast to both these studies, Wurz *et al.*, produced a library of Brd4 (bromodomain-containing protein 4) targeting PROTACs, in which both the longest and shortest (**14**) PROTACs (with linkers containing 22 and 10 atoms respectively) enabled optimal target degradation ($DC_{50} = 0.2 \mu\text{M}$ and $0.49 \mu\text{M}$ respectively).⁴² This was a surprising result considering that PROTACs with intermediary linker lengths of 13 and 16 atoms displayed a reduction in potency ($DC_{50} > 5 \mu\text{M}$). It is clear from these selected studies, that the optimal PROTAC linker length and composition is greatly dependant on the target protein. Linker composition, in addition to length, is also a crucial element of PROTAC design. This was demonstrated in work by Han *et al.*, in their design of PROTACs that targeted the androgen receptor (AR).⁴³ The lead PROTAC (**15**) incorporated a rigid, piperidine linker that was able to increase AR degradation and improve solubility in comparison to flexible PROTACs of similar length. PROTAC **15** was able to successfully degrade AR with DC_{50} values $< 1 \text{ nM}$ in three AR+ cell lines.

1.8.3 Ternary complex formation, cooperativity, and the Hook effect

The formation of the ternary complex (POI-PROTAC-E3) is essential for effective PROTAC induced degradation, as it enables the transfer of ubiquitin from E3 to the POI. Additionally, Bondeson *et al.*, showed that the binding affinity of a PROTAC for the POI does not always correlate with protein degradation.⁴⁶ For example in their work, a relatively weakly binding PROTAC for p38 α ($K_D = 11 \mu\text{M}$) had a DC_{50} of 210 nM, whereas a strongly binding VHL-PROTAC for Axl ($K_D = 26 \text{ nM}$) could not induce degradation at concentrations up to 10 μM . From this, it was proposed that ternary complex formation, rather than POI binding affinity, was more essential for target degradation. Additionally, steric interactions or unfavourable binding events between the POI and E3, can prevent the ternary complex.

For PROTAC ternary complexes, the extent of protein-protein interactions (PPIs) between the POI and E3 is termed 'cooperativity' (represented by the value α). Where there are favourable PPIs, cooperativity is positive and $\alpha > 1$, but for unfavourable or steric

interactions, the converse is true and $\alpha < 1$.⁴⁷ MZ1 (**13**) is a PROTAC designed and synthesised by the Ciulli group, which was able to degrade Brd4^{BD2} by 90% at a 1 μ M dose.⁴⁸ In 2017, they solved the crystal structure for the ternary complex Brd4^{BD2}-MZ1-VHL; providing key insights on its formation.⁴⁹ It was shown that MZ1 (**13**) folds itself in a way that allows it to 'sandwich' between both proteins, allowing the formation of new PPIs between VHL and Brd4^{BD2}. Another interesting find was an additional interaction between the PEG linker with the ternary complex; again, highlighting the importance of linker composition. Following this, the Brd4^{BD2}-MZ1-VHL complex was found to have a high cooperativity ($\alpha = 18$), as determined by isothermal titration calorimetry (ITC). To assess how cooperativity affected ternary complex formation, a Brd4^{BD2} mutant (named QVK) which lacked the key residues required for Brd4^{BD2}-VHL interactions but retained those required for MZ1 binding (**13**), was developed. When QVK was used in place of Brd4^{BD2}, MZ1 (**13**) binding was unaffected but cooperativity had been greatly reduced ($\alpha = 4$). This directly correlated to a reduction in ternary complex formation. This work emphasised the importance of positive cooperativity, rather than binding affinity, for enabling ternary complex formation.

It's well established that ternary equilibria exhibit bell-shaped dose response curves.⁴⁷ Resulting from this, if the PROTAC dose is too high, the likelihood of ternary complex formation is reduced due to the favoured formation of binary complexes (**Figure 1.10**). This event is termed the 'Hook effect' and typically occurs with PROTAC concentrations between 1 – 10 μ M.⁵⁰ In addition, it is believed that high cooperativity can minimise the Hook effect.

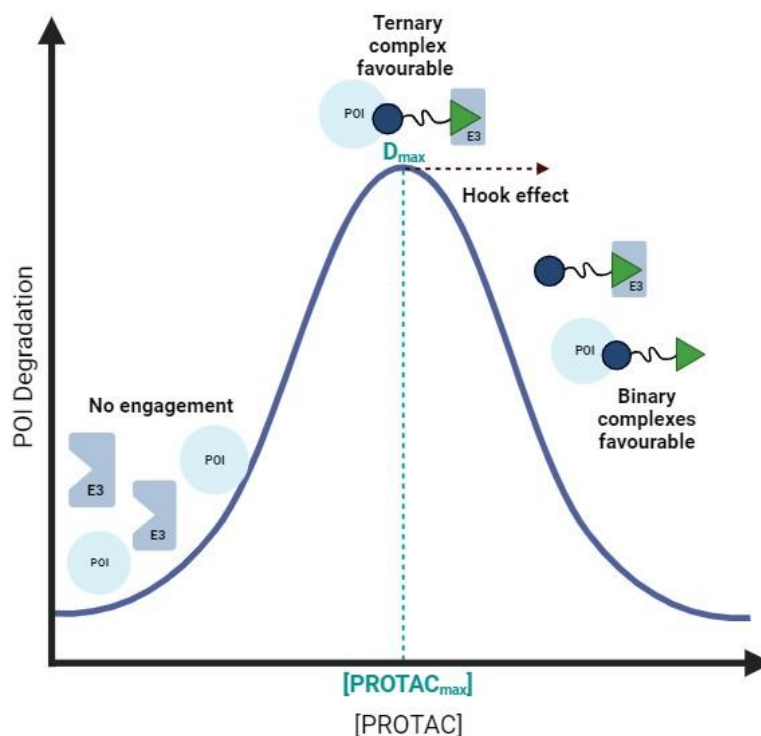


Figure 1.10 Dose-response curve for PROTAC ternary complexes. At low [PROTAC] there is little engagement between E3 and POI. As [PROTAC] increases, the formation of the ternary complex becomes favourable until the concentration reaches [PROTAC_{max}] in which POI degradation will be at its maximum (D_{max}). If [PROTAC] becomes too high, the Hook effect is observed and binary complexes are favoured. [Image created using BioRender].

1.8.4 Beyond the rule of 5 (bRO5)

As stated in **Section 1.3**, traditionally Lipinski's RO5 has been used as a metric for designing therapeutics that are likely to have good cell permeability and oral availability. As PROTACs combat intracellular targets, it is important that they can sufficiently cross cell membranes. However, PROTACs lie in the beyond rule of 5 (bRO5) chemical space, with the molecular weights for the majority of PROTACs between 600 and 1,400 Da (with many successful PROTACs even larger) (**Figure 1.11**).⁵¹ Designing PROTACs with sufficient cell permeability and aqueous solubility can be challenging. CRBN-PROTACs generally have greater permeability prospects due to the small molecule E3 ligands which fall within the RO5.⁵¹ However, it has also been shown that the folding of a PROTAC

through intramolecular hydrogen bonding can also increase its permeability by reducing its solvent exposed area.^{52,53}

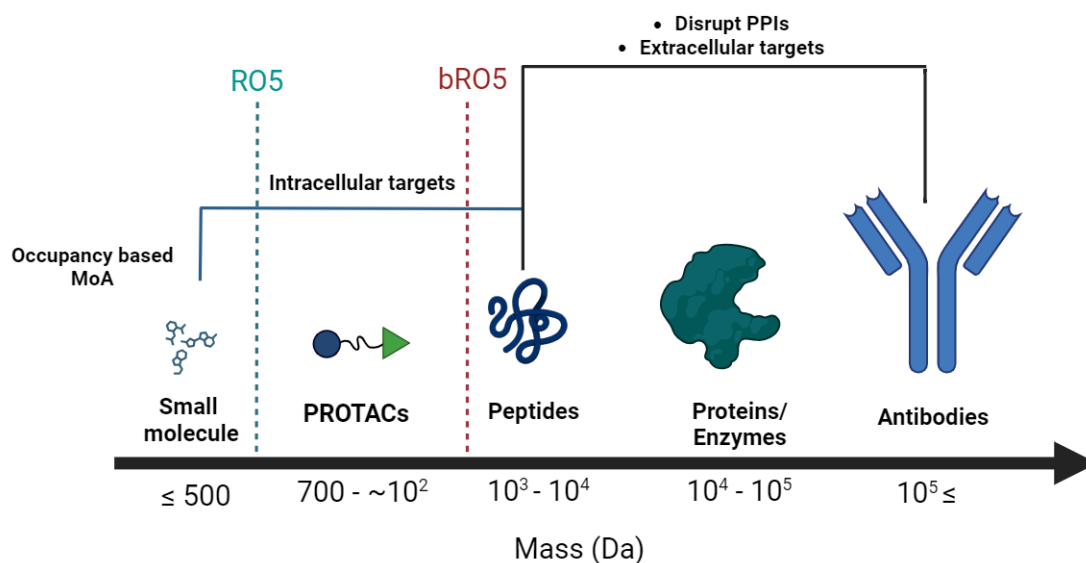


Figure 1.11 PROTACs in the chemical space of drug discovery. [Image created using BioRender].

1.9 Molecular glues (MGs)

Like PROTACs, molecular glues (MGs) also harness the UPS for targeted protein degradation. However, MGs are monovalent, small molecules with no linker and have lower MWs compared with PROTACs. They also differ in their mode of action in which they bind to E3 but may not have any affinity for the POI, inducing ternary complexes only through stabilising PPIs between E3 and the POI (**Figure 1.12**). MGs act catalytically, requiring sub-stoichiometric doses and typically they obey the RO5 leading to improved pharmacokinetic properties in comparison to PROTACs.⁵⁴ Example MGs are thalidomide (**7**) and its analogues pomalidomide (**8**) and lenalidomide (**9**) that induce degradation via CRBN. They can simultaneously bind to the shallow, hydrophobic pocket on CRBN, whilst forming a ternary complex with targets such as transcription factors IKZF1 and IKZF3, inducing their degradation.⁵⁵ This has led to the approval of lenalidomide (**9**) as a treatment for multiple myeloma (MM). Despite the demonstrated benefits of MGs, they have

historically been discovered serendipitously, whereas PROTACs have a more rational design. Though, the techniques discussed in **Section 1.2** can be used to aid their discovery.

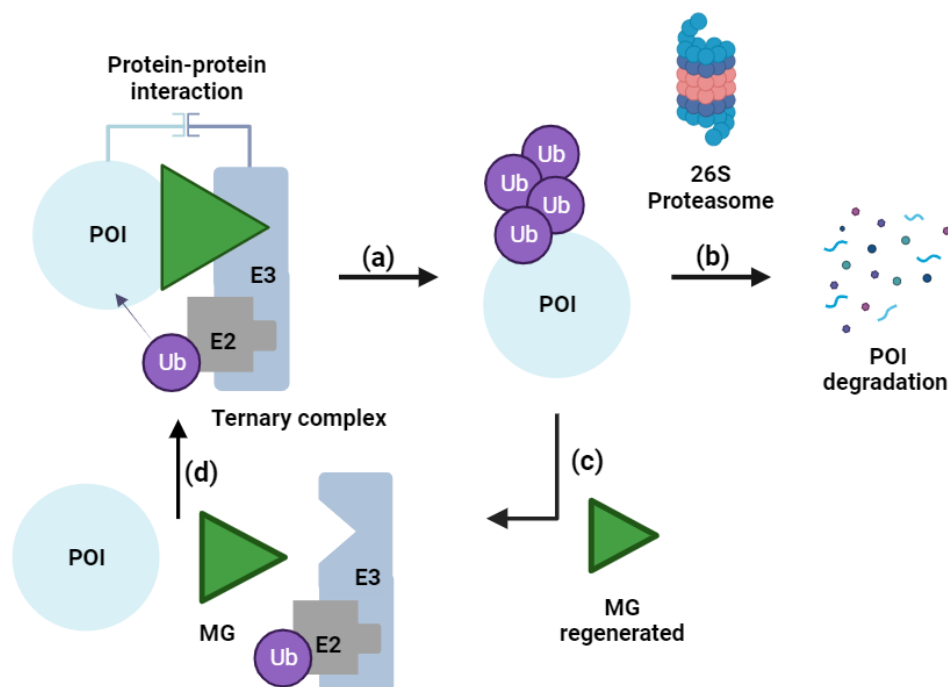


Figure 1.12 Targeted degradation using MGs. (a) Ubiquitination of the POI. (b) Proteasomal degradation of the POI. (c) MG regeneration. (d) E3-MG-POI ternary complex formation. [Diagram created using BioRender].

1.10 Lysosome targeting chimeras (LYTACs)

Lysosomes are the primary degradation compartment of a cell, containing enzymes that degrade macromolecules that enter the cell by endocytosis, phagocytosis or autophagy.²⁹ Lysosome targeting chimeras (LYTACs) have been designed to target extracellular or membrane-bound proteins that PROTACs cannot access. This work was pioneered by the Bertozzi group and allows the scope of targeted degraders to increase.³² The LYTACs designed in this initial work, exploited a lysosome-binding receptor CI-M6PR which when bound to, internalised and shuttled receptor-complexes into lysosomes where they were degraded (**Figure 1.13**). By the creation of a bivalent molecule, containing a CI-M6PR binding glycopeptide and a protein specific antibody, the degradation of extracellular

targets could be achieved. This was demonstrated effectively with a LYTAC capable of degrading membrane-bound protein EGFR. The LYTAC contained both the CI-M6PR binding glycopeptide and cetuximab – an approved antibody for EGFR. At 100 nM, the LYTAC effectively degraded > 70% of EGFR, with no impact on the level of CI-M6PR.

This work was built upon by the same group in which a different surface receptor shuttle was exploited.⁵⁶ Liver specific trafficker ASGPR, can bind glycoproteins bearing GalNAc or Gal, internalising them via clathrin mediated endocytosis. A LYTAC was designed by the Bertozzi group to exploit this receptor and degrade EGFR, with the maximum degradation occurring at 10 nM.

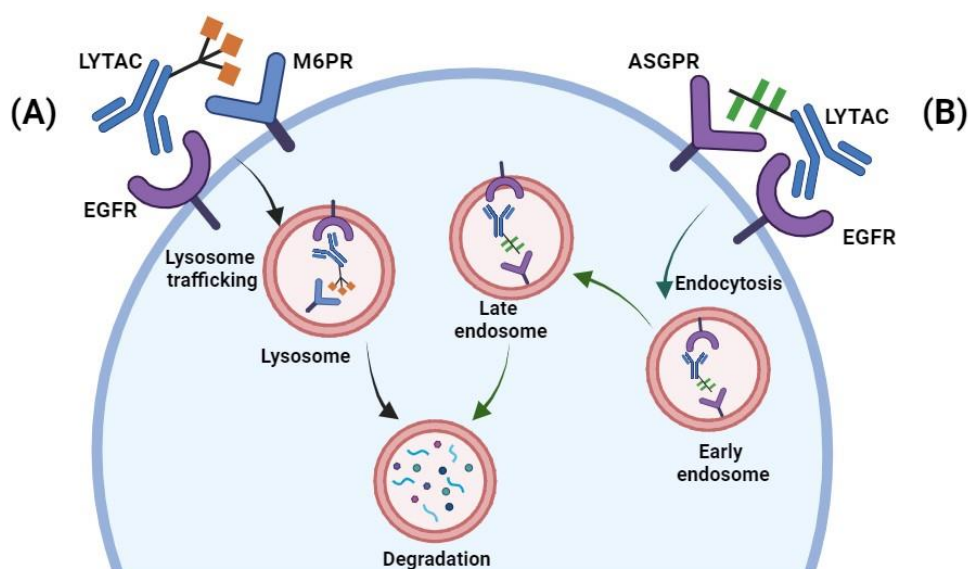


Figure 1.13 The two discussed mechanisms for targeted degradation using LYTACs. **(A)** Degradation of EGFR via lysosome receptor M6PR. Ternary complex formation between EGFR and M6PR allows internalisation into lysosomes where EGFR is degraded (M6PR is recycled back to the membrane).³² **(B)** Degradation of EGFR using membrane-bound receptor ASGPR. Ternary complex between EGFR and ASGPR allows internalisation by endocytosis. Complex goes through the early endosome, to the late endosome followed by eventual degradation of EGFR and recycling of ASGPR back to the membrane.⁵⁶ [Diagram created using BioRender].

1.11 Ribonuclease targeting chimeras (RIBOTACs)

Recently, targeted degraders have been developed for “undruggable”, non-protein substrates such as RNA. Traditional methods for the therapeutic intervention of RNA has involved the use of antisense oligonucleotides however, such molecules have proven

challenging to progress clinically due to delivery and uptake issues.⁵⁷ With more optimal pharmacokinetic properties, small molecules have been used to bind more structured regions of RNA.⁵⁸ However, typically these binders exert no biological effect leading to the characterisation of RNA as an ‘undruggable’ target. In 2023, the Disney group designed ribonuclease-targeting chimeras (RIBOTACs), connecting an RNA small molecule binder with an RNase-L recruiter, to enable the targeted degradation of RNA (**Figure 1.14**).³³ In this work they designed RIBOTAC **16** to degrade pre-miR-155, which is associated with inflammatory diseases and cancer. *In vitro* assays showed that a treatment of 100 nM of RIBOTAC **16** reduced mature miR-155 by $71 \pm 10\%$ (over 48 h) with no appreciable toxicity.

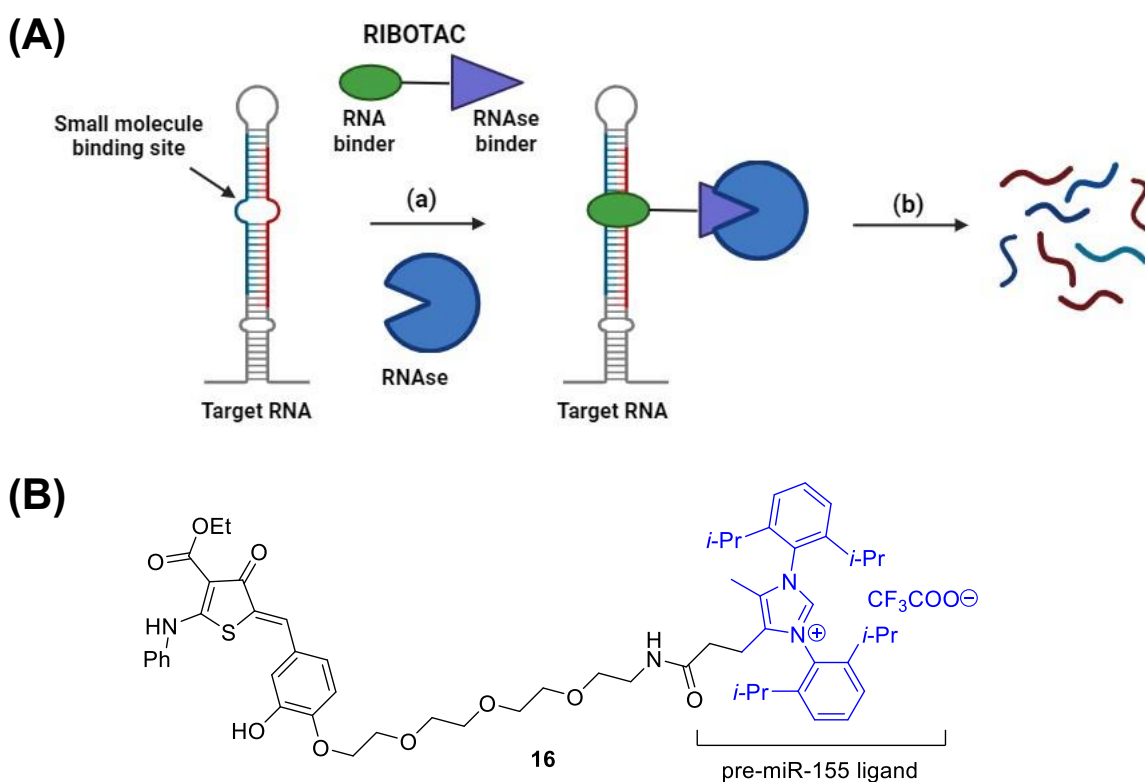


Figure 1.14 (A) Degradation of RNA using a RIBOTAC. **(a)** Ternary complex formation between RNA-RIBOTAC-RNase. **(b)** Target RNA is degraded by RNase. [Image created using BioRender]. **(B)** Chemical structure of RIBOTAC **16** from reference 33. The pre-miR-155 ligand is highlighted blue.

1.12 Peptide-based PROTACs (p-PROTACs)

In addition to PROTACs that incorporate small molecule warheads, peptide-based PROTACs (p-PROTACs) have been developed to enable the recruitment of targets with shallow, non-enzymatic binding pockets as well as to provide greater target selectivity.⁵⁹ Although the use of p-PROTACs can increase the scope of degradation targets, they can suffer from poor cell permeability and low proteolytic stability.

Wang *et al.*, developed a p-PROTAC to target FOXM1; a transcription factor associated with a variety of cancers (e.g. breast and prostate) (**Table 1.1 – Entry 1**).⁶⁰ In this work, 50 μM of PROTAC-FOXM1 was able to degrade over 50% FOXM1 in HEPG2 cells (over 24 h). Another p-PROTAC (xStAx-VHLL) was developed by Liao *et al.* to degrade β -catenin, which plays a key role in the proliferation and survival of cancer cells (**Table 1.1 – Entry 2**).⁶¹ xStAx-VHLL incorporated a stapled peptide warhead (xStAx) as this can improve peptide membrane permeability and proteolytic stability.⁶² Overall, 70 μM of xStAx-VHLL was able to significantly degrade β -catenin in HEK293T cells when treated for 24 h. Another example is PRTC which was designed by Ma *et al.*, to degrade CREPT; a protein highly expressed in pancreatic cancer (**Table 1.1 – Entry 3**).⁶³ PRTC was shown to successfully degrade CREPT with a DC_{50} of 10 μM (Panc-1 cells) and was also able to reduce mice xenograft tumours when PRTC (10 mg/kg) was administered every 2 days for 4 weeks.

Table 1.1 Example p-PROTACs. E3 ligase ligand/recruiter is shown in blue, cell-penetrating sequence shown in red and peptide warhead shown in green.

Entry	Target	Sequence	Ref
1.	FOXM1	Pomalidomide-PEG ₂ -GLSSMHAPPLR-GRKKRRQRRRPPQQ	FOXM1-PROTAC ⁶⁰
2.	β-catenin	Ac-RRWPRS ₅ LDS ₅ HVRRVWR-Ahx-ALAPYIP-NH ₂ ⁱ	xStAx-VHLL ⁶¹
3.	CREPT	KRRRR-VRALKQKYEELKKEKESLVDK-Ahx-LAP(OH)YI-NH ₂	PRTC ⁶³

ⁱS₅, S-2-(4'pentynyl alanine) is the residue used for peptide stapling. Ahx, 6-aminohexanoic acid.

1.13 Targeted protein degraders in clinical trials

As of September 2023, there were 29 targeted protein degraders in clinical trials of which 16 were PROTACs and 13 were MGs.⁶⁴ Technologies degrading extracellular targets such as LYTACs, are yet to progress into clinical trials as research is still in its infancy. An example of an MG that has moved into clinical trials is IKZF1/3 degrader CC-220 (**17**) (**Table 1.2 – Entry 1**) which is currently in phase II for the treatment of multiple myeloma (MM). CC-220 (**17**) has shown enhanced CRBN binding in comparison with traditional IMiDs (such as lenalidomide (**9**)) due to its greater molecular complexity and hydrophobicity.

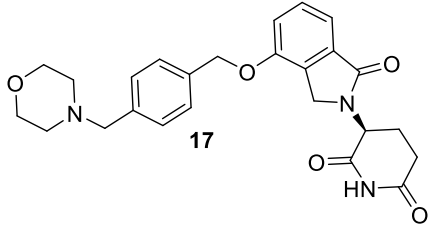
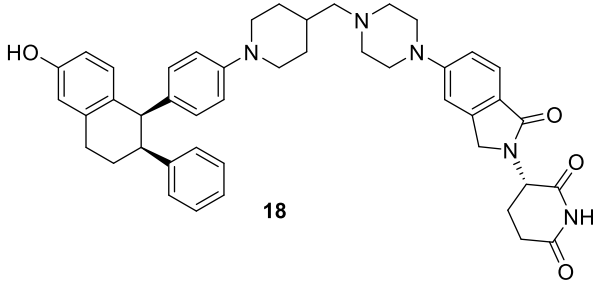
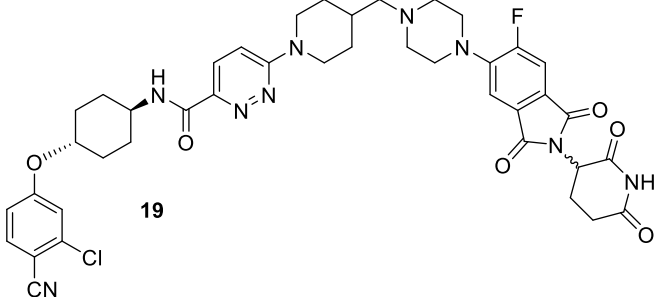
Of the PROTACs in clinical trials, 6 PROTACs target CRBN whereas only one targets VHL.ⁱⁱ It is interesting to note that the variation in biological targets is relatively low; there are 29 PROTACs in clinical trials for the degradation of 12 different targets. In addition, although this technology was initially designed to target the 'undruggable', PROTACs currently in clinical trials contain potent POI binders designed for already druggable targets.

ⁱⁱ This corresponds to PROTACs in which the E3 targeted has been made public knowledge. Out of 29 PROTACs in trials, the ligase targeted for 9 of them have not been released. One PROTAC also targets DCAF15.

The most advanced PROTACs in clinical trials are ARV-471 (**18**) and ARV-110 (**19**) developed by the company Arvinas which was founded by the original inventor of PROTAC technology Professor Craig Crews.⁶⁵ ARV-471 (**18**) (**Table 1.2 – Entry 2**) is an ER degrader used for the treatment of ER+/HER2- locally advanced or metastatic breast cancer and is currently in phase III clinical trials. ARV-110 (**19**) (**Table 1.2 – Entry 3**) is an AR degrader for the treatment of metastatic castration resistant prostate cancer (mCRPC). Initial data has shown ARV-110 (**19**) to be tolerated up to doses of 420 mg and was the first example of a PROTAC drug working successfully in humans. Both the progression of MGs and PROTACs into clinical trials represents a promising future for UPS exploiting degraders.

The structures of both PROTACs **18** and **19** were released in 2021, with both containing rigid linkers that incorporate piperazine/piperidine groups. Both PROTACs are CRBN targeting with analogues of thalidomide acting as their E3 ligand. ARV-110 (**19**) incorporates 3-fluorothalidomide, whereas ARV-471 (**18**) incorporates S-lenalidomide which is connected at the 3 position. In ARV-471 (**18**), the lenalidomide stereocenter is defined which contrasts with many CRBN-PROTACs in which the racemic form is used.

Table 1.2 Example UPS exploiting degraders that have advanced to phase II or III clinical trials. [Data obtained from reference 65].

Degrader	Structure	Target
1. CC-220 (17) (MG) ⁱⁱⁱ		IKZF1/3 (MM)
2. ARV-471 (18) (PROTAC) ^{iv}		ER+ /HER2- (Breast Cancer)
3. ARV-110 (19) (PROTAC) ^v		AR mCRPC

ⁱⁱⁱ Clinical trial number: NCT02773030

^{iv} Clinical trial number: NCT05654623

^v Clinical trial number: NCT03888612

1.14 Project Aims

The overarching aim of this work is to seek new avenues for the development of therapeutics that target chemokine ligand 2 (CCL2) and the Epstein-Barr virus nuclear antigen-1 (EBNA1). To enable this, the first aim is to further understand the mode of action for a group of small, cyclic dipeptides (diketopiperazines, DKPs), that were shown to inhibit the CCL2-mediated chemotaxis of THP-1 cells in previous work.^{66,67,68} The second aim is to incorporate the DKPs as POI warheads in potential CCL2-targeting PROTACs. Subsequently, it is an aim of this thesis to incorporate analogues of a pentapeptide sequence, that has been shown to disrupt the dimerization of EBNA1⁶⁹, into potential EBNA1-targeting PROTACs.

Small cyclic dipeptides known as diketopiperazines (DKPs) have shown potential as selective inhibitors of CCL2-mediated THP-1 chemotaxis. Early biological work pointed towards these molecules as acting as CCL2 inhibitors, however this has yet to be shown in biophysical studies. Additionally, the micromolar potency of the DKPs (within chemotaxis assays) is deemed to be too low to take forward as therapeutics *per se*. The first aim of this project is to synthesise a new library of DKPs using solid phase peptide synthesis (SPPS), allowing the incorporation of unnatural and fluorinated amino acids to expand the current library. A second aim is to test these compounds in chemotaxis assays to assess their inhibitory properties, as well as in CCR2 internalisation assays, to further assess their mode of action. It is also an aim to synthesise a series of DKPs containing functionalities that would enable their incorporation within a PROTAC by attachment to commercially obtained linkers. The PROTACs will be tested using cell-based assays to assess their degradation potential for CCL2. This will enable the assessment as to whether targeted degradation provides a more effective route of targeting CCL2 over standard small molecule inhibition.

The recombinant overexpression of CCL2 in *E. coli* will be undertaken to enable ligand-binding studies between CCL2 and the prepared DKPs. There are few CCL2 binders/inhibitors reported in literature (many of which are peptide based) so finding small molecules that are capable of its target is of key interest. To address this a second in-house library that incorporates fluorinated fragments will also be screened in an effort to identify novel CCL2 binders.

Finally, an aim of this research is to develop a series of PROTACs incorporating a short, pentapeptide POI warhead, that can selectively degrade EBNA1. EBNA1 is a protein involved in the progression of the Epstein-Barr virus (EBV) of which there are currently no clinically available treatments. The PROTACs designed will target the CRBN and incorporate a variety of linkers with different lengths, compositions and points of attachment. The PROTACs synthesised in this work will be involved in a larger library of EBNA1-PROTACs that target VHL proteins, alongside others that are completely peptide based (p-PROTACs) or small molecule based. The library will finally be screened in cell-based EBNA1 degradation assays.

1.15 References

1. N. Singh, P. Vayer, S. Tanwar, J.-L. Poyet, K. Tsaioun and B. O. Villoutreix, *Front. Drug Discov.*, 2023, **3**, 1–11.
2. D. Sun, W. Gao, H. Hu and S. Zhou, *Acta Pharm. Sin. B.*, 2022, **12**, 3049–3062.
3. N. A. M. Tamimi and P. Ellis, *Nephron – Clin. Pract.*, 2009, **113**, 125–131.
4. J. P. Hughes, S. S. Rees, S. B. Kalindjian and K. L. Philpott, *Br. J. Pharmacol.*, 2011, **162**, 1239–1249.
5. V. Blay, B. Tolani, S. P. Ho and M. R. Arkin, *Drug Discov. Today.*, 2020, **25**, 1807–1821.
6. R. Liu, X. Li and K. S. Lam, *Curr. Opin. Chem. Biol.*, 2017, **38**, 117–126.
7. M. E. A, B. R. R and R. Radhakrishnan, *J. Appl. Pharm. Sci.*, 2011, **1**, 2–10.
8. P. Szymański, M. Markowicz and E. Mikiciuk-Olasik, *Int. J. Mol. Sci.*, 2012, **13**, 427–452.
9. R. M. Eglén, T. Reisine, P. Roby, N. Rouleau, C. Illy, R. Bossé and M. Bielefeld, *Curr. Chem. Genomics.*, 2008, **1**, 2–10.
10. S. Taouji, S. Dahan, R. Bossé and E. Chevet., *Curr. Genom.*, 2009, **10**, 93 – 101.
11. S. Harald, *Kunststoffe Int.*, 2009, **99**, 37–40.
12. Y. Shi, Y. R. Wu, J. Q. Yu, W. N. Zhang and C. L. Zhuang, *RSC Adv.*, 2021, **11**, 2359–2376.
13. J. Ottl, L. Leder, J. V. Schaefer and C. E. Dumelin, *Molecules.*, 2019, **24**, 1–22.
14. Q. Li, *Front. Mol. Biosci.*, 2020, **7**, 1–13.
15. C. A. Shepherd, A. L. Hopkins and I. Navratilova, *Prog. Biophys. Mol. Biol.*, 2014, **116**, 113–123.
16. M. J. Harner, A. O. Frank and S. W. Feslik, *J. Biomol NMR.*, 2013, **56**, 65-75.
17. P. Kirsch, A. M. Hartman, A. K. H. Hirsch and M. Empting, *Molecules.*, 2019, **24**, 4309.
18. D. J. Wood, J. D. Lopez-Fernandez, L. E. Knight, I. Al-Khawaldeh, C. Gai, S. Lin, M. P. Martin, D. C. Miller, C. Cano, J. A. Endicott, I. R. Hardcastle, M. E. M. Noble and M. J. Waring, *J. Med. Chem.*, 2019, **62**, 3741–3752.
19. B. Shaker, S. Ahmad, J. Lee, C. Jung and D. Na, *Comput. Biol. Med.*, 2021, **137**, 104851.
20. M. Batool, B. Ahmad and S. Choi, *Int. J. Mol. Sci.*, 2019, **20**, 2783.
21. C. A. Lipinski, *J. Pharmacol. Toxicol. Methods.*, 2000, **44**, 235–249.

22. T. K. Neklesa, J. D. Winkler and C. M. Crews, *Pharmacol. Ther.*, 2017, **174**, 138–144.
23. X. Xie, T. Yu, X. Li, N. Zhang, L. J. Foster, C. Peng, W. Huang and G. He, *Signal Transduct. Target. Ther.*, 2023, **8**, 335-405.
24. L. Boike, N. J. Henning and D. K. Nomura, *Nat. Rev. Drug Discov.*, 2022, **21**, 881–898.
25. S. Lu and J. Zhang, *Drug Discov. Today.*, 2017, **22**, 447–453.
26. H. Lu, Q. Zhou, J. He, Z. Jiang, C. Peng, R. Tong and J. Shi, *Signal Transduct. Target. Ther.*, 2020, **5**, 213.
27. S. Zeng, Y. Ye, H. Xia, J. Min, J. Xu, Z. Wang, Y. Pan, X. Zhou and W. Huang, *Eur. J. Med. Chem.*, 2023, **261**, 115793.
28. V. Y. Berdan, P. C. Klauser and L. Wang, *Bioorganic Med., Chem.*, 2021, **29**, 115896.
29. P. Heitel, *Molecules.*, 2023, **28**, 690.
30. N. Guedeney, M. Cornu, F. Schwalen, C. Kieffer and A. S. Voisin-Chiret, *Drug Discov. Today.*, 2023, **28**, 103395.
31. J. A. Dewey, C. Delalande, S. A. Azizi, V. Lu, D. Antonopoulos and G. Babnigg, *J. Med. Chem.*, 2023, **66**, 9278–9296.
32. S. M. Banik, K. Pedram, S. Wisnovsky, G. Ahn, N. M. Riley and C. R. Bertozzi, *Nature.*, 2020, **584**, 291–297.
33. Y. Tong, Y. Lee, X. Liu, J. L. Childs-Disney, B. M. Suresh, R. I. Benhamou, C. Yang, W. Li, M. G. Costales, H. S. Haniff, S. Sievers, D. Abegg, T. Wegner, T. O. Paulisch, E. Lekah, M. Grefe, G. Crynen, M. Van Meter, T. Wang, Q. M. R. Gibaut, J. L. Cleveland, A. Adibekian, F. Glorius, H. Waldmann and M. D. Disney, *Nature.*, 2023, **618**, 169–179.
34. G. Kleiger and T. Mayor, *Trends Cell Biol.*, 2014, **24**, 352-359.
35. J. Salami and C. M. Crews, *Science.*, 2017, **355**, 1163–1167.
36. D. P. Bondeson, A. Mares, I. E. D. Smith, E. Ko, S. Campos, A. H. Miah, K. E. Mulholland, N. Routly, D. L. Buckley, J. L. Gustafson, N. Zinn, P. Grandi, S. Shimamura, G. Bergamini, M. Faelth-Savitski, M. Bantscheff, C. Cox, D. A. Gordon, R. R. Willard, J. J. Flanagan, L. N. Casillas, B. J. Votta, W. Den Besten, K. Famm, L. Kruidenier, P. S. Carter, J. D. Harling, I. Churcher and C. M. Crews, *Nat. Chem. Biol.*, 2015, **11**, 611–617.
37. Y. Liu, J. Yang, T. Wang, M. Luo, Y. Chen, C. Chen, Z. Ronai, Y. Zhou and E. Ruppin, *Nat Comm.*, 2023, **14**, 6509.
38. C. J. Diehl and A. Ciulli, *Chem. Soc. Rev.*, 2022, **51**, 8216–8257.

39. N. A. Zografou-Barredo, A. J. Hallatt, J. Goujon-Ricci, C. Cano. *Bioorg. Med. Chem.*, 2023, **88**, 117334.
40. C. Wang, Y. Zhang, Y. Wu and D. Xing, *Eur. J. Med. Chem.*, 2021, **225**, 113749.
41. R. I. Troup, C. Fallan and M. G. J. Baud, *Explor. Target. Anti-tumor Ther.*, 2020, **1**, 273–312.
42. R. P. Wurz, K. Dellamaggiore, H. Dou, N. Javier, M. C. Lo, J. D. McCarter, D. Mohl, C. Sastri, J. R. Lipford and V. J. Cee, *J. Med. Chem.*, 2018, **61**, 453–461.
43. X. Han, C. Wang, C. Qin, W. Xiang, E. Fernandez-Salas, C. Y. Yang, M. Wang, L. Zhao, T. Xu, K. Chinnaswamy, J. Delproposto, J. Stuckey and S. Wang, *J. Med. Chem.*, 2019, **62**, 941–964.
44. A. P. Crew, K. Raina, H. Dong, Y. Qian, J. Wang, D. Vigil, Y. V. Serebrenik, B. D. Hamman, A. Morgan, C. Ferraro, K. Siu, T. K. Neklesa, J. D. Winkler, K. G. Coleman and C. M. Crews, *J. Med. Chem.*, 2018, **61**, 583–598.
45. K. Cyrus, M. Wehenkel, E. Y. Choi, H. J. Han, H. Lee, H. Swanson and K. B. Kim, *Mol. Biosyst.*, 2011, **7**, 359–364.
46. D. P. Bondeson, B. E. Smith, G. M. Burslem, A. D. Buhimschi, J. Hines, S. Jaime-Figueroa, J. Wang, B. D. Hamman, A. Ishchenko and C. M. Crews, *Cell Chem. Biol.*, 2018, **25**, 78–87.
47. E. F. Douglass, C. J. Miller, G. Sparer, H. Shapiro and D. A. Spiegel, *J. Am. Chem. Soc.*, 2013, **135**, 6092–6099.
48. M. Zengerle, K. H. Chan and A. Ciulli, *ACS Chem. Biol.*, 2015, **10**, 1770–1777.
49. M. S. Gadd, A. Testa, X. Lucas, K. H. Chan, W. Chen, D. J. Lamont, M. Zengerle and A. Ciulli, *Nat. Chem. Biol.*, 2017, **13**, 514–521.
50. C. Cecchini, S. Pannilunghi, S. Tardy and L. Scapozza, *Front. Chem.*, 2021, **9**, 1–23.
51. S. D. Edmondson, B. Yang and C. Fallan, *Bioorganic Med. Chem. Lett.*, 2019, **29**, 1555–1564.
52. V. G. Klein, C. E. Townsend, A. Testa, M. Zengerle, C. Maniaci, S. J. Hughes, K. H. Chan, A. Ciulli and R. S. Lokey, *ACS Med. Chem. Lett.*, 2020, **11**, 1732–1738.
53. V. Poongavanam, Y. Atilaw, S. Siegel, A. Giese, L. Lehmann, D. Meibom, M. Erdelyi and J. Kihlberg, *J. Med. Chem.*, 2022, **65**, 13029–13040.
54. G. Dong, Y. Ding, S. He and C. Sheng. *J. Med. Chem.*, 2021, **64**, 10606 – 10620.
55. E. C. Fink and B. L. Ebert, *Blood.*, 2015, **126**, 2366–2369.

56. G. Ahn, S. M. Banik, C. L. Miller, N. M. Riley, J. R. Cochran and C. R. Bertozzi, *Nat. Chem. Biol.*, 2021, **17**, 937–946.
57. M. Gagliardi and A. T. Ashizawa, *Biomedicines.*, 2021, **9**, 433.
58. J. L. Childs-Disney, X. Yang, Q. M. R. Gibaut, Y. Tong, R. T. Batey and M. D. Disney, *Nat. Rev. Drug Discov.*, 2022, **21**, 736–762.
59. J. Jin, Y. Wu, J. Chen, Y. Shen, L. Zhang, H. Zhang, L. Chen, H. Yuan, H. Chen, W. Zhang and X. Luan, *Theranostics*, 2020, **10**, 10141–10153.
60. K. Wang, X. Dai, A. Yu, C. Feng, K. Liu and L. Huang, *J. Exp. Clin. Cancer Res.*, 2022, **41**, 1–15.
61. H. Liao, X. Li, L. Zhao, Y. Wang, X. Wang, Y. Wu, X. Zhou, W. Fu, L. Liu, H. G. Hu and Y. G. Chen, *Cell Discov.*, 2020, **6**, 1–12.
62. A. M. Ali, J. Atmaj, N. Van Oosterwijk, M. R. Groves and A. Dömling, *Comput. Struct. Biotechnol. J.*, 2019, **17**, 263–281.
63. D. Ma, Y. Zou, Y. Chu, Z. Liu, G. Liu, J. Chu, M. Li, J. Wang, S. Y. Sun and Z. Chang, *Theranostics*, 2020, **10**, 3708–3721.
64. N. R. Kong and L. H. Jones, *Clin. Pharmacol. Ther.*, 2023, **114**, 558–568.
65. M. Békés, D. R. Langlely and C. M. Crews, *Nat. Rev. Drug Discov.*, 2022, **21**, 181–200.
66. P. Klausmeyer, O. M. Z. Howard, S. M. Shipley and T. G. McCloud, *J. Nat. Prod.* 2009, **72**, 1–4.
67. M. Saleki, N. Colgin, J. A. Kirby, S. L. Cobb and S. Ali, *Med. Chem. Comm.*, 2013, **4**, 860–864.
68. A. Hudson, PhD Thesis, Durham University, 2015 (available online via Durham University DRO).
69. L. Jiang, Y. L. Lui, H. Li, C. F. Chan, R. Lan, W. L. Chan, T. Chi-Kong Lau, G. Sai-Wah Tsao, N. K. Mak and K. L. Wong, *Chem. Commun.*, 2014, **50**, 6517–6519.

2. Inhibitors of CCL2-mediated chemotaxis

2.1 An introduction to 2,5-diketopiperazines (DKPs)

2,5-Diketopiperazines (DKPs) are cyclic dipeptides formed from the condensation and cyclisation of two amino acids. The core DKP structure (**20**) contains 2 hydrogen bond acceptor (HBA) and 2 hydrogen bond donor (HBD) sites arising from two *cis* amide bonds, in addition to two chiral centres when $R \neq H$.¹

DKPs typically exist in either a planar or boat confirmation (**Figure 2.1**). The X-ray crystal structure of the simplest DKP cyclo(Gly-Gly) (**21**) was solved in 1938 and was shown to have a planar, C_{2H} structure² yet later gas phase studies revealed the preference for a boat conformation with C_2 symmetry.³ Conversely, a quantum study on a library of DKPs comprised of L-amino acids, showed that in the absence of crystallographic conditions, the lowest energy confirmation was the boat (**22**).⁴

The DKP core can be distorted by its substituents resulting in 'folded' or 'extended' structures. Phenolic substituents typically fold over the DKP core (**23**) due to interactions between the aromatic π -cloud with the amide bonds.⁵ When a DKP contains proline, a rigid constraint is imparted onto the structure and it exists as a stable boat (**24**).¹

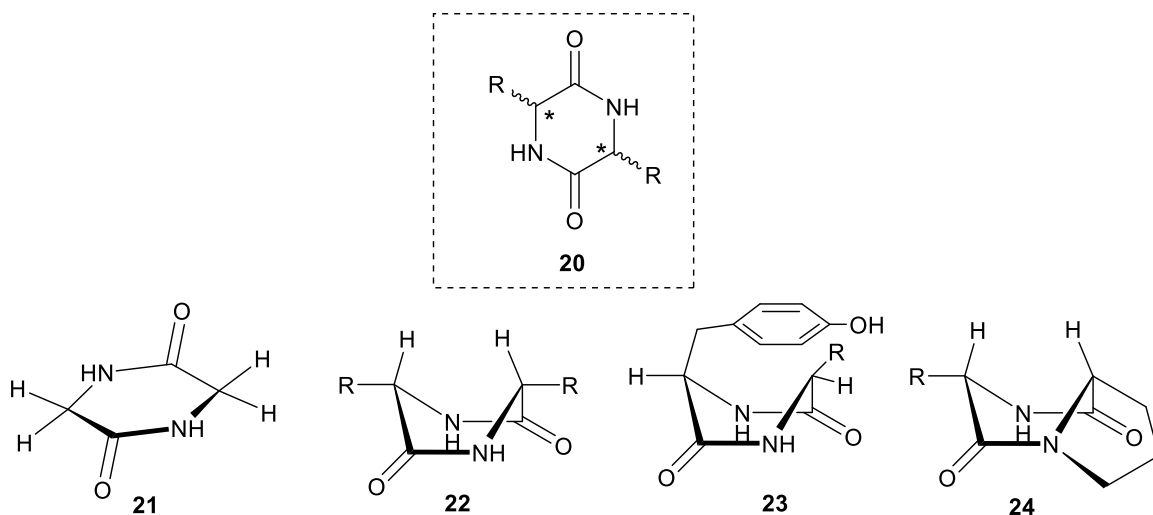


Figure 2.1 Chemical structure of basic DKP scaffold **20**. Planar conformation of cyclo(Gly-Gly) (**21**). Standard boat conformation for substituted DKPs (**22**). Folded structure often observed with phenolic DKPs (**23**). Rigid conformation imposed by proline (**24**). [Figure modified from reference 1].

2.1.1 DKP bioactivity and medicinal properties

DKPs are abundant in nature and are biosynthesised by many different microorganisms such as bacteria⁶ and marine fungi.⁷ Additionally, they are often produced as a by-product in solid phase peptide synthesis (SPPS) in which an intramolecular nucleophilic reaction liberates a DKP molecule and truncates the linear synthesis. The formation of DKPs during SPPS is highly sequence dependant, but secondary amino acids are more prone (e.g. proline).⁸

DKPs represent the pharmacophore of many biologically active molecules, drug candidates currently in clinical trials and approved medicines. An example DKP drug candidate is Plinabulin (**25**), which is currently in phase II clinical trialsⁱ as part of a combination therapy for the treatment of metastatic non-small cell lung cancer.⁹ An approved drug which incorporates the DKP backbone is Tadalafil (**26**), which is used for

ⁱ This trial is actively recruiting.

the treatment of erectile dysfunction, pulmonary hypertension and benign prostate enlargement (**Figure 2.2**).¹⁰

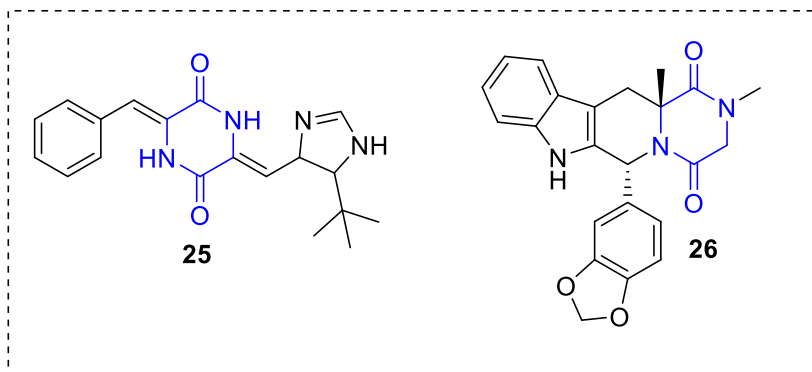
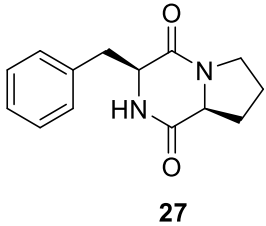
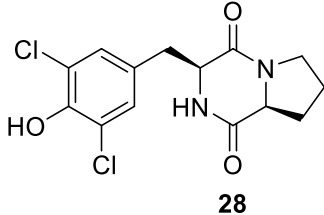
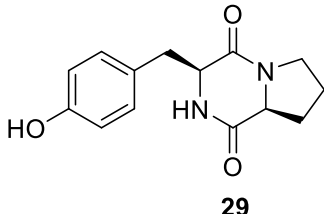
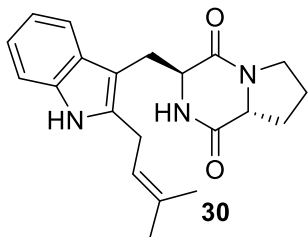
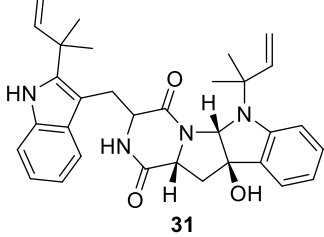


Figure 2.2 Chemical structures of DKP drug candidate Plinabulin (**25**) and approved medicine Tadalafil (**26**).^{9,10}

DKPs that incorporate proline groups, have a broad range of therapeutic properties such as anti-inflammatory, anti-bacterial, pesticidal and anti-cancer (example structures are shown in **Table 2.1**). The research in this thesis builds upon previous work in which DKP **27** and **28** (**Table 2.1 – Entries 1 and 2**) were shown to inhibit the CCL2-mediated chemotaxis of THP-1 cells (further explained in **Section 2.3.2**).^{11,12}

Table 2.1 Biologically active compounds (**27** – **31**) that contain the proline based DKP pharmacophore.

Entry	Name	Structure	Disease target
1.	Cyclo(L-Phe-L-Pro) (27)		Anti-fungal ¹³ Anti-bacterial ¹⁴ Anti-cancer ¹⁵ Anti-inflammatory ^{11,16}
2.	Cyclo(13,15-dichloro-L-Tyr-L-Pro) (28)		Anti-inflammatory ¹²
3.	Maculosin-1 (Cyclo(L-Tyr-L-Pro)) (29)		Anti-bacterial ¹⁴ Antioxidant ¹⁷ Bio-herbicide ¹⁸
4.	Ds2-Tryprostatin B (30)		Anti-cancer ¹⁹
5.	Okaramine C (31)		Insecticidal ²⁰

2.2 An introduction to chemokines

To be able to understand how DKPs **27** and **28** exert their effect as chemotaxis inhibitors, it is important to understand CCL2, the chemokine system itself and CCL2's potential as a therapeutic target. Chemokines are low molecular weight, secreted proteins constituting the largest family of cytokines whose main role is the recruitment of cells (mostly

leukocytes) in response to inflammation; a process known as chemotaxis.²¹ Chemokines induce signalling cascades which ultimately lead to chemotaxis, by coupling to their corresponding G-protein-coupled receptor (GPCR) on the surface of cells.

2.2.1 Chemokine function

Chemokines can be divided into two main groups: homeostatic or inflammatory.^{21,22} Homeostatic chemokines are expressed under physiological conditions and are essential for the maintenance of leukocytes in areas of the body such as the central nervous system (CNS), bone marrow and secondary lymphoid. In contrast, inflammatory chemokines are not constitutively expressed at high levels and are instead produced under pathological conditions. They are expressed by numerous cells and are crucial for the chemotaxis of inflammatory leukocytes into inflamed/damaged tissue, where they are essential for its repair. Whilst chemokine-leukocyte migration is essential for bodily functions, this process can become problematic in disease types that already have an immune/inflammatory response (e.g., autoimmune diseases). In such cases, interfering in this process can provide a valuable therapeutic tool.

2.2.2 Chemokine structure

Chemokines are categorised by the arrangement of four cysteine residues that form (usually two) structurally rigid disulphide bonds.²³ They are further categorised into sub-families (C, CC, CXC and CX₃C) which are defined by the first two cysteine residues of the sequence. Using this nomenclature, C represents the cysteine residue and X represents the amino acids in between. The CC chemokine contains cysteine residues that are directly linked, whereas the CXC and CX₃C chemokines contain variable amino acids (one and three respectively) inserted between their cysteine residues. The only subfamily to display only one disulphide bond are the C chemokines. The CX₃C group represents only one chemokine (CX₃CL1) that is tethered to a transmembrane domain at the C-terminus (**Figure 2.3**).²⁴

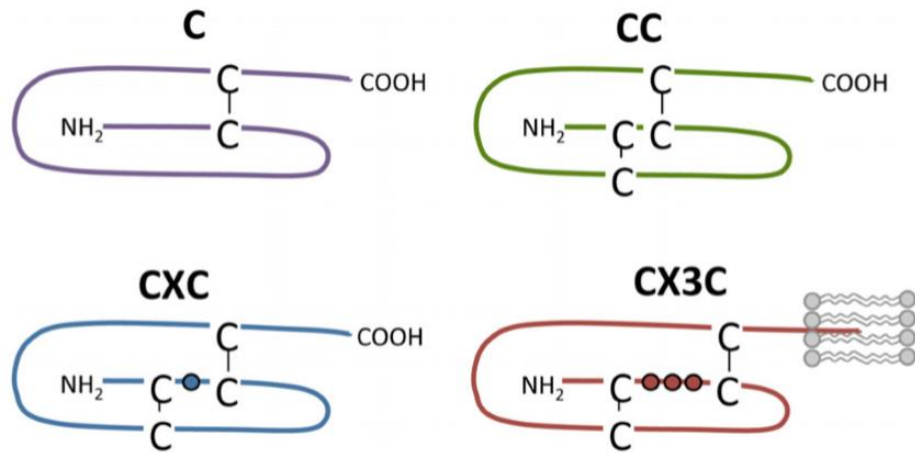


Figure 2.3 The four sub families of chemokine; C, CC, CXC, CX₃C. [Image taken from reference 24].

Chemokines belonging to the same sub-family share a high degree of structural homology, with the same tertiary structure observed throughout. This tertiary structure consists of a flexible, disordered N-terminus prior to the first two cysteine residues, followed by a more ordered N-loop connected by a 3_{10} helix to three anti-parallel β -sheets and ending with a C-terminal α -helix (**Figure 2.4**).²⁵

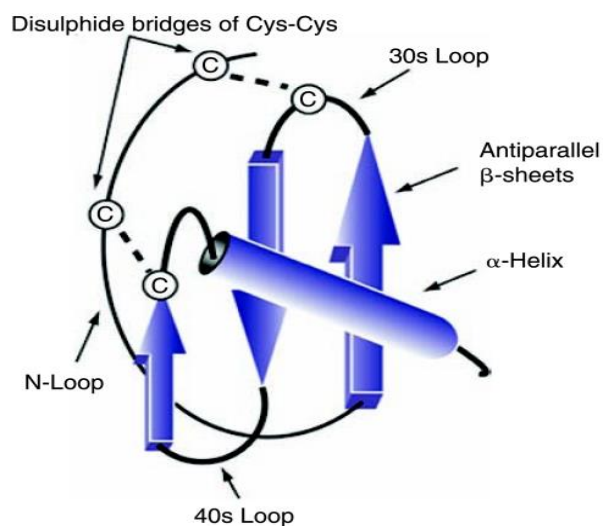


Figure 2.4 The tertiary structure shared between CC chemokines. [Image taken from reference 25].

Although the tertiary monomeric structure is consistent throughout chemokine sub-families, the quaternary structures differ substantially. CXC and CX₃C chemokines form dimers using residues from the β -strand resulting in globular structures.²⁶ For CC chemokines, dimerization through the residues in the flexible N-terminus creates a more elongated structure. As well as dimers, chemokines can form higher order quaternary structures such as tetramers and oligomers.^{27,28}

2.2.3 Chemokine therapeutics

Chemokines and their receptors are expressed in a wide range of disease types such as autoimmune²⁹, cardiovascular³⁰ and cancer³¹ and therefore represent attractive therapeutic targets. Receptor antagonism is the most researched approach and is the mechanism of all currently approved drugs that disrupt the chemokine-receptor interaction.

Maraviroc (**32**) is a clinically approved drug that is used in combination therapy for the treatment of HIV. It acts as an antagonist for CCR5 which is a co-receptor on CD4 cells that provides a secondary site for HIV-1 entry.³² Another chemokine drug is Plerixafor (**33**), which antagonises CXCR4, preventing its binding to CXCL12, resulting in the immobilisation of hematopoietic stem cells (HSCs).³³ These HSCs can be used for transplantation to treat patients suffering from multiple myeloma (MM) and non-Hodgkin's lymphoma. Recently, FDA approval was granted to cyclic dipeptide CXCR4 inhibitor Motixafortide (**34**) (September 8th 2023) which is also used for the immobilization of stem cells and is superior to Plerixafor (**33**), displaying longer receptor occupancy and extended clinical activity (over 48 h).^{34,35}

Although there is considerable interest in disrupting chemokine-receptor interactions, many drug candidates in this area have failed to gain clinical approval. Currently, of the 46 candidates that entered clinical trials, only 4 have become marketed medicines (3 of which are shown in **Figure 2.5**). This is due to their failure in phase II trials; a consequence of a lack of efficacy or due to safety concerns.^{36,37} This was the case for CCR5 antagonist

Aplaviroc (**35**), that was developed as a promising treatment for HIV (similar to antagonist **32**). Although the drug displayed promising *in vitro* and pre-clinical effects, it was ultimately withdrawn from phase II trials due to its hepatotoxicity.³⁸

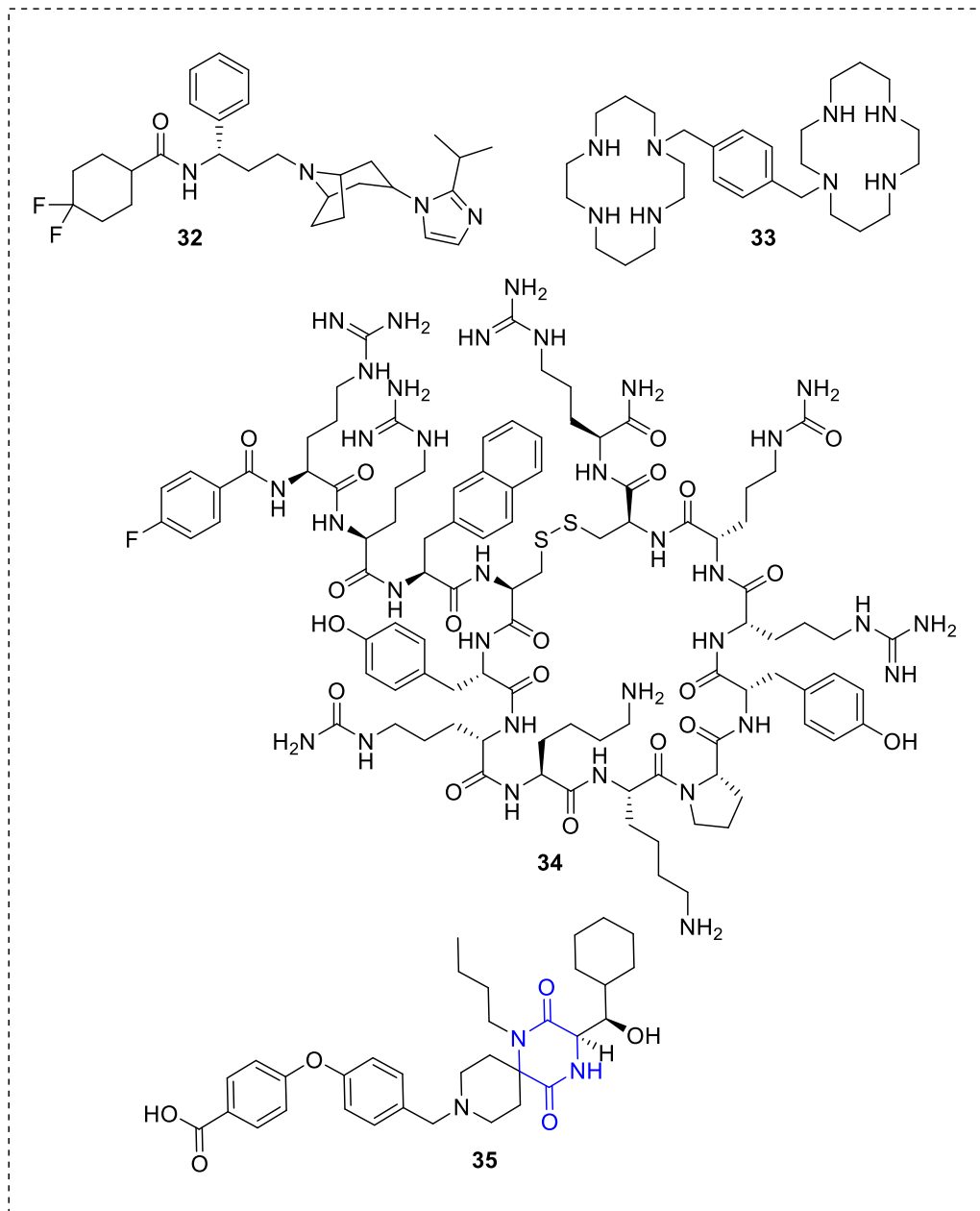


Figure 2.5 Chemical structures of HIV drug Maraviroc (**32**), treatment for non-Hodgkin's lymphoma Plerixafor (**33**), recently approved MM drug Mortixafortide (**34**) and withdrawn treatment for HIV, Aplaviroc (**35**).

2.3 An Introduction to CCL2 (MCP-1)

CCL2 (also known as MCP-1) is a 76 amino acid, CC chemokine.²⁵ Its cognate receptor is CCR2 and it is chemotactic for monocytes, memory T lymphocytes and natural killer cells.²⁵ CCL2 is an inflammatory chemokine that is expressed in a variety of autoimmune diseases such as rheumatoid arthritis (RA)³⁹ and psoriasis.⁴⁰ In RA, the chemotaxis of leukocytes plays a crucial role in the perturbation of inflammation in the synoviumⁱⁱ which ultimately leads to the destruction of cartilage and bone in the joints, causing severe pain. The CCL2-CCR2 interaction is crucial for the recruitment of Th1 cells to the synovium.³⁹ Consequently, disrupting this interaction is of therapeutic interest to minimise the damage caused by RA.

In addition, disrupting the CCL2-CCR2 interaction is of therapeutic interest for treating cancer (such as breast and prostate cancer), with CCL2 being produced by many types of cancer cell.⁴¹ CCL2 contributes to the initial stage of cancer metastasis by guiding cancer cell migration, through the interaction with surface CCR2 on tumour cells

2.3.1 Issues targeting CCL2-CCR2

A feature of the chemokine network that hinders the development of therapeutics is the promiscuity between members of the same sub-family. Cells can express several chemokine receptor types and these receptors can recognise more than one chemokine, creating a selectivity challenge. Additionally, chemokines themselves are promiscuous and can bind to many receptors (**Figure 2.6**).³⁶

ⁱⁱ The synovium is the connective tissue that lines the inside of a joint.

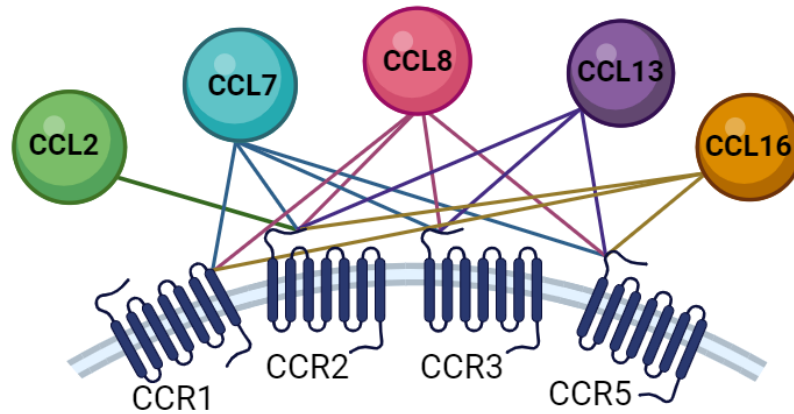


Figure 2.6 Promiscuity in the chemokine system. All 5 CC chemokines bind CCR2, but most can also bind to several other CC chemokine receptors. [Image created using BioRender].

A likely reason for the high promiscuity in the chemokine network is the shared sequence homology between chemokines of the same sub-family, which can be anywhere between 20% and 90%.²⁵ In addition to CCL2 binding, receptor CCR2 can also bind chemokines CCL7, CCL8, CCL13 and CCL16, with their corresponding binding affinities alongside shared homology with CCL2 shown in **Table 2.2**.⁴² Although CCL2 is the most potent binder for CCR2 with a K_D of 0.5 nM (**Table 2.2 – Entry 1**), other CC chemokines also have relatively high binding affinities. CCL8 for example has a K_D of 3 ± 1 nM as well as a 69% shared homology with CCL2 (**Table 2.2 – Entry 2**). To add further complexity, different chemokines can bind to the same receptor but induce different downstream signalling events resulting in different biological outcomes.⁴³ This is known as ‘biased signalling’ and the extent of this is still poorly understood.

Table 2.2 Chemokine agonists for CCR2 with corresponding binding affinities and homology with CCL2 (%). [Modified from reference 41].

Entry	Chemokine	Homology with CCL2 (%)	Binding to CCR2 (K_D / nM)
1.	CCL2	100	~0.5
2.	CCL7	73	~13
3.	CCL8	69	~3 ± 1
4.	CCL13	65	~15
5.	CCL16	31	~95

2.3.2 DKP based CCL2-CCR2 inhibitors

As mentioned in **Section 2.1.1**, certain DKPs have shown to be effective inhibitors of CCL2-mediated chemotaxis. This was first shown by Klausmeyer *et al.*, who discovered the inhibitory properties of cyclo(13,15 dichloro-L-Tyr-L-Pro) (**28**); a natural product isolated from the fungus *Leptoxyphium sp.*¹²

This was further researched by the Cobb and Ali groups (Saleki *et al.*) who modified the active scaffold and synthesised a new library of DKPs, assessing their ability to inhibit CCL2-mediated chemotaxis.¹¹ From this work, the two most effective ligands cyclo(L-Phe-L-Pro) (**27**) and cyclo(L-F-Phe-L-Pro) (**36**), were shown to significantly reduce CCL2-mediated chemotaxis at both 100 μ M and 50 μ M using Boyden chamber assays. A key finding was that DKP **36** demonstrated specificity for CCL2 chemotaxis (results shown in **Figure 2.7**). DKP **36** was able to reduce THP-1 migration in response to CCL2, however this was not the case for CCL5 and CCL7 (also a CCR2 agonist). This was an important result, highlighting the potential for selectively targeting the CCL2-CCR2 interaction, avoiding the innate cross-reactivity between chemokines and their receptors.

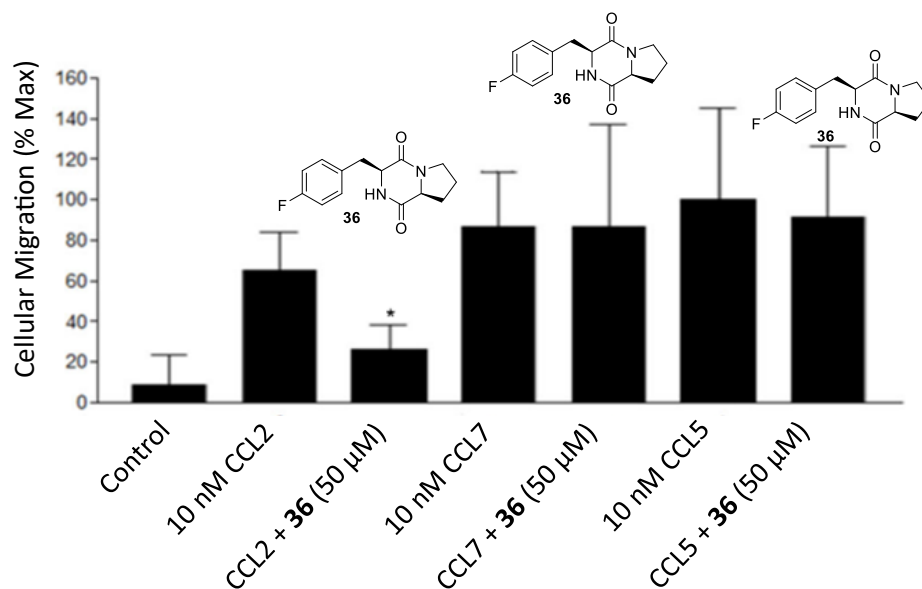


Figure 2.7 Selectivity studies using DKP **36** against CCL2, CCL5 and CCL7. DKP **36** selectively inhibited CCL2-mediated chemotaxis. [Graph modified from reference 16].

2.3.3 Mode of action for CCL2 chemotaxis inhibition

When CCL2 binds CCR2 it induces a signalling cascade that causes the phosphorylation of ERK1/2 (pERK1/2); an event that can be disrupted by receptor antagonists that prevent CCL2 binding. In the work by Saleki *et al.*, it was shown that in the presence of DKP **28** and **36** (50 μM), a reduction in pERK was not observed.¹¹ Through comparison with a known CCR2 antagonist⁴⁴, in which antagonism of the orthosteric site of the receptor caused pERK1/2 reduction, it was hypothesised that competition for the orthosteric site was unlikely to be the DKP mode of action. This was reinforced in previous work by Klausmeyer *et al.*, in which DKP **28** did not show competitive binding against radio-labelled CCL2 for the orthosteric site.¹² Therefore, based on the initial data available regarding selectivity and binding, it was hypothesised that the DKPs **27**, **28**, and **36** exhibited CCL2-CCR2 inhibition through the targeting of CCL2 itself and not antagonism of the orthosteric site.

2.3.4 A new library of DKP inhibitors

Building upon this work, former PhD student in the Cobb group Alex Hudson, prepared a new library of DKPs to probe the key structural features that were essential to their anti-

chemotactic activity.¹⁶ Alongside previous DKP (**27**), Hudson discovered that DKPs **37** and **38** (Figure 2.8) also displayed significant inhibition of CCL2-mediated chemotaxis when tested at 100 μ M.

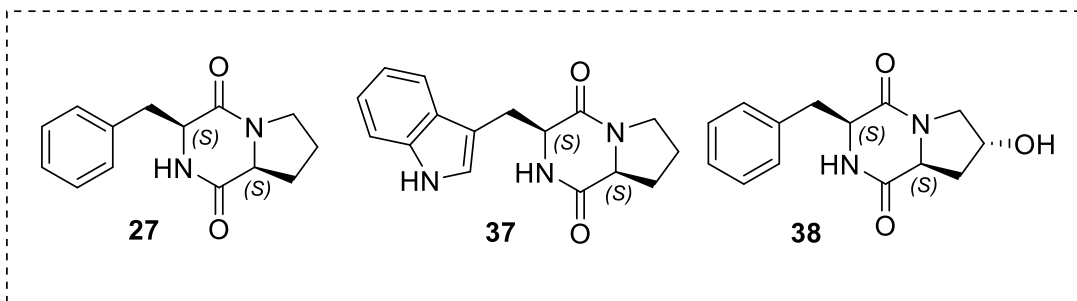


Figure 2.8 Chemical structures of DKPs **27**, **37** and **38** that were CCL2-chemotaxis inhibitors when screened at 100 μ M in work by Hudson *et al.*¹⁶

From this work, it was proposed that three DKP structural features were essential for CCL2-chemotaxis inhibition: 1) the conformationally constrained proline ring, 2) an aromatic amino acid and 3) *S,S* stereochemistry.

2.4 Aims

Throughout the past decade, a series of DKPs that demonstrated promising inhibitory activity and selectivity for CCL2-mediated chemotaxis, have been developed. The specificity displayed by DKPs for CCL2 over other CC chemokines, has led to interest in these molecules for overcoming the innate cross-reactivity associated with CCR2. Additionally, with the absence of p-ERK1/2 inhibition and competition against CCL2 for the orthosteric receptor site, the hypothesis at the beginning of this research is that DKPs exert their mode of action through CCL2 binding.

One of the key aims of this chapter is to further explore the potential of DKPs as inhibitors of CCL2-mediated chemotaxis. To achieve this, a new library of DKPs incorporating modified proline or aromatic groups, will be synthesised with their inhibitory capabilities assessed using Boyden chamber chemotaxis assays. Using the new leads, if any, obtained from the chemotaxis assays, CCR2 internalisation assays will be performed to

assess whether the active DKPs affect this pharmacological mechanism. This could provide a greater insight into the DKP mode of action. In addition, the new library of DKPs synthesised in this chapter will be used in ligand-binding experiments in **Chapter 3** to assess their ability to bind with CCL2. Finally, the synthesis of DKPs that contain suitable functional groups, that allow their incorporation into potential CCL2-targeting PROTACs in **Chapter 4**, will be undertaken.

2.4.1 Design of the 2nd generation DKP library

As explained in **Section 2.3.2**, Hudson found that the proline and the aromatic moiety alongside *S,S* stereochemistry, were crucial for the inhibitory activity of DKPs in CCL2-chemotaxis assays. Therefore, this basic structural activity relationship (SAR) constitutes the core structure of all DKPs designed in this work.

An outline of all initial DKP targets are shown in **Figure 2.9**. In **Figure 2.9 (A)** a selection of novel, fluorinated targets incorporating fluorine(s) on either the proline (DKP **39** and **40**) or aromatic moieties (DKP **41** and **42**) are shown. To date, it is estimated that 20% of pharmaceuticals contain fluorine as its incorporation can improve the pharmacokinetic/pharmacodynamic properties of drugs. More importantly to the aims of this project, the incorporation of fluorine into drug candidates has been shown in some cases to increase binding to target proteins.^{45,46} Therefore it is desirable to analyse how fluorinated DKPs function as both chemotaxis inhibitors as well as CCL2 binders (**Chapter 3**).

Shown in **Figure 2.9 (B)** are two DKP targets that incorporate fluorine in the form of a tetrafluoropyridyl group (TFP) through either the aromatic (**43**) or proline (**44**) moiety. Recent research within the Cobb group has sought to incorporate TFP into biological molecules and has so far seen some success (explained further in **Section 2.5.5**). With this said, it would be useful to analyse whether incorporation of a TFP group has any impact on anti-chemotactic activity. Additionally, it would be worthwhile to assess the tolerance of TFP-containing amino acids in the solid phase peptide synthesis (SPPS) of DKPs.

Shown in **Figure 2.9 (C)** are DKP targets **27** and **37**, that were shown to be active inhibitors of CCL2-mediated chemotaxis in previous work.^{11,16} In this current work, they will be re-synthesised for use in biological and biophysical assays. In **Figure 2.9 (D)**, two DKPs that incorporate tyrosine (**29**) or hydroxyproline (**45**) are shown. These provide a hydroxyl group acting as a vector for further modification and will be used in **Chapter 4** for the synthesis of CCL2-targeting PROTACs.

Lastly, shown in **Figure 2.9 (C)** are a group of DKPs (**46**, **47** and **48**) that have modified aromatic groups. It would be interesting to analyse how these modifications affect the structural conformation of the DKP (X-ray crystallography).

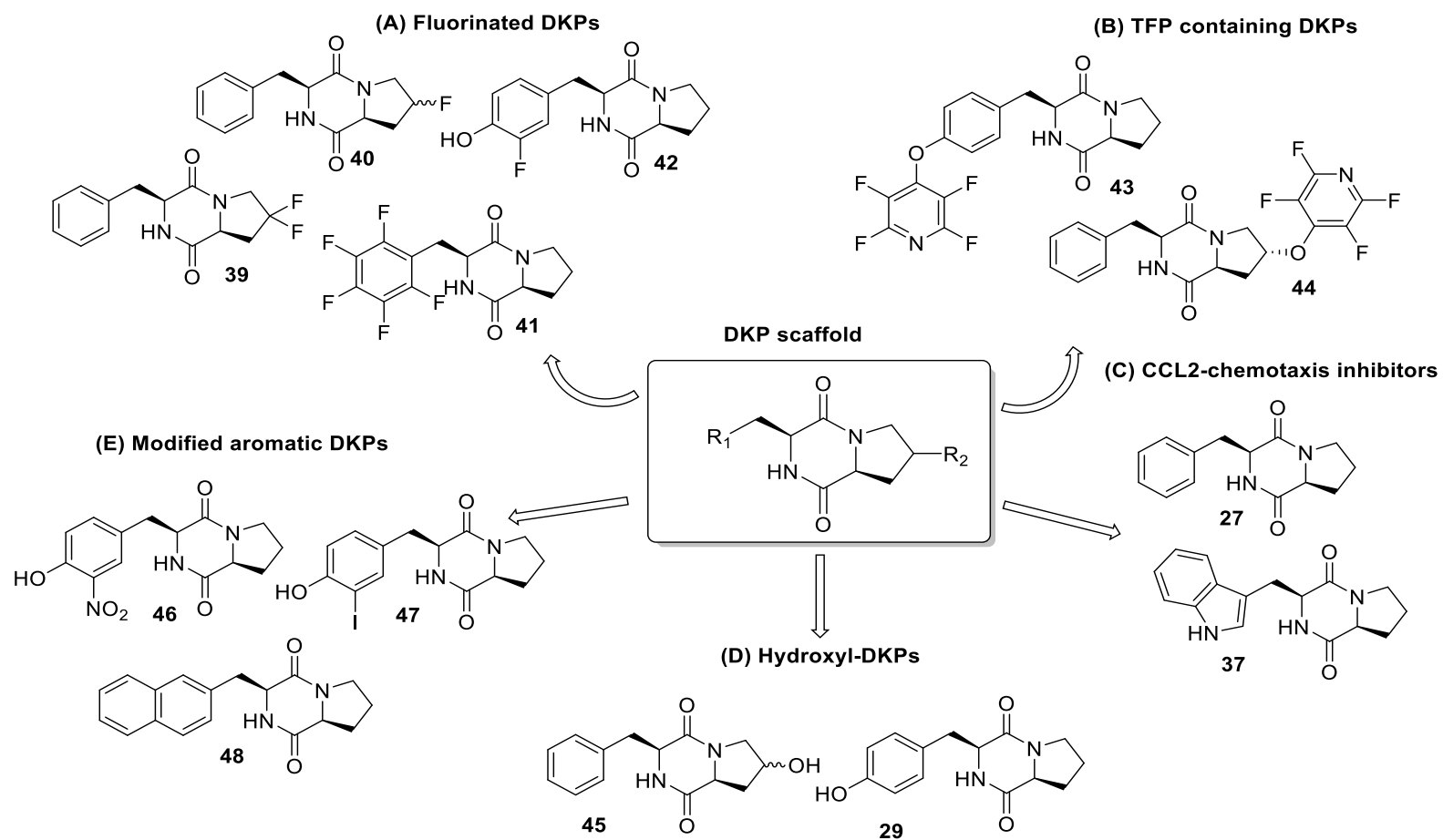
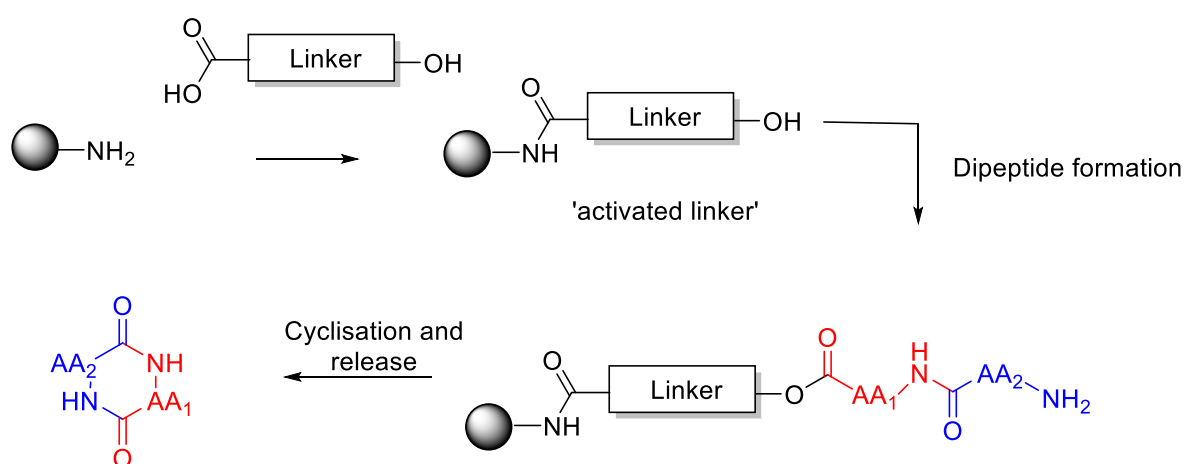


Figure 2.9 Chemical structures of the desired DKP targets in this work. **(A)** DKPs incorporating fluorine. **(B)** DKPs containing TFP groups. **(C)** DKPs that have shown anti-chemotactic activity in previous work. **(D)** DKPs containing tyrosine or hydroxyproline. **(E)** DKPs that contain modified aromatic groups.

2.5 Synthesis of the 2nd generation DKP library

There are numerous methods that can be used for the synthesis of DKPs including both solution and solid phase techniques. Solution phase methods typically involve the formation of a dipeptide by either direct amide bond formation or the 4-component Ugi reaction, followed by cyclisation in either acidic or basic conditions, or using high temperatures and/or microwave irradiation.¹ However, solution phase methods often suffer from a lack of stereocontrol, with racemisation of one of the chiral centres occurring during cyclisation.⁴⁷

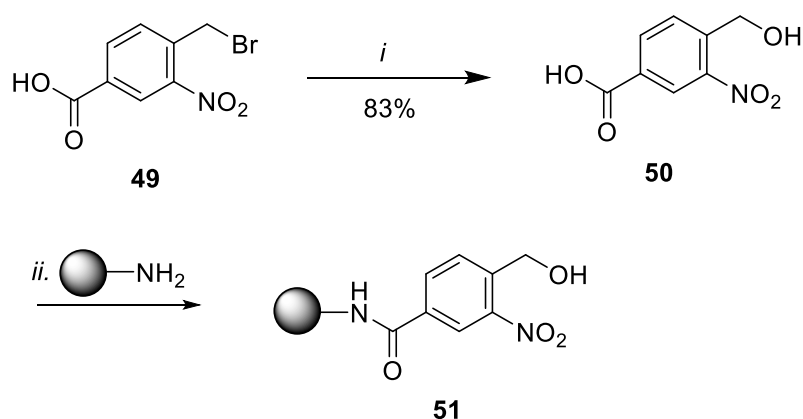
Hudson *et al.*, developed a modified synthetic methodology¹⁶ based on work by the Giralt group,⁴⁸ in which a dipeptide was built upon an 'activated resin' and subsequent intramolecular cyclative release afforded the DKP product (**Scheme 2.1**). This route could be completed in 8 h, with only one purification required to produce cyclised products with conserved stereochemistry. Additionally, this method allowed DKPs to be produced in moderate to excellent yields (30 – 86%). For these reasons, it was decided to use this method to synthesise the 2nd generation library of DKPs outlined in **Figure 2.9**.



Scheme 2.1 General SPPS of DKPs.

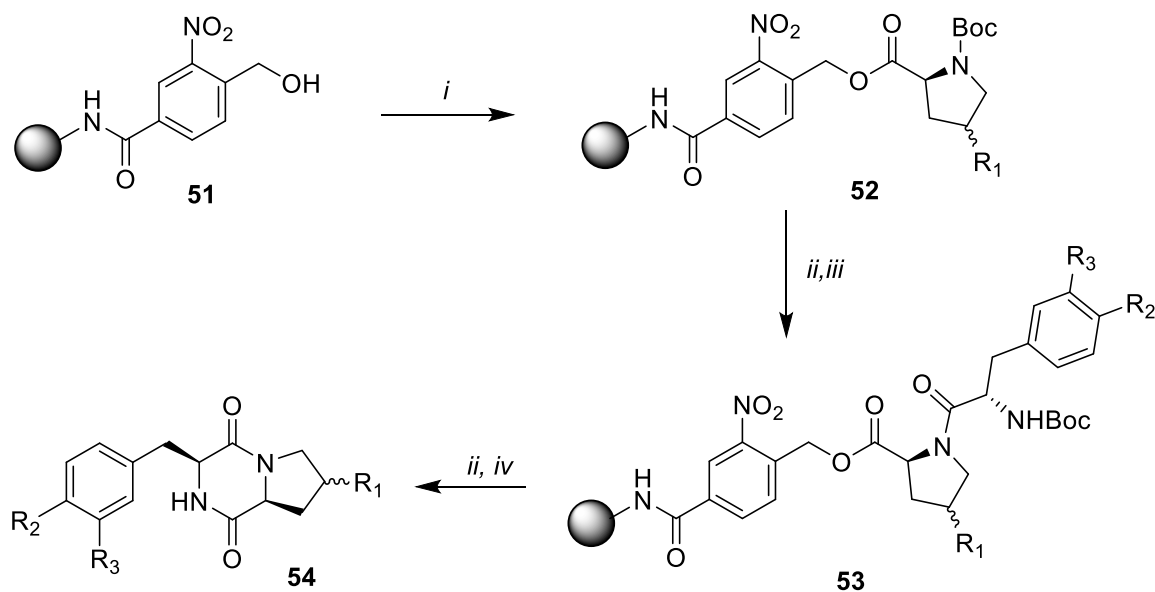
2.5.1 General DKP SPPS (N-Boc-protected)

The first stage of solid phase DKP synthesis was the formation and attachment of reactive linker **50** to a solid support to form 'activated resin' **51**. The linker (**50**) was firstly synthesised by the treatment of commercially available 4-(bromomethyl)-3-nitrobenzoic acid (**49**) with aqueous NaHCO₃, substituting the primary bromine with a hydroxyl group. This afforded linker **50** to a high yield of 83% which was subsequently coupled to a rink amide MBHA LL (low loading) resin to form the 'activated resin' **51** (**Scheme 2.2**).



Scheme 2.2 Synthesis of activated resin **51**. Reagents and conditions: *i*. 50% NaHCO₃, reflux, 16 h. *ii*. DIC, DCM, rt, 16 h.

The synthesis of DKPs using the solid phase, N-Boc protected route in this work is shown in **Scheme 2.3**. The first amino acid (**AA**₁) was coupled by an ester linkage to the free hydroxyl on the 'activated resin' (**51**). Following acidic N-Boc deprotection, the second amino acid (**AA**₂) was coupled with **AA**₁ to form the on-resin dipeptide (**53**). A final N-Boc deprotection, followed by neutralisation of the protonated terminal amine, induced intramolecular cyclisation to release the desired DKP product (**54**).



Scheme 2.3 General N-Boc SPPS for DKPs (**54**) using a cyclative release strategy. Reagents and conditions: *i.* AA₁, DIC, DMAP, DCM, rt, 30 min, x 2. *ii.* 40% TFA in DCM, rt, 10 min, x 3. *iii.* AA₂, DIPEA, PyBOP, DCM, rt, 1 h, x 2. *iv.* 10% DIPEA in DCM, rt, 10 min, x 3.

2.5.2 SPPS of cyclo(L-Phe-L-Pro) (**27**)

Cyclo(L-Phe-L-Pro) (**27**) (Figure 2.10) is the least structurally complex DKP target in this work and represents the basic scaffold for the DKP library. DKP **27** has shown a wide-range of biological potential (Table 2.2 – Entry 1) including the inhibition of CCL2-mediated chemotaxis in two independent studies from the Cobb group.^{11,16} Accordingly, its resynthesis was desirable for use in further biological and biophysical studies as well as to establish a synthetic and purification protocol that could be used for all members of the DKP library.

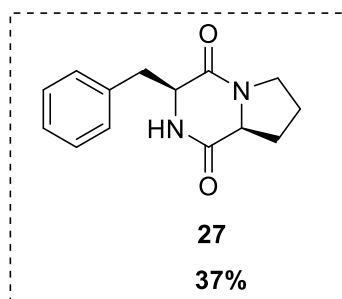


Figure 2.10 Chemical structure of DKP **27** which was obtained in a 37% yield.

The synthetic route shown in **Scheme 2.3** was carried out for the synthesis of DKP **27** using commercially available N-Boc-proline (**AA₁**) and N-Boc-phenylalanine (**AA₂**) on a 0.2 mmol scale. Upon reaction completion, the resin was drained, and the filtrate collected. The resin was further washed with DCM and the filtrates were combined and concentrated *in vacuo*, to produce the crude solid. In Hudson's methodology, DKPs were purified by preparative-thin layer chromatography (prep-TLC) using an EtOAc eluent. However, when attempted in this work, this system was found to be ineffective at removing residual DIPEA used in the final synthetic step.

As the library of DKPs were to be used in biological and biophysical assays, it was crucial that they were of high purity and therefore, the purification of DKP **27** was optimised. The corresponding ¹H NMR spectrum after each purification step is shown **Figure 2.11**. Firstly, the obtained filtrate was concentrated *in vacuo* with toluene (3 x at 60 °C) to remove excess DIPEA (**Figure 2.11 (A)**). Following this, an acidic work-up (1M aq.HCl) was effective at removing all remaining traces of DIPEA from the crude (**Figure 2.11 (B)**), which was further purified by column chromatography (prep-TLC was just as effective) using an eluent of 0 – 5% MeOH in DCM (**Figure 2.11 (C)**). This afforded DKP **27** to a high purity for use in later biological testing. Thereafter, this purification was applied to all DKPs synthesised using the N-Boc-protected SPPS strategy.

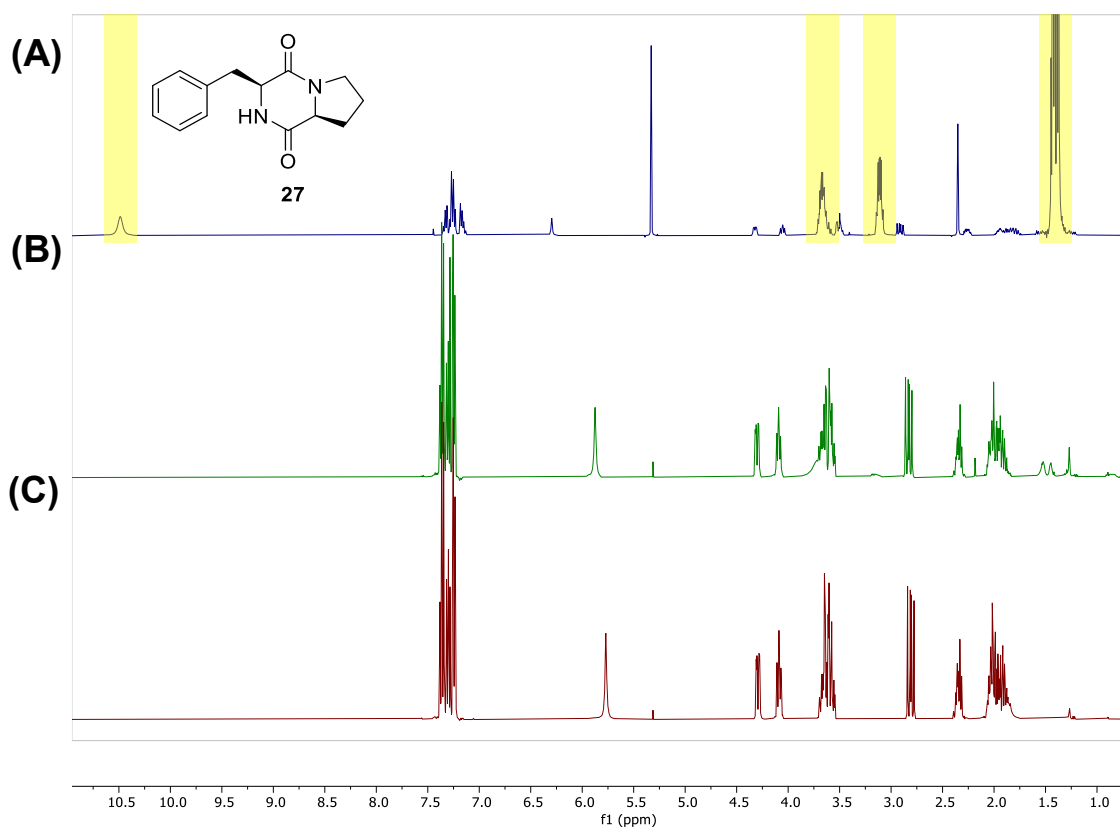


Figure 2.11. ^1H NMR spectra (400 MHz, CDCl_3) corresponding to each step in the purification of DKP **27**. Peaks corresponding to DIPEA are highlighted in yellow. **(A)** ^1H NMR spectrum following concentration *in vacuo* with toluene (3 x at 60 $^\circ\text{C}$). **(B)** ^1H NMR spectrum following an acidic work-up, which was effective at removing all trace quantities of DIPEA. **(C)** ^1H NMR spectrum of pure DKP **27** obtained following column chromatography.

2.5.3 SPPS of the DKP library (N-Boc)

The synthesis and purification described in **Section 2.5.2** was used to make an additional seven DKPs (**Figure 2.12**). The compounds were synthesised on a 0.1 – 0.2 mmol scale producing DKPs in low to moderate yields (13 – 45%). The obtained yields were lower than those produced by Hudson, a possible consequence from additional purification steps. Despite this, 10 mg or more of each DKP was obtained (with the exception of DKP **41**) which provided sufficient material for further biological analysis. As part of this library, DKP **55** which contained 3-methyl proline and DKP **58**, a fluorophenyl analogue with *R,S* stereochemistry, was also synthesised.

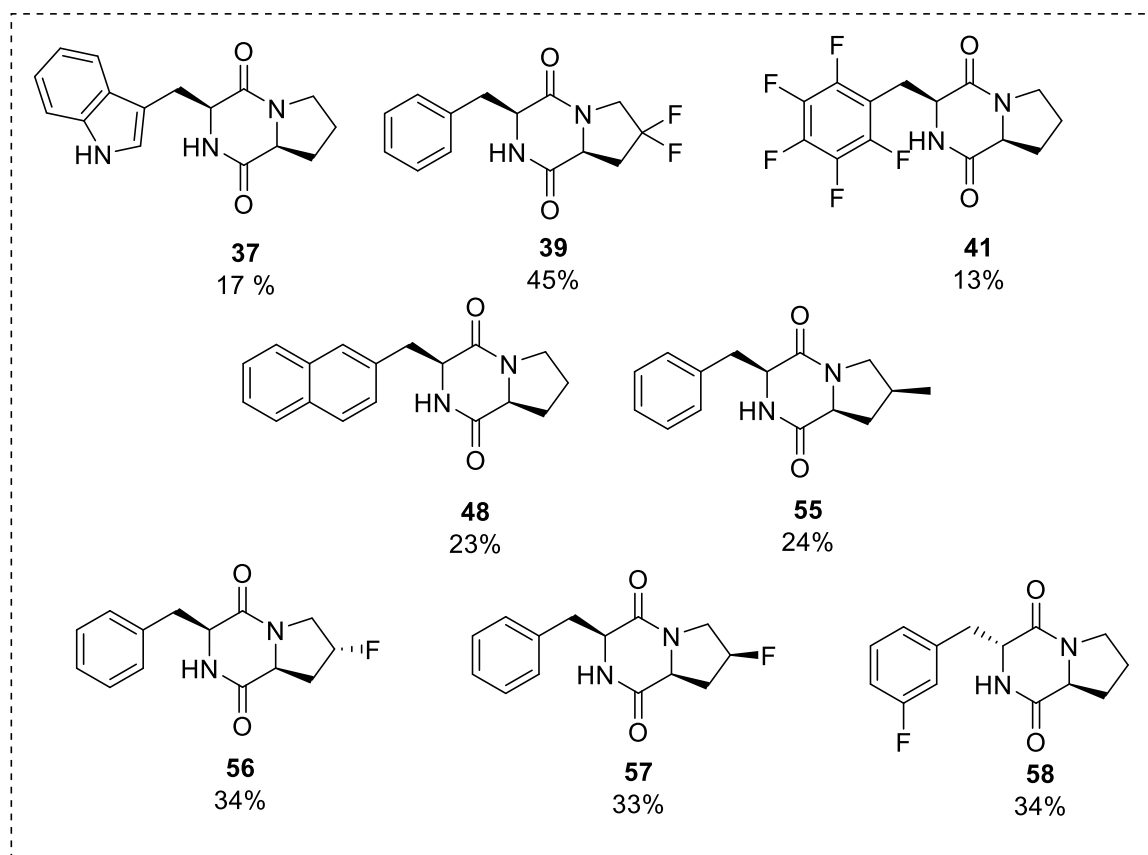
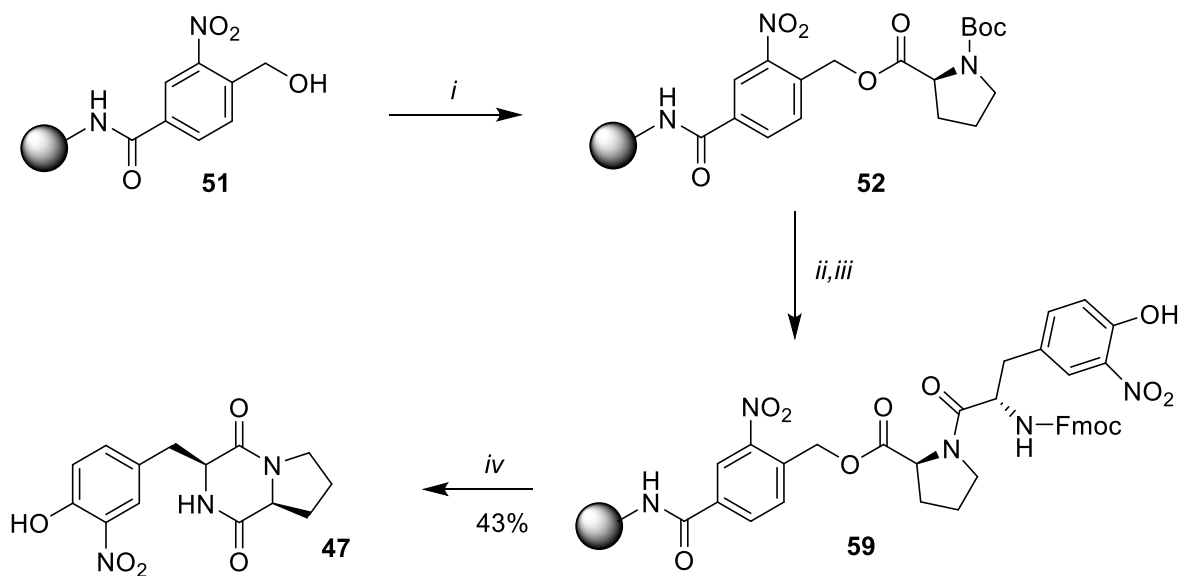


Figure 2.12 Chemical structures of the DKPs synthesised using N-Boc protected SPPS.

2.5.4 Modified SPPS of cyclo(L-Nitro-Tyr-L-Pro) (**47**)

For the synthesis of DKP **47**, the constituent amino acid 3-nitro-L-tyrosine was available in the laboratory in the Fmoc-protected form, hence its incorporation into DKP **47** using SPPS required slight modifications^{viii} to the original synthetic route (**Scheme 2.4**). Following the coupling of N-Boc-proline (**AA₂**) and subsequent acidic N-Boc deprotection, Fmoc-3-nitro-tyrosine was coupled as the second amino acid (**AA₂**). DKP **47** was released from the resin following the simultaneous Fmoc-deprotection and cyclisation of the on-resin peptide (**59**) using 20% piperidine in DMF. The resin was washed with DMF and the filtrates were collected and combined.

^{viii} This is based on a synthetic route previously designed by Hudson.¹⁶



Scheme 2.4 Modified route for the SPPS of DKP **47**. Reagents and conditions: *i.* Boc-Pro-OH (**AA**₁), DIC, DMAP, DCM, rt, 30 min x 2. *ii.* 40% TFA in DCM, rt, 10 min x 3. *iii.* Fmoc-3-Nitro-Tyr (**AA**₂), DIPEA, PyBOP, DCM, 1 h, x 2. *iv.* 20% Piperidine in DMF, rt, 10 min, x 3.

The synthetic route shown in **Scheme 2.4** is typically avoided due to excess DMF and piperidine in the obtained filtrate and the associated challenges with their removal/separation from mixtures. To remove excess DMF, the crude was concentrated *in vacuo* with toluene (5 x at 60 °C) before purification by column chromatography (Combi-Flash). Initially, an elution gradient of 0 – 100% EtOAc/Hexane was used to purify DKP **47** however this was a poor system, with DKP **47** only obtained following a lengthy EtOAc ‘flush’. This was likely due to the limited solubility of DKP **47** in EtOAc. From this initial purification, the ¹H NMR spectrum corresponding to DKP **47** showed baseline impurities and therefore an additional purification step was required. DKP **47** has greater solubility in DCM and therefore a 5% MeOH/DCM solvent system was used for its repurification (prep-TLC) affording DKP **47** in a 43% yield.

2.5.5 Attempted SPPS of cyclo(L-TFP-Tyr-L-Pro) (43) and cyclo(L-TFP-Hyp-L-Pro) (44)

As explained in **Section 2.4.1**, work within the Cobb group seeks to incorporate the TFP group into bioactive molecules in addition to its use as a protecting group in organic synthesis.^{49,50,51} In recent work by Perea^{ix} *et al.*, TFP-containing small molecule **60** (**Figure 2.13**) was shown to have low micromolar antiparasitic activity (EC_{50} (*L. Mexicana promastigotes*); 1.33 μ M, EC_{50} (*L. Mexicana amastigotes*); 0.433 μ M, IC_{50} (*T. cruzi epimastigotes*); 1.55 μ M, EC_{50} (*T. cruzi infected stage*); 0.05 μ M.⁵¹ An aim of this current work was to analyse whether the incorporation of TFP within DKPs could improve their inhibition of CCL2-mediated chemotaxis and CCL2 binding.

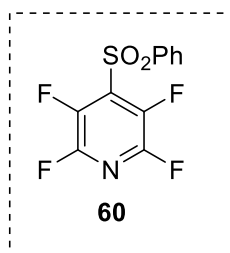


Figure 2.13 Chemical structure of anti-parasitic agent **60**.

The two proposed DKPs **43** and **44** (**Figure 2.14**), contain TFP-ethers attached to tyrosine or hydroxyproline respectively. In previous work by Brittain *et al.*, a synthesis was devised for producing TFP-ethers to high yields with minimal, if any, further purification required.⁴⁹ Using this method, the TFP ether of N-Boc-tyrosine and N-Boc-hydroxyproline were synthesised (**Scheme 2.5**).

^{ix} Previous PhD student in the Cobb group.

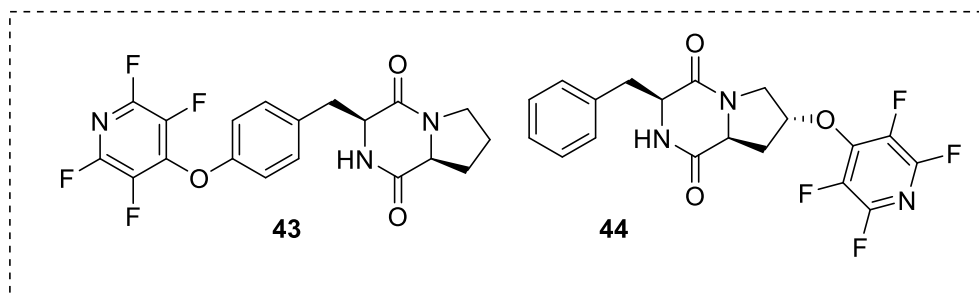
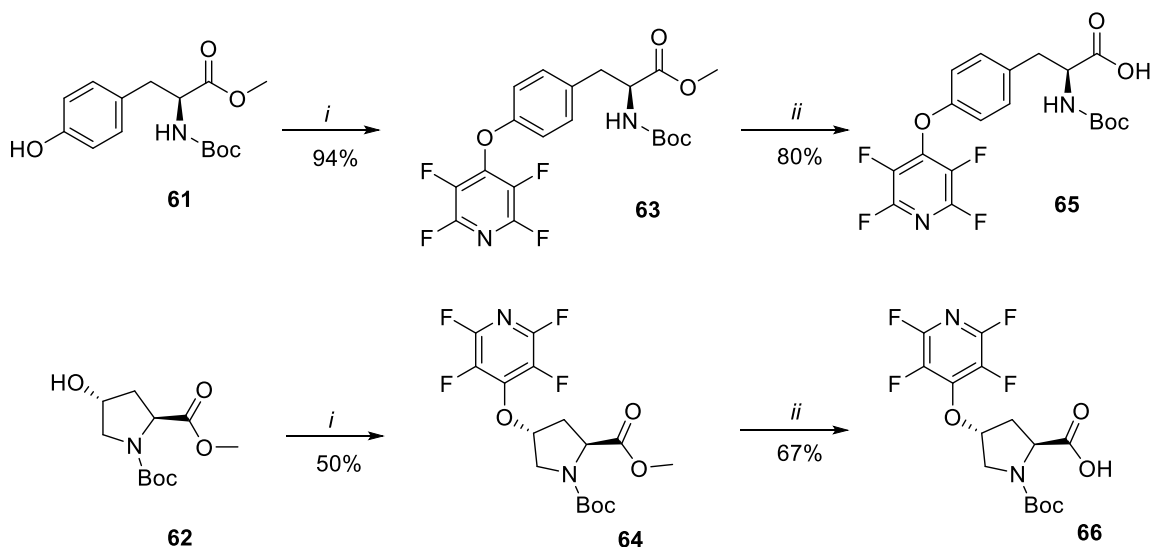


Figure 2.14 Chemical structures of desired TFP-incorporating DKPs **43** and **44**.

The amino acids **61** and **62** were stirred with pentafluoropyridine (PFP) and K_2CO_3 in MeCN to produce the corresponding TFP ethers **63** and **64**. The synthesis of tyrosine derivative **63** is established in literature⁴⁹ and produced excellent yields at each step, whereas hydroxyproline derivative **64** was produced in more moderate yields (**Scheme 2.5**). Following this, ester hydrolysis was achieved under basic conditions to produce acids **65** and **66**.



Scheme 2.5 Synthesis of TFP-containing amino acids **65** and **66**. Reagents and conditions: *i*. PFP, K_2CO_3 , MeCN, rt, 16 h. *ii*. LiOH.H₂O, 50% H₂O/THF, rt, 24 h.

Both modified amino acids were used in the attempted synthesis of TFP-containing DKPs **43** and **44**. However, this was unsuccessful using the solid phase route shown in **Scheme**

2.3, with neither the analysis of crude ^1H NMR spectra nor LCMS showing the presence of the desired products. The additional steric bulk imparted by the larger TFP group could have obstructed cyclisation of the product in the final stage. Nevertheless, it was clear that this route was not effective at producing TFP-containing DKPs.

2.5.6 SPPS of hydroxyl-containing DKPs (N-Boc protected)

Although the solid phase method outlined in **Section 2.5.2** sufficiently produced 8 DKPs on a milligram scale, this route afforded hydroxyl-containing DKPs (**Figure 2.15**) in low yields.

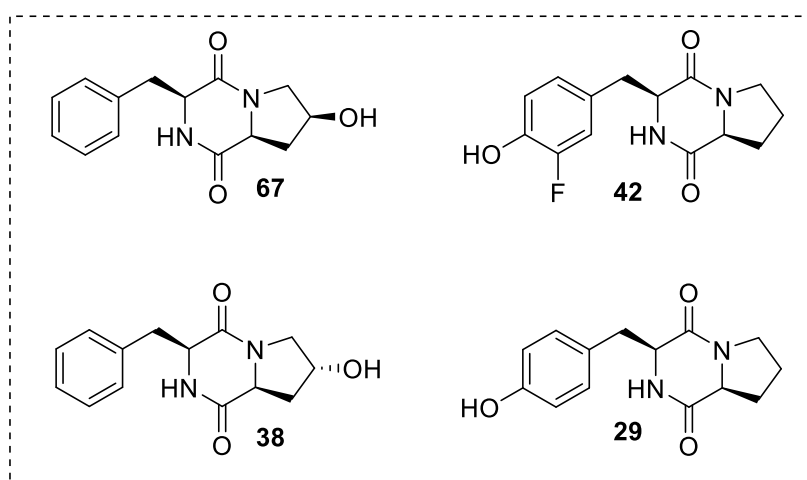


Figure 2.15 Chemical structures of the four hydroxyl-containing DKPs **67**, **42**, **38** and **29**.

DKPs **42** and **67** were synthesised using standard SPPS (**Scheme 2.3**) with analysis of the corresponding LCMS chromatograms indicating the successful formation of both products. However, following purification by prep-TLC, less than 2 mg of each DKP was obtained and analysis of the corresponding ^1H NMR spectra revealed significant quantities of DIPEA still present. Both DKPs **42** and **67** were characterised by analysis of ^1H NMR spectra (or ^{19}F NMR spectra) but due to the low yield recovered, high quality ^{13}C NMR spectra could not be obtained, and further repurification was avoided.

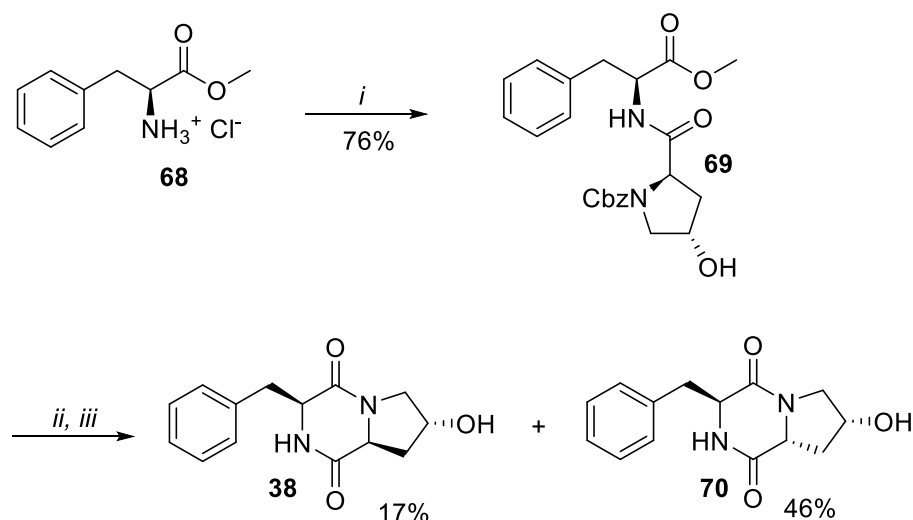
Similar issues were encountered in the attempted SPPS of hydroxyl-containing DKPs **29** and **38**. Equally low yields were obtained and it was also found that following the acidic work-up, both products had transferred into the aqueous phase (as shown by LCMS

analysis) and negligible material remained in the organic phase (DCM). Due to this, the two DKPs were resynthesized but the acidic work-up was removed. The pure products were obtained following column chromatography to afford DKP **29** and **38** in low yields of 9% and 2% respectively. Hydroxyl-containing DKPs can lack solubility in DCM and therefore, could require DMF to aid solubility in the final resin cleavage step; although as explained in **Section 2.5.4** this is less ideal as it increases the complexity of the final work-up and purification. As one of the aims was to incorporate DKPs **29** and **38** into CCL2-PROTACs, a greater yielding route was required.

2.5.7 Solution phase DKP synthesis

Solution phase DKP synthesis typically runs the risk of racemisation, particularly under harshly acidic or basic conditions.⁴⁷ However, in work by Ueda *et al.*, dipeptides were successfully cyclised by refluxing in a low boiling point solvent such as MeOH or EtOH.⁵² This route typically produced DKP products in high yields and was stereocontrolled. Consequently, it was decided to follow this method to produce hydroxyl-containing DKPs **29** and **38**.

Firstly, the formation of precursor Cbz-protected dipeptides were synthesised using an EDC/HOBt coupling strategy. Following this, removal of the Cbz group was achieved by transfer hydrogenation using catalytic Pd/C and an excess of ammonium formate. Cyclisation was induced through reflux in MeOH for 24 h, until complete conversion to the cyclised product was observed. For the synthesis of DKP **38** (**Scheme 2.6**), firstly phenylalanine-OMe (**68**) was coupled to Cbz-hydroxyproline on a 11.2 mmol scale, affording Cbz-dipeptide **69** in a good yield (76%). However, following Cbz removal, cyclisation in MeOH afforded two DKP products.



Scheme 2.6 Solution phase synthesis for hydroxyl-containing DKP **38**. Reagents and conditions: *i*. Cbz-Hyp-OH, EDC.HCl, HOBT, DIPEA, DCM, rt, 16 h. *ii*. Pd/C, NH₄COOH, MeOH, reflux, 4 h. *iii*. MeOH, reflux, 24 h.

The two products could be separated by column chromatography (0-8% MeOH in DCM) with a very slow gradient increase. From analysis of the ¹H NMR spectrum corresponding to the major product and from comparison with existing literature, it was determined that racemisation at the proline α-carbon (*S,R*) had occurred, resulting in the formation of diastereoisomer **70**.⁵³ However, due to the scale of the reaction, 250 mg of the desired DKP **38** was obtained which was sufficient for future biological evaluation and PROTAC synthesis.

The synthesis of DKP **29** was initially attempted on a 5.0 mmol scale with the undesired diastereoisomer **71** produced as the major product. Again, both diastereoisomers produced distinctly different ¹H NMR spectra that could be confirmed by cross-referencing with existing literature.⁵⁴ The synthesis afforded 30 mg of DKP **29** (17% yield) which was insufficient for future synthesis and biological evaluation. The distinctly different ¹H NMR spectra corresponding to the diastereoisomers DKP **29** and DKP **71** are shown in **Figure 2.16**.

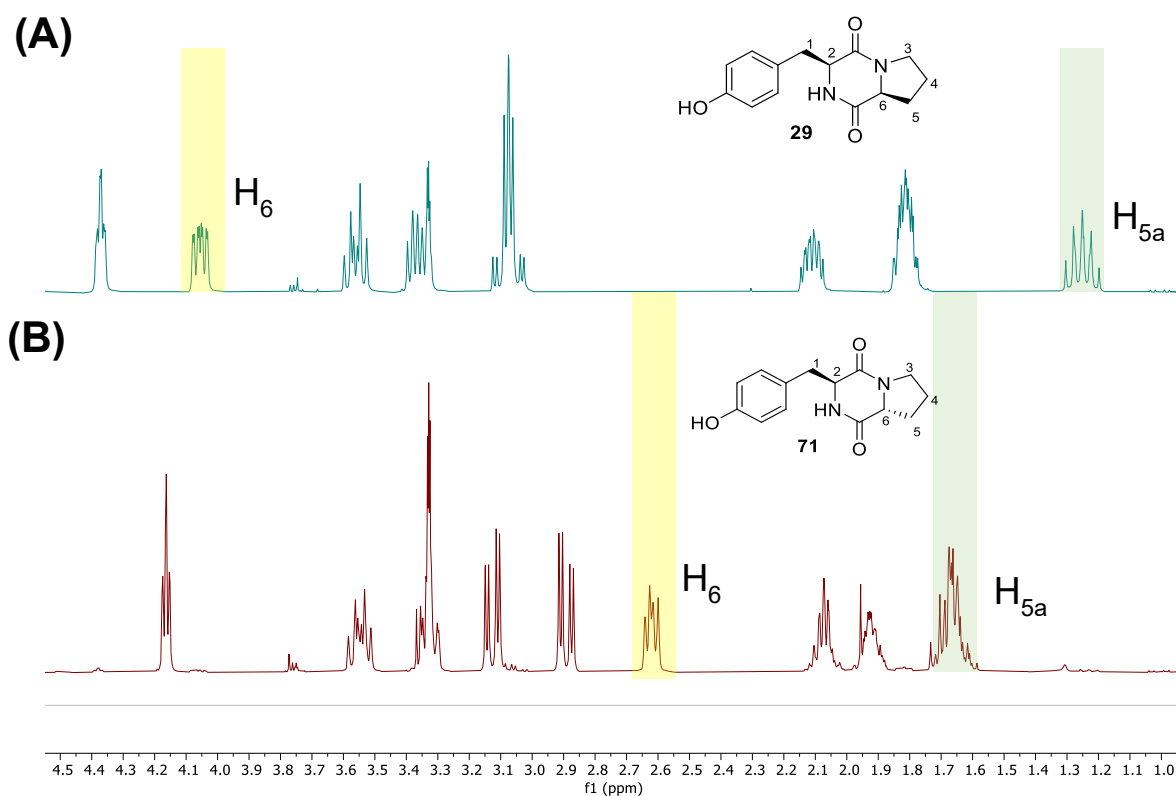


Figure 2.16 ¹H NMR spectra (400 MHz, MeOD) corresponding to the diastereomers of cyclo(Tyr,Pro) produced by solution phase DKP synthesis. **(A)** ¹H spectrum of desired DKP **29**. **(B)** ¹H spectrum of DKP **71**.

When the stereochemistry at position 6 is changed from *S*- (**29**) to *R*- (**71**), H₆ shifts up field (from 4.05 ppm to 2.51 ppm) due to an increased interaction with the aromatic C-H protons.⁵⁵ The opposite is true for H_{5a}, which experiences a reduced interaction with the aromatic ring and shifts downfield from 1.24 to 1.67 ppm. Following this initial attempt, the synthesis of **29** was repeated on a 24.6 mmol scale and the only product that was formed was the desired stereoisomer **71**, with a yield of 44% obtained over the final two steps (**Scheme 2.7**)

2.5.9 DKP crystal structures

To further understand the potential relationship between DKP structure and activity, an attempt was made to obtain crystal structures for all members of the 2nd generation DKP library. To achieve this, a slow evaporation technique was used to form single crystals suitable for X-ray diffraction.

In this work, X-ray crystal structures were produced for 7 DKPs from the 2nd generation library (**Figure 2.17**). DKP **36** which had been synthesised by Neil Colgin (previous Cobb group PDRA) and was the lead compound in previously published work was also crystallised.¹¹ For the DKPs synthesised by SPPS, stereochemistry was always conserved highlighting a major benefit of this technique.

One suggestion posed from research by Hudson, was that DKPs with a folded shape were less active than those with an elongated shape; though this was not thoroughly investigated as few crystal structures were obtained. In the crystal structures obtained in this current work, when a tyrosine (or modified tyrosine) was incorporated into the DKP structure, a folded confirmation was observed, which aligned with expectations from literature.¹ Phenylalanine, however, did not fold over the ring, instead preferring an elongated confirmation. DKP **43**, in which the tyrosine is coupled to a TFP group, also preferred an elongated confirmation. This is likely due to the electron-withdrawing effect of the TFP group which 'deactivates' the attached aromatic ring, as has been shown previously by Brittain *et al.*, resulting in minimal interactions between the aromatic π -cloud and the DKP core.⁵⁶

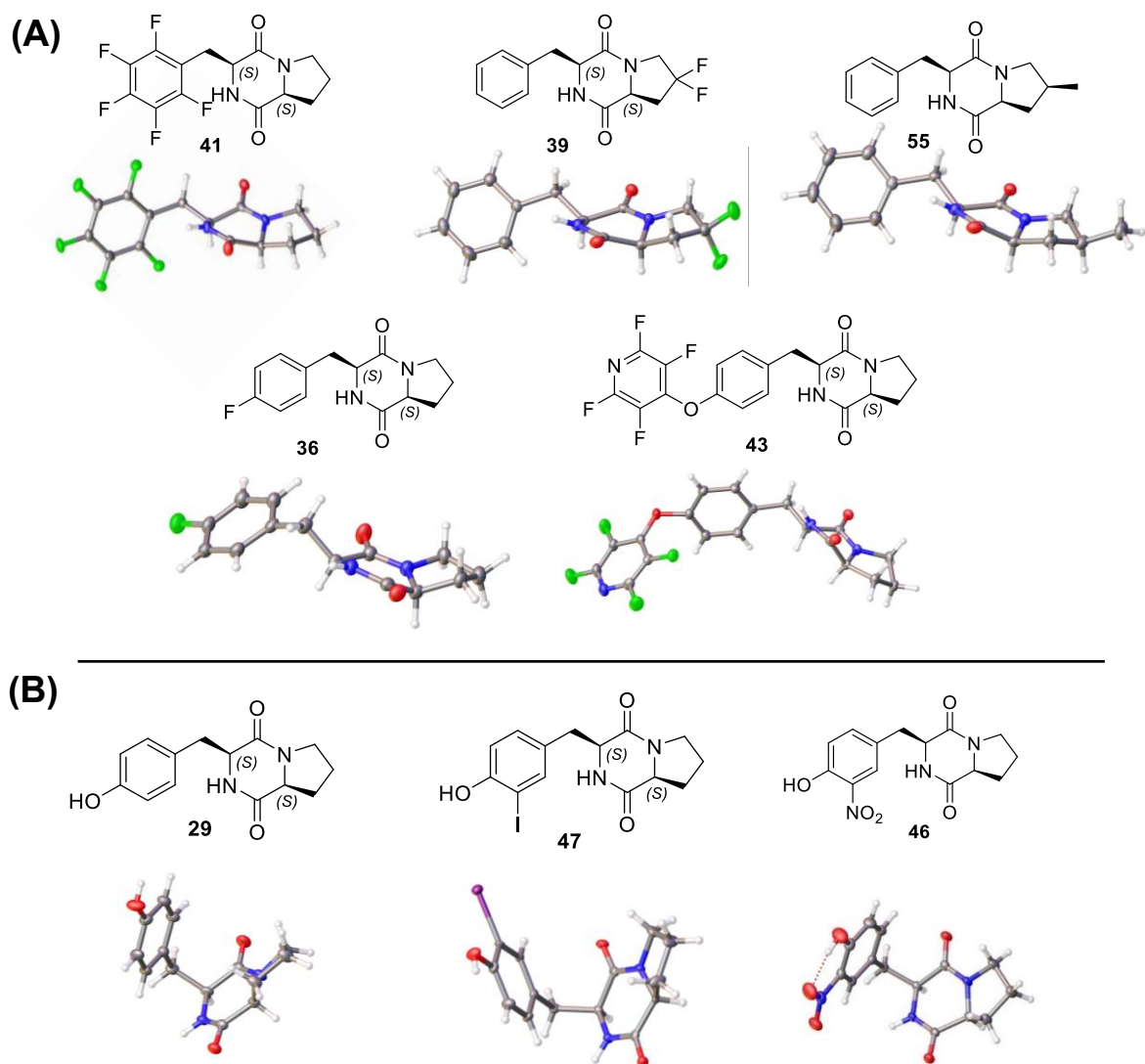


Figure 2.17 X-ray crystal structures of 8 DKPs. **(A)** DKPs with elongated structures. **(B)** DKPs with folded structures. All molecular structures showing 50% probability anisotropic displacement ellipsoids.

2.6 Molecular Biology^x

2.6.1 Chemotaxis assays

Chemotaxis (cell migration) assays are frequently employed for the analysis of leukocyte movement in response to chemical stimuli (chemotactic response).⁵⁷ Migration assays are typically performed using a Boyden chamber, which can also be used for the evaluation of leukocyte chemotaxis inhibitors.⁵⁸

The standard Boyden chamber set-up (**Figure 2.18 (A)**) consists of polycarbonate membrane inserts containing leukocytes, that are placed into 24 (or 96) well plates that contain chemoattractant supplemented media. The chemoattractant induces the directed migration of cells through the insert where they either adhere to the underside of the membrane or pass into the supplemented media (**Figure 2.18 (B)**). Wells containing media only are used as a negative control. There are two established methods for producing a migrated cell count: (1) by fixing the cells and removing the membrane to count cells using a haemocytometer (**Figure 2.18 (C)**) or (2) by detaching adhered cells into solution and producing a cell count by flow cytometry (**Figure 2.18 (D)**).⁵⁹ Cell counts are commonly reported as the relative migration (RM) of cells in response to chemical

In previous work, Saleki *et al.*, used Boyden chamber assays to measure the migration of THP-1 cells^{xi} in response to CCL2, with or without DKP inhibitors.¹¹ In this work, a cell count was produced following the method shown in **Figure 2.18 (C)**. This current work seeks to analyse the potential of the DKP library synthesised in **Section 2.5** as inhibitors of the CCL2-mediated chemotaxis of THP-1 cells.

^x All the work in this Section was undertaken at the Newcastle Medical school with the assistance and guidance of Prof. Simi Ali and Mr. Chong Yun Pang (Ali Group).

^{xi} THP-1 cells used are monocytes isolated from a patient with acute monocytic leukemia.

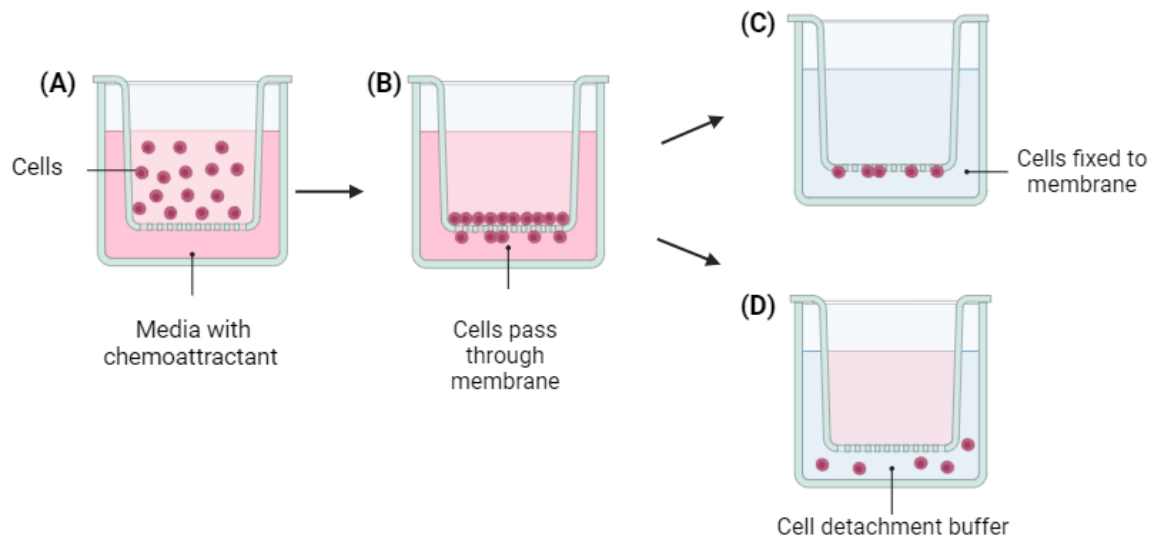


Figure 2.18 Standard set-up for Boyden chamber assays. **(A)** Trans-well inserts containing cell suspensions are placed into plate wells containing media supplemented with chemoattractant. **(B)** The chemoattractant induces the movement of cells through the membrane into the lower well. **(C)** Cells adhere to the underside of the membrane and can be fixed onto the membrane, and subsequently counted using a haemocytometer. **(D)** Cell detachment buffer can be used to detach cells from the underside of the membrane into solution and produce a cell count using flow cytometry. [Image created using BioRender].

2.6.2 CCL2-mediated chemotaxis assay development

Optimising the chemoattractant (chemokine) concentration is an important first step in the development of a successful chemotaxis assay. Chemotaxis typically exhibits a bell-shaped dose-response curve, therefore high concentrations of the chemoattractant can lead to a decrease in chemotaxis. Due to this, it is important to find the concentration that induces the maximal chemotactic response.⁶⁰ Previous work by Saleki *et al.*, found a CCL2 concentration of 10 nM to be optimal¹¹, whereas Buttacharya *et al.*, used a concentration of 1.2 nM,⁶¹ hence the optimal concentration of the chemoattractant can vary significantly.

In this current work, Boyden chamber assays were used to assess the migration of THP-1 cells in response to six concentrations of CCL2: 50 nM, 25 nM, 12.5 nM, 6.25 nM, 3.13 nM and 1.56 nM. The Boyden chambers were incubated at 37 °C using 5% CO₂ for 3 h (the optimised conditions from previous work)¹¹ (**Figure 2.19 (A)**). Following this, the flowthrough was removed and placed aside (**Figure 2.19 (B)**) and cell detachment solution Acttase® was added to the wells (with the insert still in place). The chambers were

agitated at 37 °C for 5 min (**Figure 2.19 (C)**) which allowed the adhered cells to be detached from the membrane, into the Accutase® solution. This cell suspension was combined with the previously obtained flowthrough and the samples were processed for analysis by flow cytometry. The final cell sample was mixed with a fixed volume of CountBright cell counting beads to deduce an absolute cell count determined by the ratio of beads to cell events (**Equation 2.1**).

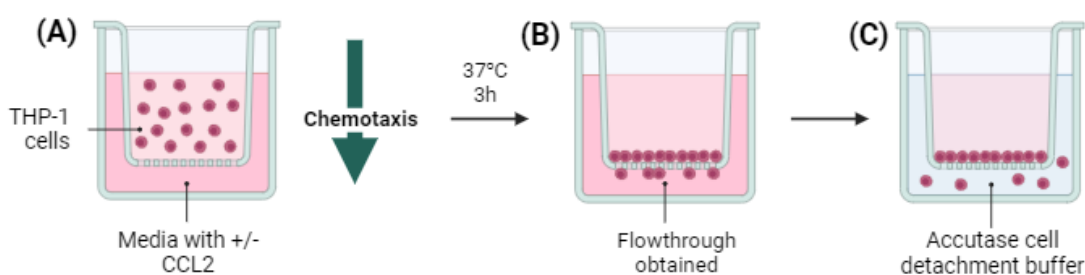


Figure 2.19 Experimental set up for Boyden chamber assays measuring THP-1 cellular migration in response to different concentrations of CCL2. **(A)** Inserts containing THP-1 cells were placed into wells containing media supplemented with CCL2. **(B)** Incubation of the plate for 3 h, subsequently cells in the insert were discarded and the flowthrough was obtained. **(C)** Accutase® was used to detach cells from the membrane and the solution was combined with the flowthrough previously set aside. [Image created using BioRender].

Equation 2.1 Absolute cell count for migrated THP-1 cells

$$Absolute\ count\ \left(\frac{cells}{\mu L}\right) = \frac{(Cell\ count\ x\ counting\ bead\ vol)}{(Counting\ bead\ count\ x\ cell\ vol)} \times Counting\ beads\ conc\ \left(\frac{beads}{\mu L}\right)$$

The flow cytometry gating strategy for the CCL2 optimisation assay, is shown in **Figure 2.20**. In **Figure 2.20 (A)** the representative scatter plots are shown for the cell gating corresponding to baseline THP-1 cell migration (the negative control, CCL2 concentration = 0). The first plot shows the gating of the whole population (cells and beads), the second plot shows the gating of single cells only and the last plot shows separate gating of cells and beads. The representative scatter plots corresponding to THP-1 migration in response to 3.13 nM of CCL2 is shown in **Figure 2.20 (B)**. The RM was determined from the absolute cell counts corresponding to each concentration of CCL2 (determined using **Equation 2.1**) and the overall results are shown in **Figure 2.20 (C)**.

The highest concentration of CCL2 (50 nM) was unable to induce any significant THP-1 migration (RM = 1). However, as the concentration of CCL2 was decreased, THP-1 cell migration significantly increased, reaching a maximum at 3.13 nM (RM = 4.2). At 1.56 nM of CCL2, the cell migration was slightly reduced (RM = 3.8) which would be consistent with the bell-shaped dose-response curve expected.

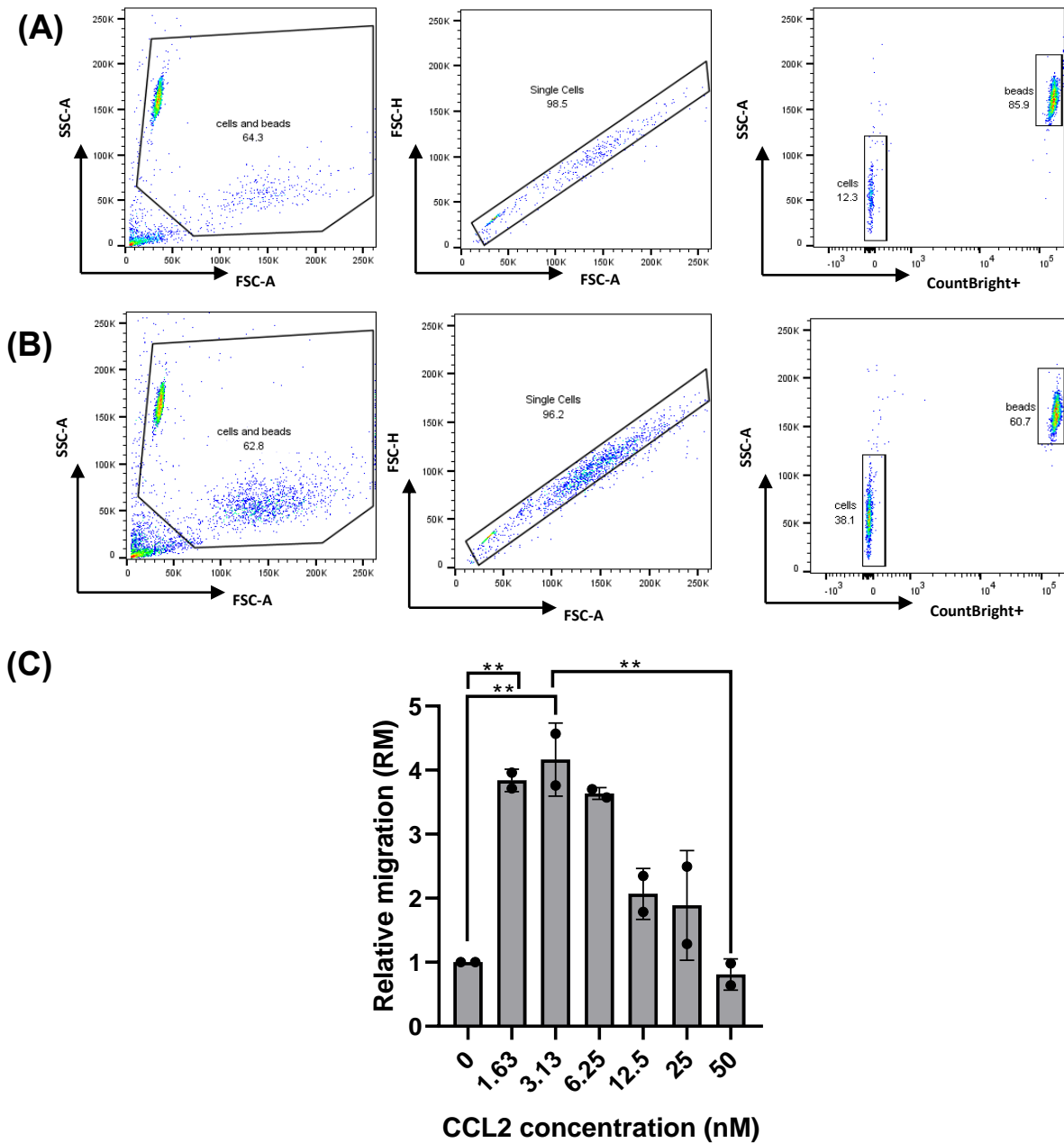


Figure 2.20 THP-1 migration (RM) in response to 6 concentrations of CCL2. **(A)** The cell gating strategy for baseline THP-1 migration (no CCL2). **(B)** The representative scatter plots for the THP-1 migrated cell count in response to 3.13 nM of CCL2. **(C)** The RM of THP-1 cells in response to each concentration of CCL2. The data shown is from biological and technical duplicates. Significance was assessed using one-way ANOVA and Dunnett's test (n = 2). **p<0.001.

2.6.3 CCL2-mediated chemotaxis assay – inhibitor testing

With initial optimisation steps completed, Boyden chamber assays were used to evaluate the inhibitory properties of the 2nd generation library of DKPs on CCL2-mediated THP-1 migration. 12 DKPs^{xii} synthesised in **Section 2.5** were included alongside DKP **36**^{xiii}; one of the lead compounds from previous work by Saleki *et al.*¹¹ Members of this library **27** and **36** had previously shown, using Boyden chamber assays, to reduce THP-1 migration to approximately 50% and 75% respectively when tested at 50 μ M.¹¹ DKP **36** also substantially reduced THP-1 migration to less than 50% in selectivity chemotaxis assays (**Figure 2.7**). Additionally, when tested at 100 μ M, both DKPs **27** and **36** reduced THP-1 migration to less than 50%. This was also observed in work by Hudson *et al.*, in which an 100 μ M dose of DKP **27** reduced THP-1 migration to approximately 30%.¹⁶ In the same work, DKPs **37** and **38** also reduced THP-1 migration to 35% and 40% respectively (when tested at 100 μ M).

In addition to the DKPs that had shown inhibitory activity in previous work, the novel, fluorinated DKPs **39**, **41**, **43**, **56**, **57** and **58** were tested in the CCL2 chemotaxis assays in this current work. Hydroxyl-containing DKP (**29**) had been tested in previous work by Klausmeyer¹² and Hudson¹⁶ (at 100 μ M) and was shown to not significantly reduce THP-1 migration. Therefore, it was not included in the current work.

CCL2 was used at a concentration of 3 nM, as determined optimal from work in **Section 2.6.2**. Each inhibitor was dissolved in DMSO and added to the media supplemented with chemokine (producing a final DMSO concentration of 0.2%). The positive control was media supplemented with chemokine only (0.2% DMSO) and the negative control was media only. Small molecule CCR2b receptor antagonist RS 504393 (**74**) (**Figure 2.21**), which inhibits THP-1 chemotaxis at an IC₅₀ of 330 nM,⁶² was included as an additional positive control to validate the experimental changes in the current work. The percentage

^{xii} DKP **47** was not included as accurate results over three repeats were unable to be obtained.

^{xiii} This compound was synthesised by previous member of the Cobb group, Dr Neil Colgin.

migration of THP-1 cells in response to CCL2 and each inhibitor, in comparison to CCL2 only, was used to assess the inhibitory potential of each compound. The results from this inhibitor screen are presented in **Figure 2.22**.

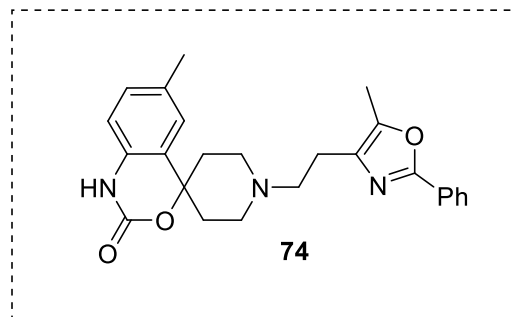


Figure 2.21 Chemical structure of CCR2b antagonist RS 50439 (**74**).

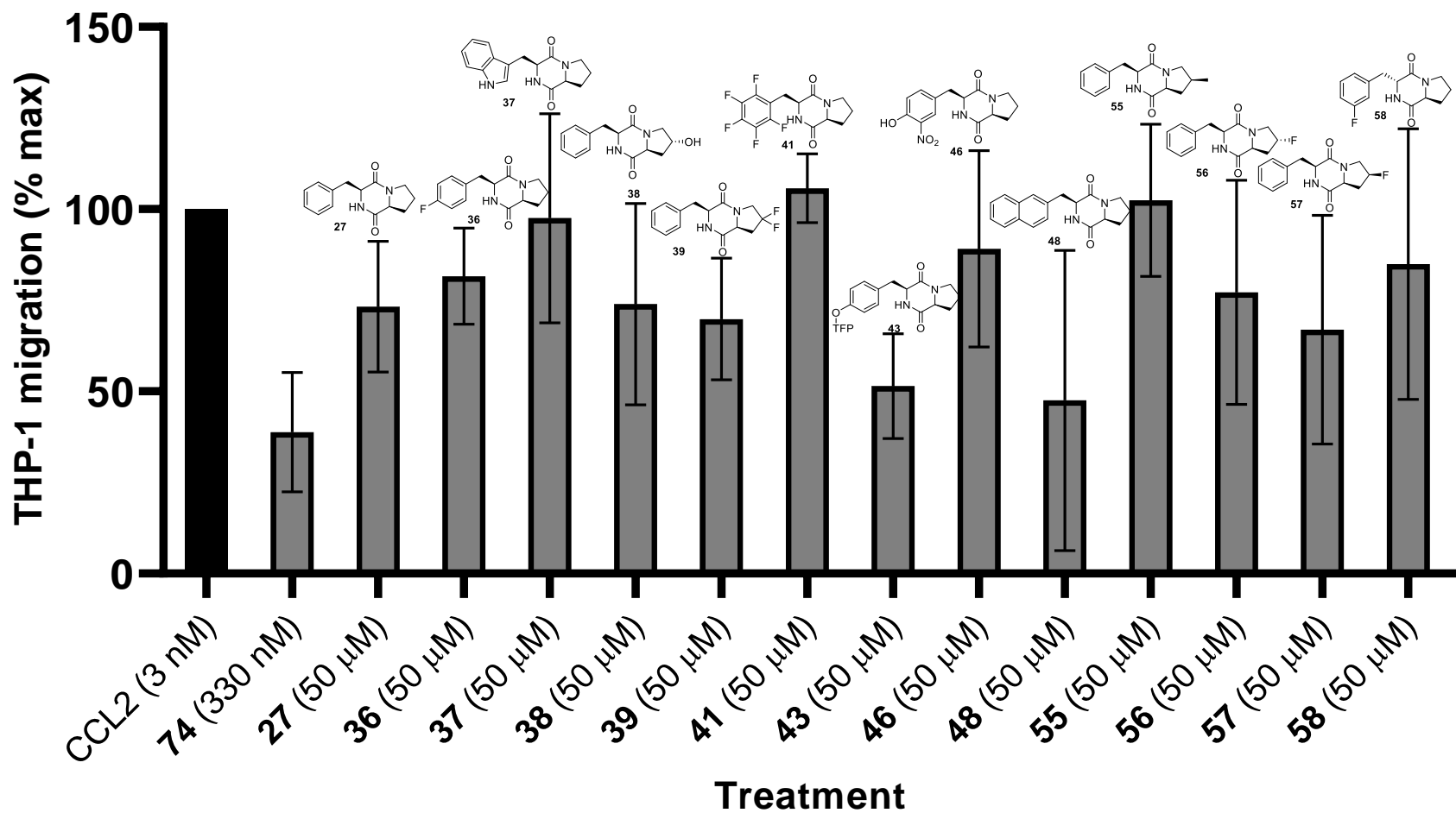


Figure 2.22 THP-1 migration (%) in response to CCL2 +/- DKP inhibitors or RS 504393 (**74**). Baseline CCL2 migration has been subtracted from cell counts and the data is normalised to 100% with 3 nM CCL2 in absence of chemokine. The results are from technical duplicates and biological triplicates (n = 3).

Positive control RS 504393 (**74**) reduced THP-1 migration to $39 \pm 9\%$ in line, if not slightly higher, than the reduction expected at the concentration tested. This result validated the robustness of the chemotaxis assay. DKPs **27** and **36** induced a small change in THP-1 migration (to 73% and 82% respectively) although this was not a statistically significant result. This contradicts previous work by Saleki *et al.*, in which THP-1 migration was reduced to around 50% for DKP **27** and 75% for DKP **36** (at 50 μM).¹¹ It is possible that changes in the experimental set up, such as the reduced CCL2 concentration and the use of a cell detachment solution, could have caused a discrepancy between the results. DKPs **37** and **38**, that were previously tested by Hudson at 100 μM , did not significantly reduce THP-1 migration when tested at 50 μM in this current work. Again, this could result from the experimental changes or from the lack of potency of the DKPs at the reduced concentration.

Of the 9 DKPs that had not previously been tested, DKPs **39** and **43** showed a statistically significant reduction in THP-1 migration at 50 μM (as shown in **Figure 2.23**). DKP **43** which incorporates a TFP group through the tyrosine of the DKP core, was the most potent inhibitor with the mean THP-1 migration reduced to $51\% \pm 8\%$. DKP **39** which incorporates a difluorinated proline, reduced THP-1 migration to a lesser but still significant extent of $70\% \pm 9\%$. DKP **48** which incorporates a naphthalene group reduced mean THP-1 migration to $48\% \pm 24\%$. However, overall this result was not determined to be significant ($p = 0.092$). This was likely due to the high variation between the three biological repeats, with THP-1 migration reduced to 0 in one experiment. This contrasts with the additional two repeats, in which THP-1 migration was reduced to 71% and 72%.

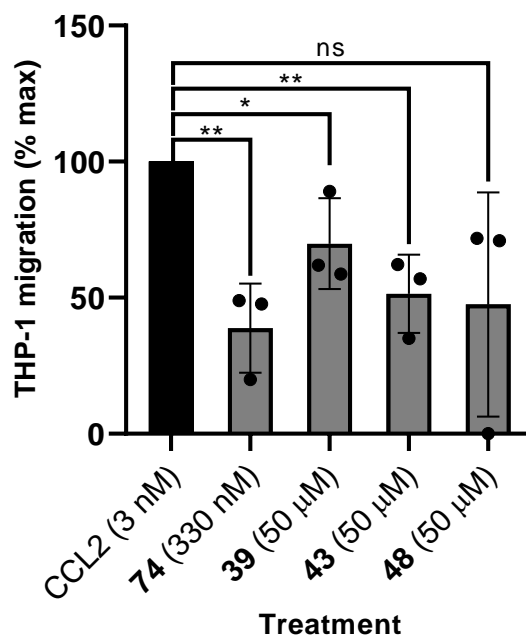


Figure 2.23 Active CCL2 chemotaxis inhibitors with statistical analysis applied. Two-tailed students *t*-tests were used to show statistically significant decrease in THP-1 migration (%) in comparison to CCL2 only. The represented data is normalised to 100% migration in response to 3 nM CCL2 (n = 3). ** p < 0.001, * p = 0.05, ns = non-significant.

A degree of variance was observed between biological repeats for some of the DKPs tested. Chemotaxis assays are challenging, and they are known for a low signal to noise ratio with the potential for high variability.⁶³ Therefore, producing consistent results can be difficult due to experimental factors that can affect the outcome. An example of this is the formation of air pockets in the media below the insert which can disrupt the chemotactic gradient. To counter this, visible air pockets in the plate wells are burst using the tip of a needle before the insert is placed into the well.⁶⁴ However, even with these precautions, the formation of air pockets can be difficult to remove completely.

As part of this work, attempts were made to determine the IC₅₀ of DKP **43** in CCL2 chemotaxis assays. However producing consistent results, in which the controls were working as expected, was unattainable. At this point, the THP-1 cells had become less chemotactic with little difference in the number of THP-1 cells migrating in response to CCL2 in comparison to the baseline migration levels. This could have resulted from the

high passage number that the THP-1 cells had reached (20+ at this stage) or from a potential mycoplasma contamination. Prior to the pandemic, there were regular mycoplasma screenings in the Ali research group, but at the time of writing, this had not been reinstated. Mycoplasma contamination can affect the behaviour and properties of the infected cells, which could have attributed to the sudden failing of the chemotaxis assays.

2.6.4 THP-1 apoptosis assays

THP-1 cell apoptosis assays were undertaken to ensure that DKPs **39**, **43** and **48** did not induce THP-1 cell death. To assess apoptosis, THP-1 cells were incubated with 50 μ M of each compound at 37 °C for 3 h. After this time, FITC-Annexin V and fluorescent dye propidium iodide (PI) were added to each sample and subsequently analysed by flow cytometry. Untreated cells acted as the control for a healthy cell count. Initially, cell incubation with 400 μ M hydrogen peroxide (37 °C for 3 h) was used as a positive control but surprisingly this did not induce cell death. As an alternative positive control, a sample of the cells were halved, with one half exposed to a heat shock (65 °C for 1 min).

The flow cytometry gating strategy utilised 4 quadrants (Q1-Q4) representing different stages of cell death. In **Figure 2.24** the representative scatter plots corresponding to untreated cells, the positive control and DKP **43** are shown. For the untreated cells (**Figure 2.24 (A)**) a small but significant amount of necrotic and early apoptotic cells were detected which could be a result of the staining protocol. For the positive control (**Figure 2.24 (B)**) an increase in late apoptotic and early apoptotic cells were observed, and the cell death in response to DKP **43** (**Figure 2.24 (C)**) was comparable to the negative control.

In **Figure 2.24 (D)**, the stages of necrotic, early apoptotic, late apoptotic and healthy cells are shown as a percentage of the overall cell population for each treatment. The

percentage of healthy to dead cells was determined from this and shown in **Figure 2.24 (E)**. Both data sets show that 50 μM treatments of DKPs **39**, **43**, and **48** did not significantly induce THP-1 death in comparison with the untreated cells. Comparatively, the heat shock control significantly reduced the number of healthy cells.

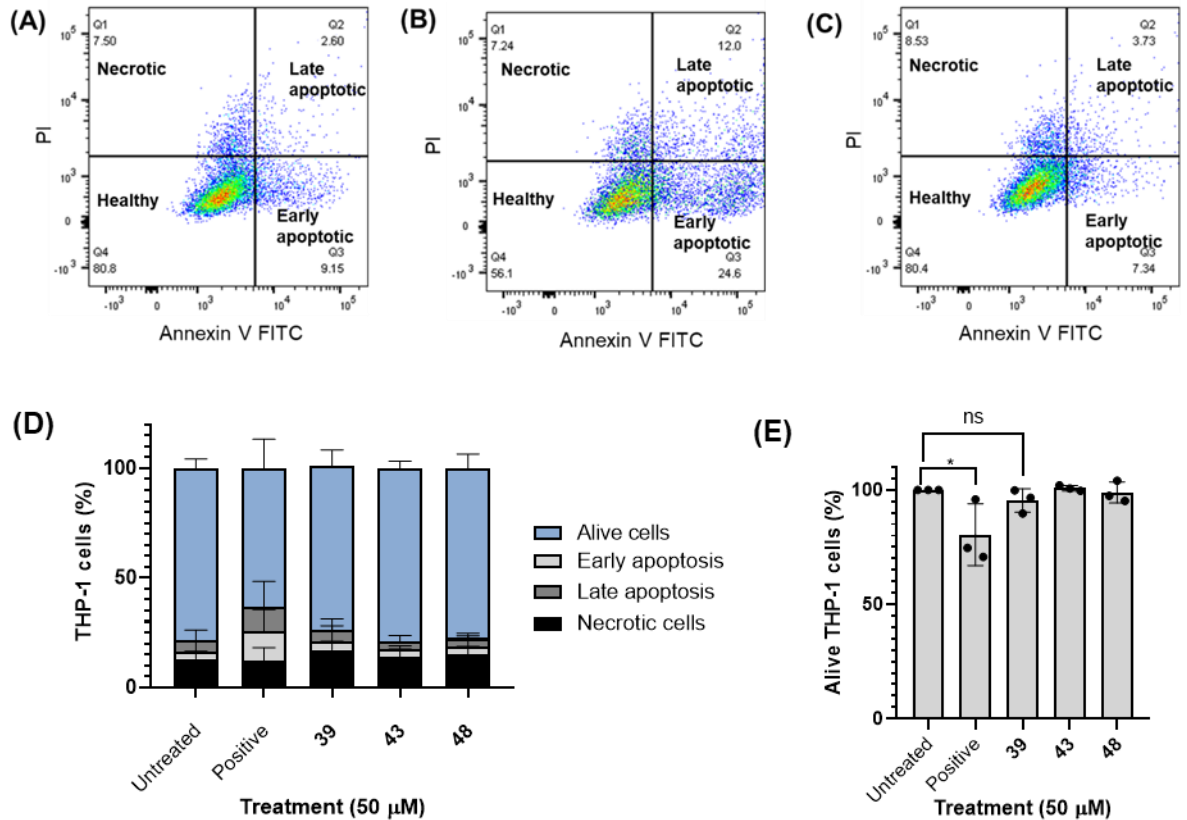


Figure 2.24 THP-1 cell apoptosis assay. **(A-C)** Flow cytometry cell gating strategy for THP-1 cells. **(A)** Untreated cells. **(B)** Positive control. **(C)** Treatment with 50 μM of DKP **43**. **(D)** The % necrotic, early apoptotic, late apoptotic, and alive THP-1 cells as a result of each DKP treatment. **(E)** The % alive cells for each treatment compared to the non-treated cells. The assays were carried out in technical duplicate and biological triplicate. Significance was assessed using one-way ANOVA and Dunnett's test ($n = 3$). * $p < 0.05$, ns = non-significant.

2.6.5 CCR2 internalisation assays

The chemokine-receptor interaction induces signalling via ERK1/2 phosphorylation as well as cytosolic Ca^{2+} influx and hence antagonism of this interaction can inhibit these signalling pathways.⁶⁵ Additionally, receptor internalisation occurs under excess chemokine concentrations, as a mechanism to prevent the overstimulation of the cell.⁶⁶ The disruption

of both signalling events, and receptor internalisation, in response to potential antagonists is commonly investigated and can help gain a greater understanding of the antagonist mode of action.^{67,68} As pERK1/2 inhibition had been investigated in previous work, we sought to determine if DKP **43**, and previous lead **27**, could act on CCR2 to prevent its internalisation. It was proposed that the DKPs could act in two ways; (1) by inducing CCR2 internalisation and reducing surface binding sites for CCL2 or (2) by outcompeting CCL2 for the receptor and thus preventing internalisation.

In the CCR2 internalisation assay DKP **27** was tested at 100 μ M, as previous work had shown this concentration to be effective at reducing THP-1 migration to < 50%.^{11,16} DKP **43** was tested at two different concentrations; 100 μ M for direct comparison with DKP **27** and 50 μ M; the concentration that effectively reduced THP-1 migration to approximately 50% (current work). An additional THP-1 apoptosis assay, using the same procedure explained in **Section 2.6.4**, showed that DKP **43** did not induce cell death at 100 μ M (**Figure 2.25 (B)**).

For CCR2 internalisation assays, THP-1 cells were incubated with CCL2, CCL2 and inhibitors or inhibitors alone, at 37 °C for 30 min. Upon assay completion, the cells were immediately placed onto ice to prevent the receptor recycling to the surface, and subsequently an antibody was added to each sample to detect surface levels of CCR2. Several additional controls were used: an isotype control (to ensure nonspecific binding), an untreated sample and an unstained sample.

Upon incubation of THP-1 cells with CCL2, a reduction in surface CCR2 was expected due to internalisation. In this assay, the extent of internalisation was determined by the shift in median fluorescence intensity (MFI) which is directly related to the levels of surface CCR2. A visual example of this is the corresponding histogram in **Figure 2.25 (A)**, which shows the change in MFI corresponding to each treatment.

The average MFI values across three biological repeats are shown in **Figure 2.25 (C)**. For untreated cells, the average MFI produced was 2921. This was reduced to 1914 upon incubation with CCL2, indicating that CCL2 effectively induced CCR2 internalisation. With the addition of DKP **27** (only) at a concentration of 100 μ M, no significant change in MFI (compared to untreated cells) was observed. When DKP **27** was tested alongside CCL2, there was also no significant change in MFI compared with CCL2 alone.

DKP **43** was tested at both 100 μ M and 50 μ M, with neither inducing a significant change in the average MFI in comparison to the untreated cells. A minor decrease in the average MFI was observed when the concentration of DKP **43** was increased from 50 μ M to 100 μ M, however this was found not be statistically significant. When co-treated with CCL2 at both concentrations, there was no observable difference in the average MFI compared to CCL2 only. The percentage of cells expressing surface CCR2 is shown in **Figure 2.25 (D)**. On average, 64% of cells expressed surface CCR2, which was reduced to 13% when THP-1 cells were incubated with CCL2. No changes were observed with the addition of DKPs **27** and **43** either alone or with CCL2.

From this work it can be determined that DKPs **27** and **43** do not affect the internalisation pathway of CCR2. When tested alone, they do not agonise this process and when co-treated with CCL2, they do not outcompete. This suggests that they do not act to antagonise the orthosteric site on CCR2 and do not exert their pharmacological mode of action by affecting the receptor internalisation pathway.

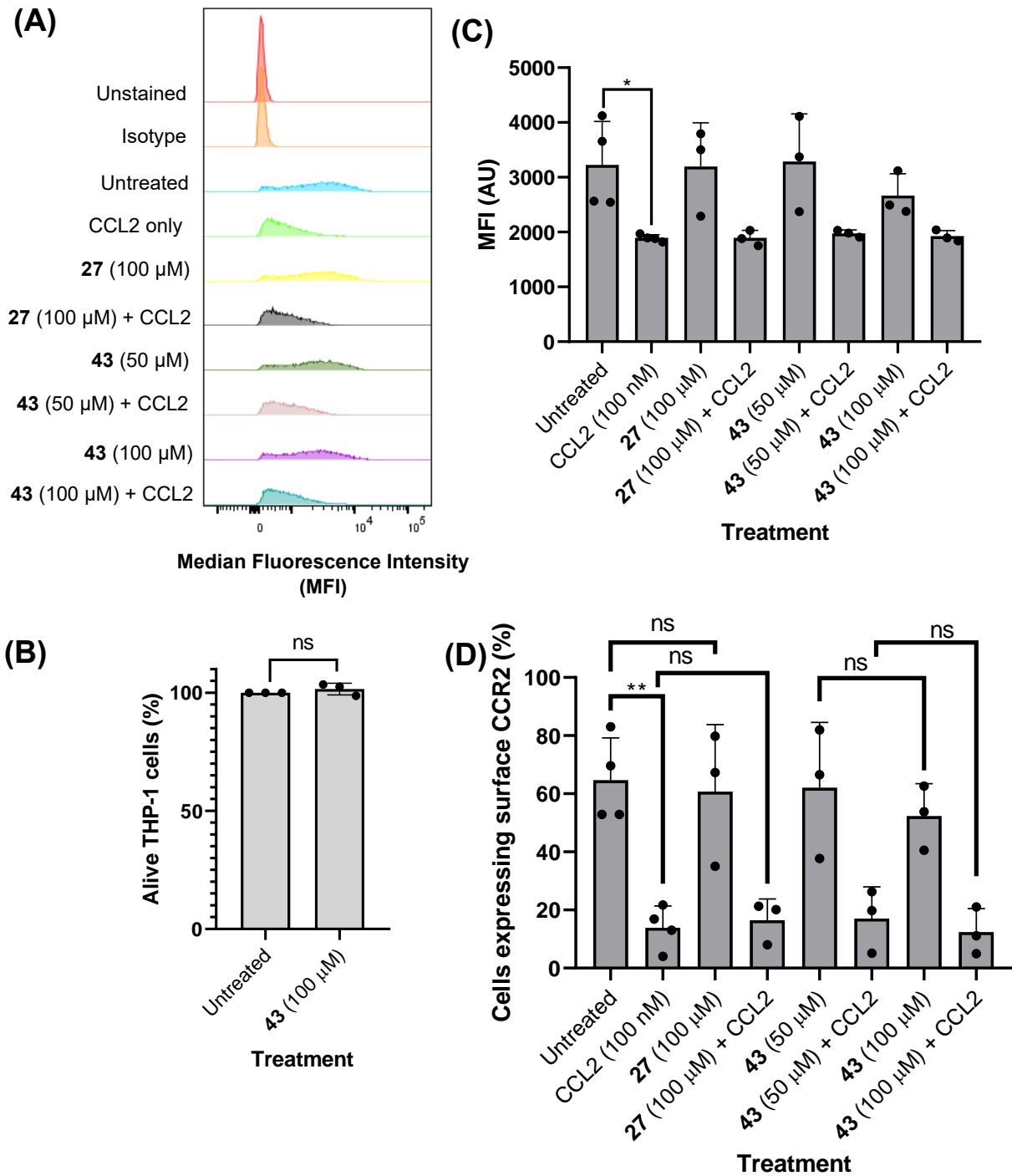


Figure 2.25 CCR2 internalisation assay. **(A)** A representative histogram showing the shift in MFI corresponding with each treatment. **(B)** Cell apoptosis assay for DKP 43 (100 μM). **(C)** The overall MFI shift corresponding to each treatment. **(D)** The cells expressing surface CCR2 (%) in response to each treatment. Experiments were undertaken in triplicate. Significance was assessed using one-way ANOVA and Dunnett's test (n = 3). **p < 0.001, *p ≤ 0.05, ns = non-significant.

2.6.6 Chapter summary

In this chapter a library of 13 DKPs were successfully synthesised. This library included DKPs that had previously shown inhibition of CCL2-mediated chemotaxis, as well as novel compounds that incorporated fluorinated and unnatural amino acid building blocks.

For the synthesis of hydroxyl-containing DKPs, the N-Boc protected SPPS produced very low yields. However, hydroxyl-containing DKP **47**, which incorporated the Fmoc-nitro-tyrosine building block, was successfully synthesised using a modified SPPS. Regardless, DKPs **29** and **38**, were re-synthesised by a solution phase route to provide sufficient material for future incorporation into potential CCL2-targeting PROTACs (**Chapter 4**). SPPS was also shown to be insufficient at producing TFP-containing DKPs **43** and **44**. However, TFP-containing DKP **43** was produced instead from precursor DKP **29**; using the conditions for TFP-ether formation outlined in **Scheme 2.5**. Crystal structures were obtained for 8 DKPs, with structures containing tyrosine or modified tyrosine substituents, preferring a folded conformation over elongated (**Figure 2.17**). An exception was DKP **43**, in which an elongated conformation was preferred.

The inhibitory potential of the DKP library for CCL2-mediated chemotaxis was assessed using a Boyden chamber assay (**Figure 2.22**). Of the DKP inhibitors, **43** was the most potent, reducing THP-1 migration to an average of $51\% \pm 8\%$ (at $50 \mu\text{M}$). DKPs **27**, **36**, **37** and **38**, that had shown anti-chemotactic activity in previous work, did not show any significant inhibition of THP-1 migration in this current work. This could be attributed to the changes in experimental set up or the different concentrations screened (e.g. $50 \mu\text{M}$ in this work but $100 \mu\text{M}$ previously). Fluorinated DKP **39** also showed significant anti-chemotactic activity, reducing THP-1 migration to an average of $70\% \pm 9\%$.

The inhibitors that displayed a significant reduction in the chemotaxis of THP-1 cells, were tested in cell apoptosis assays ($50 \mu\text{M}$) in which no significant cell death was observed (**Figure 2.24**). DKPs **27** and **43** were also screened in CCR2 internalisation assays, to assess their agonistic and antagonistic potential for this process (**Figure 2.25**). However,

the results showed that the DKPs did not impact this process and therefore do not inhibit chemotaxis via a receptor internalisation mechanism. Additionally, this reinforces previous work that showed the DKPs to not outcompete CCL2 binding to CCR2 and therefore the working hypothesis remains that the DKPs bind directly to CCL2. In order to confirm this hypothesis, it was a necessity to directly probe the ligand-binding interactions between the DKPs and CCL2 (**Chapter 3**).

2.7 References

1. A. D. Borthwick, *Chem. Rev.*, 2012, **112**, 3641 – 3716.
2. R. B. Corey, *J. Am. Chem. Soc.*, 1938, **60**, 1598–1604.
3. F. L. Bettens, R. P. A. Bettens, R. D. Brown and P. D. Godfrey, *J. Am. Chem. Soc.*, 2000, **122**, 5856–5860.
4. Y. Zhu, M. Tang, X. Shi, Y. Zhao, *Int. J. Quantum. Chem.*, 2007, **107**, 745.
5. A. Pérez-Mellor, I. Alata, V. Lepère and A. Zehnacker, *J. Phys. Chem. B.*, 2019, **123**, 6023–6033.
6. M. R. Bofinger, L. S. De Sousa, J. E. N. Fontes and A. J. Marsaioli, *ACS Omega.*, 2017, **2**, 1003–1008.
7. C. Y. Wang, X. H. Liu, Y. Y. Zheng, X. Y. Ning, Y. H. Zhang, X. M. Fu, X. Li, C. L. Shao and C. Y. Wang, *Front. Microbiol.*, 2022, **13**, 1–8.
8. Y. Yang and L. Hansen, *ACS Omega.*, 2022, **7**, 12015–12020.
9. Pembrolizumab in Combination With Plinabulin and Docetaxel For Metastatic NSCLC After ICIs. NCT05599789. Clinical Trials.gov. 2023. <https://www.clinicaltrials.gov/study/NCT05599789?cond=plinabulin&rank=5>
10. M. P. Curran and G. M. Keating, *Drugs.*, 2003, **63**, 2203–2212.
11. M. Saleki, N. Colgin, J. A. Kirby, S. L. Cobb and S. Ali, *Med. Chem. Comm.*, 2013, **4**, 860–864.
12. P. Klausmeyer, O. M. Z. Howard, S. M. Shipley and T. G. McCloud, *J. Nat. Prod.*, 2009, **72**, 1–4.
13. K. Ström, J. Sjögren, A. Broberg and J. Schnürer, *Appl. Environ. Microbiol.*, 2002, **68**, 4322–4327.
14. P. J. Milne, A. L. Hunt, K. Rostoll, J. J. Van Der Walt and C. J. M. Graz, *J. Pharm. Pharmacol.*, 1998, **50**, 1331–1337.
15. C. Lotufo, E. R. Silveira, O. D. L. Pessoa, L. V. Costa-Lotufo and P. C. Jimenez, *Chem. Biodivers.*, 2016, **13**, 1149–1157.
16. A. Hudson, PhD Thesis, Durham University, 2015 (available online via Durham University DRO).
17. B. Paudel, R. Maharjan, P. Rajbhandari, N. Aryal, S. Aziz, K. Bhattarai, B. Baral, R. Malla and H. D. Bhattarai, *Pharm. Biol.*, 2021, **59**, 933–936
18. M. M. Bobylev, L. I. Bobyleva and G. A. Strobel, *J. Agric. Food Chem.*, 1996, **44**, 3960-3964.
19. H. D. Jain, C. Zhang, S. Zhou, H. Zhou, J. Ma, X. Liu, X. Liao, A. M. Deveau, C. M. Dieckhaus, M. A. Johnson, K. S. Smith, T. L. Macdonald, H. Kakeya, H. Osada and J. M. Cook, *Bioorganic Med. Chem.*, 2008, **16**, 4626–4651.

20. Y. Shiono, K. Akiyama and H. Hayashi, *Biosci. Biotechnol. Biochem.*, 2000, **64**, 103–110.
21. B. Moser and K. Willmann, *Ann. Rheum. Dis.*, 2004, **63**, 84–89.
22. P. Tang and J. M. Wang, *Cell. Mol. Immunol.*, 2018, **15**, 295–298.
23. E. J. Fernandez and E. Lolis, *Annu. Rev. Pharmacol. Toxicol.*, 2002, **42**, 469–499.
24. S. M. De Munnik, M. J. Smit, R. Leurs and H. F. Vischer, *Front. Pharmacol.*, 2015, **6**, 1–27.
25. S. L. Deshmane, S. Kremlev, S. Amini and B. E. Sawaya, *J. Interf. Cytokine Res.*, 2009, **29**, 313–325.
26. I. Kufareva, *Physiol. Behav.*, 2016, **30**, 27–37.
27. J. Lubkowski, G. Bujacz, L. Boqué, P. J. Domaille, T. M. Handel and A. Wlodawer, *Nat. Struct. Biol.*, 1997, **4**, 64–69
28. C. L. Salanga and T. M. Handel, *Exp. Cell. Res.*, 2011, **317**, 590–601.
29. I. Shachar and N. Karin, *J. Leukoc. Biol.*, 2013, **93**, 51–61.
30. P. Aukrust, B. Halvorsen, A. Yndestad, T. Ueland, E. Øie, K. Otterdal, L. Gullestad and J. K. Damås, *Arterioscler. Thromb. Vasc. Biol.*, 2008, **28**, 1909–1919.
31. T. Kakinuma and S. T. Hwang, *J. Leukoc. Biol.*, 2006, **79**, 639–651.
32. C. M. Perry. *Adis. Drug. Rev.*, 2010, **70**, 1189–1213
33. S. P. Fricker. *Transfus. Med. Hemother.*, 2013, **40**, 237–245.
34. J. Stewart, Aphexda FDA Approval History, 2023, <https://www.drugs.com/history/aphexda.html>.
35. Z. D. Crees, M. P. Rettig, R. G. Jayasinghe, K. Stockerl-Goldstein, S. M. Larson, I. Arpad, G. A. Milone, M. Martino, P. Stiff, D. Sborov, D. Pereira, I. Micallef, G. Moreno-Jiménez, G. Mikala, M. L. P. Coronel, U. Holtick, J. Hiemenz, M. H. Qazilbash, N. Hardy, T. Latif, I. García-Cadenas, A. Vainstein-Haras, E. Sorani, I. Gliko-Kabir, I. Goldstein, D. Ickowicz, L. Shemesh-Darvish, S. Kadosh, F. Gao, M. A. Schroeder, R. Vij and J. F. DiPersio, *Nat. Med.*, 2023, **29**, 869–879.
36. W. Y. Lai and A. Mueller, *Biochem. Soc. Trans.*, 2021, **49**, 1385–1395.
37. R. Solari, J. E. Pease and M. Begg, *Eur. J. Pharmacol.*, 2015, **746**, 363–367.
38. W. G. Nichols, H. M. Steel, T. Bonny, K. Adkison, L. Curtis, J. Millard, K. Kabeya and N. Clumeck, *Antimicrob. Agents Chemother.*, 2008, **52**, 858–865.
39. F. Moadab, H. Khorramdelazad and M. Abbasifard, *Life Sci.*, 2021, **261**, 119034.
40. S. Behfar, G. Hassanshahi, A. Nazari and H. Khorramdelazad, *Cytokine.*, 2018, **110**, 226–231.
41. S. Y. Lim, A. E. Yuzhalin, A. N. Gordon-weeks and R. J. Muschel. *Oncotargets.*, 2016, **7**, 28697–28710.

42. S. She, L. Ren, P. Chen, M. Wang, D. Chen, Y. Wang and H. Chen, *Front. Immunol.*, 2022, **13**, 1–16.
43. T. Kenakin, *Br. J. Pharmacol.*, 2023, 1–23.
44. C. M. Brodmerkel, R. Huber, M. Covington, S. Diamond, L. Hall, R. Collins, L. Leffet, K. Gallagher, P. Feldman, P. Collier, M. Stow, X. Gu, F. Baribaud, N. Shin, B. Thomas, T. Burn, G. Hollis, S. Yeleswaram, K. Solomon, S. Friedman, A. Wang, C. B. Xue, R. C. Newton, P. Scherle and K. Vaddi, *J. Immunol.*, 2005, **175**, 5370–5378.
45. G. Chandra, D. V. Singh, G. K. Mahato and S. Patel, *Chem. Pap.*, 2023, **77**, 4085–4106.
46. P. Shah and A. D. Westwell, *J. Enzyme Inhib. Med. Chem.*, 2007, **22**, 527–540.
47. P. M. Fischer, *J. Pept. Sci.*, 2003, **9**, 9–35.
48. M. Teixidó, E. Zurita, R. Prades, T. Tarrago and E. Giralt, *Adv. Exp. Med. Biol.*, 2009, **611**, 227–228.
49. W. D. G. Brittain and S. L. Cobb, *Org. Biomol. Chem.*, 2019, **17**, 2110–2115.
50. L. N. D. Beardmore, S. L. Cobb and W. D. G. Brittain, *Org. Biomol. Chem.*, 2022, **20**, 8059–8064.
51. W. D. H. N. Perera, University of Durham, 2023, *unpublished*.
52. T. Ueda, M. Saito, T. Kato and N. Izumiya, *Bull. Chem. Soc. Jpn.*, 1983, **56**, 568–572.
53. W. Xiang, Q. Liu, X. Li, C. Lu and Y. Shen, *Nat. Prod. Res.*, 2020, **34**:15, 2219–2224.
54. P. Wattana-Amorn, W. Charoenwongsa, C. Williams, M. P. Crump & B. Apichaisataienchote., *Nat. Prod. Res.*, 2016, **30**, 1980–1983.
55. T. Ishizu, P. Sato, S. Tsuyama, R. Nagao, K. Fujiki and A. Yamaji, *Anal. Sci. Adv.*, 2022, **3**, 38–46.
56. W. D. G. Brittain and S. L. Cobb, *J. Org. Chem.*, 2020, **85**, 6862–6871.
57. D. Cooper, J. M. Ilarregui, S. A. Pesoa, D. O. Croci, M. Perretti and G. A. Rabinovich, *Methods Enzymol.*, 2010, **480**, 199–244.
58. D. J. Webb, H. Zhang and A. F. Horwitz, *Cell migration: an overview.*, 2005, vol. 294.
59. I. Del Molino Del Barrio, J. Kirby and S. Ali, *The Role of Chemokine and Glycosaminoglycan Interaction in Chemokine-Mediated Migration in Vitro and in Vivo*, Elsevier Inc., 1st edn., 2016, vol. 570.
60. R. H. De Wit, S. M. De Munnik, R. Leurs, H. F. Vischer and M. J. Smit, *Molecular Pharmacology of Chemokine Receptors*, Elsevier Inc., 1st edn., 2016, vol. 570.

61. B. Darlot, J. R. O. Eaton, L. Geis-Asteggiante, G. K. Yakala, K. Karuppanan, G. Davies, C. V. Robinson, A. Kawamura and S. Bhattacharya, *J. Biol. Chem.*, 2020, **295**, 10926–10939.
62. T. Mirzadegan, F. Diehl, B. Ebi, S. Bhakta, I. Polsky, D. McCarley, M. Mulkins, G. S. Weatherhead, J. M. Lapierre, J. Dankwardt, J. Morgans D., R. Wilhelm and K. Jarnagin, *J. Biol. Chem.*, 2000, **275**, 25562–25571.
63. A. Das and L. Yan, *Anti-CCL-2/MCP-1: Directed Biologicals for Inflammatory and Malignant Diseases*, Elsevier Inc., 2006, vol. 1.
64. B. M. Sicari, L. Zhang, R. Londono and S. F. Badylak., *Methods. Mol. Biol.*, 2014, **1202** 103–110.
65. A. Steen, O. Larsen, S. Thiele and M. M. Rosenkilde, *Front. Immunol.*, 2014, **5**, 1–13.
66. N. F. Neel, E. Schutyser, J. Sai, G. H. Fan and A. Richmond, *Cytokine Growth Factor Rev.*, 2005, **16**, 637–658.
67. C. Auvynet, C. Baudesson De Chanville, P. Hermand, K. Dorgham, C. Piesse, C. Pouchy, L. Carlier, L. Poupel, S. Barthélémy, V. Felouzis, C. Lacombe, S. Sagan, B. Salomon, P. Deterre, F. Sennlaub and C. Combadière, *FASEB J.*, 2016, **30**, 2370–2381.
68. S. Kredel, M. Wolff, S. Hobbie, M. Bieler, P. Gierschik and R. Heilker, *J. Biomol. Screen.*, 2011, **16**, 683–693.

3. Small molecule CCL2 binders

3.1 CCL2 structure

As discussed in **Chapter 2**, CCL2 is a CC chemokine containing two directly linked disulphide bonds. The crystal structure of CCL2 was solved in 1997 by Lubkwocki *et al.*, (**Figure 3.1**) and it showed CCL2 monomersⁱ (**Figure 3.1 (A)**) to have triple stranded antiparallel β -sheets, with an α -helix located on top and two disulfide bridges in a left-handed spiral conformation, followed by a flexible, disordered N-terminus.¹ CCL2 forms two different quaternary structures: either a dimer consisting of two monomers (**Figure 3.1 (B)**) or a tetramer constituting two dimers (**Figure 3.1 (C)**). At pH > 7.0 and in the presence of inorganic ions, the tetramer is the predominant form of CCL2.

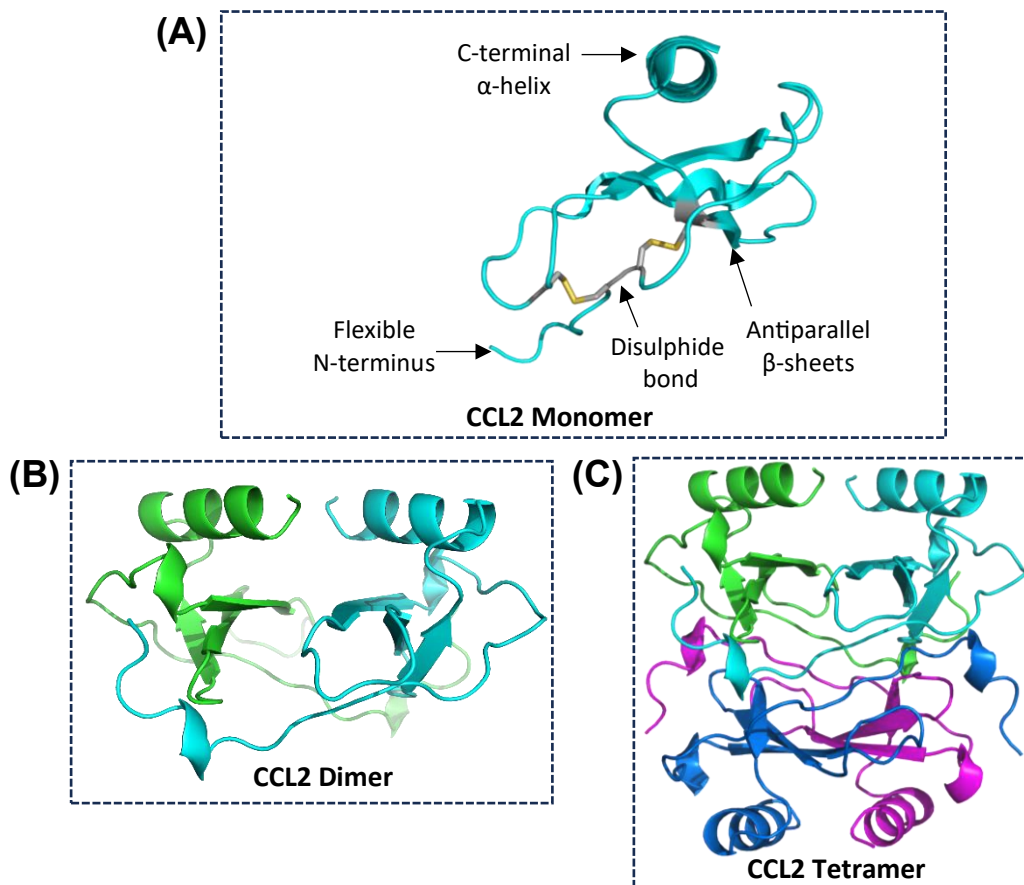


Figure 3.1 Crystal structures of the CCL2 (A) monomer, (B) dimer and (C) tetramer. Crystal structures reproduced by Lubkowski *et al.*, (PDB:1DOL) and (PDB:1DOK).

ⁱ Inclusion of the two disulfide bonds in the monomeric structure results in β -sheets that are not flattened.

3.2 CCL2-CCR2 binding

Although CCL2 exists as a dimer in solution, it has also been reported to bind to CCR2 as a monomer, though this has been an area of controversy. In work by Proudfoot *et al.*, monomeric CCL2 was able to induce leukocyte chemotaxis *in vitro* but was unable to replicate this result *in vivo*, suggesting that oligomerisation was required for CCL2-CCR2 binding.² However, this was disputed in work by Tan *et al.*, in which an obligate dimer of CCL2 was unable to bind CCR2 (at concentrations up to 1 μ M) and was inactive in calcium influx assays (compared with wild-type CCL2).³ Monomeric mutants of CCL2 have also demonstrated wild-type potency in chemotaxis and calcium influx assays, in addition to wild-type CCR2 binding.⁴ Therefore, it is accepted that although dimeric CCL2 is essential for physiological functions associated with *in vivo* leukocyte chemotaxis, CCL2 binds CCR2 as a monomer.

Monomeric CCL2 binds to CCR2 according to the two-site model: (1) the N-terminus of the receptor interacts with the globular core of the chemokine at the chemokine receptor site 1 (CRS1), (2) simultaneously the transmembrane domains (TM) of the receptor bind the N-terminus of the chemokine at the chemokine receptor site 2 (CRS2). Although CCL2-CCR2 crystal structures have not yet been reported, the structure of the CCL2-CCR2-G protein complex has been solved using Cryo-EM by Shen *et al.*, confirming the two-site binding model (**Figure 3.2**).⁵ At the CRS1, the N-terminus of CCR2 was shown to form hydrophobic and hydrogen-bond interactions with the N-terminus, the N-loop and nearby β -sheet region of CCL2. At CRS2, CCL2 locates itself at the orthosteric binding pocket which is split into major (TM 1 - 3) and minor (TM 3 - 7) sub-pockets, with the N-terminus of CCL2 oriented towards the minor pocket. Another key interaction is the N-terminal glutamine of CCL2 which forms extensive hydrogen bonds with the TM3 and extracellular loop 1 (ECL1) on CCR2.

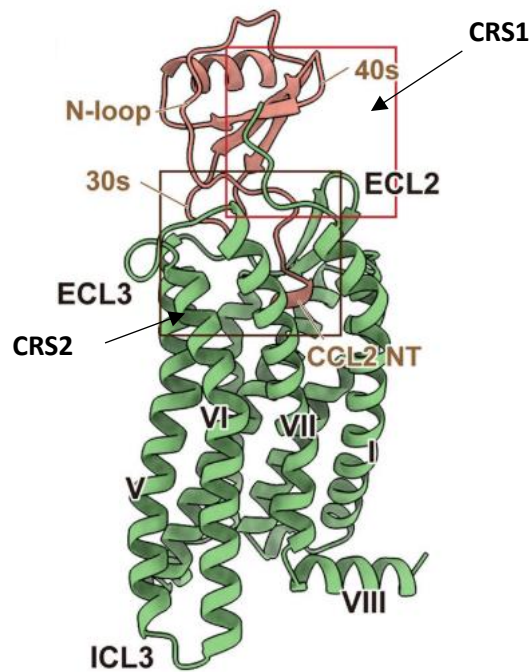


Figure 3.2 Cryo-EM side view of CCL2 (red) binding to the membrane spanning CCR2 (green). [Image modified from reference 5].

3.3 CCR2 antagonists

Despite the limited success of chemokine targeting drugs, there is considerable therapeutic potential in targeting chemokine-receptor interactions (discussed in **Chapter 2**). To disrupt the CCL2-CCR2 interaction, CCR2 antagonists (typically small molecules) or CCL2 binders (typically peptides or biologics) can be used. The majority of CCR2 antagonists exert their effect by outcompeting CCL2 for the orthosteric site. In addition, antagonists that bind to allosteric extracellular or intracellular binding sites have also been discovered. Example CCR2 antagonists are shown in **Figure 3.3**.

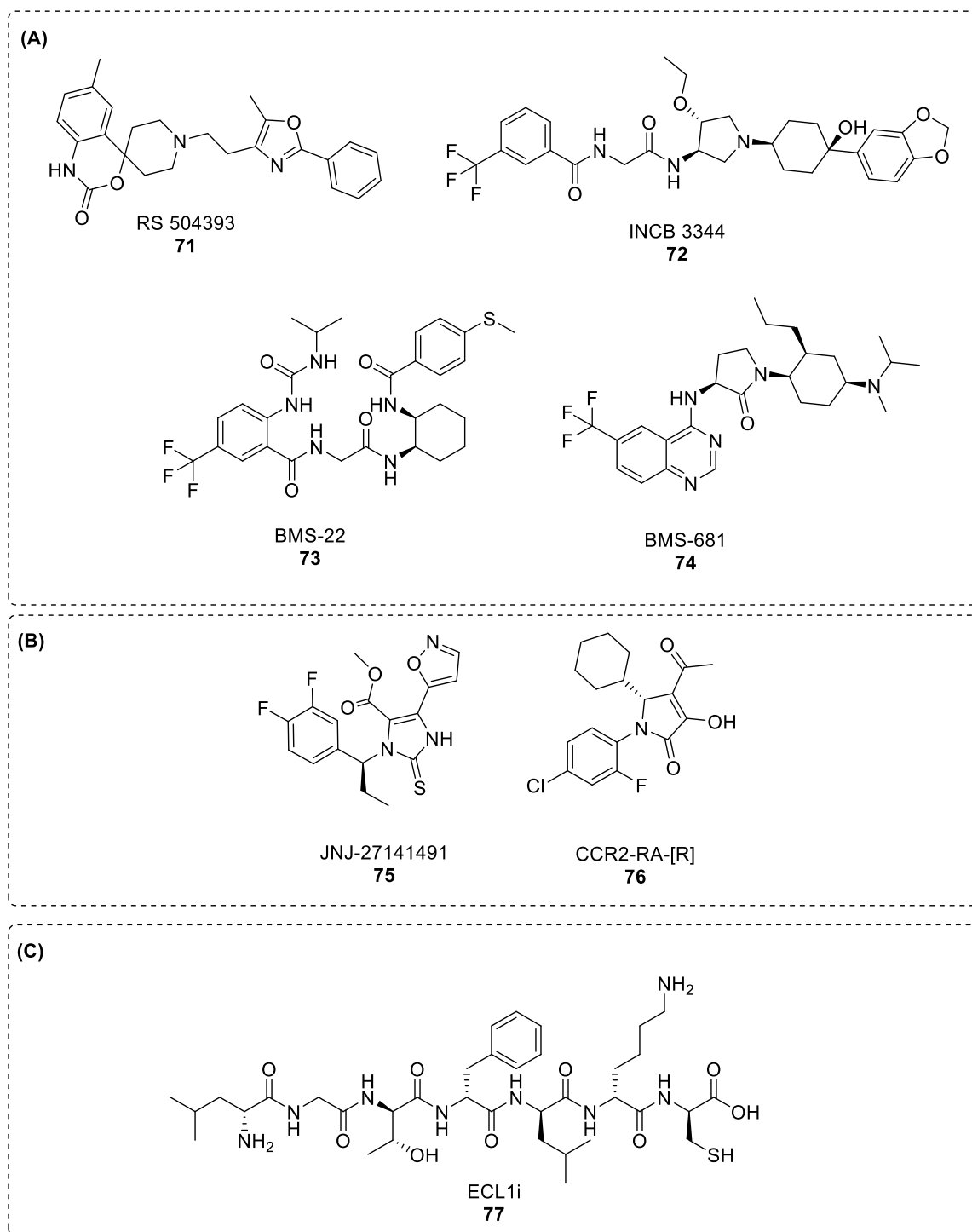


Figure 3.3 Chemical structures of CCR2 antagonists. **(A)** Orthosteric CCR2 antagonists. **(B)** Intracellular allosteric CCR2 antagonists. **(C)** Extracellular allosteric antagonist **77**.

INCB3344 (**72**) is a CCR2 antagonist discovered by Broadmarkel *et al.*, that inhibited CCL2-mediated chemotaxis of HEK293 cells at an IC_{50} of 3.8 nM and displaced CCL2 with an binding affinity of 7 nM.^{6,7} Additionally, antagonist **72** inhibited calcium influx and

ERK1/2 phosphorylation. RS504393 (**71**)ⁱⁱ and BMS-22 (**73**) are also CCR2 binders, with binding affinities of 89 ± 63 nM and 5.1 ± 3.6 respectively, that outcompete CCL2 for the orthosteric site.^{8,9} The basic nitrogen of RS504393 (**71**) interacts with the Glu²⁹⁴ between sub-pockets on CCR2 and is essential for binding.⁹ It is also likely that INCB3344 (**72**) interacts in the same way due to its pyrrolic nitrogen. Conversely, BMS-22 (**73**) does not interact with Glu²⁹⁴ but utilises adjacent residue threonine 292 (Thr²⁹²).⁸

Other CCR2 antagonists interact with a highly conserved intracellular allosteric binding pocket. In work by Zweemer *et al.*, BMS-22 (**73**) and RS 504393 (**71**) were able to displace [³H]INCB3344 from CCR2, which suggested that they shared a common binding site.¹⁰ However, CCR2 antagonists JNJ-27141491 (**75**) and CCR2-RA-[R] (**76**), which block CCL2 binding by 172 ± 15 and 103 ± 18 nM respectively, were unable to displace [³H] INCB3344. Additionally, antagonists **71**, **72** and **73** were unable to displace [³H] CCR2-RA-[R] from CCR2. This indicated that antagonists **75** and **76** share a separate site binding site to **71** - **73**. Structurally, both antagonists **75** and **76**, lack basic nitrogen atoms and have lower molecular weights than **71** - **73**. It was later confirmed in work by Zheng *et al.*, in which CCR2 was crystalised in a ternary complex with orthosteric antagonist BMS-681 (**74**) and CCR2-RA-[R] (**75**), that antagonist **75** occupied an intracellular allosteric binding pocket on CCR2 (**Figure 3.4**).¹¹ Conversely, BMS-681 (**74**), was shown to bind predominantly to the minor sub-pocket of the orthosteric site, with no direct interaction with Glu²⁹⁴. It was proposed in this work by Zheng *et al.*, that orthosteric binders such as **74** disrupt CCL2 binding directly and G-protein coupling indirectly, forming a conformation where G-protein binding is not possible. Conversely, intracellular binders such as **75**, disrupt the G-protein directly effectively 'switching' off the receptor from interacting with CCL2.

ⁱⁱ RS504393 (**71**) was the small molecule CCR2 antagonist used as the positive control for chemotaxis assays undertaken in **Chapter 2**.

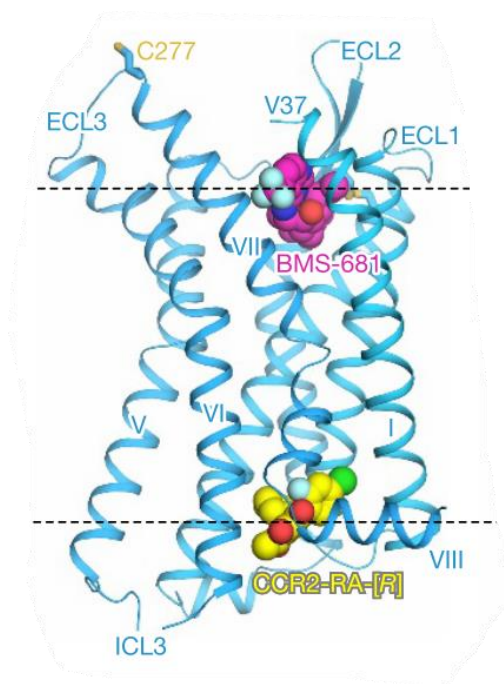


Figure 3.4 The crystal structure of the CCR2 ternary complex with BMS-681 and CCR2-RA-[R]. [Image from reference 11].

Peptide CCR2 antagonist, ECL1i (**77**) (dLGTFLKC) was designed by Auvynet *et al.*, from the hexapeptide sequence of the extracellular loop 1 (ECL1) of CCR2.¹² ECL1i (**77**) inhibited the chemotaxis of CHO-CCR2 cells ($IC_{50} \sim 2 \mu M$) and displayed CCR2 binding (using cellular ITC) with a maximum heat release of $-281 \mu J$ at $150 \mu M$. In addition, competition experiments showed that antagonist **77** was unable to prevent CCL2-CCR2 binding when tested up to $60 \mu M$. The antagonist was also unable to inhibit calcium influx or ERK1/2 phosphorylation and had no effect on CCL2 stimulated CCR2 internalisation. It was predicted that ECL1i (**77**) acted as an extracellular allosteric antagonist of CCR2, binding to the ECL1 and ‘trapping’ CCR2 into a conformation, in which signals away from chemotaxis but is still intact for other signalling events.

3.4 CCL2 binders

As an alternative to CCR2 antagonism, peptides or larger biologics can be used to neutralise CCL2 itself. NOX-E36 is a spiegelmer (a mirror-image aptamer consisting of L-ribonucleotides) that binds CCL2 with a K_D of $1.4 nM$.¹³ It is also promiscuous for other CC chemokines, binding CCL8, CCL11 and CCL13 (K_D of 3.35 , 3.06 and $22 nM$ respectively).

Additionally evasins, which are a small group of proteins secreted from ticks, have demonstrated chemokine binding and have inspired further research into the synthesis of chemokine inhibiting peptides.¹⁴ P672 is an 104 amino acid protein, secreted from the tick *Rhipicephalus pulchellus*, that was found to bind CCL3, CCL3L1 and CCL8 with nano-molar potency.¹⁵ Darlot *et al.*, used P672 as a template to develop a series of peptides that showed promiscuous binding and inhibition of CC chemokines.¹⁶ Their lead peptide BK1.3 was able to displace P672ⁱⁱⁱ from CCL2 at an IC₅₀ of 6 ± 4 μM and moderately inhibited CCL2-mediated THP-1 chemotaxis when tested at 10 μM. However, BK1.3 was most potent for CCL8, reducing the chemotaxis of THP-1 cells with an IC₅₀ of 7 ± 4 nM and binding CCL8^{iv} with a K_D of 217 nM.

The only published small molecule binder to CCL2 is flavonoid Baicalin (**Figure 3.5**), which was shown in work by Li *et al.*, to interrupt the chemokine-receptor interaction for a range of CC and CXC chemokines.¹⁷ In this work, Baicalin significantly reduced CCL2-chemotaxis of HEK293 cells at a dose of 320 μg/mL. A decade later, work by Joshi *et al.*, sought to further investigate Baicalin's mode of action, revealing its potent binding to CCL2 in both the monomeric and dimeric state, with a K_D of ~ 270 nM ± 20 nM (determined by fluorescence quenching experiments).¹⁸

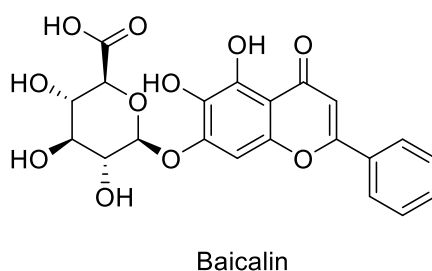


Figure 3.5 Chemical structure of small molecule CCL2 binder Baicalin.

ⁱⁱⁱ Using an AlphaScreen displacement assay.

^{iv} K_D acquired from isothermal calorimetry (ITC).

3.5 CCL2 production

To elucidate the ligand-binding interactions of a chemical library with a specific protein, the production and isolation of the protein is firstly required. This is commonly achieved through recombinant protein overexpression in *E. coli*. However for lower molecular weight proteins, production can also be achieved using solid phase peptide synthesis (SPPS). Grygiel *et al.*, reported the synthesis of CCL2, in which CCL2 peptide fragments were synthesised and assembled by native chemical ligation (NCL).¹⁹ Synthetic CCL2 was biologically characterised by competition experiments with ¹²⁵I-CCL2, in addition to calcium influx assays, which both showed similar behaviour to recombinant CCL2. Additionally, the crystal structure of synthetic CCL2 was solved, with a similar structure to that previously reported in work by Lubkowski *et al.*¹ Previously a member of the Cobb group, Alex Hudson, attempted to use a similar SPPS strategy for the synthesis of CCL2, however this proved to be challenging. Although formation of CCL2 peptide fragments was largely successful, they were unable to be assembled using NCL to form the complete protein.²⁰

3.6 Aims

From previous work carried out within the Cobb group (discussed in **Chapter 2**) it was proposed that the DKP inhibitors of CCL2-mediated chemotaxis, exert their mode of action through direct binding with CCL2 and not the receptor CCR2. As the aim of this project is to incorporate DKPs into PROTACs capable of degrading CCL2, it is crucial to analyse their binding capabilities.

To achieve this goal, it is aimed to produce recombinant CCL2 in sufficient quantities to enable the application of biophysical methods to probe ligand-binding between the DKPs and CCL2. This would enable the suitability of DKPs as the POI warhead in CCL2-PROTACs to be assessed. Additionally, as explained in **Section 3.4**, small molecule CCL2 binders are rare. Therefore, a small fragment screen will be undertaken using the

expressed CCL2 and an available in-house library, with the aim of discovering new small molecule CCL2 binders.

3.7 HsCCL2 overexpression in *E. coli*^v

CCL2 (*hsCCL2*) was expressed with an N-terminal His₆-tag in addition to a thrombin cleavage site that allows for the removal of the tag (plasmids obtained from Genescript). His₆-tags are often incorporated into protein constructs as they enable purification by immobilised metal affinity chromatography (IMAC) and are small and flexible with a low impact on biophysical or crystallographic assays.²¹ *HsCCL2* is a small protein with a predicted mass of 10,979 Da and an isoelectric point (pI) of 9.9 (as calculated using EXPACY PROT PARAM).

3.7.1 Medium scale *hsCCL2* preparation

The *hsCCL2* plasmid was transformed into BL21(DE3) competent cells and the protein was over-expressed on a 6 litre scale. The bacterial cultures were grown, using a pre-culture, at 37 °C using standard incubator shakers. When an optical cell density (OD₆₀₀) of 0.6 was reached, protein expression was induced using 1 mM isopropyl β-D-1-thiogalactopyranoside (IPTG). At the point of induction, the temperature was reduced to 30 °C and the cultures were incubated overnight. Following this, cell pellets were obtained and stored at -80 °C until required for purification.

The cell pellets were purified by IMAC, using a 1 mL HisTrap column (Ni-NTA affinity chromatography). The desired protein was obtained in elution volumes (EV) 8 - 13 (**Figure 3.6 (A)**) displaying strong bands between 10 and 15 kDa on the corresponding SDS-PAGE gel (**Figure 3.6 (B)**). The column flow-through and wash were analysed on the same gel and showed no presence of *hsCCL2*.

^v The work in this section was carried out with the support from members of the Pohl group.

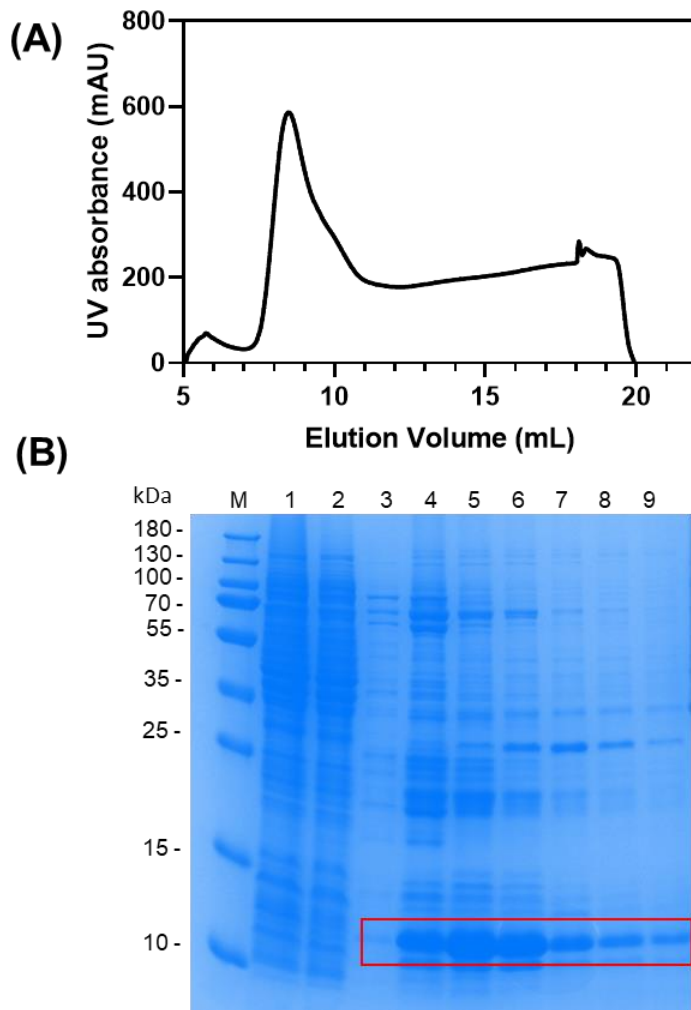


Figure 3.6 (A) Chromatogram for the Ni-NTA of *hsCCL2*. **(B)** SDS-PAGE analysis of elution fractions from the Ni-NTA; M = marker with MWs of bands on the left. 1 = lysate; 2 = column flow-through; 3 = column wash; 4 – 9 = protein fractions. Bands corresponding to *hsCCL2* (MW = 11 kDa) are indicated with a red box.

Contaminants were observed, particularly in **lanes 4 - 7 (Figure 3.6 (B))**, that were close in molecular weight to *hsCCL2* and therefore ion-exchange chromatography (IEX) was used as a second purification step. Elution volumes (EV) corresponding to **lanes 4 - 9** were purified using a Mono-S column (cation exchange) with the corresponding chromatogram (**Figure 3.7 (A)**) displaying a sharp peak between 30 and 38 EV (*hsCCL2*). A reduction in UV absorbance of the *hsCCL2* peak (600 mAU to 55 mAU) was observed in comparison to the previous Ni-NTA purification (**Figure 3.7 (B)**). However, strong protein

bands between 10 and 15 kDa were observed on the corresponding SDS-PAGE gel (**Figure 3.7 (B)**). The protein fractions of the highest purity were present in **lanes 4 - 6** with additional impurities around 25 kDa observed in **lanes 7 - 8**. 1.5 mg of *hsCCL2* (elution volumes corresponding to **lanes 4 - 6**) was obtained from this preparation.

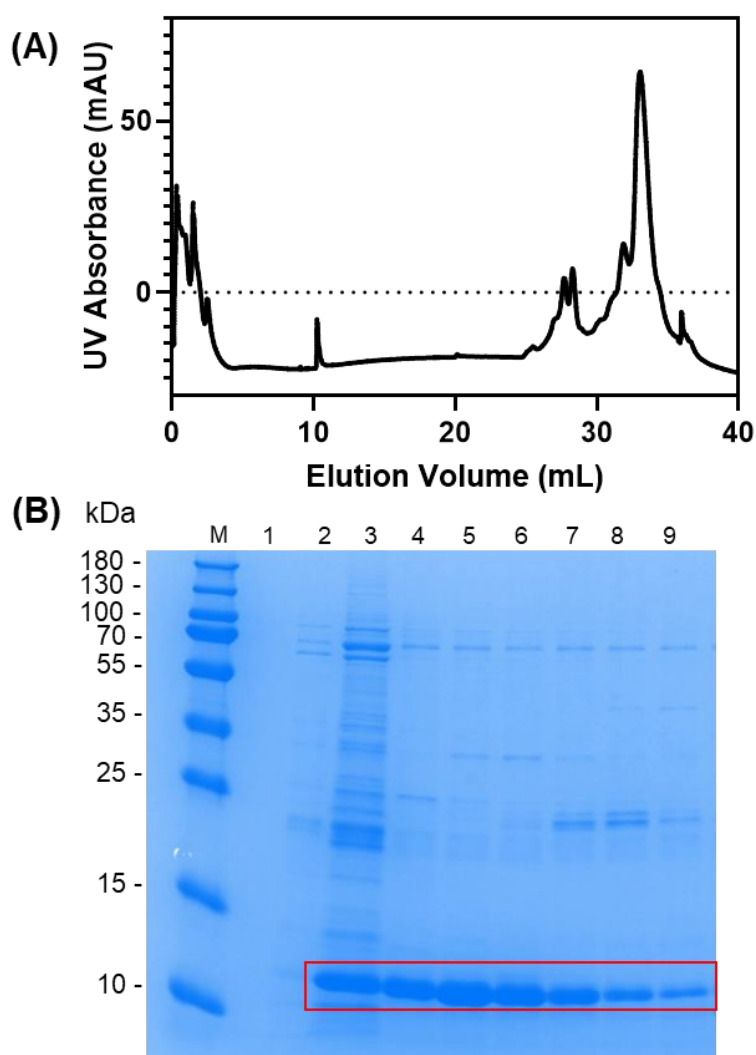


Figure 3.7 (A) Chromatogram from the Mono-S of *hsCCL2*. **(B)** SDS-PAGE analysis of elution fractions from the Mono-S. M = marker with MWs of bands on the left; 1 = flow-through from spin concentrator; 2 = column flow-through; 3 = sample prior to Mono-S; 4 – 10 = protein fractions. Bands corresponding to *hsCCL2* (MW = 11 kDa) are indicated with a red box.

The molecular mass of the obtained protein, as determined by mass spec (TOF ES⁺), was 10,847 Da; -132 Da lower than predicted. However, this is commonly observed when an N-terminal methionine is cleaved by bacterial enzymes (**Figure 3.8**).²² In addition, the

identity of the protein band present between 10 and 15 kDa (SDS-PAGE gel in **Figure 3.7 (B)**) was confirmed to be human CCL2 by trypsin digest mass spec (data shown in **Appendix 8.1**).

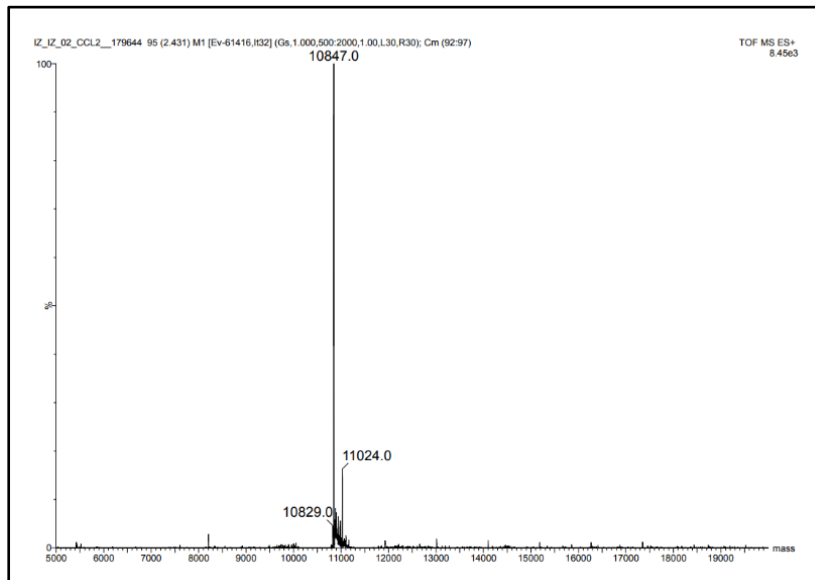


Figure 3.8 Mass Spec (ES⁺ TOF) corresponding to the mass of [*hsCCL2*-Met]

3.7.2 Large scale *hsCCL2* preparation

Following this, *hsCCL2* production was carried out on a larger scale using a Harbinger LEXTM-48 bioreactor, in an effort to increase the quantity of protein obtained. 10 litres of bacterial culture were grown under a constant air flow which in theory, enables a greater bacterial growth.²³ Consequently, bacterial cultures can be grown to a greater cell-density (OD₆₀₀) before IPTG induction. The aim was to produce a pre-induction OD₆₀₀ of over 1.5 however after 5 h, cultures had plateaued at an OD₆₀₀ of approximately 1.25. From this preparation, cell pellets obtained from 6 litres of culture were purified by Ni-NTA affinity chromatography: using the same method shown in **Section 3.7.1**. The SDS-PAGE gel corresponding to this purification is shown in **Figure 3.9**, with *hsCCL2* bands observed in **lanes 7 - 10** (red box). **Lane 7 - 10** show *hsCCL2* present at a higher purity in comparison with **Figure 3.6 (B)** however the bands were much weaker indicating a lower quantity of protein obtained.

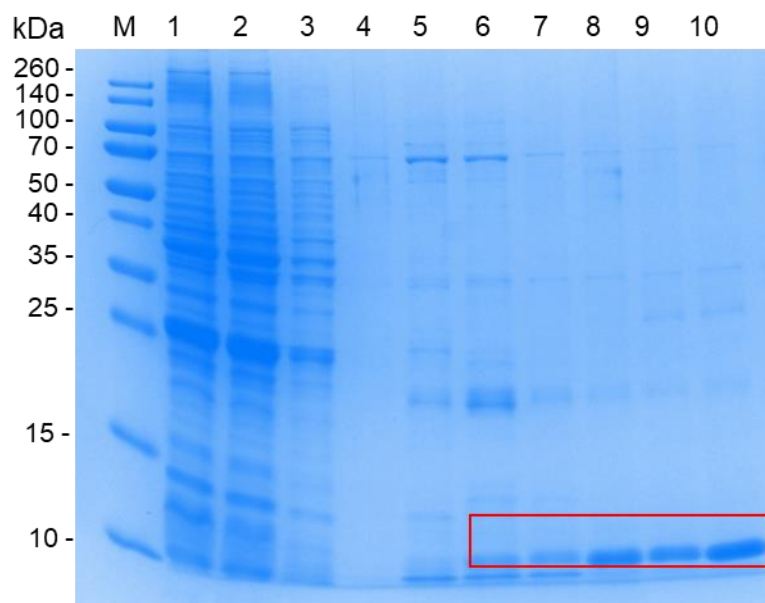


Figure 3.9 SDS-PAGE gel analysis of elution fractions from the Ni-NTA of *hsCCL2* (from the protein production that used the Harbinger™-48 bioreactor). M = marker with MWs of protein bands on the left; 1 = cell lysate; 2 = column flow-through; 3 = column wash; 4 – 12 = protein fractions. Bands corresponding to *hsCCL2* (MW = 11 kDa) are indicated with a red box.

The remaining pellets (from 4 litres of culture) were also purified by Ni-NTA affinity chromatography. However, analysis of the corresponding SDS-PAGE gel showed *hsCCL2* had been obtained again in low quantities (**Figure 3.10**). A sample of cell pellet was run in **lane 2**, which revealed the presence of a protein band between 10 and 15 kDa (white box). This band was analysed using trypsin digest MS and it was confirmed as human CCL2. As there was little improvement in the quantity of *hsCCL2* produced using the bioreactor, further *hsCCL2* preparations did not use this method.

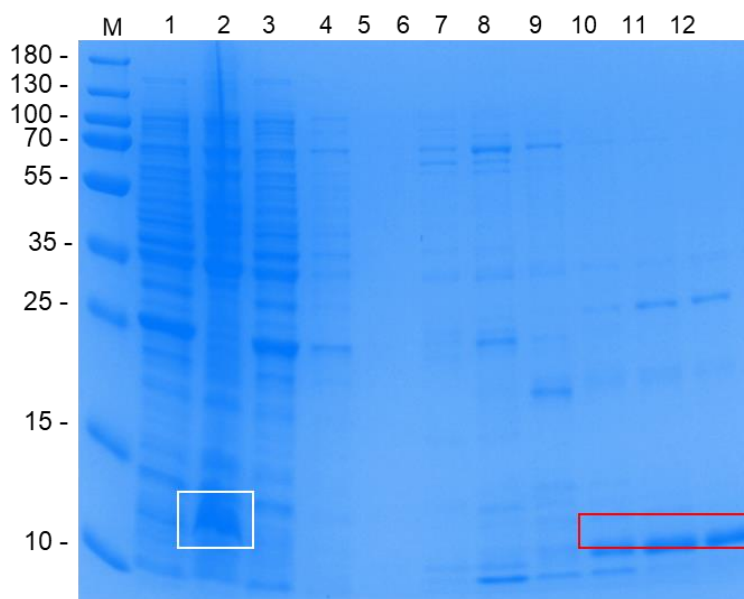


Figure 3.10 SDS-PAGE analysis of elution fractions from Ni-NTA of *hsCCL2* (from the protein production using the Harbinger™-48 bioreactor). M = marker with MWs of protein bands on the left; 1 = column flow-through; 2 = cell-pellet; 3 = column wash; 4 – 12 = protein fractions. A white box corresponds to *hsCCL2* found in the pellet. Bands corresponding to *hsCCL2* (MW = 11 kDa) are indicated with a red box.

3.7.3 Medium scale *hsCCL2* preparation (SEC purification)

Presence of *hsCCL2* in the cell pellet was indicative of potential protein solubility issues. A solution for improving the solubility of proteins in *E. coli* overexpression is to reduce the induction temperature.²⁴ Therefore, the procedure explained in **Section 3.7.1** was repeated on a 6 litre scale, however in this preparation the induction temperature was reduced from 30 °C to 20 °C. Following this, the protein was purified by Ni-NTA affinity chromatography with the corresponding chromatogram (**Figure 3.11 (A)**) displaying an increased UV absorbance of the *hsCCL2* peak (800 mAU increased from 600 mAU (**Figure 3.6**)). This was an indication that a greater quantity of protein had been produced. This corresponded with strong *hsCCL2* bands on the SDS-PAGE gel (**Figure 3.11 (B)**).

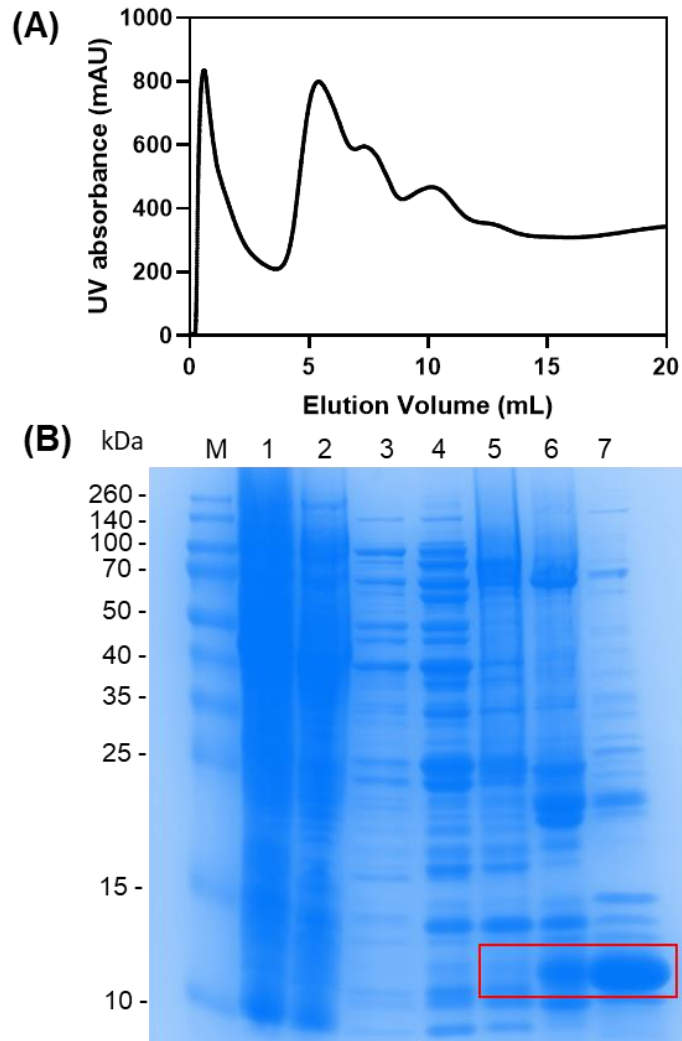


Figure 3.11 (A) Chromatogram from the Ni-NTA of *hsCCL2* (undertaken by *I. Edwards and D. Page*^{vi}) **(B)**: SDS-PAGE analysis of elution fractions Ni-NTA (*I. Edwards and D. Page*). M = marker with MWs of bands to the left; 1 = cell lysate; 2 = column flow-through; 3 = column wash; 4 – 7 = protein fractions. Bands corresponding to *hsCCL2* (MW = 11 kDa) are indicated with a red box.

Size exclusion chromatography (SEC) was used to further purify *hsCCL2* and to assess if this afforded a greater quantity of pure protein. Before SEC, the protein was dialysed into H_2PO_4 and stored at 4 °C for 3 days. However, this led to partial precipitation. It was decided to remove the precipitate and retain the solute for purification, with the potential that the precipitate was formed from impurities

^{vi} Laboratory technicians in the Pohl group.

The corresponding chromatogram and SDS-PAGE gel for the SEC purification of *hsCCL2* are shown in **Figure 3.12**. In the first gel shown in **Figure 3.12 (B)**, **lane 1** corresponds to the sample loaded onto the column (following removal of precipitate) and a strong band corresponding to *hsCCL2* was observed. This indicates that either *hsCCL2* had not entirely denatured or the removed precipitate was formed from impurities. The fractions corresponding to each peak in the chromatogram shown in **Figure 3.12 (A)** were run on the same SDS-PAGE gel, with *hsCCL2* bands corresponding to the final peak. Elution volumes (mL) 85 - 86, 87 - 90 and 91 - 95 were combined and run on the second gel shown (**lanes 2,3** and **4** respectively). **Lanes 2** and **3** display protein bands in medium strength with a small amount of contaminant, and **lane 4** displays weak bands corresponding to *hsCCL2* alongside a greater quantity of contaminant. From elution volumes 85 – 90, 2 mg of protein was obtained.

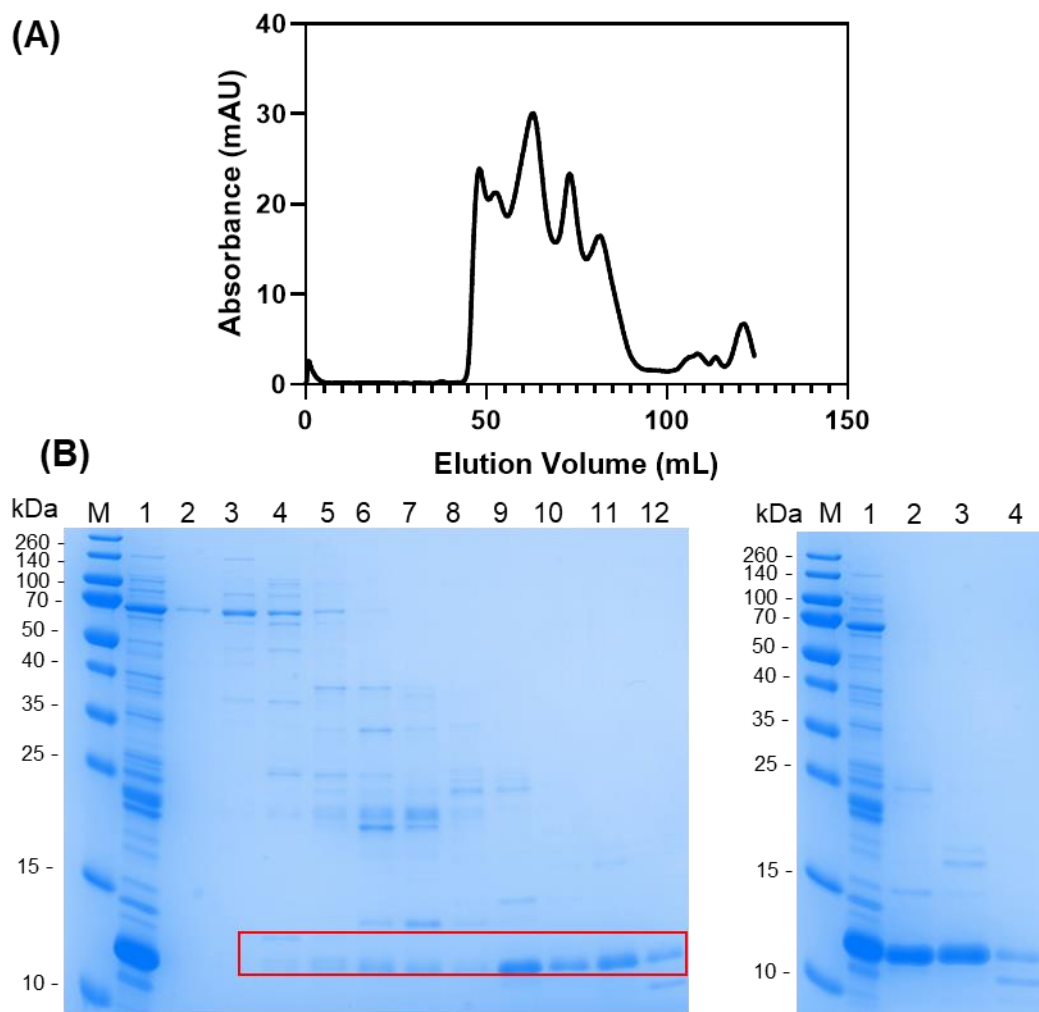


Figure 3.12 (A) Chromatogram from the SEC of *hsCCL2*. **(B) Right;** SDS-PAGE analysis of elution fractions from SEC. M = marker with MWs of bands on the left; 1 = sample prior to SEC; 2 - 14 = protein fractions. Bands corresponding to *hsCCL2* (MW = 11 kDa) are indicated with a red box. **Left;** SDS-PAGE analysis of combined fractions. M = marker with MWs of bands; 1 = sample prior to SEC; 2 = protein fractions 85 mL - 86 mL; 3; protein fractions 87 mL - 90 mL; 4 = protein fractions 91 mL - 95 mL.

3.7.4 CCL2 folding

Correct *hsCCL2* folding was determined by analysis of the corresponding circular dichroism (CD) spectrum. As explained in **Section 3.1**, CCL2 contains both α -helices and β -sheets therefore, peaks corresponding to both secondary structures would be expected. The CD spectrum (**Figure 3.13**) obtained was reasonably jagged, nonetheless, the -ve peak at 208 nm is typical for an α -helix. Another -ve peak is expected around 220 nm but could be minimised due to the presence of β -sheets, which present a -ve peak around 218 nm (in addition to a +ve band around 195 nm).²⁵

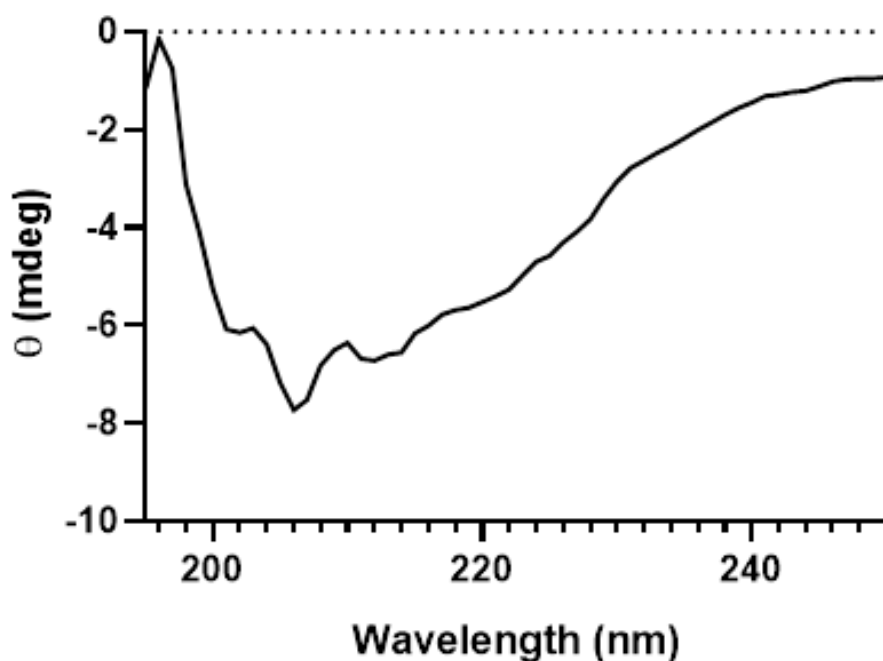


Figure 3.13 CD spectrum of *hsCCL2* in buffer H₂PO measured between 195 - 260 nm.

3.8 CCL2-DKP ligand-binding studies

A moderate quantity of pure *hsCCL2* was obtained from the work shown in **Section 3.7**. This enabled surface plasmon resonance (SPR) to be undertaken using the DKP library (synthesised in **Chapter 2**) and *hsCCL2*.

3.8.1 Surface plasmon resonance (SPR)

HsCCL2-DKP ligand-binding was investigated using surface plasmon resonance (SPR) assays. In SPR assays, a bioactive molecule (protein) is immobilised onto the metal (gold) surface of an SPR chip. The ligand is then passed over surface and any resulting interactions with the immobilised molecule, leads to a change in mass at surface. This impacts the refractive index, resulting in a changed reflection angle of incoming light. In SPR assays, the change in mass corresponds to the response unit measured (RU), which is equal to a critical shift angle of 10^{-4} .²⁸

3.8.2 SPR screening of DKPs with *hsCCL2* and *btnCCL2*^{vii}

When undertaking SPR experiments, the first step is to ensure sufficient protein immobilisation. Protein immobilisation can be achieved in numerous ways depending on the type of tag attached. In this current work, *hsCCL2* was immobilised onto an NTA SPR (Cytiva) chip using a 'capture-couple' method (**Figure 3.14**).²⁹

To achieve protein immobilisation, the chip was firstly saturated with Ni^{2+} ions to chelate the surface NTA molecules. Following this, the surface amines were activated for coupling using a mixture of EDC and NHS. Subsequently, *hsCCL2* was injected over the surface for orientated coupling. Any remaining uncoupled primary amines were capped with ethanolamine and a final EDTA wash was used to remove both excess Ni^{2+} ions and un-covalently attached proteins. The RU corresponding to immobilised *hsCCL2* was 4799.

^{vii} The work in this section was carried out with the support of Dr. Matthew Martin (CRUK, Newcastle drug discovery unit).

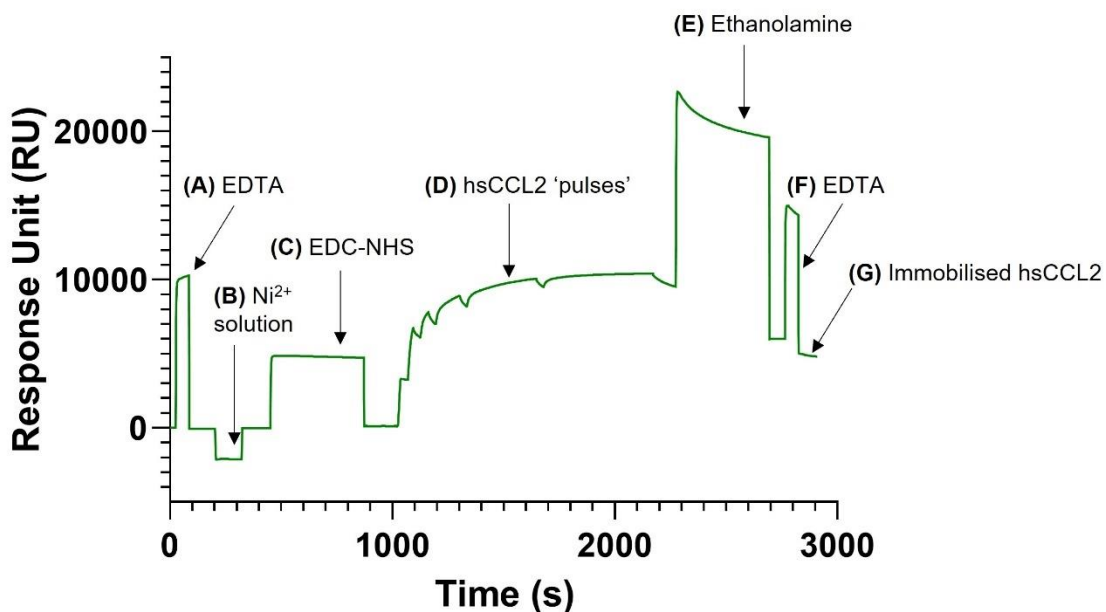


Figure 3.14 SPR sensorgram corresponding to the immobilisation of *hsCCL2* onto a NTA SPR chip. **(A)** Injection of 350 mM EDTA ‘stripping’ solution. **(B)** Surface NTA molecules chelated with Ni^{2+} ions following an injection of aq. NiCl_2 . **(C)** Surface primary amines ‘activated’ with an EDC-NHS solution. **(D)** *hsCCL2* injected onto the chip in ‘pulses’ until the surface saturation was achieved. **(E)** Uncoupled primary amines capped with ethanolamine. **(F)** Injection of 350 mM EDTA ‘stripping’ solution. **(G)** Immobilised *hsCCL2*.

Following successful *hsCCL2* immobilisation, ligand-binding assays with the DKPs were undertaken. A sample of CCL2-binding peptide BK1.3^{viii} (described in **Section 3.4**) was used as a control. However, at the time, BK1.3 [sequence YEDEDYEDFFKPVTCYF] was only available in a small quantity thus it was only possible to test at a single concentration (10 μM). This was not ideal as it is standard to use an SPR control to assess the competency^{ix} of the immobilised protein surface and should therefore be tested in a concentration range that encompasses the K_D to determine the maximum response (R_{max}). Nonetheless, 10 μM of BK1.3 produced a response of 15 RU which provided enough confidence in the immobilised protein surface to screen the DKP library.

^{viii} Provided by Professor A. Kawamura (Kawamura group - Newcastle University).

^{ix} Competency refers to how active the immobilised protein surface of the chip is.

Following this, the ligand-binding between the DKP library (full compound list and chemical structures are given in **Appendix 8.2**) and *hsCCL2* was assessed using single cycle kinetics across 4 concentrations: 100 μM , 10 μM , 1 μM and 0.1 μM . However, none of the DKPs tested displayed any binding events. **Figure 3.15** shows an example sensorgram corresponding to DKP **43** (lead CCL2-chemotaxis inhibitor from **Chapter 2**) which displayed no change in RU at any of the concentrations tested.

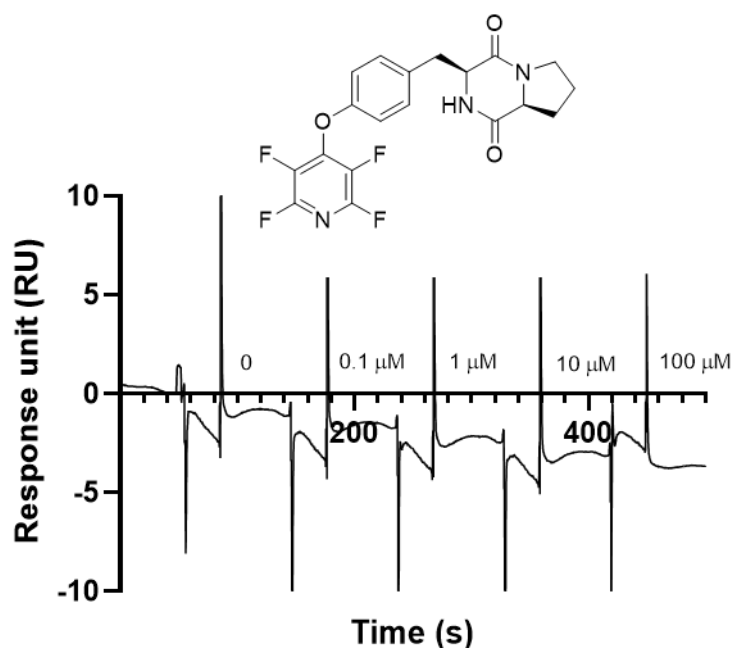


Figure 3.15 Sensorgram corresponding to the interaction between immobilised *hsCCL2* and DKP **43**. No binding events were observed across 4 concentrations: 100 μM , 10 μM , 1 μM and 0.1 μM

A possibility for the lack of binding could have been attributed to the N-terminal His₆Tag disrupting the CCL2-DKP binding site. As explained in **Section 3.2**, the N-terminus of CCL2 is crucial for CCR2 binding; particularly the terminal Glu residue. It was theorised that instead, immobilisation via the C-terminus of CCL2 would minimally disrupt any N-terminal binding sites potentially allowing CCL2-DKP interactions to be observed. For this reason, a sample of CCL2^x that contained a C-terminal biotin tag (btnCCL2), was obtained.

^x Provided by Professor A. Kawamura (Kawamura group - Newcastle University).

This was immobilised onto a streptavidin (SA) SPR chip using a capture (non-covalent) method (**Figure 3.16**).

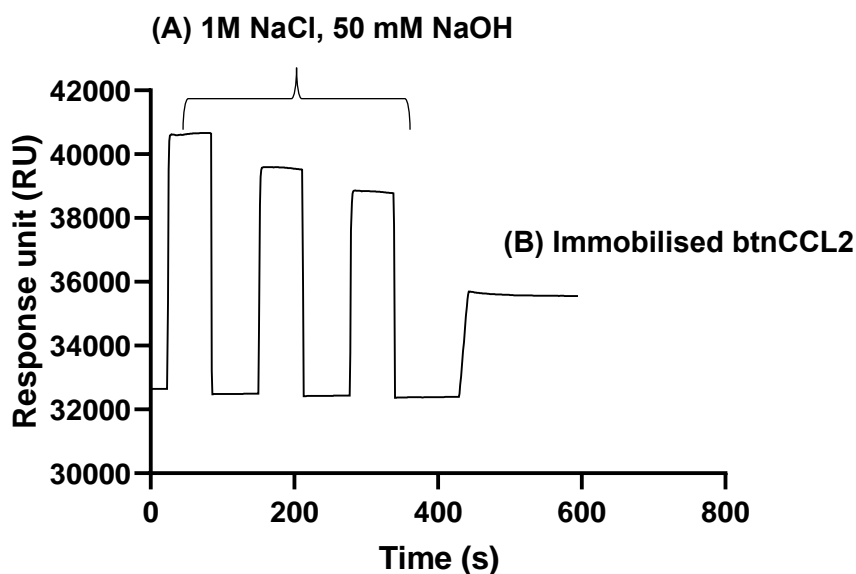


Figure 3.16 Sensorgram corresponding to immobilisation of btnCCL2 onto a streptavidin (SA) SPR chip. **(A)** Regeneration of chip surface (3 x injections of 1 M NaCl, 50 mM NaOH). **(B)** Immobilisation of btnCCL2 onto the chip surface.

The DKPs were tested in a more comprehensive titration series than with *hsCCL2*; 200 μ M, 100 μ M, 50 μ M, 25 μ M, 5 μ M and 2.5 μ M. However, like previously observed results, none of the DKPs displayed any binding events. From the results of the two SPR experiments using two differently tagged samples of CCL2, there was no evidence to suggest that the DKPS directly bind CCL2.

3.9 New CCL2 binders

In addition to DKP-CCL2 screening, a small fragment screen composed of 25 small-molecule fragments (synthesised in-house)^{xi} were assessed by SPR with the goal to discover new CCL2 binders. The compounds screened in this library were fluorinated molecules with the majority containing the fluorinated pyridyl backbone introduced in **Chapter 2** (full compound list in and chemical structures are given in **Appendix 8.3**). The fragments' molecular weights in some cases were out of the range usually considered in

^{xi} Synthesised by previous Cobb group members Dr. William Brittain and Dr. Hirunika Perera.

a fragment screen (the RO3 as explained in **Chapter 1**) however all align with (or are close) to Lipinski's RO5.

The fragment screen was conducted in the same experiment as the DKP screen in **Section 3.8.4**, using the same 4 concentrations (100 μM , 10 μM , 1 μM and 0.1 μM). In this work, a series of compounds containing the 4-benzenesulfonyl-tetrafluoropyridine core, with substitutions at the 5- (**78**) or 6- (**79**) position (**Figure 3.17**) displayed binding events at both 100 μM and 10 μM . Antiparasitic agent **60** (introduced in **Chapter 2**) which represents the TFP-containing core, did not display any binding events, indicating that extension through the R groups was required for CCL2 binding. Binding events were also observed with fragment **80** which also contains the fluorinated pyridyl core.

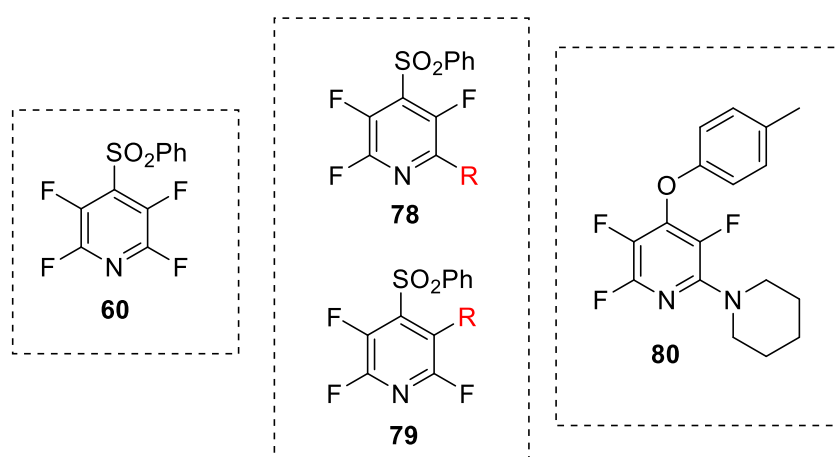


Figure 3.17 Chemical structures of antiparasitic agent **60**, the benzenesulfonyl-tetrafluoropyridine core substituted either at the 5- (**78**) or 6- position (**79**) and binding fragment **80**.

To expand upon this work and confirm binding, a new fragment screen was undertaken in which btnCCL2 was used as the immobilised protein. As micromolar affinity was observed prior, a greater concentration range was assessed (200 μM , 100 μM , 50 μM , 25 μM , 5 μM and 2.5 μM). Firstly, btnCCL2 was immobilised onto the surface of a SA-chip, with a corresponding RU of 3884.

Additional quantities of control peptide BK1.3^{xii} were obtained, which enabled the competency of the immobilised protein surface to be assessed. To assess potential decay of the protein surface during the experiment, BK1.3 was run as both the first and the last ligand screened. The sensorgrams corresponding to the control runs are shown in **Figure 3.18**. At the start, binding events with BK1.3 were observed at 200 μM , 100 μM , 50 μM and slightly at 25 μM , reaching a maximum RU of 304. For an 100% active surface, the maximum RU expected for this peptide is 760; a value over double observed in this work. Potentially, this indicated a partially active surface, which can be affected by protein dimerization. Moreover, higher concentrations may be required to elicit the maximum response as the ligand did not achieve saturation. Additionally, these factors likely contributed to the unexpectedly high binding affinity estimated in the experiment (K_D of 192 μM – BK1.3 start). Gradual decay of the immobilised protein surface was observed with a maximum response of 191 at the end of the run; an approximate signal reduction of a third. Nonetheless, BK1.3 produced binding events in a dose-responsive manner, providing confidence for further fragment screening.

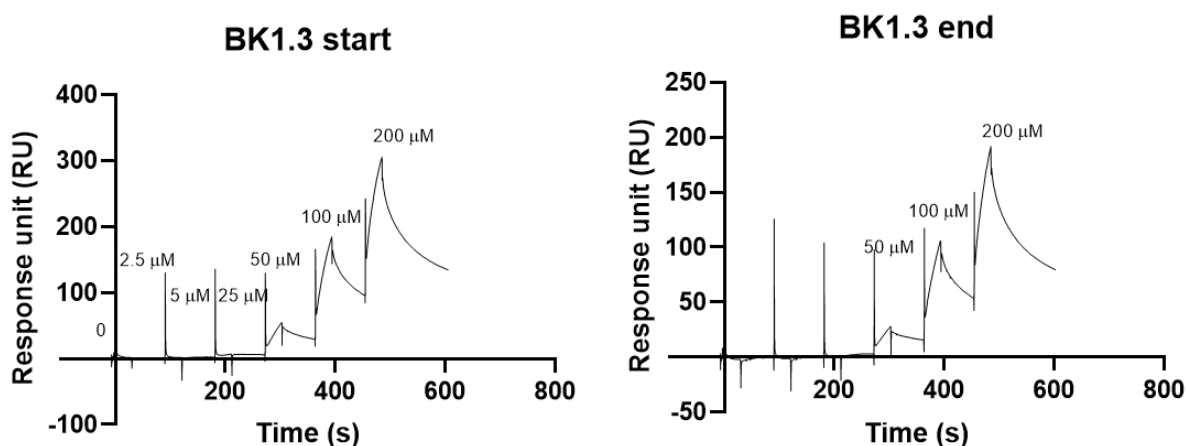


Figure 3.18 Sensorgrams corresponding to BK1.3 binding to Btn-CCL2 at the start (*left*) and the end (*right*) of the SPR experiment.

^{xii} Provided by Professor A. Kawamura (Kawamura group - Newcastle University).

Following this, 12 of the 25 fragments (**Figure 3.19**) initially screened against *hsCCL2* were rescreened against *btnCCL2*, as these had shown promising indications of binding. The fragments' corresponding *btnCCL2* and *hsCCL2* binding sensorgrams are shown in **Table 3.1**. The K_D values in most cases could not be accurately determined, due to the lack of saturation by the compounds/control, so in most cases a more qualitative assessment of the binding events are provided.

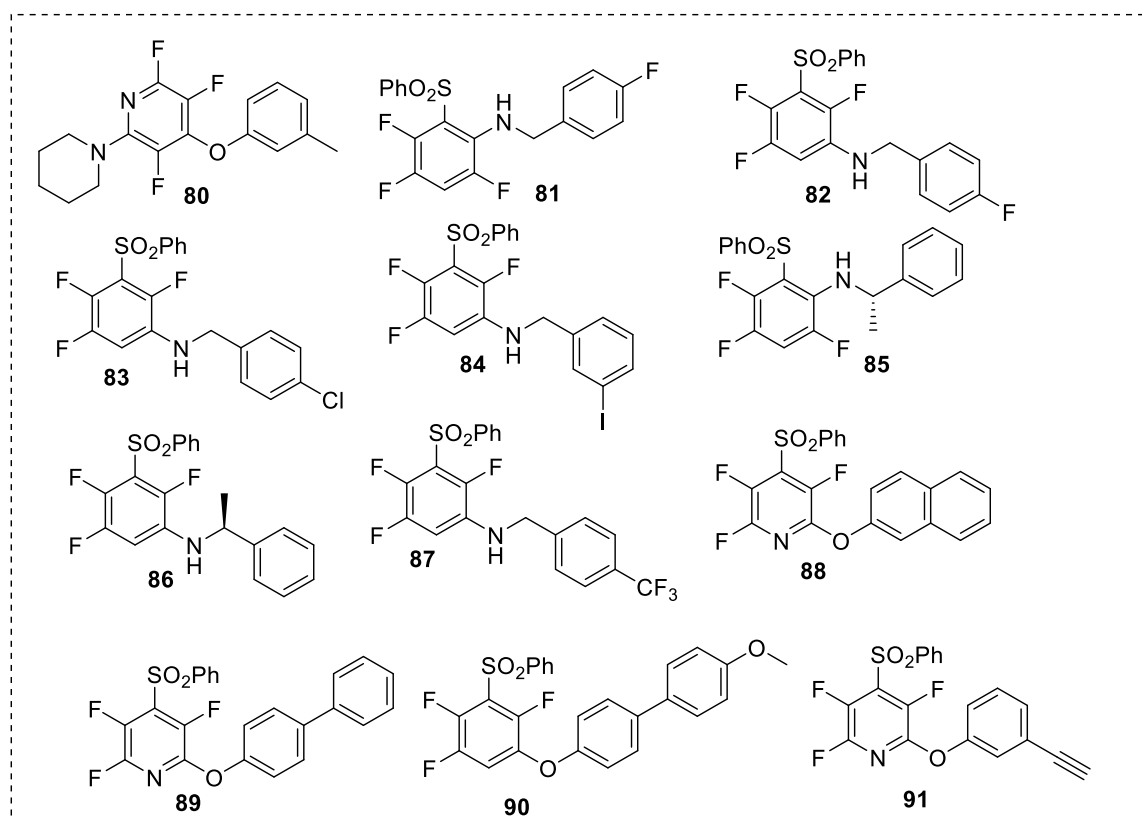


Figure 3.19 Chemical structures of the compounds **80 - 91** tested in the SPR experiment using *btnCCL2*.

Compound **80** (**Table 3.1 - Entry 1**) was the most promising binder for both immobilised *btnCCL2* and *hsCCL2*, producing a maximum RU value of 41 and 48 respectively. The molecular weight of compound **80** is significantly lower (322 g/mol) than that of control BK1.3, therefore the maximum RU expected is reduced to 110 and 142 for *btnCCL2* and *hsCCL2* respectively. Similarly to BK1.3, the maximum RU obtained was lower than

expected, suggesting again, a less active immobilised surface or that a higher concentration of ligand was required to reach saturation. Nonetheless, the binding affinity of **80** with btnCCL2 could be estimated, corresponding to a K_D of 81.6 μM .

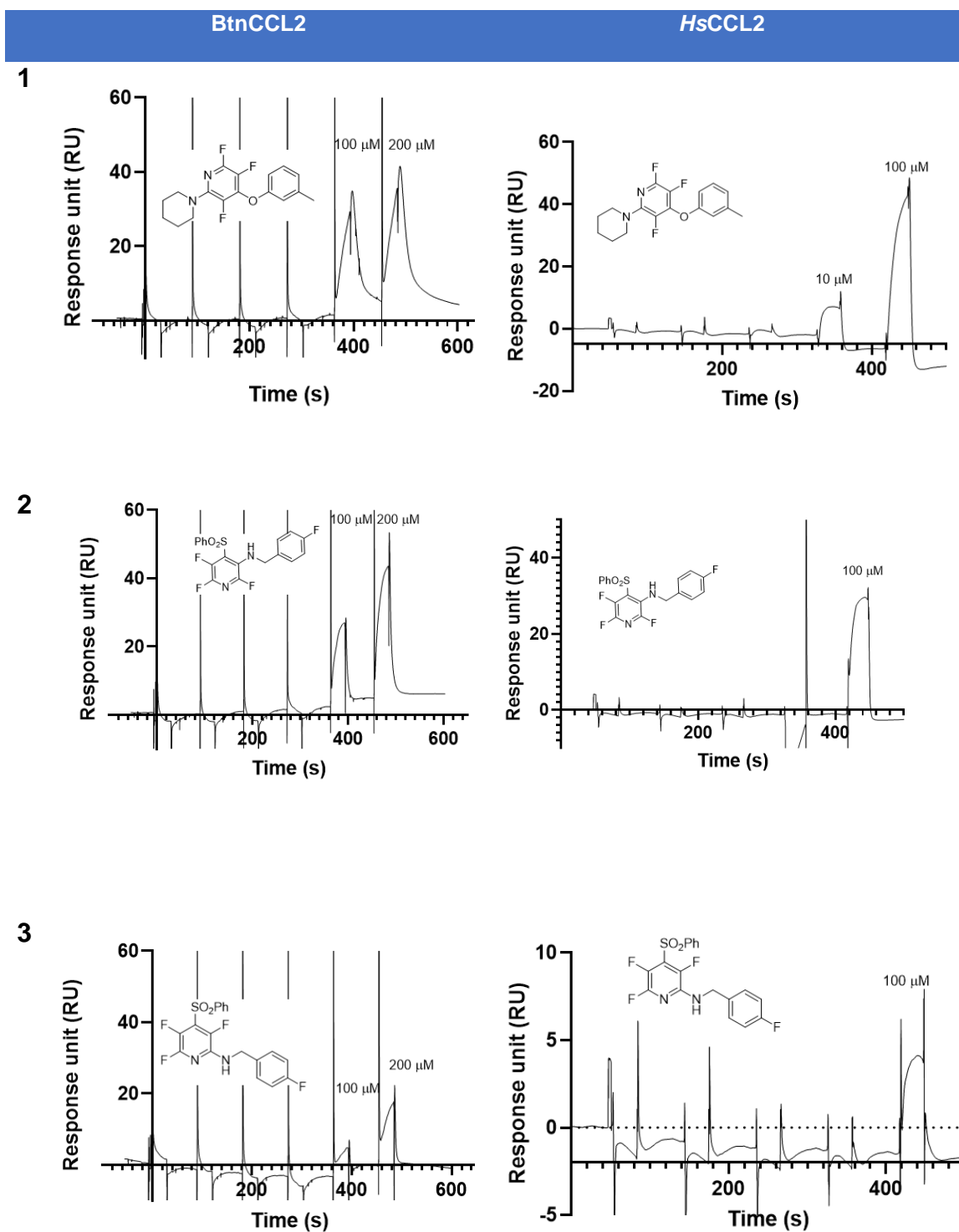
In **Table 3.1 - Entries 2 - 8**, the compounds screened contain a 4-benzenesulfonyl-tetrafluoropyridine substituted with modified benzylamine groups. The sensorgrams corresponding to compounds **81** and **82** (**Table 3.1 - Entries 2 and 3**), which contain a fluorobenzylamine group substituted at 5- or 6- position respectively, present binding interactions with both btnCCL2 and *hsCCL2*. The predicted btnCCL2 maximum response for compounds **81** and **82** was estimated to be 136, but the maximum response obtained in this work was 53 and 17 respectively. Notably, for these structural isomers, the change in substituent from the 5- to the 6-position resulted in a loss of binding affinity. In support of this, the same trend was observed when screened against *hsCCL2*. Binding affinity for compound **81** was able to be estimated as a K_D of 191 μM (btnCCL2).

Chlorinated compound **83** and iodinated compound **84** (**Table 3.1 - Entries 4 and 5** respectively) showed promising binding events for both btnCCL2 and *hsCCL2*. For ethylbenzylamine substituted compounds **85** and **86** (**Table 3.1 - Entries 6 and 7**) binding events were observed displaying maximum responses of 22 and 20 respectively (with btnCCL2) with no significant difference in binding between the two structural isomers. The maximum response expected for compound **85** and **86** was 134, so the obtained response was far less than expected.

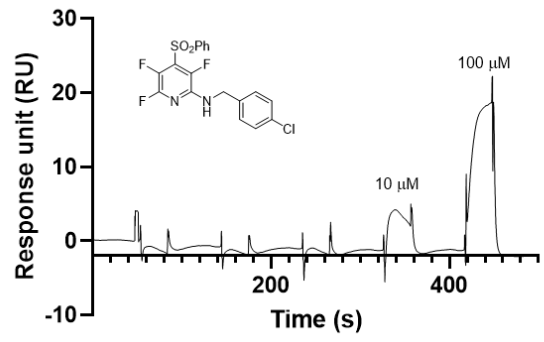
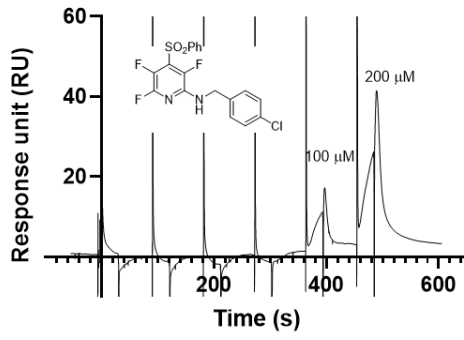
For CF_3 containing compound **87** (**Table 3.1 - Entry 8**) the corresponding btnCCL2 binding event shows a long dissociation time (response does not reach baseline following wash). This can be a result from a strong, potentially covalent, binding interaction but can also be due to the insolubility of the compound, preventing its removal from the surface after each run. This same trend was not observed in the corresponding *hsCCL2* sensorgram, in which very minimal binding is observed at 100 μM . No binding was observed with fragments **88** and **89** (data not shown).

The sensorgrams for fragments **90** (**Table 3.1 - Entry 9**) and **91** (data not shown) also did not display any binding events. However, it is worth noting that these compounds were screened at the end of the run when the protein surface had started to decay.

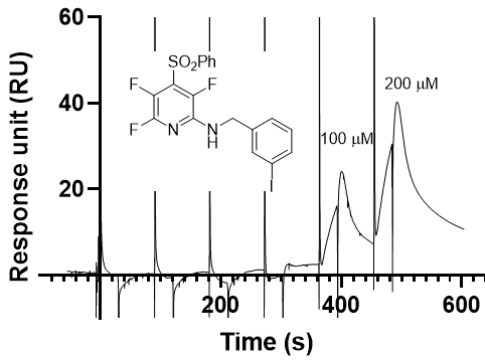
Table 3.1 Comparison of fluorinated fragments screened against BtnCCL2 or HsCCL2 and their corresponding sensorgrams.



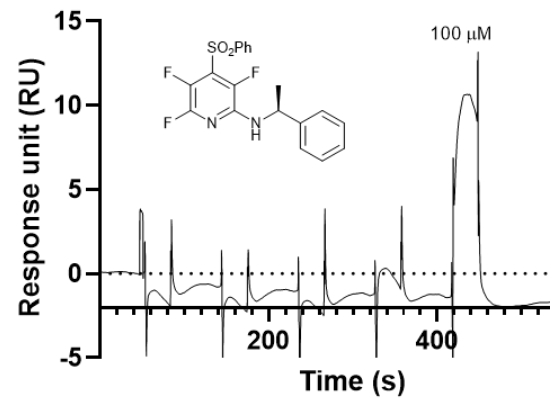
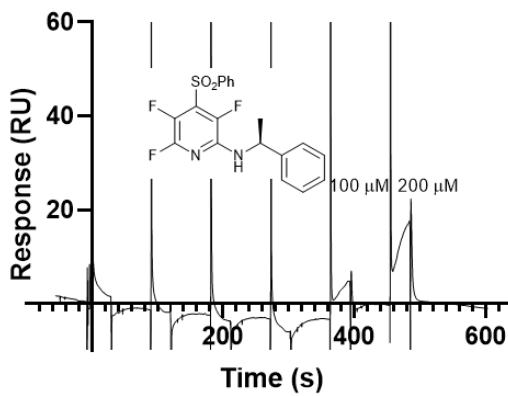
4



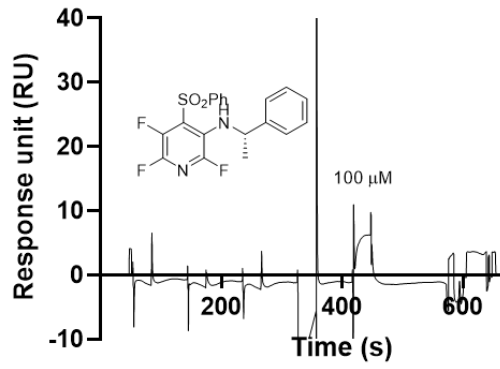
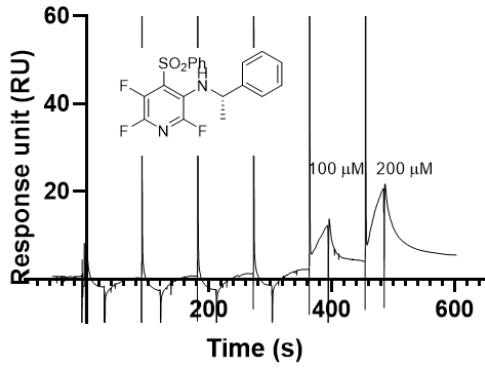
5



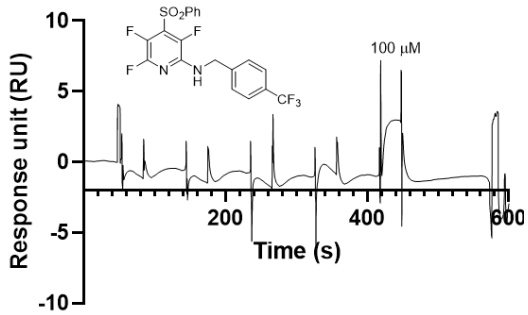
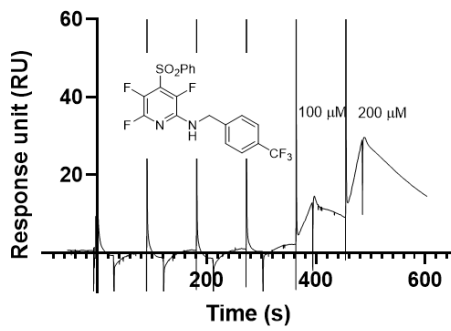
6



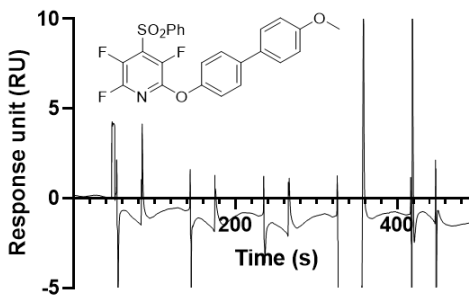
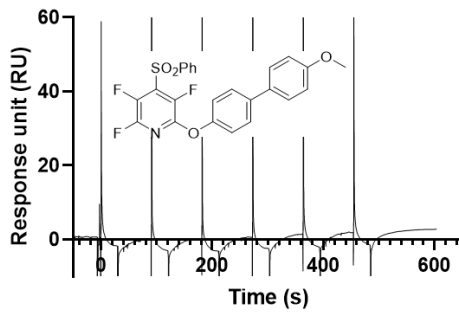
7



8



9



3.10 Chapter summary

The fundamental aim of this chapter was to evaluate the ligand-binding interactions between the DKP library (synthesised in **Chapter 2**) and CCL2. This was important to the overarching goal of the project which is the synthesis of CCL2-PROTACs.

HsCCL2 was successfully overexpressed in *E. coli* and purified by Ni-NTA affinity chromatography, which was followed by additional purifications using IEX (Mono-S) or SEC, affording moderate quantities of high purity *hsCCL2*. In the first protein preparation that used a standard incubator shaker on a 6 litre scale, 1.5 mg of pure protein was obtained following purification. To improve the quantity of protein obtained, a large-scale overexpression using a Harbinger-LEXTM-48 bioreactor was undertaken. This did not improve the quantity of protein obtained, but potentially improved the overall purity (**Figure 3.9** and **3.10**). A sample of the cell pellet was run on an SDS-PAGE gel, which indicated the presence of *hsCCL2*, that was later confirmed by trypsin digest MS. Presence of the desired protein in the cell-pellet can indicate solubility issues. Therefore, in the next preparation, the induction temperature was reduced from 30 °C to 20 °C, with the aim of improving the protein solubility. The protein was purified by Ni-NTA affinity chromatography, with an increase in the UV absorption (**Figure 3.11**) of *hsCCL2* on the corresponding chromatogram observed. Following a final purification using SEC, 2 mg of *hsCCL2* was obtained.

Following this, the binding of the DKP library (**Appendix A2**) for *hsCCL2* was assessed using SPR assays. *HsCCL2* was successfully immobilised onto a Ni-NTA SPR chip (**Figure 3.14**) and the SPR control BK1.3 successfully produced an RU of 15. The binding potential of the DKP library was then assessed however, no binding events were observed. To rule out potential binding site disruption, *btnCCL2* which was tagged through the C-terminus, was used in additional SPR DKP binding assays. *BtnCCL2* was successfully immobilised by a non-covalent 'capture' method to an SA-SPR chip (**Figure 3.16**) however when the DKPs were screened, again, no binding events were observed. From the results

of these two experiments, it is unlikely that the DKPs tested in this work, bind directly to CCL2.

Finally, SPR assays were undertaken in which the CCL2 binding of a small library of in-house fragments were assessed. Of the fragments tested, several showed binding events when screened against both btnCCL2 and *hsCCL2* (**Table 3.1**). Although for the majority of the compounds tested, this provided only a qualitative result, the K_D of fragment **80** was able to be determined as 81.6 μM (btnCCL2) and showed binding events against both *hsCCL2* and btnCCL2 (**Table 3.1 – Entry 1**). This work provides an exciting starting point for the development of future small molecule CCL2 binders, of which there are very few known in literature.

3.11 References

1. J. Lubkowski, G. Bujacz, L. Boque, P. J. Dommie, T. M. Hande and A. Wlodawer, *Nature.*, 1997, **4**, 64–69.
2. A. E. I. Proudfoot, T. M. Handel, Z. Johnson, E. K. Lau, P. LiWang, I. Clark-Lewis, F. Borlat, T. N. C. Wells and M. H. Kosco-Vilbois, *Proc. Natl. Acad. Sci. U. S. A.*, 2003, **100**, 1885–1890.
3. J. H. Y. Tan, M. Canals, J. P. Ludeman, J. Wedderburn, C. Boston, S. J. Butler, A. M. Carrick, T. R. Parody, D. Taleski, A. Christopoulos, R. J. Payne and M. J. Stone, *J. Biol. Chem.*, 2012, **287**, 14692–14702.
4. C. D. Paavola, S. Hemmerich, D. Grunberger, I. Polsky, A. Bloom, R. Freedman, M. Mulkins, S. Bhakta, D. McCarley, L. Wiesent, B. Wong, K. Jarnagin and T. M. Handelt, *J. Biol. Chem.*, 1998, **273**, 33157–33165.
5. Z. Shao, Y. Tan, Q. Shen, L. Hou, B. Yao, J. Qin, P. Xu, C. Mao, L. N. Chen, H. Zhang, D. D. Shen, C. Zhang, W. Li, X. Du, F. Li, Z. H. Chen, Y. Jiang, H. E. Xu, S. Ying, H. Ma, Y. Zhang and H. *Cell. Discov.*, 2022, **8**, 44.
6. C. M. Brodmerkel, R. Huber, M. Covington, S. Diamond, L. Hall, R. Collins, L. Leffet, K. Gallagher, P. Feldman, P. Collier, M. Stow, X. Gu, F. Baribaud, N. Shin, B. Thomas, T. Burn, G. Hollis, S. Yeleswaram, K. Solomon, S. Friedman, A. Wang, C. B. Xue, R. C. Newton, P. Scherle and K. Vaddi, *J. Immunol.*, 2005, **175**, 5370–5378.
7. C. B. Xue, A. Wang, D. Meloni, K. Zhang, L. Kong, H. Feng, J. Glenn, T. Huang, Y. Zhang, G. Cao, R. Anand, C. Zheng, M. Xia, Q. Han, D. J. Robinson, L. Storace, L. Shao, M. Li, C. M. Brodmerkel, M. Covington, P. Scherle, S. Diamond, S. Yeleswaram, K. Vaddi, R. Newton, G. Hollis, S. Friedman and B. Metcalf, *Bioorganic Med. Chem. Lett.*, 2010, **20**, 7473–7478.
8. R. J. Cherney, R. Mo, D. T. Meyer, D. J. Nelson, Y. C. Lo, G. Yang, P. A. Scherle, S. Mandlekar, Z. R. Wasserman, H. Jezak, K. A. Solomon, A. J. Tebben, P. H. Carter and C. P. Decicco, *J. Med. Chem.*, 2008, **51**, 721–724.
9. T. Mirzadegan, F. Diehl, B. Ebi, S. Bhakta, I. Polsky, D. McCarley, M. Mulkins, G. S. Weatherhead, J. M. Lapierre, J. Dankwardt, J. Morgans D., R. Wilhelm and K. Jarnagin, *J. Biol. Chem.*, 2000, **275**, 25562–25571.
10. A. J. M. Zweemer, I. Nederpelt, H. Vrieling, S. Hafith, M. L. J. Doornbos, H. De Vries, J. Abt, R. Gross, D. Stamos, J. Saunders, M. J. Smit, A. P. IJzerman and L. H. Heitman, *Mol. Pharmacol.*, 2013, **84**, 551–561.
11. Y. Zheng, L. Qin, N. V. O. Zacarías, H. De Vries, G. W. Han, M. Gustavsson, M. Dabros, C. Zhao, R. J. Cherney, P. Carter, D. Stamos, R. Abagyan, V. Cherezov,

- R. C. Stevens, A. P. Ijzerman, L. H. Heitman, A. Tebben, I. Kufareva and T. M. Handel, *Nature*, 2016, **540**, 458–461.
12. C. Auvynet, C. Baudesson De Chanville, P. Hermand, K. Dorgham, C. Piesse, C. Pouchy, L. Carlier, L. Poupel, S. Barthélémy, V. Felouzis, C. Lacombe, S. Sagan, B. Salomon, P. Deterre, F. Sennlaub and C. Combadière, *FASEB J.*, 2016, **30**, 2370–2381.
 13. D. Oberthür, J. Achenbach, A. Gabdulkhakov, K. Buchner, C. Maasch, S. Falke, D. Rehders, S. Klusmann and C. Betzel, *Nat. Commun.*, 2015, **6**, 1–11.
 14. R. P. Bhusal, J. R. O. Eaton, S. T. Chowdhury, C. A. Power, A. E. I. Proudfoot, M. J. Stone and S. Bhattacharya, *Trends Biochem. Sci.*, 2020, **45**, 108–122.
 15. J. R. O. Eaton, Y. Alenazi, K. Singh, G. Davies, L. Geis-Asteggiante, B. Kessler, C. V. Robinson, A. Kawamura and S. Bhattacharya, *J. Biol. Chem.*, 2018, **293**, 6134–6146.
 16. B. Darlot, J. R. O. Eaton, L. Geis-Asteggiante, G. K. Yakala, K. Karuppanan, G. Davies, C. V. Robinson, A. Kawamura and S. Bhattacharya, *J. Biol. Chem.*, 2020, **295**, 10926–10939.
 17. B. Q. Li, T. Fu, W. H. Gong, N. Dunlop, H. F. Kung, Y. Yan, J. Kang and J. M. Wang, *Immunopharmacology*, 2000, **49**, 295–306.
 18. N. Joshi, D. Kumar and K. M. Poluri, *ACS Omega*, 2020, **5**, 22637–22651.
 19. T. L. R. Grygiel, A. Teplyakov, G. Obmolova, N. Stowell, R. Holland, J. F. Nemeth, S. C. Pomerantz, M. Kruszynski and G. L. Gilliland, *Biopolymers.*, 2010, **94**, 350–359.
 20. A. Hudson, PhD Thesis, Durham University, 2015 (available online via Durham University DRO).
 21. J. A. Bornhorst and J. J. Falke, *Methods Enzymol.*, 2000, **326**, 245–254.
 22. P. Wingfield, *Curr. Protoc. Protein Sci.*, 2017, **88**, 6.14.1–6.14.3.
 23. M. Lopes, I. Belo and M. Mota, *Biotechnol. Prog.*, 2014, **30**, 767–775.
 24. D. M. Francis and R. Page, *Curr. Protoc. Protein Sci.*, 2010, 1–29.
 25. N. J. Greenfield, *Nat. Protoc.*, 2007, **1**, 2876–2890.
 26. K Huynh and C. L. Partch, *Curr. Protoc. Protein Sci.*, 2015, **79**, 28.9.1–28.9.14.
 27. C. Elgert, A. Rühle, P. Sandner and S. Behrends, *J. Pharm. Biomed. Anal.*, 2020, **181**, 113065.
 28. H. H. Nguyen, J. Park, S. Kang and M. Kim, *Sensors (Switzerland)*, 2015, **15**, 10481–10510.
 29. A. J. Kimplea, R. E. Mullera, D. P. Siderovskia and F. S. Willarda, *Methods Mol Biol.*, 2010, **629**, 91–100.

4. CCL2-targeting PROTACs

4.1 CCL2 degradation

As explained in **Chapter 2**, CCL2 is expressed in a variety of autoimmune diseases and cancers, hence inhibition of the CCL2-CCR2 interaction is of therapeutic interest. It is hypothesised in this work, that disruption of this interaction could be achieved through CCL2 'knockout' by harnessing the UPS for targeted proteasomal degradation.

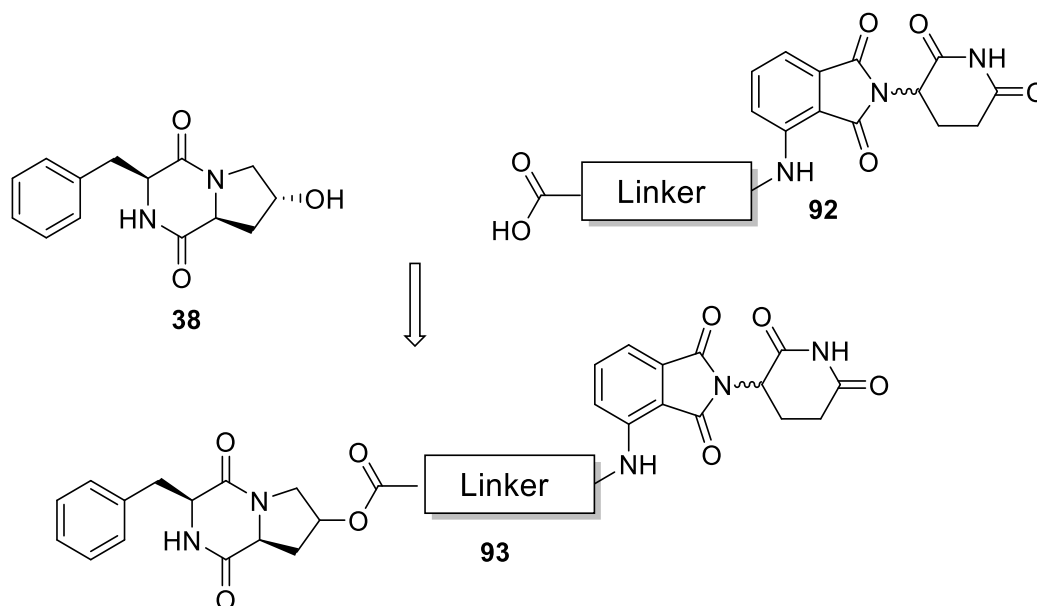
It is proposed that CCL2 degradation can be achieved through incorporation of DKPs, that were shown to inhibit CCL2-mediated chemotaxis in previous work, as the POI warhead in CCL2-PROTACs. As DKPs have shown selectivity for the CCL2-CCR2 interaction, these represent promising warheads for PROTAC incorporation. In addition, although their individual potency is too low for use as CCL2 therapeutics on their own, PROTACs require a transient binding mode to the POI.

However, it must be noted that due to the restricted lab access because of the COVID-19 pandemic, at the time of this work, access to labs other than the primary (synthetic) lab for this research was not granted. Therefore, the work in this Chapter was conducted before the biophysical studies in **Chapter 3**. Consequently, the PROTACs are designed based on the initial hypothesis that DKPs inhibit CCL2 binding.

4.2 Aims

This chapter seeks to incorporate hydroxyl-containing DKPs **29** and **38** (synthesis shown in **Chapter 2**), as the POI warhead in CCL2-targeting PROTACs. Thalidomide-linker conjugates (**92**) will be synthesised and subsequently connected to DKP **29** or **38** through an ester linkage, to afford the desired PROTAC (**93**). The general synthetic route is shown

in **Scheme 4.1**. Subsequently, the PROTACs will be tested *in vitro* to determine their ability to degrade CCL2.



Scheme 4.1 General synthesis of CCL2-PROTACs using example POI warhead, DKP **38**.

4.2.1 PROTAC design

As explained in **Chapter 1**, PROTACs are hetero-bifunctional molecules consisting of three components: a POI ligand, an E3 ligand and a flexible linker of appropriate length and composition. The solution phase synthesis of DKP **29** and **38** was carried out in **Chapter 2** with > 200 mg of each compound produced. At the time of PROTAC synthesis, the DKP mode of binding with CCL2 and appropriate point of attachment is unknown. Consequently, the PROTAC design seeks to incorporate DKPs through either the hydroxyproline or tyrosine moieties (**Figure 4.1**).

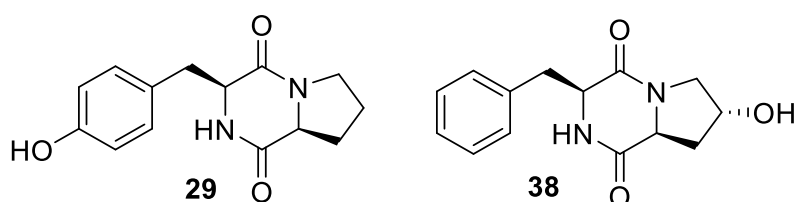


Figure 4.1 Chemical structures of the two DKP warheads, **29** and **38** (synthesis shown in **Chapter 2**).

The CCL2-PROTACs will contain thalidomide ligands to enable degradation via CRBN. Thalidomide E3 ligands have several advantages, such as superior physicochemical properties as well as ease of synthesis, in comparison to VHL ligands (discussed in **Chapter 1**).¹ Additionally, the majority of PROTACs currently in clinical trials are CRBN targeting.² Without crystallographic information to aid rationale PROTAC design, the linker length and composition must be designed on a 'trial and error' basis. Since it has been proposed that the incorporation of PEG chains as PROTAC linkers can increase plasticity and thus aid ternary complex formation, initial PROTAC design seeks to incorporate these linkers.³ Additionally, a variety of PEG linkers with different pendant functional groups are available commercially.

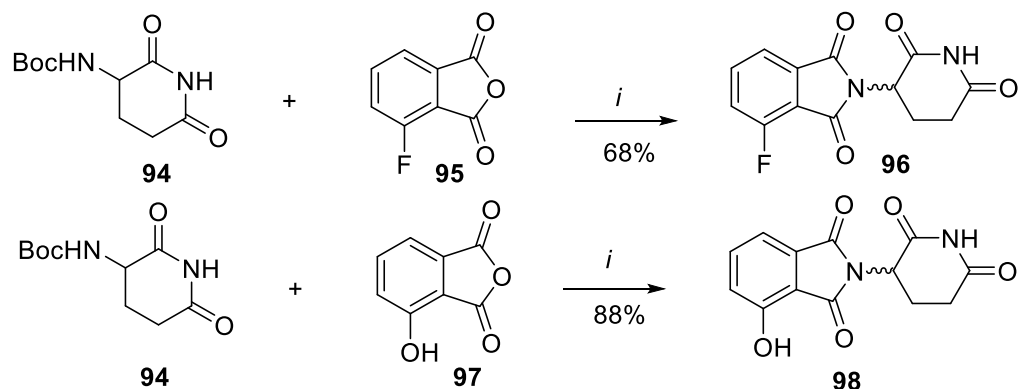
The final assembly of CCL2-PROTACs involves attachment of the hydroxyl-containing DKP to the thalidomide-linker conjugate through an ester linkage. Amides are typically used to connect the POI to a PROTAC linker however work by Klein *et al.*, showed that replacing an amide for an ester (to connect the POI warhead), increased PROTAC permeability and produced overall more potent degraders.⁴

4.3 PROTAC synthesis

4.3.1 Synthesis of thalidomide-linker conjugates

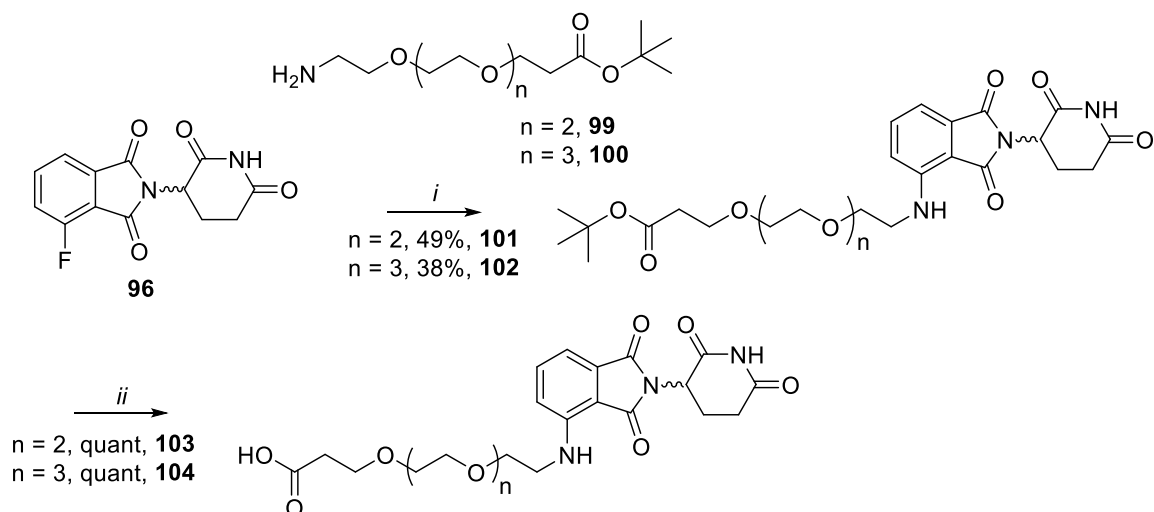
Thalidomide-linker complexes were synthesised using a literature method with precursor 4-fluorothalidomide (**96**).⁵ In this synthesis, the aromatic fluorine is displaced by a nucleophilic (amine) linker. For the synthesis of thalidomide analogues, Burslem *et al.*, designed a one-pot, microwave assisted route for their quick and efficient synthesis affording products in moderate to excellent yields (55 – 95%).⁶ Following this procedure glutarimide **94** and phthalimide **95** were suspended in trifluoroethanol (TFE) and heated to 150 °C under microwave (mw) conditions (**Scheme 4.2**). 4-Fluorothalidomide (**96**) was precipitated from solution following cooling and the addition of minimal ice-cold EtOAc. The precipitate was filtered and washed with cold EtOAc, affording 4-fluorothalidomide (**96**) in a good yield (68%) without the requirement for further purification (high purity

determined from analysis of ^1H and ^{13}C NMR spectra). This was comparable to the 69% yield obtained by Burslem *et al.* The same route was used to produce hydroxythalidomide (**98**) from precursors **94** and **97** which afforded **98** with an 88% yield; the same as obtained in literature.



Scheme 4.2 Synthesis of thalidomide analogues **96** and **98**. Reagents and conditions: *i*. TFE, mw, 150 °C, 2 h.

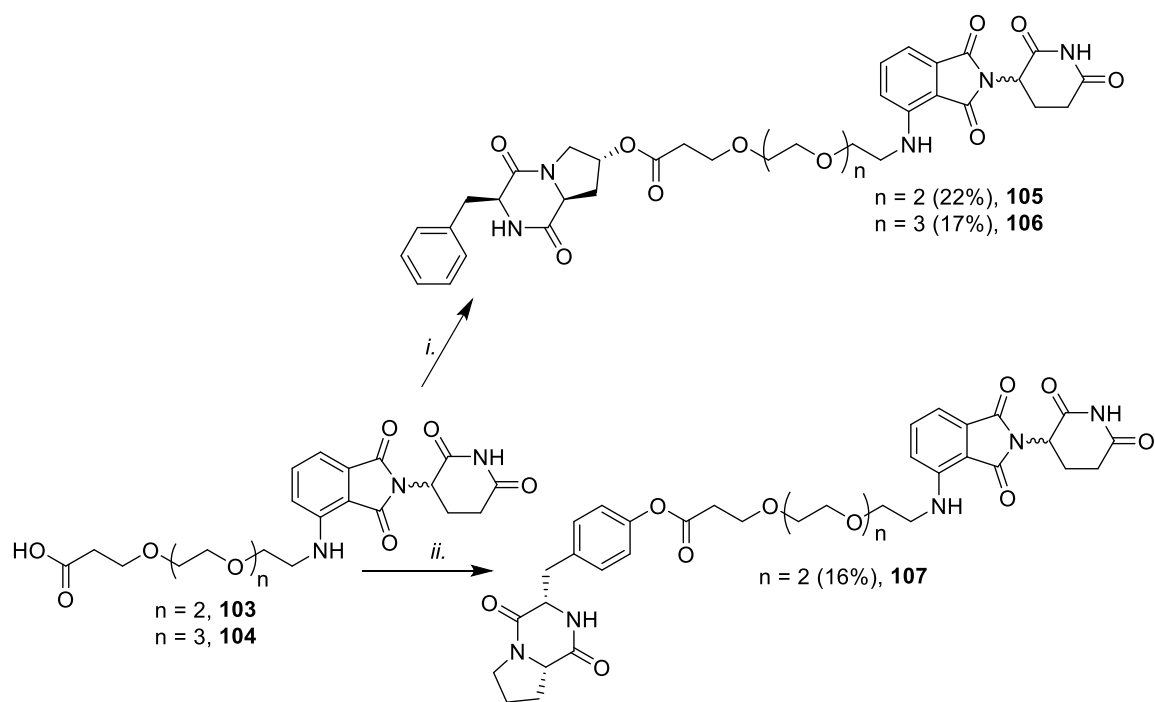
For the synthesis of the thalidomide-linker conjugates, commercially obtained linkers **99** or **100** were stirred with 4-fluorothalidomide (**96**) at 90 °C in DIPEA and DMF for 16 h (**Scheme 4.3**). Following an acidic work-up, the crudes were purified by column chromatography to afford conjugates **101** and **102** in moderate yields of 49% and 38% respectively. Conjugate **101** was produced in a similar yield to literature (50%). In addition, the yield was also improved for the synthesis of conjugate **102** (compared to literature which was 22%).⁵ Following this, removal of the *tert*-butyl protecting group was achieved using 50% TFA in DCM to afford thalidomide-linker conjugates **103** and **104** in quantitative yields.



Scheme 4.3 Synthesis of thalidomide-linker conjugates **103** and **104**. Reagents and conditions: *i.* DIPEA, DMF, N_2 , 90 °C, 16 h. *ii.* 40% TFA in DCM, rt, 30 min.

4.3.2 PROTAC assembly

Using the building blocks prepared (**Chapter 2** and **Section 4.2**) three CCL2-PROTACs (**105** – **107**) were synthesised (**Scheme 4.4**). The DKP warheads were attached to the thalidomide-linker conjugates using Steglich esterification. Steglich esterification is commonly used for the synthesis of esters under mild and neutral conditions, employing a dicyclohexylcarbodiimide coupling reagent with catalytic amounts of DMAP.⁷ In this current work, 1-Ethyl-3-(3-dimethylaminopropyl) carbodiimide (EDC) was chosen, as its resultant urea by-product can be readily removed using an aqueous work-up.



Scheme 4.4 Synthesis of CCL2-targeting PROTACs. Reagents and conditions: *i.* DKP **38**, EDC.HCl, DMAP, DIPEA, DCM, rt, 16 h. *ii.* DKP **29**, EDC.HCl, DMAP, DIPEA, DCM, rt, 16 h.

PROTAC **106**, the longest PROTAC in this work, incorporated DKP **38** as the POI warhead and contained a 4-PEG linker. The crude PROTAC was purified using flash column chromatography and was determined to have sufficient purity for biological analysis (as determined by analysis of the corresponding ^1H NMR spectrum). Analysis of the corresponding analytical HPLC chromatogram also showed **106** to be of high purity (**Figure 4.2**). PROTAC **107**, that incorporated DKP **29** with a shorter, 3-PEG linker, was synthesised using the same approach. Subsequent to column chromatography, an additional purification using prep-TLC was required to afford the pure product. The corresponding analytical HPLC showed that following purification, the product was obtained to a high purity (**Figure 4.2**). However, the corresponding ^1H NMR spectrum revealed a doubling of the NH peak and the ^{13}C NMR spectrum also displayed additional peaks. This could be attributed to either the PROTACs inherent diastereochemistry or due to conformational isomerism. Despite this, the purity of PROTAC **107**, as determined by

analysis of the HPLC chromatogram, led to the continuation of the material for initial biological evaluation.

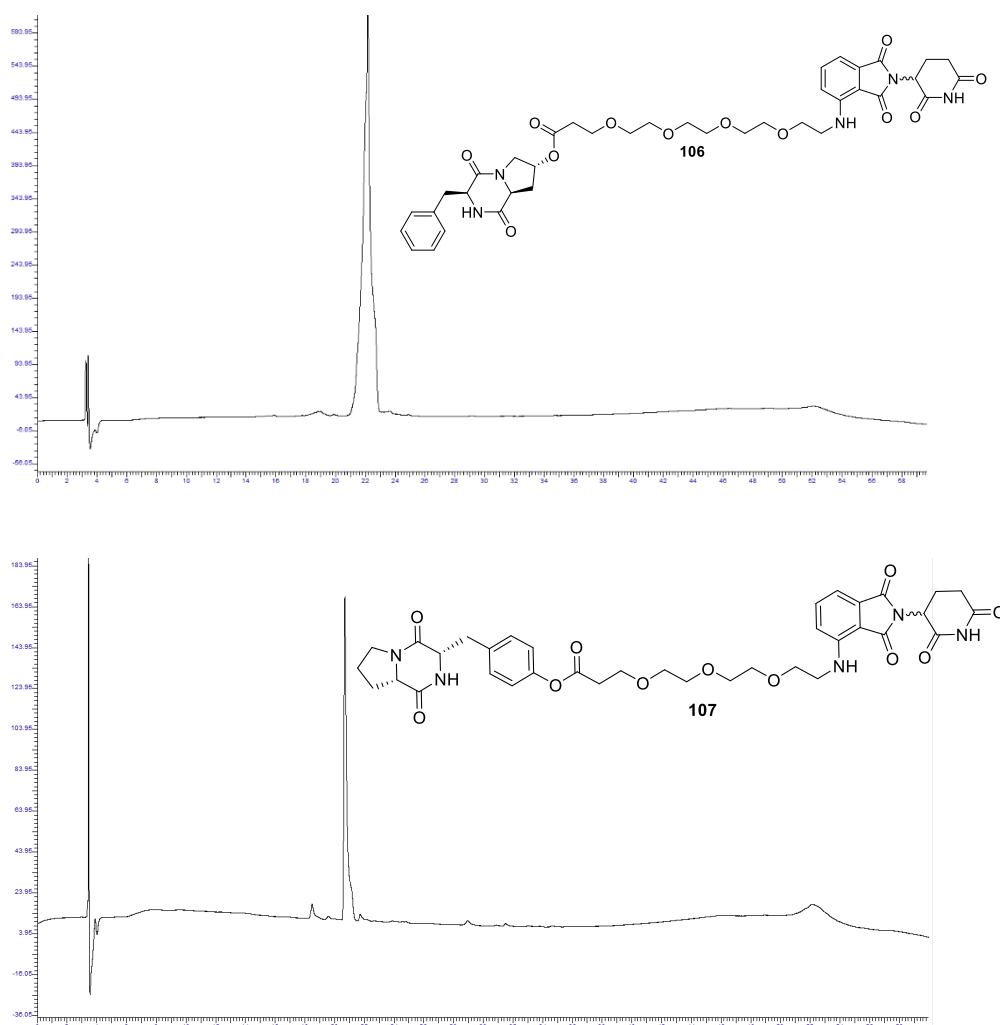


Figure 4.2 Analytical HPLC chromatograms ($\lambda = 220 \text{ nm}$) for PROTAC **106** and PROTAC **107**.

PROTAC **105** was assembled from DKP **38** and contained a 3-PEG linker. Unfortunately, the final product was found to be impure, with extra peaks visible in the ^1H NMR spectrum corresponding to the DKP starting material. The presence of this DKP impurity was confirmed through comparison of the ^1H NMR spectrum with that obtained for the pure DKP precursor (**38**). The ratio of DKP **38** to PROTAC **105** was estimated from NMR to be 1:1. Analytical HPLC also showed the presence of the DKP starting material (small peak at t_r 12.9 min) (**Figure 4.3**). Due to COVID-19 lab access restrictions at the time, further

purification of PROTAC **105** by prep-HPLC could not be undertaken. Although, PROTAC **105** was not pure, given that the impurity had been identified as the DKP precursor, the decision was made to still include it in the preliminary biological screening. If this project was to be taken any further, however, this would require further purification by prep- HPLC to ensure an entirely pure product was tested.

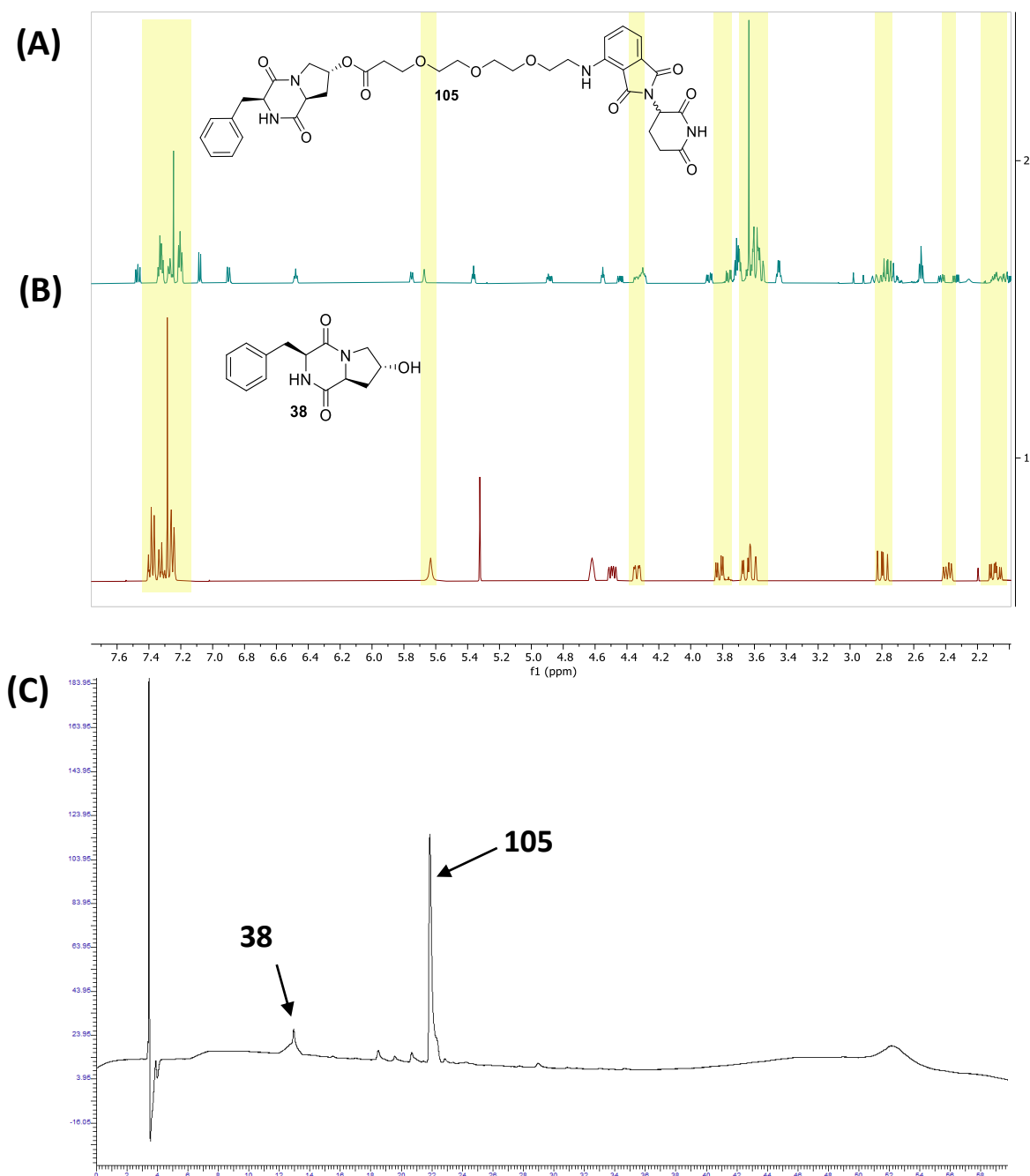


Figure 4.3 Analysis of PROTAC **105**. ¹H NMR spectra (400 MHz, CDCl₃) for (A) PROTAC **105** mixture and (B) DKP **38** precursor. (C) Analytical HPLC chromatogram ($\lambda = 220$ nm) for PROTAC **105**.

4.4 CCL2-PROTAC *in vitro* testing

With the three potential CCL2-PROTACs synthesised, their ability to degrade CCL2 was assessed.ⁱ This presented a challenge as secreted proteins are not typical PROTAC targets due to the proteasomal machinery existing intracellularly. However, it was proposed by our collaborators in the Ali group at the Newcastle Medical school, that with a cell permeable PROTAC, CCL2 could be degraded at the point of production prior to secretion outside the cell.

4.4.1 PROTAC toxicity

Prior to PROTAC testing, the toxicity of each compound for HMEC-1 cells (that were to be used in subsequent degradation assays) was assessed using a calorimetric cell viability assay. In this work none of the PROTACs, which were tested in a 10-fold dilution series from 10 μ M down to 0.1 nM, were toxic to HMEC-1 cells over the course of 24 h (data provided in **Appendix 8.4**).

4.4.2 CCL2 degradation assays

To assess the efficacy of PROTACs **105 – 107**, a novel CCL2 degradation assay was designed. Firstly, HMEC-1 cells, which do not constitutively produce CCL2, were treated with cytokine TNF- α to stimulate CCL2 production inside the cells. Simultaneously, HMEC-1 cells were treated with each PROTAC and following incubation (24 h), the CCL2 concentration of the secreted media was analysed and compared to the untreated, stimulated control. The concentration of CCL2 in the secreted media was analysed by a CCL2 specific enzyme-linked immunosorbent assays (ELISA). ELISAs specifically detect proteins present in a complex mixture and are highly sensitive, producing quantitative protein concentration readouts.⁸

This was a challenging assay to establish and several issues were encountered in its execution. Firstly, there are no known CCL2-PROTACs and thus a functional control was

ⁱ The work was carried out with the support of the Ali group (Newcastle Medical School). Experiments were designed by Mr Chong Pang Yun who also assisted with their execution.

absent. Additionally, at the outset of the experiments there was little knowledge regarding the time point in which to treat the cells; therefore 24 h was chosen as starting point.

4.4.3 Preliminary degradation assay

The catalytic mode of action is a key benefit of PROTACs and therefore the dose required is typically lower (nanomolar) than equivalent small molecule inhibitors. Given this, the PROTACs were screened at two initial concentrations (10 μM and 0.01 μM). The result from this experiment is shown in **Figure 4.4**.

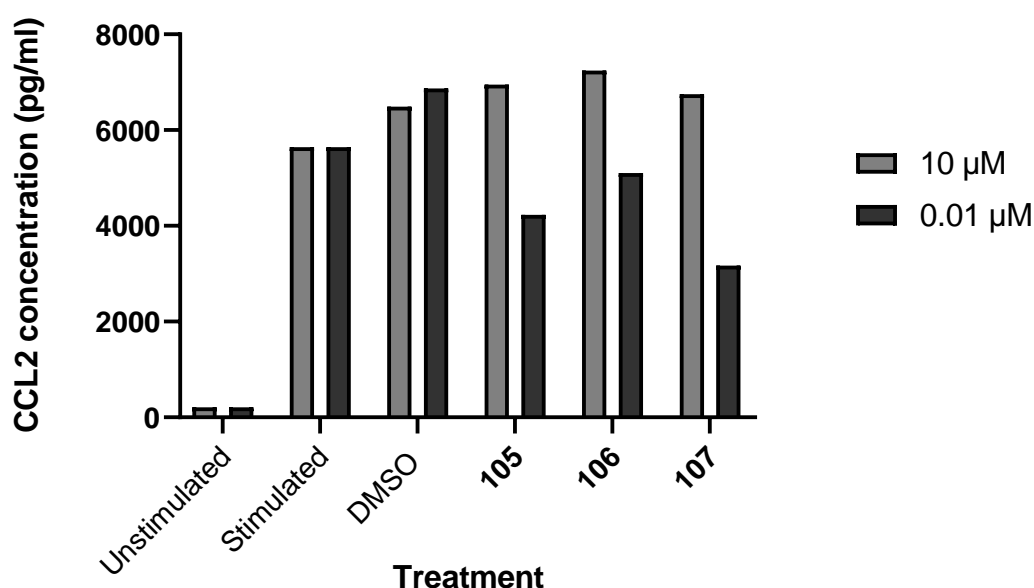


Figure 4.4 CCL2 concentration in the secreted media after 24 h in response to either a 10 μM or 0.01 μM dose of each PROTAC. Unstimulated cells refer to blank media without any treatments. Stimulated cells are only treated with TNF- α . The vehicle control refers to stimulated cells, treated with DMSO (0.0001%). This representative of 1 preliminary experiment carried out in technical triplicate. *The data presented here corresponds to repeat 3.*

As shown in **Figure 4.4** none of the PROTACs were effective at reducing the concentration of CCL2 (in comparison to the stimulated control) when tested at 10 μM . However, when tested at 0.01 μM , there was a more significant reduction in CCL2 (particularly for PROTAC **107**). It was proposed that the lack of activity at the higher concentration was a result of the Hook effect (explained in **Chapter 1**) in which binary complex formation is favoured and typically occurs at PROTAC concentrations between 1 and 10 μM .⁹

4.4.4 CCL2-PROTAC degradation assay

Two more iterations of the CCL2 degradation assay were conducted using a 0.01 μM concentration of each PROTAC. The individual repeats, alongside the combined data set, are shown in **Figure 4.5**. Overall, in response to each PROTAC treatment there was no statistically significant reduction in secreted CCL2 (**Figure 4.5 (A)**) likely resulting from the lack of a uniform trend between repeats (**Figure 4.5 (B)**). For example in repeat 1, there was a substantial reduction in secreted CCL2 when cells were treated with PROTAC **105**, however this was not consistent in repeat 2 and 3.

The lack of a consistent trend could be attributed to the inconsistent concentration of CCL2 produced in response to TNF- α (stimulated control). Stimulated CCL2 was relatively consistent between repeat 1 and 3, with an average of 6207 pg/mL and 5400 pg/mL produced respectively, but a lower concentration was produced in repeat 2 (3636 pg/mL). It is possible that the fluctuations in the concentration of stimulated CCL2 introduced additional error and prevented the observation of consistent trends (for secreted CCL2 reduction in response to each PROTAC) and hence limited the reproducibility of the assay.

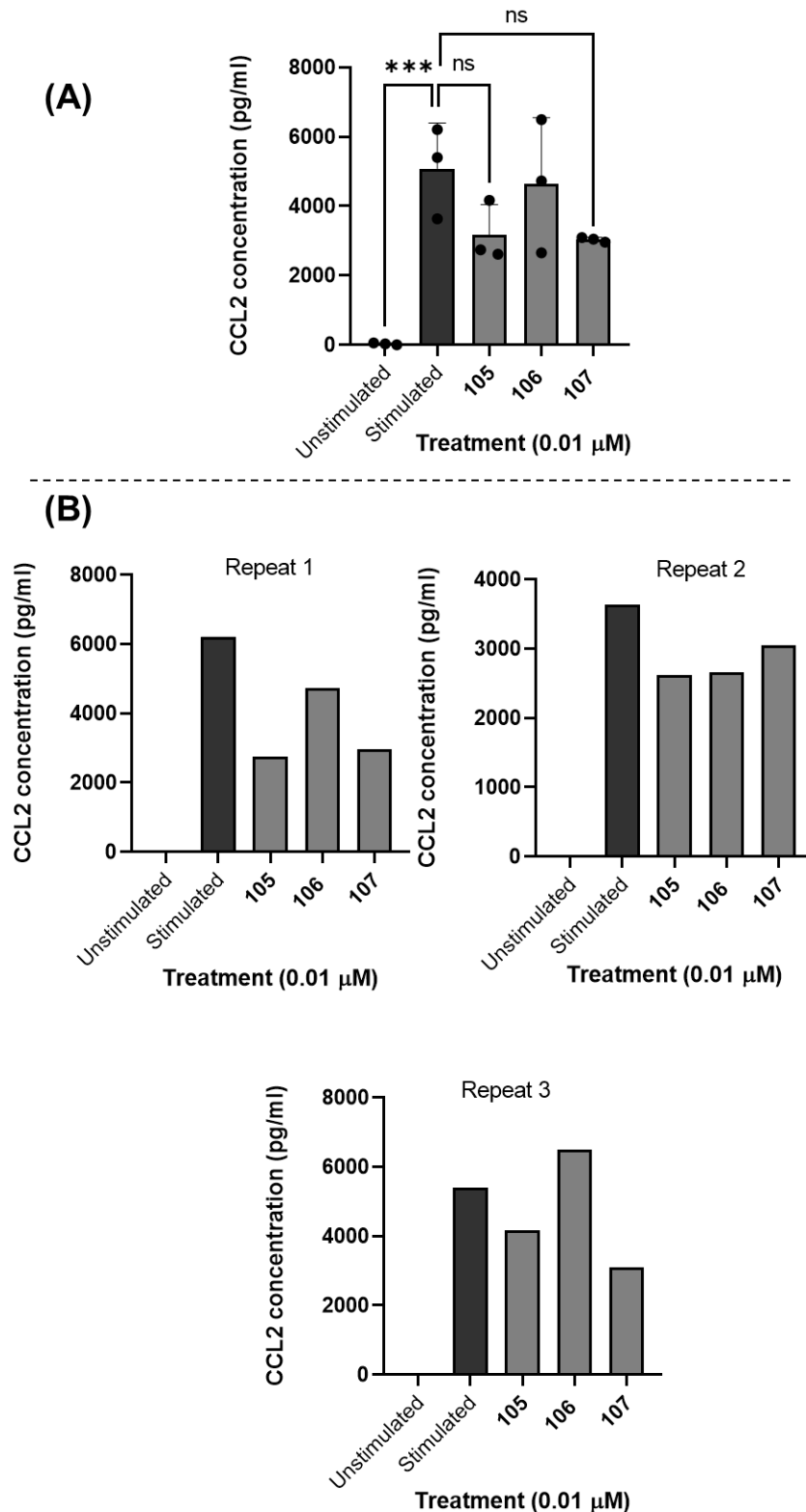


Figure 4.5 CCL2 concentration in secreted media after 24 h in response to a 0.01 μM dose of each PROTAC. **(A)** Compiled data showing no significant difference in CCL2 concentration measured in culture media when cells were co-treated with TNFα and each of the PROTACs ($n = 3$). *** $p < 0.001$, ns = non-significant. Significance was determined using one-way ANOVA with Dunnett's multiple comparison test. The assays were carried out in technical and biological triplicate. **(B)** Displays the variance shown between the individual repeats - which is relatively high with no uniform trends observed.

4.5 SPR analysis of CCL2-targeting PROTACs

All three PROTACs **105**, **106** and **107**, were screened in an SPR assay using btnCCL2 as previously detailed in **Chapter 3**. The PROTAC binding to btnCCL2 was evaluated over a concentration range; 200 μM , 100 μM , 50 μM , 25 μM , 5 μM and 2.5 μM . No PROTAC-CCL2 binding was observed for any of the PROTACs across all concentrations. This is consistent with the SPR data obtained for the individual DKP ligands themselves.

4.6 Chapter Summary

Three potential CCL2 targeting PROTACs (**105**, **106** and **107**) were synthesised, incorporating DKPs as their POI warhead (**Scheme 4.4**). The DKPs were attached by an ester linkage through either their proline or aromatic moieties. Despite issues with the purity of PROTAC **105**, they were all advanced for preliminary *in vitro* screening.

An assay was developed in collaboration with the Ali group (Newcastle university) in which the change in CCL2 secreted by HMEC-1 cells in response to each PROTAC could be analysed. However, when tested at 0.01 μM , none of the PROTACs were able to significantly reduce the levels of CCL2 (compared to the unstimulated control). This was likely due to the high variance between repeats as there was no general trend observed. The inconsistent concentration of stimulated CCL2 likely contributed to this. SPR analysis of the PROTACs also indicated that they do not bind CCL2 and therefore, with the data obtained from this chapter, alongside the biophysical data obtained in **Chapter 3**, this project was not taken further. Nonetheless, this chapter outlines a novel degradation assay that could be used to assess the degradation of secreted proteins which could provide a starting point for further work within this field.

4.7 References

1. C. Wang, Y. Zhang, Y. Wu and D. Xing, *Eur. J. Med. Chem.*, 2021, **225**, 113749.
2. N. R. Kong and L. H. Jones, *Clin. Pharmacol. Ther.*, 2023, **114**, 558–568.
3. R. I. Troup, C. Fallan and M. G. J. Baud, *Explor. Target. Anti-tumor Ther.*, 2020, **1**, 273–312.
4. V. G. Klein, A. G. Bond, C. Craigon, R. S. Lokey and A. Ciulli, *J. Med. Chem.*, 2021, **64**, 18082–18101.
5. *US. Pat.*, WO2019/118728A1, 2019.
6. G. M. Burslem, P. Ottis, S. Jaime-Figueroa, A. Morgan, P. M. Cromm, M. Toure and C. M. Crews, *ChemMedChem.*, 2018, **13**, 1508–1512.
7. A. Jordan, K. D. Whymark, J. Sydenham and H. F. Sneddon, *Green Chem.*, 2021, **23**, 6405–6413.
8. S. Aydin, *Peptides.*, 2015, **72**, 4–15.
9. C. Cecchini, S. Pannilunghi, S. Tardy and L. Scapozza, *Front. Chem.*, 2021, **9**, 1–23.

5. EBNA1-targeting PROTACs

5.1 Introduction to EBV

In 1964, scientists Epstein and Barr discovered a new γ -herpes virus associated with Burkitt's lymphoma.¹ The virus, termed the Epstein Barr Virus (EBV), is believed to be present in over 90% of the world-wide population.² Although EBV is non-symptomatic in most infected people, it is associated with many cancers such as Hodgkins and non-Hogkins lymphoma³ as well as nasopharyngeal cancer.⁴ Furthermore, EBV is believed to cause immune related illnesses such as multiple sclerosis (MS).⁵ However, despite its ubiquitous nature, there is currently no clinically effective treatment for EBV.

5.2 EBV structure and mode of infection

Like all λ -herpes viruses, EBV consists of a double-stranded DNA molecule surrounded by a nucleocapsid (**Figure 5.1**).⁶ The outermost layer of the cell is the envelope and between this and the nucleocapsid exists a viral tegument consisting of protein clusters. The outer side of the envelope is lined with glycoprotein spikes which are essential for the virus' ability to infect the host cell.⁷

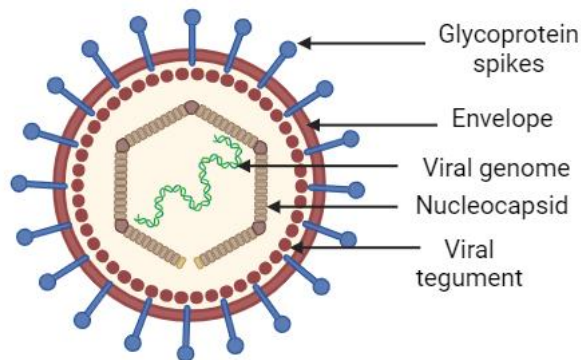


Figure 5.1 Structure of EBV. [Image created using BioRender]

When infecting B-cells (EBV is considered a B-lymphotropic virus) the outer glycoproteins interact with the cell surface receptor CR2(CD21).⁸ This interaction induces the endocytosis of the virus-receptor complex into a low pH compartment.⁵ Here, the virus fuses with the cell membrane of the host and is able to enter and infect.

5.3 Introduction to EBNA1

Epstein-Barr virus nuclear antigen 1 (EBNA1) is a dimeric protein essential for the DNA replication and episome maintenance of EBV.⁹ EBNA1 itself is a 641 amino acid (AA) protein, existing as a dimer both alone in solution as well as in complex with DNA.^{10,11} EBNA1 contains two major structural domains; (1) a DNA-binding domain (DBD) located at the C-terminus and (2) an N-terminal domain that is involved in replication and ensures episome persistence.¹² At the C-terminus, the DBD consists of AA 459 to 614 and has been crystallised in complex with DNA numerous times.^{10,13} The N-terminal domain contains two linking regions LR1 and LR2, that are responsible for chromosomal binding.¹⁴ These domains are connected through glycine-alanine (gly-ala) repeating regions that have been shown to regulate mRNA translation¹⁵ as well as shield EBNA1 from proteasomal degradation.¹⁶

Ori-P is a 1.7 kb region on EBV that is responsible for replication of the viral plasmid and cellular DNA within the host cell.¹¹ This process is mediated through interactions with EBNA1, which binds to two major sites on *ori-P*: the dyad symmetry element (DS) and the family of repeats (FR). These sites mediate different cells processes, with the DS involved in EBV DNA replication and the FR required for episome maintenance.

5.4 Peptide inhibitors of EBNA1 dimerisation

In work by Kim *et al.*, a library of 64 EBNA1 DNA binding peptides were synthesised.¹⁷ Each member of the library consisted of 15 AA, overlapping in 5 residues from AA 347 – 641 in the EBNA1 sequence. In this work three consecutive peptides p83, p84 and p85, almost entirely inhibited EBNA1 binding to DNA (at 1.2 μ M), with all peptides incorporating

the ₅₆₀CYFMVFL₅₆₆ sequence. P85 was the most potent, inhibiting DNA binding at a concentration of 0.6 μ M. The binding of p85 was analysed using SPR assays in which it was found to strongly associate, but not dissociate with the DBD (1 μ M). This work suggested that p85 acted as an irreversible EBNA1 binder.

To enable the specific imaging of EBNA1 *in vitro*, Jiang *et al.*, designed peptide-conjugates **108** and **109**, that incorporated three distinct parts; a positively charged chromophore (green), an EBNA1 targeting peptide (red) and a nucleus penetrating peptide, R_rRK (blue) (**Figure 5.2**).¹⁸ The conjugates incorporated two peptide sequences **110** and **111**, that were synthesised by previous Cobb group member Sam Lear. Peptides **110** and **111** differ only by the position of the YFMVF and R_rRK sequences (separated by a glycine (GG) spacer).

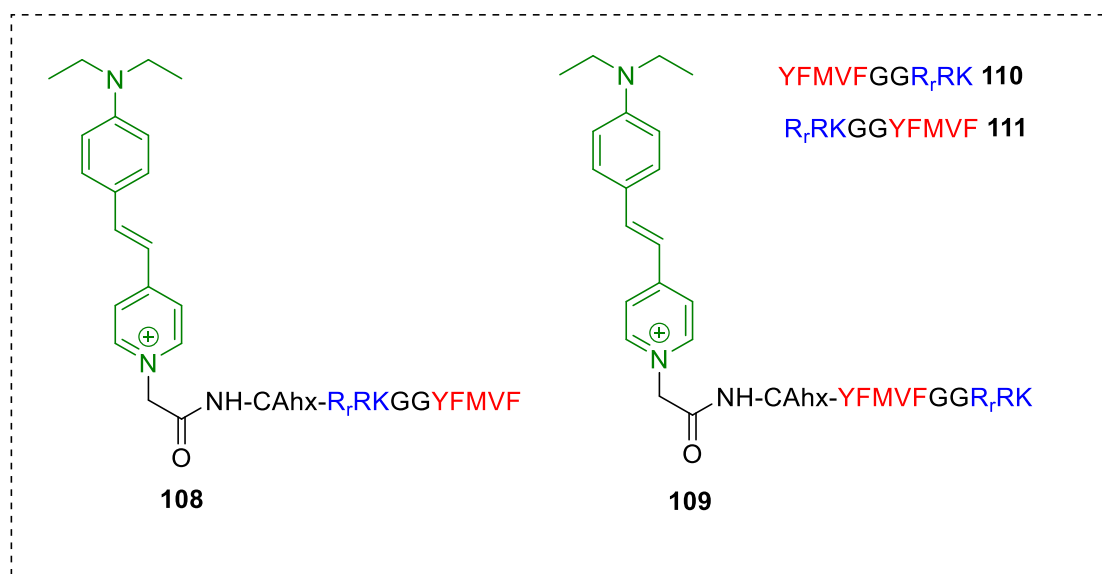


Figure 5.2 Chemical structures of EBNA1-targeting peptide-conjugates **108** and **109**, as well as peptide sequences **110** and **111** synthesised by Lear. These contain a positively charged chromophore, an EBNA1 targeting sequence and a nucleus penetrating sequence.

Peptide-conjugate **109**, in which the nucleus penetrating peptide is at the C terminus, was the most promising conjugate when tested *in vitro* and *in vivo*.¹⁸ To assess the binding of conjugate **109** to WT-EBNA1, a luminescence titration experiment was carried out. In response to the addition of 4 μ M EBNA1 to a solution of conjugate **109**, there was an 8.8-

fold increase in emission and a 25 nm blue shift. *In vitro* imaging was also undertaken and showed conjugate **109** to have a greater cellular uptake compared to conjugate **108**. Additionally, conjugates **108** and **109** effectively localised in nuclei of EBV+ cells (C666-1 and NPC43 cells). Conjugate **109** also displayed cytotoxicity to EBV+ cells ($IC_{50} \approx 15 \mu M$) but displayed no cytotoxicity to EBV- cells at 50 μM . Lastly, *in vivo* tumour imaging, using mice carrying C666-1 xenografts, was performed with peptide **110** and conjugate **109**. From this work it was found that at day 7, a biweekly treatment of **109** or **110** (4 μg) was able to reduce the tumour weight by an average of 86.6% and 92.8% respectively (**Figure 5.3**).

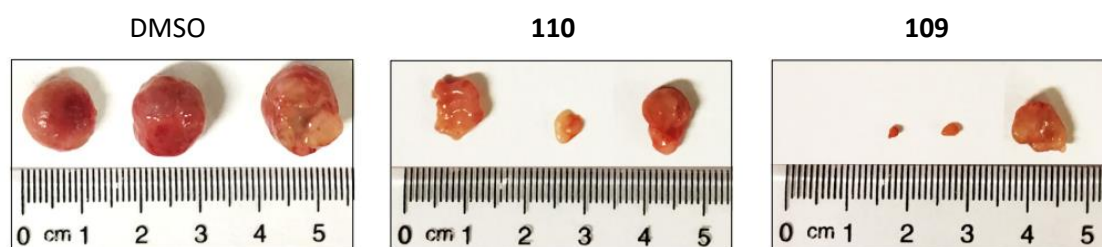


Figure 5.3 Tumour reduction over 7 days for the DMSO vehicle control, peptide **110** and conjugate **109**. [Image modified from reference 18].

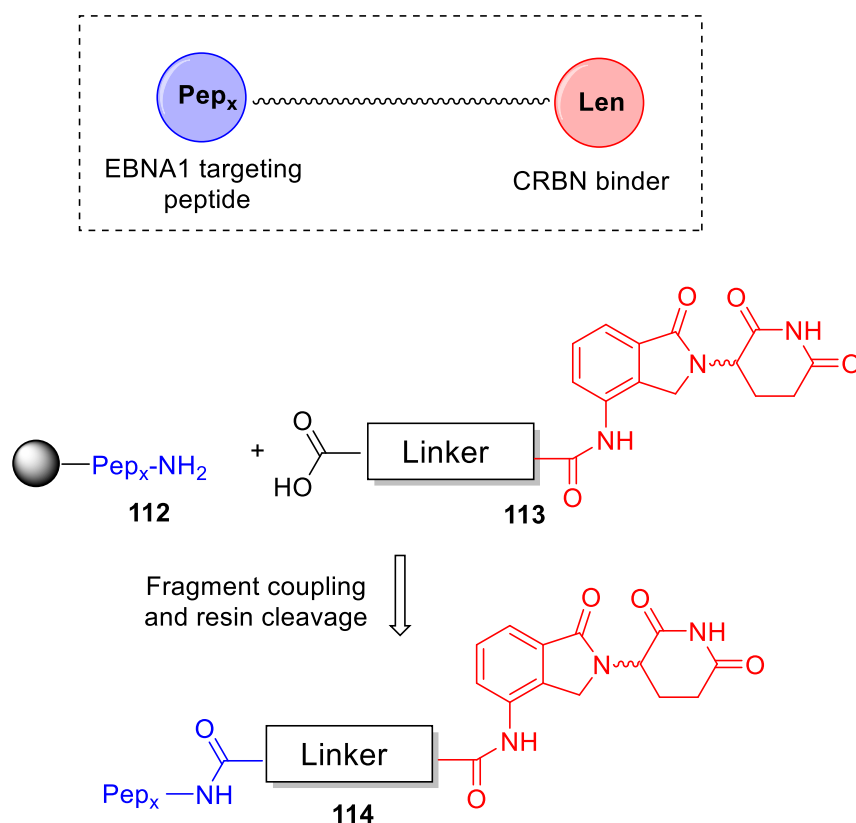
5.5 Aims

The aim of this chapter is to incorporate the EBNA1 targeting peptide motif YFMVF-NH₂ (or analogues thereof) into PROTACs that enable EBNA1 degradation. To achieve this a library of PROTACs incorporating linkers which are varied in length and composition, that facilitate CRBN mediated degradation, will be designed and prepared. The final PROTAC assembly will be carried out by either solid phase amide bond formation (Group 1 PROTACs) or by click chemistry, incorporating a 1,2,3-triazole into the PROTAC linker (Group 2 PROTACs). PROTACs have already shown to be effective against viral proteins. For example, in work by de Wispelaere *et al.*, PROTACs were developed that were able to degrade HCV protease and overcome the resistance the virus had developed to small molecule inhibitors.¹⁹

The work in this Chapter was undertaken as part of a larger collaborative project with Eleanor Taylor-Newman (current PhD Cobb group) and Dr Graham Taylor at the University of Birmingham (UK). The PROTACs shown in this chapter will also be included into a library of potential EBNA1 degraders also synthesised by Taylor-Newman (not reported in this thesis). The overarching goal of the project is to create a library of EBNA1 targeting PROTACs, with a wide range of structural features (different EBNA1 warheads, different linker lengths and compositions and ligands targeting different E3 ligases), to further the understanding of the attributes essential for EBNA1 degradation.

5.6 Group 1 EBNA1-PROTAC synthesis

The Group 1 EBNA1-PROTACs contained short linkers and were assembled by solid phase amide synthesis (general synthesis shown in **Scheme 5.1**). Initially, the peptide warheads (**112**) were synthesised by automated Fmoc-SPPS and were retained on resin. In addition, a series of lenalidomide-linker conjugates (**113**), that contained pendant carboxylic acids, were synthesised by solution phase amide coupling. The on-resin attachment of the two fragments, followed by resin cleavage, afforded the desired PROTACs (**114**).



Scheme 5.1 General synthesis of Group 1 EBNA1-PROTACs.

5.6.1 Synthesis of PROTAC warheads

The amino acid sequences $\text{YFMVFGGR}_r\text{RK-NH}_2$ (**110**) and $\text{R}_r\text{RKGGYFMVF-NH}_2$ (**111**) incorporated both an EBNA1 targeting peptide and a nucleus penetrating peptide (Figure 5.2). It was decided that for this early stage PROTAC development, only the EBNA1 binding peptide would be incorporated into the design. It was deemed that the use of the full peptide sequence would result in PROTACs having large molecular weights that could hinder their cell permeability. The majority of PROTACs are between 600 and 1400 g/mol,²⁰ thus it was decided to adhere to this range in current work.

As there is little structural evidence (for example an X-ray crystal structure) for the binding of YFMVF-NH_2 to EBNA1, the optimal position for PROTAC attachment was unknown. Sequence YFMVF-NH_2 (**115**) and the reverse sequence FVMFY-NH_2 (**116**) allow different points of attachment to the N-terminus of the peptide (Figure 5.4). The addition of two glycines to form warheads GGYFMVF-NH_2 (**117**) and GGFVMFY-NH_2 (**118**) provides extra

space between the EBNA1 peptide and the PROTAC linker, a potential aid to ternary complex formation.

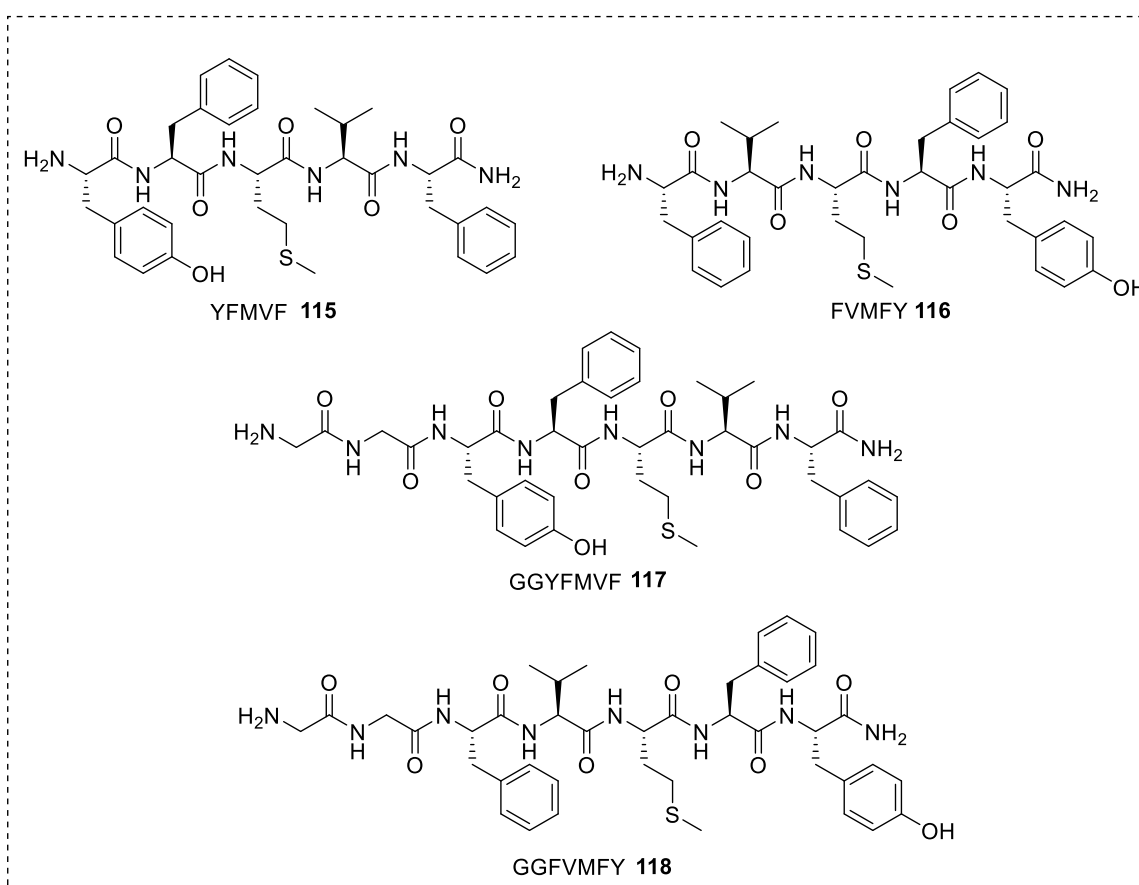
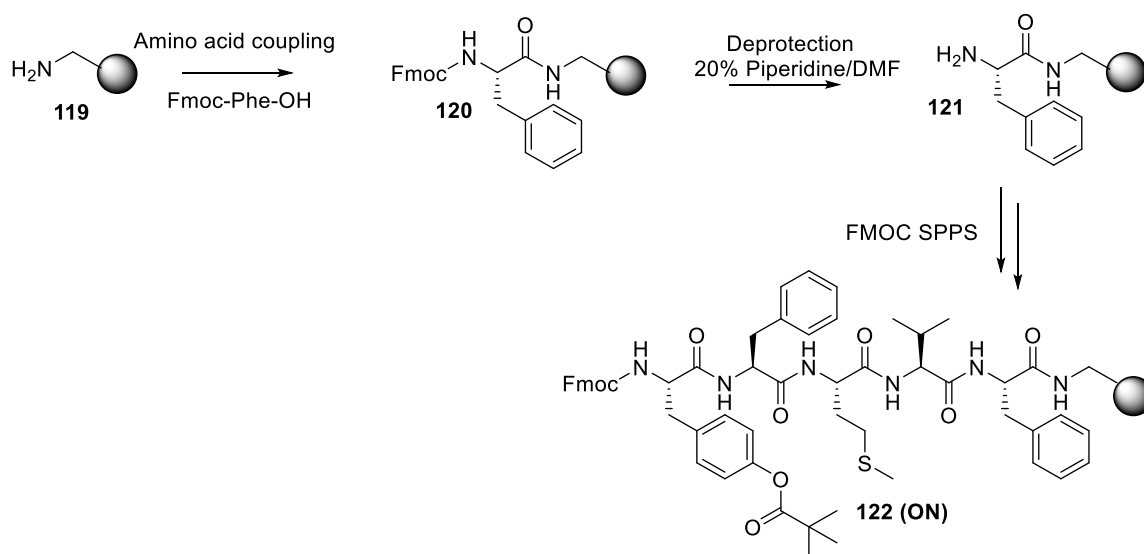


Figure 5.4 Chemical structures of peptide warheads (**115 – 118**).

Peptides **115 – 118** (**Figure 5.4**) were synthesised using an automated microwave peptide synthesiser (Liberty Blue 2.0 – CEM) on a rink amide MBHA resin (**119**) (1.0 mmol). The on-resin peptides (**120**) were synthesised using microwave assisted, single couplings of each Fmoc-amino acid (5.0 equiv.), with a coupling mixture of DIC (10.0 equiv.) and HOBT (5.0 equiv.). Between each coupling, Fmoc-deprotection was achieved using 20%

piperidine in DMF. **Scheme 5.2** shows this route for the synthesis of peptide **122 (ON)**ⁱ (Fmoc-protected **115**).



Scheme 5.2 General automated SPPS for peptide POI warheads in this project. The sequence shown in the reaction scheme is for peptide **122 (ON)**.

Following synthesis, test cleavage (using a 90:5:5, TFA:H₂O:TIPS mixture) and subsequent analysis by LCMS (+ve) showed the successful synthesis of peptides **115** – **118**. For example, the LCMS trace corresponding to the test cleavage of peptide **122** (Fmoc-protected YFMVF-NH₂) is shown in **Figure 5.5**. The expected peak for [M+H]⁺ = *m/z* 927.6 is present at 3.0 min.

ⁱ **ON** refers to peptide retained on resin.

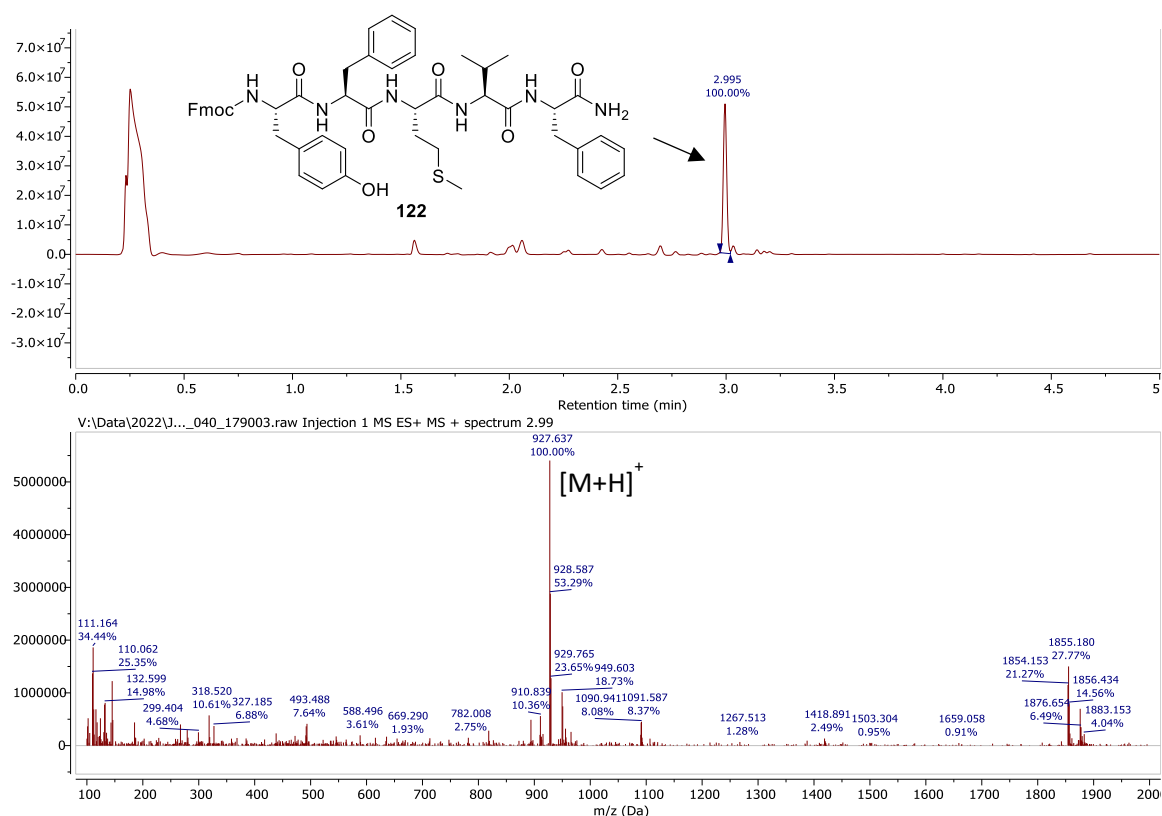


Figure 5.5 The LCMS (+ve mode) trace ($\lambda = 220$ nm) corresponding to the test cleave of peptide **122** (ON).

5.6.2 Synthesis of lenalidomide-linker conjugates

Lenalidomide (**9**) was chosen as the E3 ligand in this work, as the literature suggests it to be preferable to pomalidomide (**8**), in addition to being commercially available and inexpensive. In work by Remillard *et al.*, the BRD9 targeting PROTAC (**123**) that incorporated lenalidomide (**9**) as its CRBN binder, showed enhanced degradation over comparable PROTACs containing pomalidomide (**8**) (**Figure 5.6**).²¹ Furthermore, the absence of the phthalimide carbonyl group increases metabolic and chemical stability.²²

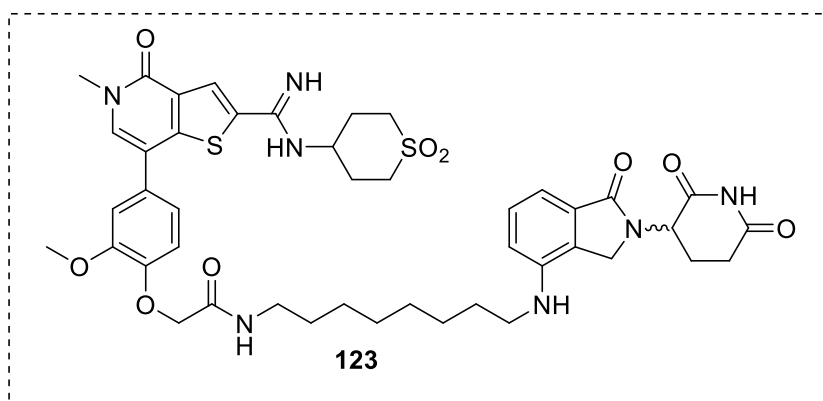
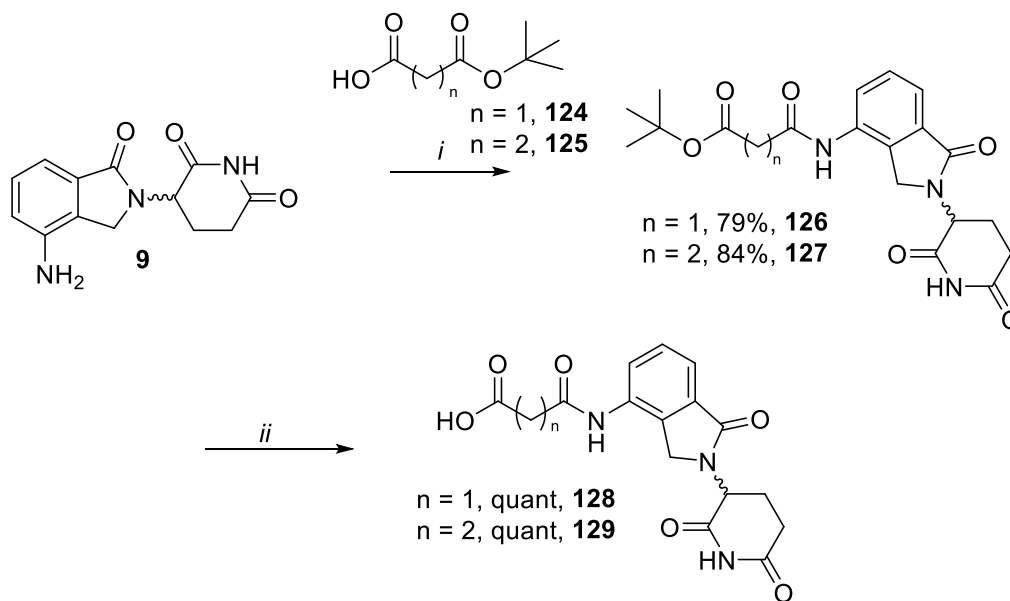


Figure 5.6 Chemical structure of BRD9 targeting PROTAC (**123**) from work by Remillard *et al.*²¹

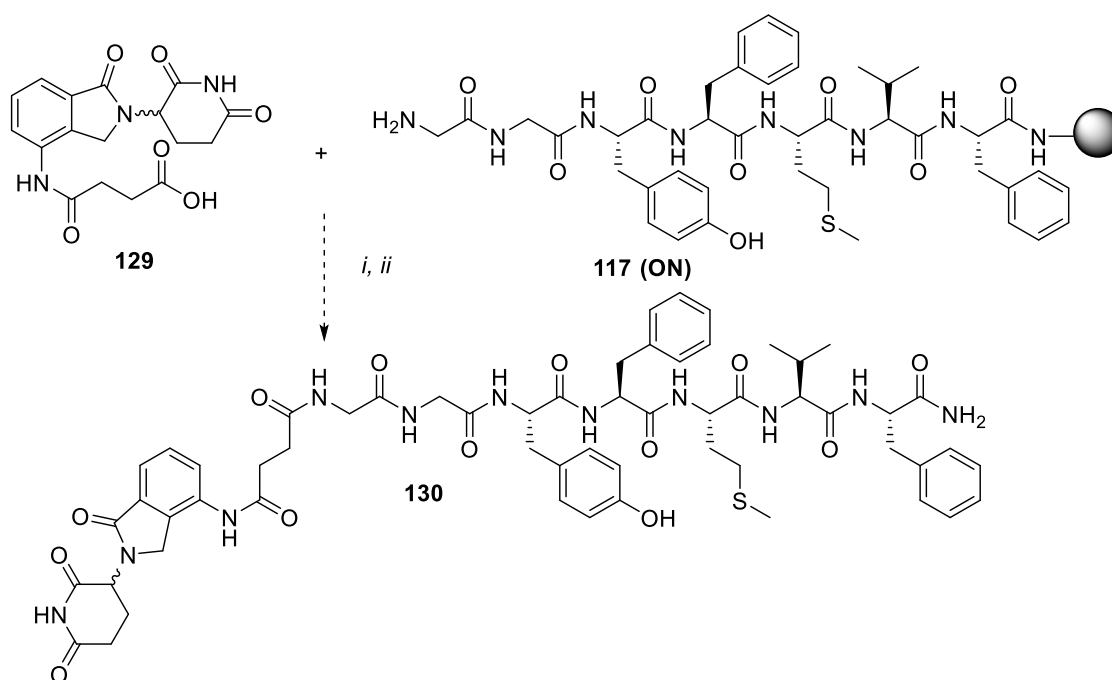
Lenalidomide-linker conjugates **128** and **129** contained pendant carboxylic acids to enable their attachment to the peptide warheads through an amide linkage. Mono-*tert*-butyl protected dicarboxylic acids **124** and **125**, were coupled to lenalidomide in solution, using coupling reagent EDC and a catalytic quantity of DMAP (**Scheme 5.3**). The DMF solvent was removed *in vacuo* and an aqueous work-up was used to remove the EDC urea by-product. Following this, products **126** and **127** precipitated as amorphous solids and were washed with EtOAc to remove any uncoupled linker (the lenalidomide analogues **126** and **127** have low solubility in most organic solvents). The products were filtered and dried under high vacuum to afford conjugates **126** and **127** in good yields (79% and 84% respectively) with sufficient purity (from analysis of corresponding ¹H NMR and ¹³C NMR spectra) to continue on to the next synthetic step. Finally, the *tert*-butyl protecting groups were removed using 50% TFA in DCM. TFA was removed by concentration *in vacuo* followed by lyophilisation to afford acids **128** and **129**.



Scheme 5.3 Synthesis of lenalidomide-linker conjugates **128** and **129**. Reagents and conditions: *i*. EDC.HCl, DMAP (cat), DMF, rt, 16 h. *ii*. 50% TFA in DCM, rt, 30 min.

5.6.3 Optimisation of PROTAC assembly

Prior to PROTAC assembly, the on-resin Fmoc-peptides were deprotected using 20% piperidine in DMF. The initial target PROTAC (**130**) consisted of a 2-carbon alkyl linker and the GGYFMVF-NH₂ peptide warhead. For the synthesis of PROTAC **130**, it was proposed that peptide **117 (ON)** and lenalidomide-linker conjugate **129**, could be attached using on-resin amide coupling, with subsequent resin-cleavage affording the desired PROTAC (**130**) (Scheme 5.4).



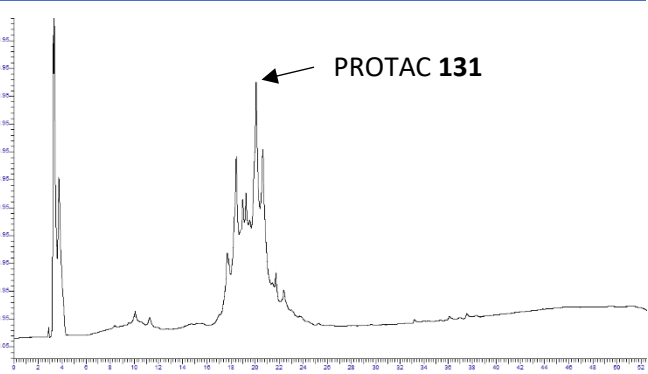
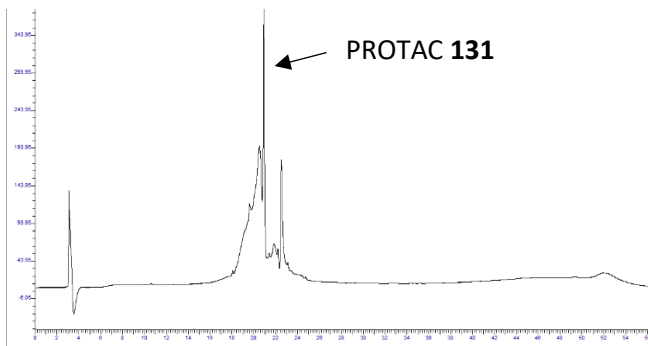
Scheme 5.4 Proposed synthesis for PROTAC assembly using on-resin amide coupling. Reagents and conditions: *i.* coupling conditions (**Table 5.1**). *ii.* TFA, TIPS, H₂O, 4 h, rt. The sequence shown is for PROTAC **130**.

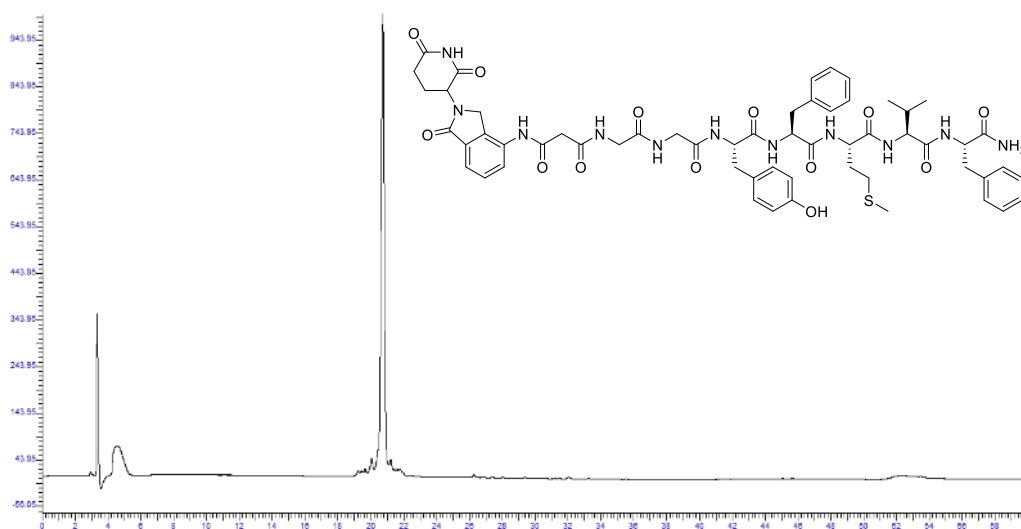
Optimisation of the amide coupling conditions was attempted for the synthesis of PROTAC **130** (**Table 5.1**) with the majority of attempts utilising a manual (non-microwave) SPPS shaker plate. The outcome of each coupling was determined through analysis of LCMS data corresponding to a test cleave of the on-resin material. When overnight, double couplings with reagent DIC (4.0 equiv) and DIPEA (6.0 equiv.) were used (**Table 5.1 - Entry 1**) a low conversion of the on-resin dipeptide (**117 (ON)**) to PROTAC was observed. Following this, the synthesis was reattempted with an increased quantity of DIC (6.0 equiv) and a higher reaction temperature of 50 °C (**Table 5.1 - Entry 2**). Using these conditions, the starting material was consumed but the main peak observed corresponded to an undeterminable by-product with an *m/z* of 971. An alternative coupling mixture of HATU (4.5 equiv.) and DIPEA (10.0 equiv.) was used, however again this was ineffective at forming the desired PROTAC (**Table 5.1 - Entry 3**). The use of PyBOP (4.0 equiv.) was also ineffective at producing any of the desired product, with no conversion of the on-resin peptide **117 (ON)** (**Table 5.1 - Entry 4**). As DIC had been the only coupling reagent to

The synthesis of PROTAC **131** was attempted using two different conditions (**Table 5.2**). The first attempt used double couplings of DIC (4.0 equiv.) and DIPEA (6.0 equiv.) with overnight, manual agitation (**Table 5.2 - Entry 1**). Analysis of LCMS (+ve) data indicated the successful synthesis of PROTAC **131**. The PROTAC was cleaved from the resin and the purity of the crude was assessed using analytical HPLC, which showed the presence of multiple overlapping impurity peaks (**Table 5.2 - Entry 1**). As the impurities were close in retention factor (R_t) to the desired product, obtaining pure material using reverse-phase HPLC would have been challenging.

The synthesis was re-attempted, instead using the microwave peptide synthesiser (using DIC and HOBT) which successfully produced a crude product with fewer overlapping impurities (from analysis of analytical the HPLC chromatogram) (**Table 5.2 - Entry 2**). The crude was purified by reverse-phase HPLC and the desired PROTAC (**131**) was obtained to high purity (92%) (**Figure 5.8**).

Table 5.2 The conditions and corresponding crude analytical HPLC chromatograms ($\lambda = 220$ nm) for PROTAC **131** synthesis.

Entry	Conditions	Analytical HPLC trace
1.	Acid 128 (4.0 equiv.), DIC (4.0 equiv.), DIPEA (6.0 equiv.), DMF, rt, 2 h 2 x coupling.	
2.	Acid 128 (3.0 equiv.), DIC (10.0 equiv.), HOBt (5.0 equiv.) DMF, mw, 2 x coupling. (Using the Liberty Blue 2.0 – CEM).	



5.6.4 Group 1 EBNA1-PROTACs

The assembly of five additional PROTACs (**Figure 5.9**) was carried out using the coupling conditions from **Table 5.2 - Entry 2**. All PROTACs were purified by preparative reverse-phase HPLC to a purity > 90%.

PROTACs **131** and **132** contained the warhead sequence GGYFMVF-NH₂ and GGFVVMFY-NH₂ respectively and contained the shortest linkers (n = 1). PROTACs **133** and **134** also contained the shortest linker, in addition to shorter warhead sequences YFMVF-NH₂ and FVMFY-NH₂ respectively. Finally, PROTACs **135** and **136** contained the YFMVF-NH₂ and FVMFY-NH₂ sequences but with slightly longer, 2-carbon alkyl linkers.

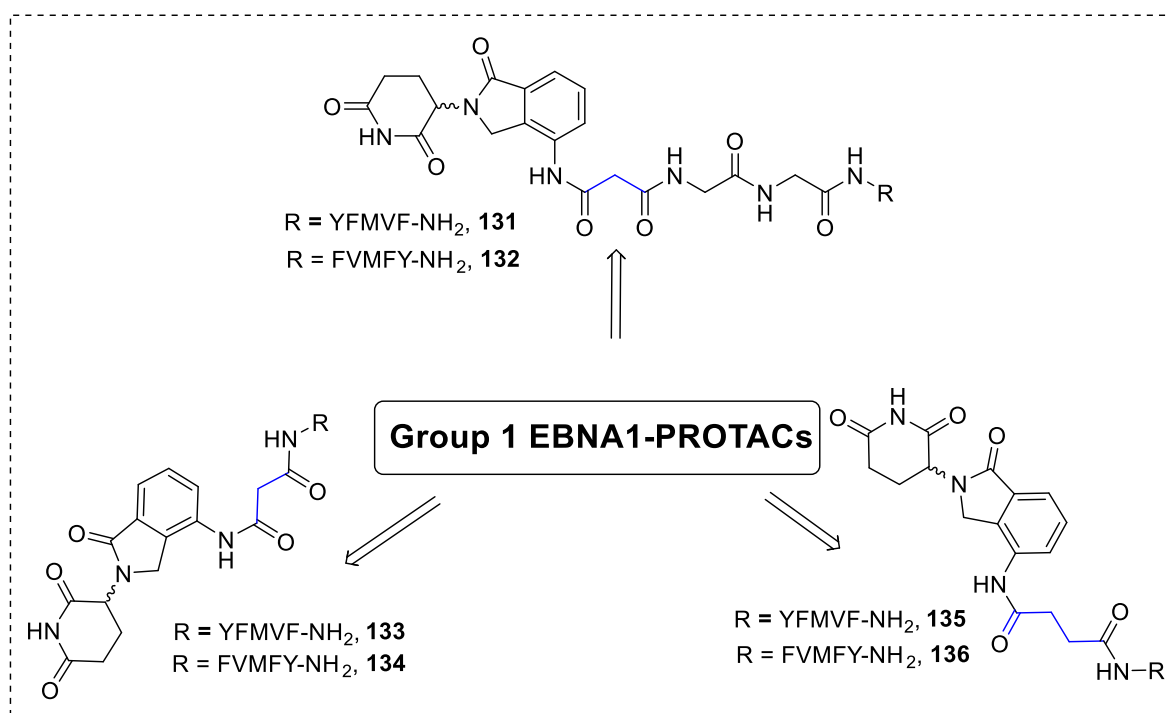
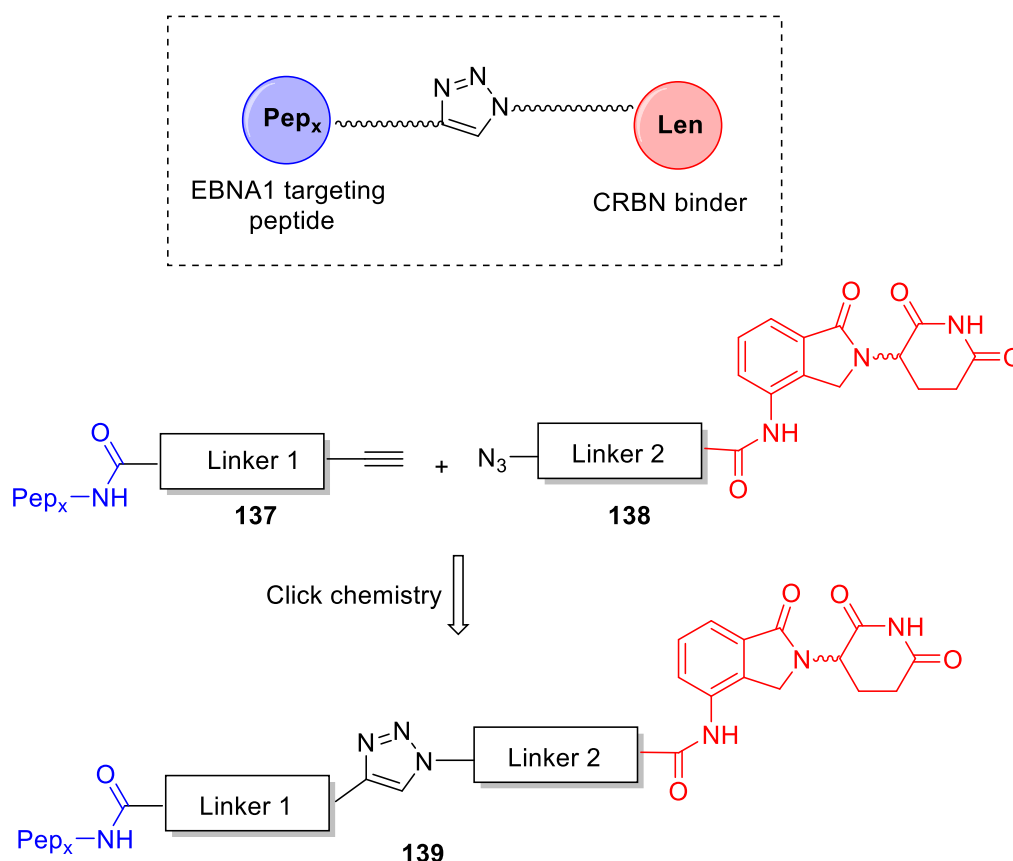


Figure 5.9 Chemical structures of the Group 1 EBNA1-PROTACs (**131 – 136**).

5.7 Group 2 EBNA1-PROTAC synthesis

As explained in **Chapter 1**, the copper(I) catalysed azide-alkyne cycloaddition (click-chemistry) is widely used for PROTAC assembly, incorporating a 1,2,3-triazole into the PROTAC linker. This strategy was used to create the Group 2 EBNA1-PROTACs, which incorporated longer alkyl linkers to add diversity to the PROTAC library.

Again, lenalidomide (**9**) was used as the E3 ligand and YFMVF-NH₂ (or GGYFMVF-NH₂) provided the POI warhead. In this work, Group 2 PROTACs (**139**) were formed from click chemistry between peptide-alkyne conjugates (**137**) and lenalidomide-azide conjugates (**138**) (**Scheme 5.5**).

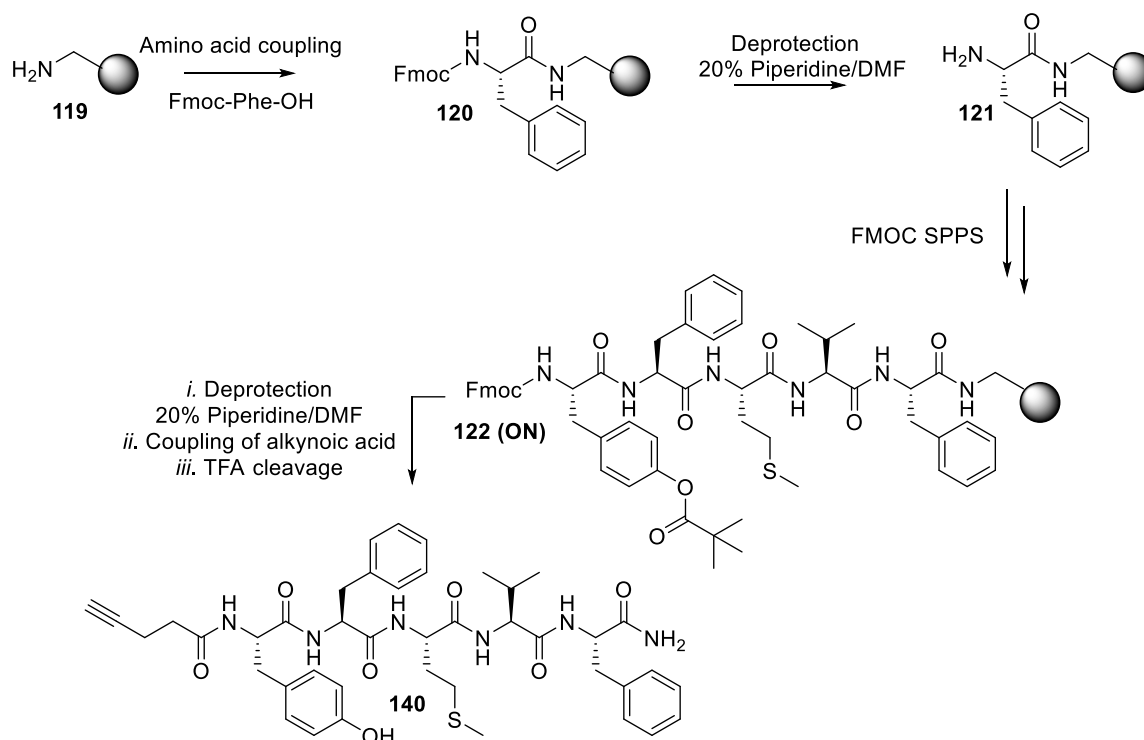


Scheme 5.5 General synthesis of Group 2 PROTACs.

5.7.1 Synthesis of peptide-alkyne conjugates

As the attachment of linkers to the on-resin peptides using the Liberty blue synthesiser, was successful for the synthesis of Group 1 PROTACs, it was proposed that these conditions could be used for the synthesis of the peptide-alkyne conjugates (**137**) (**Scheme 5.6**). Again, Fmoc-SPPS was used to synthesise the on-resin peptide. Following Fmoc-deprotection of the N-terminal amino acid, the corresponding alkynoic acid was

coupled using DIC and HOBT. For all peptide-conjugates prior to resin cleavage, analysis of the corresponding LCMS data showed their successful synthesis.



Scheme 5.6 General synthesis for alkyne-peptide conjugates. The route shown is for peptide-alkyne conjugate **140**.

Subsequent to resin cleavage, the peptide-alkyne conjugates were precipitated in Et₂O, lyophilised and used in the next synthetic step without further purification. Four peptide-alkyne conjugates (**140 – 143**) were synthesised using this method (**Figure 5.10**). Peptide-conjugates **140**, **141** and **142** contained the YFMVF-NH₂ peptide sequence and 2-, 3- or 4- carbon alkyl chains respectively. To enable the synthesis of longer PROTACs, peptide conjugate **143** which contained the GGYFMVF-NH₂ sequence and 4-carbon alkyl chain, was synthesised.

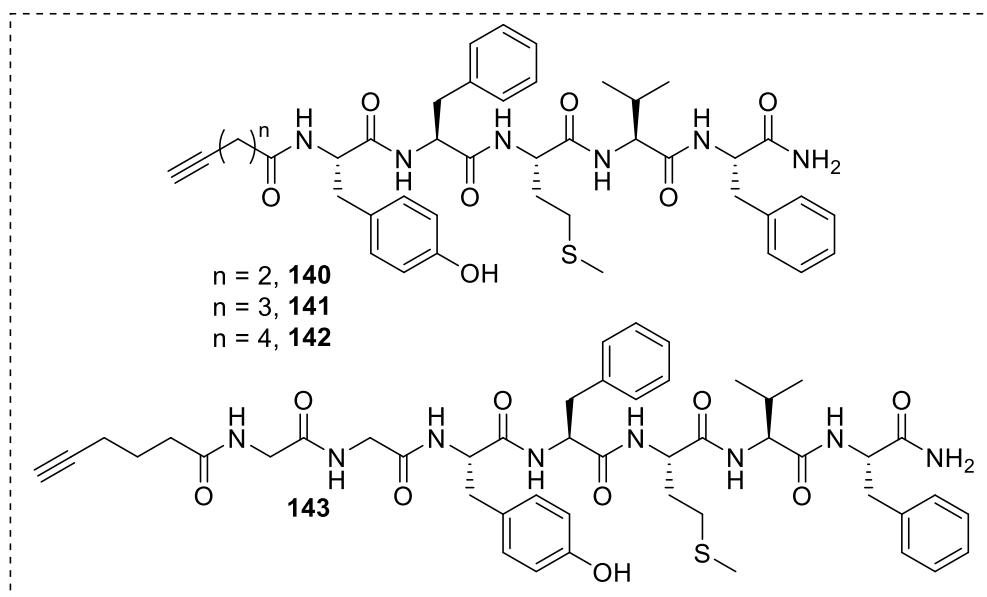
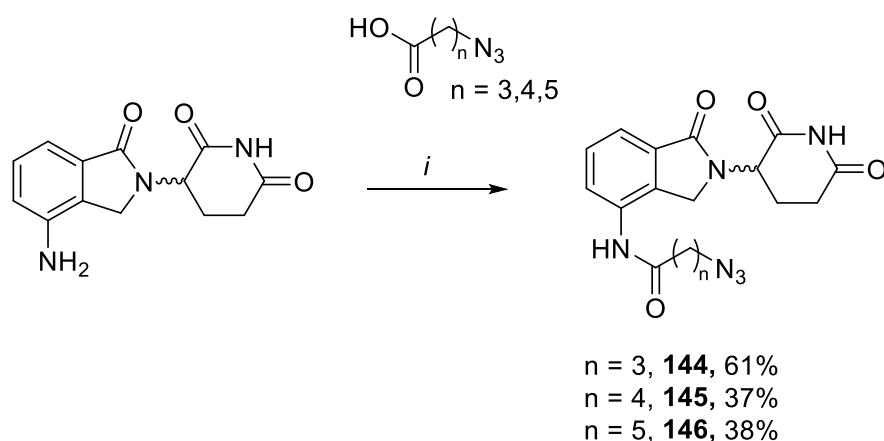


Figure 5.10 Chemical structures of peptide-alkyne conjugates **140 – 143**.

5.7.2 Synthesis of lenalidomide-azide conjugates

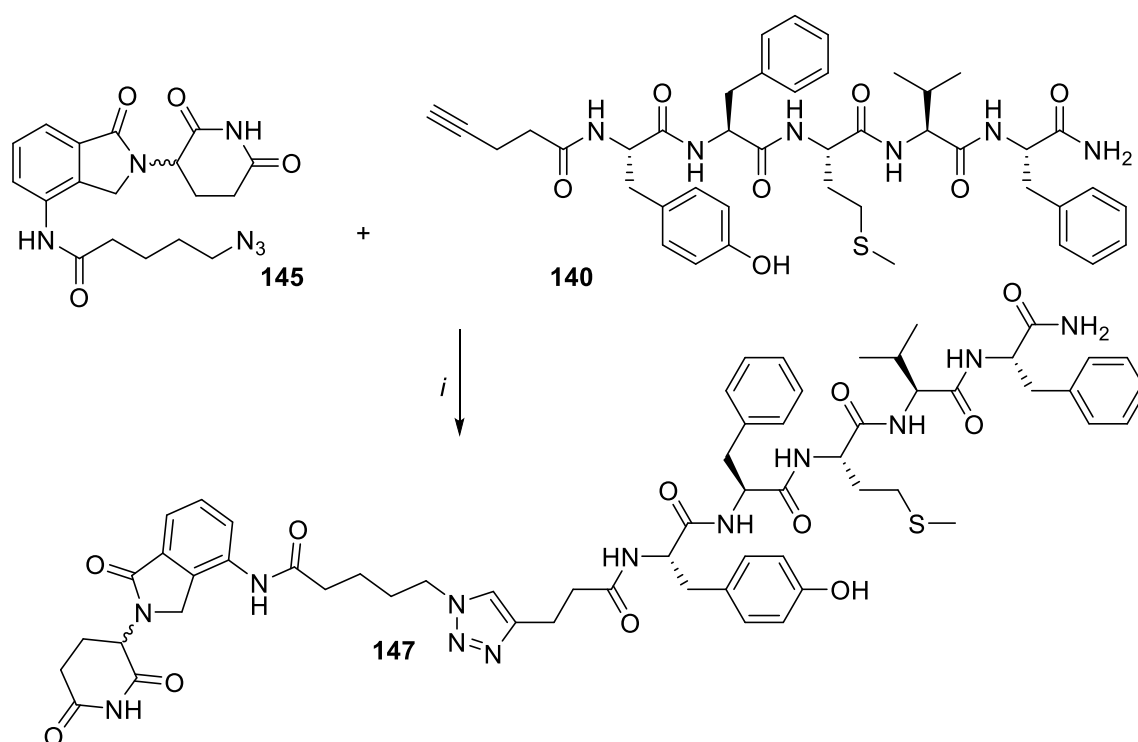
Lenalidomide-azide conjugates (**144 – 146**), were synthesised by solution phase amide coupling of acyl azides (-3,-4 and -5 carbon alkyl chains respectively) with lenalidomide (**9**) (**Scheme 5.7**). Following the removal of DMF and an aqueous work-up, the precipitate was filtered, washed with EtOAc and subsequently dried under high vacuum. The conjugates were deemed sufficiently pure by analysis of ^1H and ^{13}C NMR spectra to be taken forward to the next step without further purification.



Scheme 5.7 Synthesis of lenalidomide-azide conjugates **144** - **146**. Reagents and conditions: *i*. EDC.HCl, DMAP(cat), DMF, rt, 16 h.

5.7.3 Group 2 EBNA1 PROTAC assembly

With the synthesis of peptide-alkyne conjugates and lenalidomide-azide conjugates completed, the PROTACs were assembled using click chemistry. The fragments were stirred in DMF with catalytic quantities of CuSO_4 and sodium ascorbate, and heated at 75°C under microwave conditions for 2 h (**Scheme 5.8**). For Group 2 PROTACs, disappearance of the starting materials and formation of the desired products were apparent by LCMS reaction tracking. Following the synthesis, the mixture was filtered, and the DMF was removed by concentration *in vacuo* with toluene (3 x at 60°C). Subsequently, the crude material was lyophilised before purification by reverse-phase HPLC.



Scheme 5.8 General synthesis of Group 2 EBNA1 PROTACs using click chemistry. Reagents and conditions: *i.* CuSO₄, Na-ascorbate, DMF, mw, 75 °C, 2 h. The route shown is for PROTAC **147**.

The route shown in **Scheme 5.8** was used to synthesise seven Group 2 PROTACs (**147** – **153**) (**Figure 5.11**) which were purified by reverse-phase HPLC to >90% purity. PROTACs **147** – **152** incorporated the YFMVF POI warhead, whereas the longest PROTAC in the library (**153**) incorporated GGYFMVF. PROTAC **147** was the shortest of the series, with a linker that consisted of 9 atoms. PROTACs **148** and **150** both contained linkers of 10 atoms, but with different placement of the triazole group. PROTACs **149** and **151**, contained linkers of 11 atoms, again, with different placement of the triazole. Both PROTACs **152** and **153** had linkers consisting of 12 atoms, however PROTAC **153** was the larger of the two, due to incorporation of the GGYFMVF warhead.

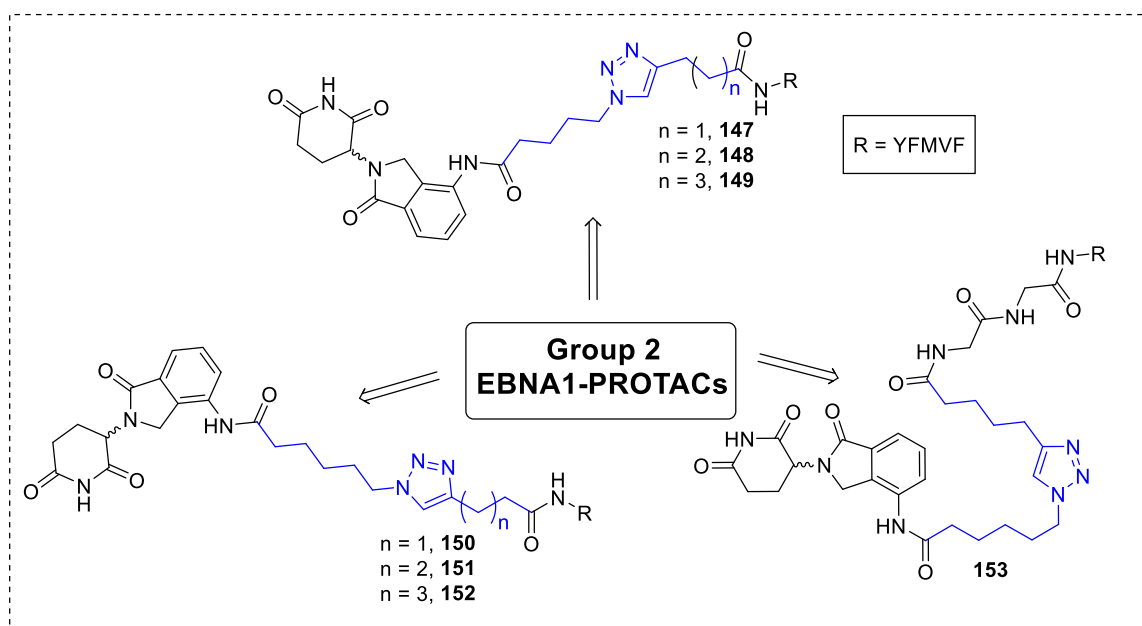


Figure 5.11 Chemical structures of Group 2 EBNA1-PROTACs **147 – 153**.

5.8 EBNA1-targeting PROTACs *in vitro* testing

Note – The work in this section was carried out by Eleanor Taylor-Newman (PhD Cobb group) and Dr. Graham Taylor at Birmingham University (UK).

5.8.1 EBNA1 degradation assay design

The PROTACs synthesised in this chapter were assessed for their ability to degrade EBNA1 as part of a wider 28 EBNA1 targeting PROTAC library. This diverse library also included PROTACsⁱⁱ that targeted VHL for degradation (**154**), incorporated small molecule POI warheads (**155**) or were entirely peptide based (**156**) (**Figure 5.12**). The degradation potential of each PROTAC was assessed using a GFP fluorescence-based assay. In this work, HEK293 cells were transfused with a GFP-EBNA1 or GFP-EBNA1ΔGA (in which the gly-ala repeat unit is deleted) fusion-construct. The GFP-EBNA1ΔGA construct was included in this work, as the gly-ala repeat unit has been shown to interfere with proteasomal degradation.¹⁶ In this work, cells expressing GFP-EBNA1 or GFP-

ⁱⁱ Synthesised by Eleanor Taylor Newman (Cobb Group).

EBNA1 Δ GA could be treated with each PROTAC, with a reduction in fluorescence expected from resulting EBNA1 degradation.

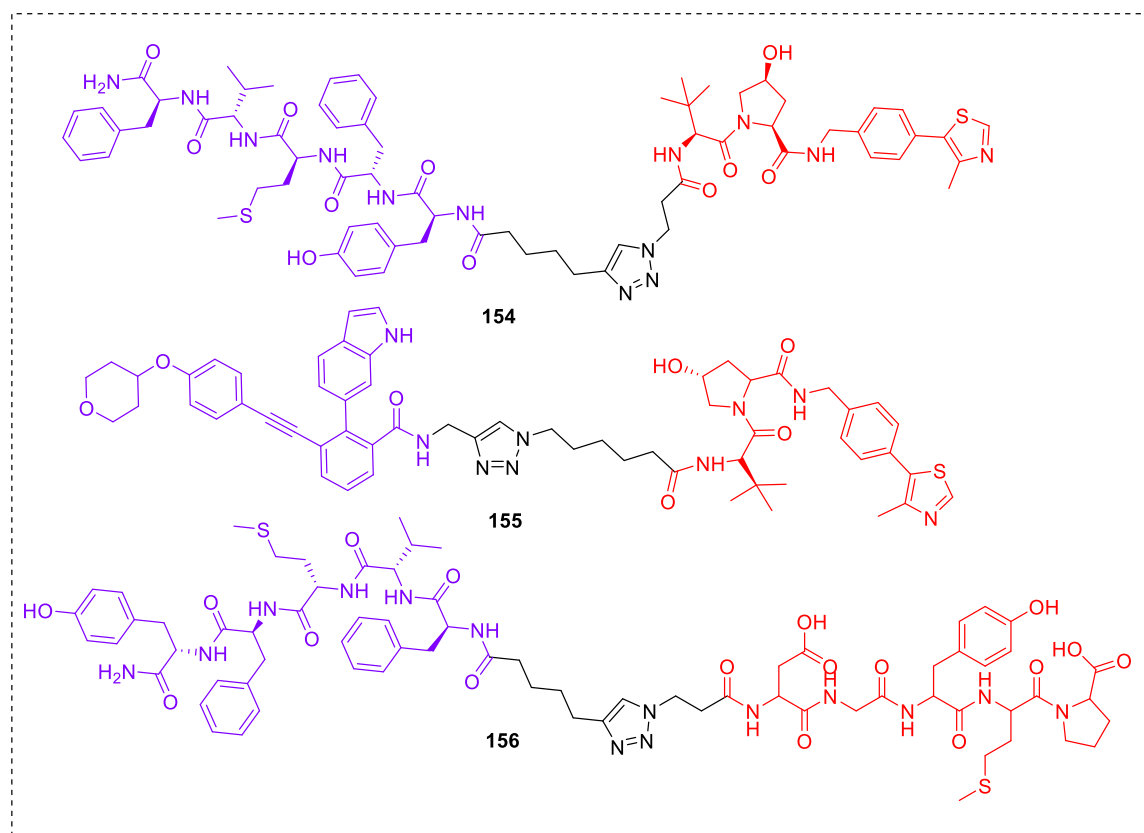


Figure 5.12 Chemical structures of example EBNA1 PROTACs designed and synthesised by Taylor-Newman. The POI binder is shown in purple, E3 ligand is in red and linker is in black.

As this was a novel degradation assay, initial experiments used the degradation tag (dTAG) system for its validation. dTAGs were created by Nabet *et al.*, to degrade the fusion protein FKBP12^{F36V} via CRBN.²³ One of their lead PROTACs, dTAG-13 (**157**) (**Figure 5.13**), was able to significantly reduce the levels of FKBP12^{F36V} at 100 nM. Additionally, it was shown that when desired protein targets KRAS^{G12V} and BRD4 were fused with FKBP12^{F36V}, the proteins could also be degraded using a dTAG PROTAC.

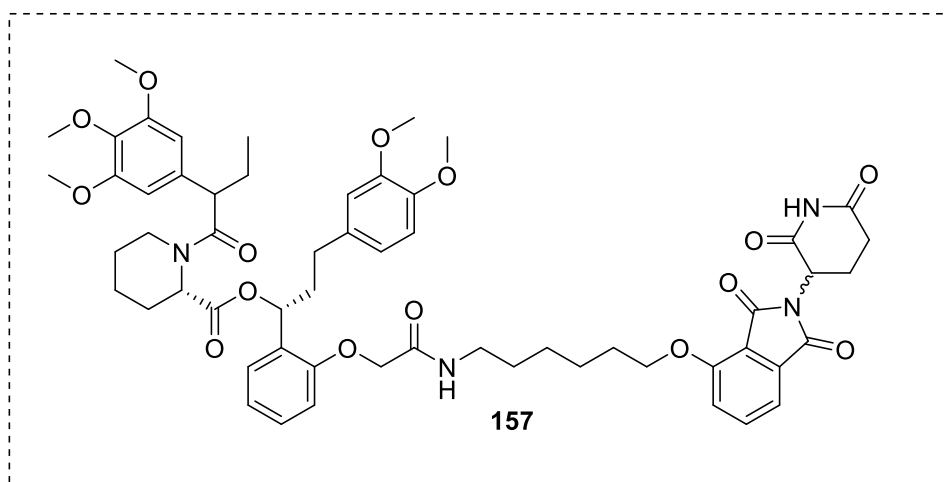


Figure 5.13 Chemical structure of dTAG-13 (**157**) designed by Nabet *et al.*²³

To effectively use the dTAG system, HEK293 cells were transfected with additional FKBP12^{F36V} fused constructs of GFP, GFP-EBNA1 and GFP-EBNA1ΔGA. Degradation of the protein and therefore a reduction in fluorescence, would be expected when the cells were treated with a known dTAG. This system was shown to work with dTAG **157**, which induced a reduction in fluorescence for GFP-EBNA1-FKBP12^{F36V} at 5, 50 and 500 nM. A reduction in fluorescence was also observed for GFP-FKBP12^{F36V} and GFP-EBNA1ΔGA-FKBP12^{F36V} but not for the negative control (GFP only). The fused constructs and dTAG-13 (**157**) were incorporated as controls in subsequent EBNA1-PROTAC degradation experiments.

Next, degradation assays for all 28 PROTACs were undertaken. As a control, cells transfected with GFP-EBNA1, GFP-EBNA1ΔGA or GFP-FKBP12^{F36V} were also treated with dTAG-13 (**157**) at 5 nM and 500 nM. The treatments of PROTACs were screened at (10 μM, 1 μM and 0.1 μM) and fluorescence was measured at four-time intervals; 12 h, 24 h, 40 h and 60 h.

Of the PROTAC library, 10 potential 'hits' were found in which GFP-EBNA1ΔGA fluorescence had been reduced to ≤ 80%. Interestingly, the fluorescence corresponding to full length GFP-EBNA1 was not affected; a possible result of the proteasomal shielding

from the gly-ala repeat region. Of the 'hit' PROTACs discovered, 3 of those synthesised in this chapter showed > 80% degradation for GFP-EBNA1 Δ GA. These were PROTACs **147**, **149** and **153** (Figure 5.14); members of the Group 2 EBNA1-PROTACs containing longer linkers (9, 11 and 12 atoms respectively).

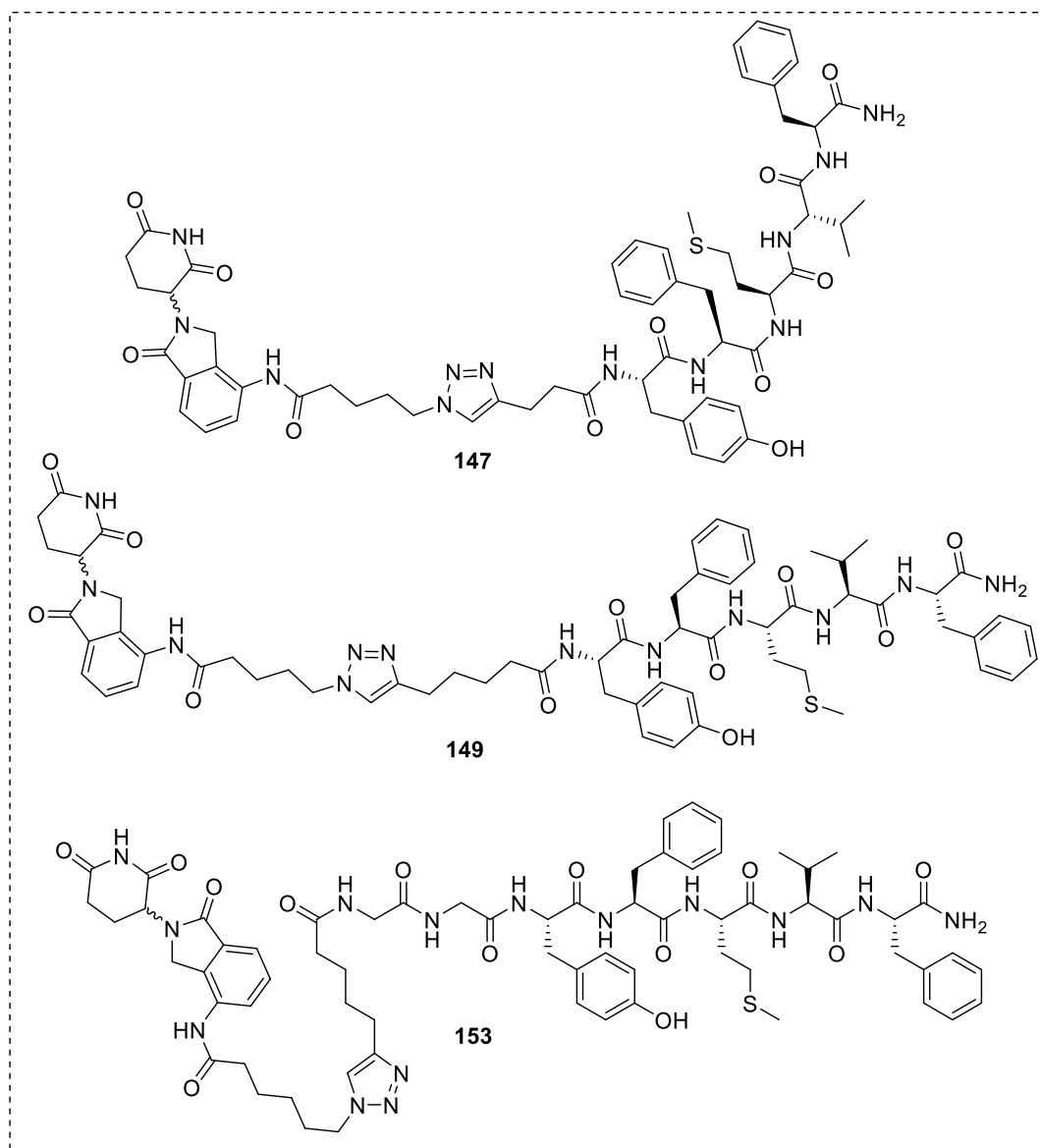


Figure 5.14 Chemical structures of EBNA1-PROTAC 'hits' **147**, **149** and **153** identified in the initial studies.

Interestingly, PROTACs **148** and **150** were not a hits despite containing only 1 atom less or one atom more than PROTAC **149** respectively. However, this pattern was also observed for Brd4-targeting PROTACs in work by Wurz *et al.*, (explained in **Chapter 1**).

Furthermore, **151** contained the same number of carbons as PROTAC **149**, but a different position of the triazole and was not found as a 'hit'. In addition, none of the Group 1 PROTACs were active 'hit's suggesting that they were either too short or too inflexible for effective ternary complex formation.

From these initial results a 1 μM concentration of PROTAC was the most effective, with a lowered change in fluorescence observed when the concentration of each PROTAC treatment was increased to 10 μM (attributed to the Hook effect). Another interesting observation was that the level of GFP-EBNA1 Δ GA was consistent over the four time points. The change of fluorescence for GFP-EBNA1 Δ GA when treated with each of the PROTACs (10 μM) is shown in **Figure 5.15**. The longest PROTAC **153** displayed the largest reduction in GFP-EBNA1 Δ GA fluorescence, producing a reduction of 53% compared to the DMSO only control.

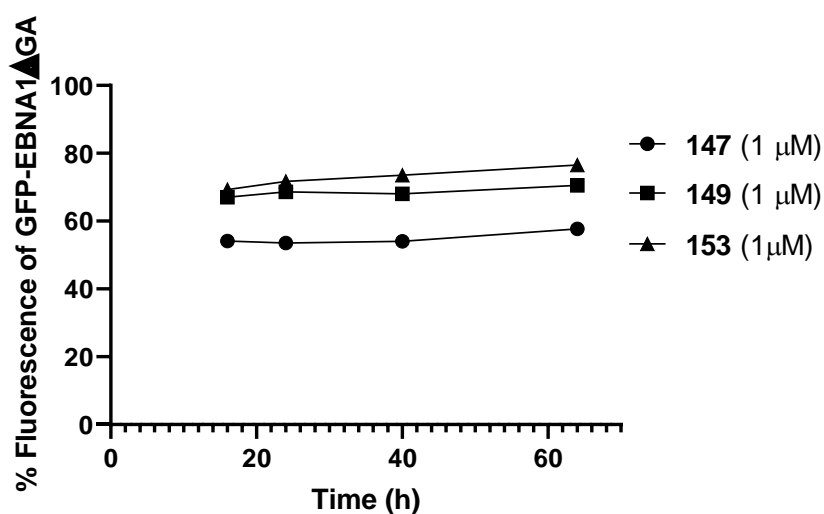


Figure 5.15 Change in fluorescence (%) of GFP-EBNA1 Δ GA (in comparison to the DMSO control) when HEK293 cells were treated with PROTAC **147**, **149** and **153**. This data is representative of technical duplicates and a biological singlet.

The control dTAG (**157**) was also tested and its ability to impact the fluorescence of GFP-FKBP12^{F36V} was determined. As shown in **Figure 5.16**, a steady decrease in fluorescence was observed over the 4 time points, reducing GFP-FKBP12^{F36V} to 50% after 60 h. As expected, dTAG-13 had no effect on GFP-EBNA1 Δ GA or GFP-EBNA1. Although this data

was promising, the results of the assay were unable to be repeated (prior to the submission of this thesis).

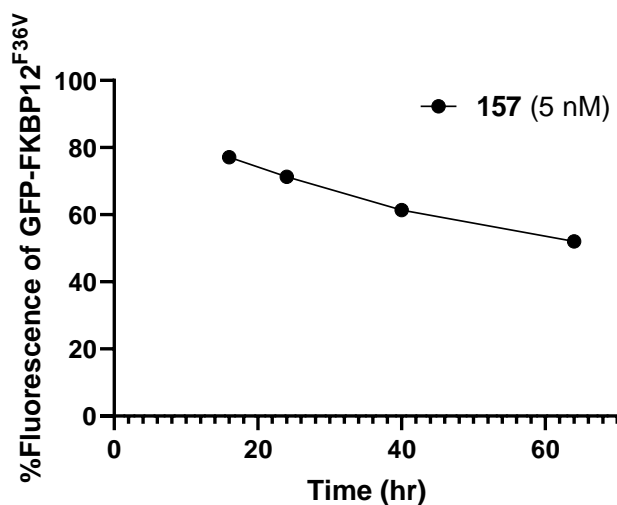


Figure 5.16 Change in fluorescence (%) of GFP-FKBP12^{F36V} (in comparison to the DMSO control) when HEK293 cells were treated with dTAG-13. This data is representative of technical duplicates and a biological singlet.

5.8.2 PROTAC PAMPA

This work was undertaken by Siddique Amin (PhD student) at Newcastle University (UK), Chemistry Department.

As proteasomal degradation takes place intracellularly, it is crucial that PROTACs have sufficient cell permeability to reach this target. To assess this, parallel artificial membrane permeability assays (PAMPA) (**Figure 5.17**), which are an *in-vitro* model of passive transport, were undertaken with all members of the PROTAC library.

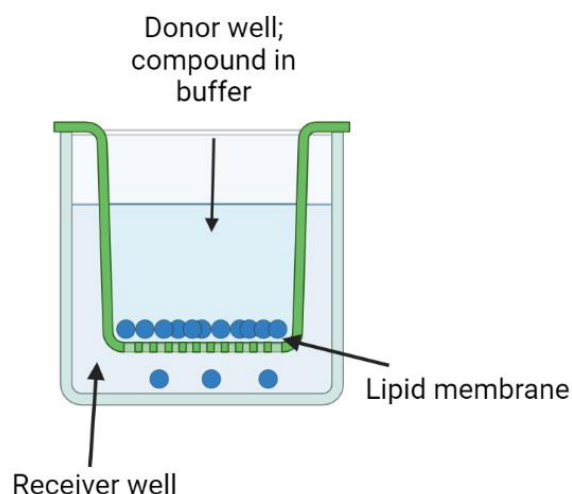


Figure 5.17 Experimental set-up for a PAMPA [Image created using BioRender].

Using this model, none of the PROTACs synthesised in this chapter were able to cross the artificial membrane. In fact, only 2 out of 28 members of the overall PROTAC library (including PROTACs synthesised by Taylor-Newman) were determined to be permeable using the PAMPA. The two PROTACs that were able to cross the lipid membrane were small molecule based PROTACs **157** and **158** that were synthesised by Taylor-Newman (**Figure 5.18**).

This was an interesting result as the lack of cell permeability could hinder the potential of peptide-based EBNA1 PROTACs. Both peptides and PROTACs themselves can suffer from lack of cell permeability as both exist in a chemical space that extends far beyond the RO5.²⁴ However, it is important to note that PAMPA suffers several drawbacks when assessing PROTAC permeability. Firstly, assays of this type do not account for any active transport mechanisms. Secondly, they have shown to be inaccurate for PROTACs in certain cases. For example, in work by Guo *et al.*, PROTAC RC-1 was a potent degrader of BTK in MOLM-14 cells ($DC_{50} = 6.6$ nM) however, when cell permeability was assessed using PAMPA, the PROTAC was unable to cross the membrane.²⁵ In this case, it is clear that PAMPA is not suitable for PROTAC permeability analysis.

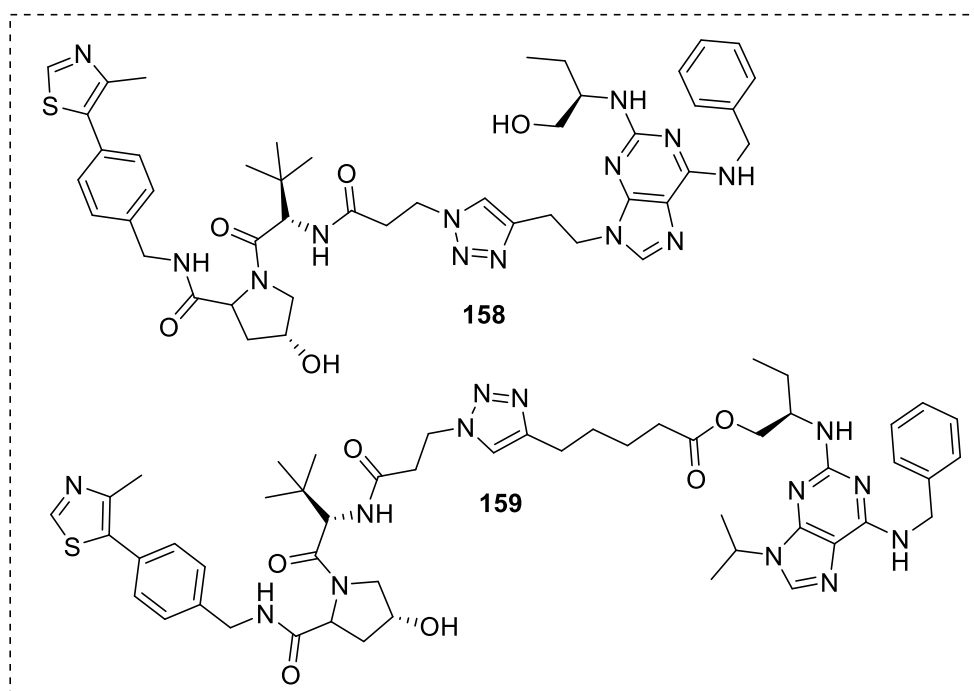


Figure 5.18 Chemical structures of EBNA1-PROTACs **158** and **159** that were permeable using PAMPA (performed by Amin).

5.9 Chapter Summary

In this chapter, a library of 13 PROTACs that utilise an EBNA1 targeting peptide, were successfully synthesised with purity sufficient for biological evaluation. Group 1 PROTACs (**Figure 5.10**) were assembled by solid phase amide bond formation and incorporated shorter length chains. Group 2 consisted of PROTACs assembled by click chemistry and incorporated longer linker lengths (**Figure 5.11**).

This PROTACs synthesised in this work contributed to a larger library of 28 PROTACs that undertook preliminary EBNA1 degradation testing. A novel assay was designed in which the change in fluorescence corresponding to changing levels of EBNA1 could be detected. This assay was validated using a dTAG system, in which dTAG-13 effectively reduced GTP-FKBP12^{F36V} fluorescence. Following this, the change in fluorescence of 28 PROTACs was assessed, in which 10 potential ‘hits’ were discovered. Three of the ‘hits’ were PROTACs synthesised in this chapter, all from Group 2, incorporating longer linkers (**Figure 5.14**). Whilst the initial results were promising, additional experiments (repeats)

could not be carried out prior to submission of the thesis. Additionally, PAMPA indicated a lack of PROTAC permeability which could impact their ability to access the proteasomal machinery within the cell. However, it must be noted that PAMPA does not consider active transport and has in some cases, shown to be insufficient for assessing PROTAC cell permeability. Overall, the work undertaken in this chapter represents a promising starting point for the discovery of EBNA1 degraders and the project is still ongoing within the Cobb group.

5.10 References

1. M. A. Epstein, B. G. Achong and Y. M. Barr, *Lancet.*, 1964, **7335**, 702–703.
2. M. K. Smatti, D. W. Al-Sadeq, N. H. Ali, G. Pintus, H. Abou-Saleh and G. K. Nasrallah, *Front. Oncol.*, 2018, **8**, 1-16.
3. C. Shannon-Lowe, A. B. Rickinson and A. I. Bell., *Phil. Trans. R. Soc. B*, 2017, **372**, 20160271.
4. Z. Y. Su, P. Y. Siak, C. O. Leong and S. C. Cheah, *Front. Microbiol.*, 2023, **14**, 1–17.
5. S. S. Soldan and P. M. Lieberman, *Nat. Rev. Microbiol.*, 2023, **21**, 51–64.
6. J. Dutkiewicz, *Handb. Occup. Saf. Heal.*, 2010, **100**, 385–400.
7. O. A. Odumade, K. A. Hogquist and H. H. Balfour, *Clin. Microbiol. Rev.*, 2011, **24**, 193–209.
8. E. K. J Tanner, J Weis, D Fearon, Y Whang, *Cell Press*, 1987, **2**, 203-213.
9. L. Frappier, *Scientifica (Cairo).*, 2012, **2012**, 1–15.
10. A. Bochkarev, J. A. Barwell, R. A. Pfuetzner, W. Furey, A. M. Edwards, L. Frappier and C. Ln., *Cell*, 1995, **83**, 39–46.
11. Y. Mei, T. E. Messick, J. Dheekollu, H. J. Kim, S. Molugu, L. J. C. Muñoz, V. Moiskeenkova-Bell, K. Murakami and P. M. Lieberman, *J. Virol.*, 2022, **96**, 1-14.
12. J. L. Yates, S. M. Camiolo and J. M. Bashaw, *J. Virol.*, 2000, **74**, 4512–4522.
13. A. Bochkarev, J. A. Barawell, R. A. Pfuetzner, E. Bochkareva, L. Frappier and A. M. Edwards, *Cell*, 1996, **84**, 791–800.
14. G. Coppotelli, N. Mughal and M. G. Masucci, *Biochem. Biophys. Res. Commun.*, 2013, **431**, 706–711.
15. K. Shire, P. Kapoor, K. Jiang, M. N. T. Hing, N. Sivachandran, T. Nguyen and L. Frappier, *J. Virol.*, 2006, **80**, 5261–5272.
16. N. P. Dantuma, S. Heessen, K. Lindsten, M. Jellne and M. G. Masucci, *Proc. Natl. Acad. Sci. U. S. A.*, 2000, **97**, 8381–8385.
17. S. Y. Kim, K. A. Song, E. Kieff and M. S. Kang, *Biochem. Biophys. Res. Commun.*, 2012, **424**, 251–256.
18. L. Jiang, R. Lan, T. Huang, C. F. Chan, H. Li, J. Z. , Sam Lear, W. Y. Wong, M. M. L. Lee, B. D. Chan, W. L. Chan, W. S. Lo, N.K Mak, M. Li Lung, H. L Lung, G. S. Taylor. , S.W. Tsao, Z. X. Bian, W. C. S. Tai, G. L. Law, W. T. Wong, S. L. Cobb. and K.L. Wong., *Nat. Biomed. Eng.*, 2017, **1**, 1–10.

19. M. de Wispelaere, G. Du, K. A. Donovan, T. Zhang, N. A. Eleuteri, J. C. Yuan, J. Kalabathula, R. P. Nowak, E. S. Fischer, N. S. Gray and P. L. Yang, *Nat. Commun.*, 2019, **10**, 3468.
20. S. D. Edmondson, B. Yang and C. Fallan, *Bioorganic Med. Chem. Lett.*, 2019, **29**, 1555–1564.
21. D. Remillard, D. L. Buckley, J. Paulk, G. L. Brien, M. Sonnett, H. S. Seo, S. Dastjerdi, M. Wühr, S. Dhe-Paganon, S. A. Armstrong and J. E. Bradner, *Angew. Chemie - Int. Ed.*, 2017, **56**, 5738–5743.
22. M. Hoffmann, C. Kasserra, J. Reyes, P. Schafer, J. Kosek, L. Capone, A. Parton, H. Kim-Kang, S. Surapaneni and G. Kumar, *Cancer Chemother. Pharmacol.*, 2013, **71**, 489–501.
23. B. Nabet, J. M. Roberts, D. L. Buckley, J. Paulk, S. Dastjerdi, A. Yang, A. L. Leggett, M. A. Erb, M. A. Lawlor, A. Souza, T. G. Scott, S. Vittori, J. A. Perry, J. Qi, G. E. Winter, K. K. Wong, N. S. Gray and J. E. Bradner, *Nat. Chem. Biol.*, 2018, **14**, 431–441.
24. P. Matsson and J. Kihlberg, *J. Med. Chem.*, 2017, **60**, 1662–1664.
25. W. H. Guo, X. Qi, X. Yu, Y. Liu, C. I. Chung, F. Bai, X. Lin, D. Lu, L. Wang, J. Chen, L. H. Su, K. J. Nomie, F. Li, M. C. Wang, X. Shu, J. N. Onuchic, J. A. Woyach, M. L. Wang and J. Wang, *Nat. Commun.*, 2020, **11**, 1–16.

6. Conclusions and future work

The overarching aims of this thesis were to seek new avenues for developing therapeutics that could potentially target the proteins CCL2 and EBNA1, which are associated with autoimmune diseases and cancer. Prior to this work, it had been shown that diketopiperazines (DKPs) could function as inhibitors of CCL2-mediated chemotaxis,¹ therefore it was sought to gain a further understanding of their mode of action and to incorporate these as protein of interest (POI) warheads in CCL2-PROTACs. Secondly, this programme of work sought to incorporate a previously designed pentapeptide,² that could disrupt the dimerization of EBNA1, into PROTACs capable of targeted EBNA1 degradation.

In **Chapter 2** a library of 13 DKPs (**Figure 6.1**) were synthesised based around a core structure that was found previously to be essential for the inhibition of CCL2-mediated chemotaxis (Hudson *et al*).³ In this current work, novel DKPs that incorporated fluorine and/or bulky aromatic substituents, were designed and synthesised to assess this impact on their biological and biophysical properties.

Solid phase peptide synthesis (SPPS) was used to stereoselectively produce 9 DKPs (**Figure 2.12**) in low to moderate yields (13-50%). However, this method was unsuccessful at producing hydroxyl-containing DKPs **29**, **38**, **42** and **67**, or TFP-containing DKPs **43** and **44**, in a sufficient yield and purity. Consequently, the only hydroxyl-containing DKP successfully synthesised by SPPS was DKP **46**, in which the second amino acid added (**AA₂**) was Fmoc-protected. For this reason, a solution phase method was subsequently used for the synthesis of DKP **29** and **38**, as these were to be incorporated into CCL2-targeting PROTACs in later work. However, the solution phase method lacked stereocontrol, with the synthesis of DKPs **29** and **38** also producing diastereoisomers **71** and **70** respectively as the major products (**Section 2.5.7**). However, when a larger scale synthesis of DKP **29** was carried out, the desired product (**29**) was the only isomer

produced. This product was also used as a precursor for the synthesis of TFP-containing DKP **43** and iodinated-DKP **47**, which were both produced to high yields (98 and 94% respectively).

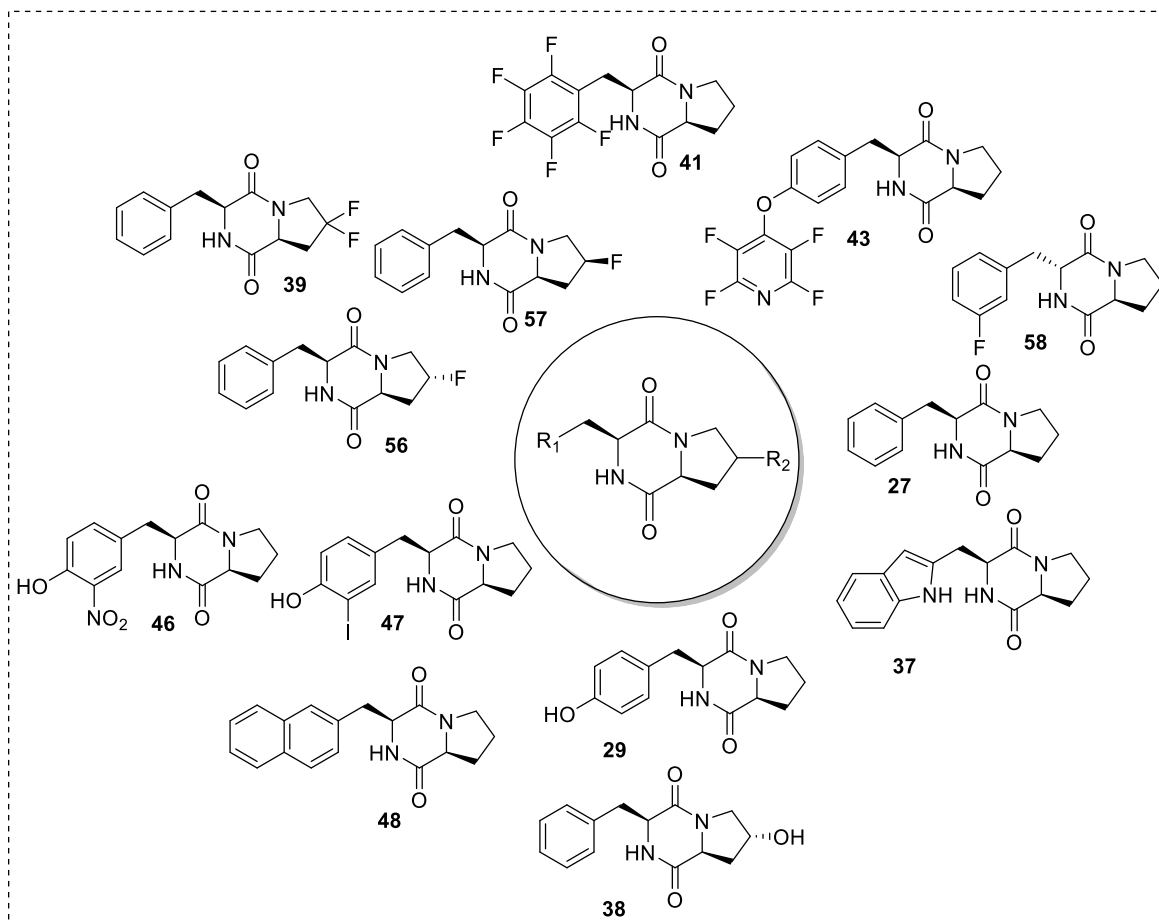


Figure 6.1 Chemical structures of the DKPs synthesised in this work.

Having prepared a series of DKPs (**Figure 6.1**), Boyden chamber assays were used to evaluate them, in addition to previous lead DKP **36**, as inhibitors of CCL2-mediated chemotaxis (at 50 μ M) (shown in **Section 2.6.3**). A modified experimental set-up was used (in comparison to those utilised by Saleki¹ and Hudson³) with three main differences; a reduced concentration of CCL2, a cell detachment solution to remove adhered cells and a cell count produced by flow cytometry. This set-up was validated using known CCR2 antagonist **74**, which was able to reduce THP-1 migration to $39 \pm 9\%$ when screened at its IC_{50} concentration (330 nM).

DKPs **27** and **36** were identified as inhibitors of CCL2-mediated chemotaxis in previous work by the Cobb and Ali groups.¹ When these were retested using Boyden chamber assays, THP-1 chemotaxis was reduced to 73% and 86% respectively; although this was determined to be a statistically insignificant reduction. The results obtained in current work, differed to those obtained previously in which THP-1 migration was reduced to approximately 50% and 75% for DKP **27** and **36** respectively.¹ The discrepancy between results could be attributed to the modified experimental design. Additionally, in work by Hudson, DKPs **37** and **38** were screened for CCL2 chemotaxis inhibitory properties at 100 μ M and were able to reduce THP-1 migration to 35% and 40% respectively. In this current work, both DKPs **37** and **38** were screened at 50 μ M, but no significant reduction in THP-1 migration was observed.

Two novel CCL2-chemotaxis inhibitors that significantly reduced THP-1 migration, were found in this current work. The two fluorinated DKPs **39** and **43** were able to reduce THP-1 migration to $70\% \pm 9\%$ and $51\% \pm 8\%$ respectively and were more potent than the retested leads from previous work (**27** and **36**). In addition, DKP **48** also showed promising inhibitory properties, reducing THP-1 migration to 71% and 72% in two individual repeats. However, there was a lack of consistency between repeats with THP-1 migration reduced to 0% in one experiment. For the most potent DKP (**43**) IC_{50} determination was attempted, however a reduction in THP-1 motility was observed and this prevented its accurate determination. This could have resulted from the high passage number the THP-1 cells had reached or from potential mycoplasma contamination. Future work should look to repeat the chemotaxis assays with fresh THP-1 cells, or cells with lower freeze-thaw cycles and passage numbers. Alternatively, human peripheral blood mononuclear cells (PBMCs) could provide an alternative cell-line, as they are used immediately upon isolation from the donor and are consequently more motile. Although, their incorporation would further complicate the experimental design and analysis techniques.

DKPs **39**, **43** and **48**, that were shown to be the most potent chemotaxis inhibitors in this current work, were subsequently tested in apoptosis assays to evaluate their toxicity to THP-1 cells at 50 μM (**Section 2.6.4**). This was to ensure that the reduction in THP-1 migration in response to these compounds, was not a consequence of cell death. The results shown in **Figure 2.24**, indicated that DKPs **39**, **43** and **48** were non-toxic to THP-1 cells at 50 μM (incubated for 3 h) with no cell death observed as a result of any of the DKP treatments in comparison to the untreated control. Additionally DKP **43** was screened at 100 μM , as it was to be tested at this concentration in subsequent CCR2 internalisation assays. At 100 μM , DKP **43** did not induce significant cell death in comparison to the untreated control (**Figure 2.25**).

As explained in both **Chapter 2** and **Chapter 3**, signalling events, such as pERK1/2 and calcium influx, as well as CCR2 internalisation, are commonly probed pathways to gain a greater understanding of the mode of action of CCR2 antagonists. No change in CCL2 ERK1/2 phosphorylation was observed with DKP **27** and **36** in previous work¹ however, their effect on receptor internalisation had not been investigated. In this current work, the change in surface CCR2 levels were investigated, in response to DKPs only or in co-treatment with CCL2. Changes in CCR2 levels were probed using a CCR2 antibody which measured the shift in median fluorescence intensity (MFI) in response to each treatment (**Section 2.6.5**). The impact on CCR2 internalisation of the most potent inhibitor from this current work (**43**) and previous lead (**27**), was assessed (**Figure 2.25**). It was hypothesised that the DKPs could act in two ways; by inducing internalisation (agonists) or by outcompeting CCL2 and preventing internalisation (antagonists). Neither DKP **27** nor **43** when tested alone, induced a change in MFI. This suggested that they did not induce internalisation; hence are not agonists for this pathway. At the same time, neither of the DKPs disrupted the internalisation of CCR2 when they were co-treated with CCL2. This work showed that DKPs **27** and **43** had no impact on the internalisation mechanism of CCR2 and therefore this was not contributing to the reduced chemotaxis observed in both

this work and previous work. The data gathered suggests that the DKPs are not orthosteric antagonists for CCR2 which reinforced previous work by Klausmeyer *et al.*, in which DKP **28** was unable to outcompete CCL2 in competition binding assays.⁴ In the absence of data showing otherwise, at this stage of the project the working hypothesis remained that DKPs acted as CCL2 ligands.

In **Chapter 3, Section 3.7** his-tagged CCL2 (*hsCCL2*) was successfully produced in a moderate yield, but to a high purity, by recombinant protein overexpression in *E. coli*. In the first protein preparation, 6 litres of culture were purified using Ni-NTA affinity chromatography, followed by ion exchange chromatography (IEX). This route afforded 1.5 mg of *hsCCL2* (**Section 3.7.1**). To increase protein production, overexpression using a Harbinger-LEXTM-48 bioreactor was undertaken. However, this method afforded little improvement on the quantity of protein obtained. In the final preparation on a 6 litre scale, the induction temperature was reduced from 30 °C to 20 °C, in an attempt to increase the solubility of *hsCCL2* (**Section 3.7.3**). Subsequent purification by Ni-NTA, followed by size-exclusion chromatography (SEC), afforded 2 mg of *hsCCL2*. Before the final purification by SEC, the protein had been stored at 4 °C for 3 days, which had caused a precipitate to form. It is likely that some of this precipitate contained denatured *hsCCL2*, therefore future preparations should seek to purify the protein as soon as possible after the initial Ni-NTA chromatography. This would further prevent the risk of protein denaturation. In addition, future work could seek to incorporate a SUMO-tag into the protein construct as these are often incorporated to increase protein expression and solubility in *E. coli*.⁵

A fundamental aim of this research was to assess the ligand binding between the DKP library and CCL2 in an attempt to confirm the working hypothesis with respect to the mode of action. Using SPR assays, the library of DKPs synthesised in **Chapter 2**, alongside previous leads (**27**, **28** and **36**), were screened against immobilised *hsCCL2*. Firstly, a capture-couple method was used for the oriented covalent coupling of *hsCCL2* to a Ni-NTA SPR chip. The sensorgram shown in **Figure 3.16** displays effective immobilisation of

hsCCL2 onto the chip surface (with a final response unit 4799 RU). Following this, each DKP ligand was passed over the immobilised *hsCCL2* surface, in a concentration series of 100 μM , 10 μM , 1 μM and 0.1 μM . However, none of the DKPs showed binding events (change in response unit) at any of the concentrations tested. It was suggested that immobilisation through the N-terminus, could have disrupted the potential CCL2 binding site, consequently limiting CCL2 binding events observed using SPR. To investigate this further, SPR analysis was undertaken with a sample of biotinylated-CCL2 (btnCCL2) which allowed protein immobilisation on to a SA-SPR chip through the C-terminus of the protein. The DKPs were screened at a more comprehensive concentration series of 200 μM , 100 μM , 50 μM , 25 μM , 5 μM and 2.5 μM . However, again no binding events were observed between any members of the DKP library and btnCCL2.

With the biological and biophysical data obtained from **Chapter 2** and **3** respectively, DKPs are unlikely to act as CCL2 binders but could inhibit chemotaxis by allosteric antagonism of CCR2. As discussed in **Chapter 2** and **3**, orthosteric inhibitors (**Figure 3.3 (A)**) out-compete CCL2 binding and inhibit common signalling pathways such as ERK1/2 phosphorylation. However, from the work carried out in this thesis and previous work, in which the DKPs were shown not to inhibit pERK1/2 or CCL2-induced CCR2 internalisation, it is unlikely that they function as orthosteric antagonists. There are another group of antagonists (**Figure 3.3 (B)**) that bind to a well-defined, intracellular allosteric site on CCR2; however, these also disrupt CCL2 binding, by forcing the orthosteric site into a closed conformation. Therefore, it is also unlikely that DKPs act as antagonists of this intracellular site. However, there is a third class of antagonist (**Figure 3.3 (C)**) that binds to an extracellular allosteric site on the extracellular loop. This was the case for peptide-based antagonist ECL1i (**77**) (described in **Chapter 3, Section 3.3**), which was able to inhibit CCL2-mediated chemotaxis, but not downstream signalling events (such as pERK1/2) or CCL2 induced-CCR2 internalisation.⁶ The rationale for this is that ECL1i binds to an (extracellular) allosteric site that locks CCR2 into a conformation that signals

away from chemotaxis but is still intact for other signalling events. As DKPs have thus far shown similar behaviour, it is not unreasonable to hypothesise that they are also acting as allosteric inhibitors by a similar mechanism. As the data indirectly points to this, future work could seek to directly prove this and investigate further the DKP binding site (on CCR2). In work by Auvynet *et al.*,⁶ in which they analyse the pharmacological mechanisms of ECL1i, intracellular ITC was used to show binding to CCR2 (non-competitive). This could be used to elucidate whether the DKPs **39** and **43**, in addition to previous inhibitors **27**, **28** and **36**, do actually bind to CCR2. Additionally, ligand bound co-crystal structures would provide a clearer indication of the DKP-CCR2 binding site but this is likely to be highly challenging to carry out.

Additionally in **Chapter 3**, a library (**Appendix A3**) of novel fluorinated fragments were screened against both *hsCCL2* and *btnCCL2* using SPR assays (**Section 3.9**). The competency of the immobilised *btnCCL2* surface was assessed using known CCL2 binding peptide BK1.3. The K_D obtained for BK1.3 at the start of the SPR experiment was much larger (192 μM) than expected ($EC_{50} \approx 6 \mu\text{M}$ determined by Darlot *et al.*,⁷) which could have been due to a less competent (active) immobilised protein surface. This can be affected by either insufficient protein immobilisation or other factors such as dimerization. Additionally, decay of the immobilised surface was observed with BK1.3, with fragments screened at the end of the SPR assay likely to be affected. Nonetheless, several binding events were detected for members of the fragment library, with promising binders containing the fluoropyridine core **78** and **79**, in addition to fragment **80** (**Figure 6.2**). For example, fragment **80** (**Table 3.1 - Entry 1**) produced binding events when screened against both *btnCCL2* and *hsCCL2*, with a determined K_D of 81.6 μM (*btnCCL2*).

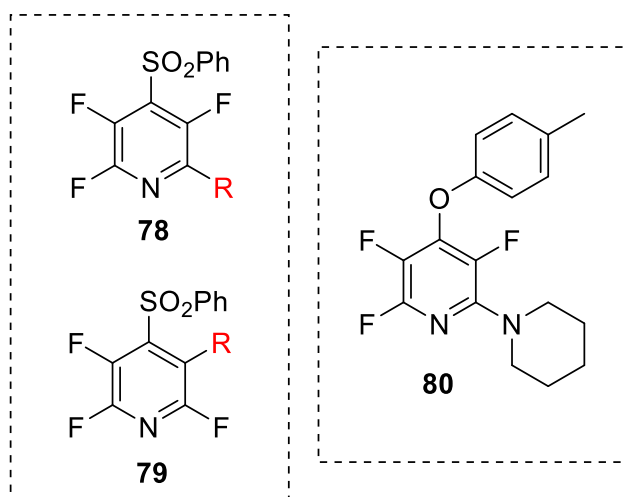


Figure 6.2 Chemical structures of small molecule CCL2 binders **78 - 80**.

This was an exciting discovery as very few small molecule ligands for CCL2 are known (to the knowledge of this author the only other small molecule CCL2 binder is Baicalin – **Section 3.4**). In order to take this work forward, orthogonal assays should be undertaken to further confirm CCL2 binding; especially as the competency of the immobilised surface was unlikely to be 100%. Recently the Pohl and Morris group at Durham University acquired a Dianthus, which measures the change in fluorescence intensity resulting from ligand-protein binding.⁸ A major benefit of this technology is it allows accurate K_D determination with very little quantities of protein (low nanomolar to high picomolar). As this is not an immobilisation technique, future work could seek to use this technology to provide an orthogonal assay to complement the results obtained by SPR and enable accurate binding constants to be determined. Supplementary methods, such as chemotaxis assays or signalling experiments, could also be undertaken to assess their biological potential.

The work in **Chapter 4** was undertaken at a stage in the project where the DKPs inhibitors were still believed (based on the data available at the time) to directly bind to CCL2. Given this, it was hypothesised that the DKPs could be incorporated as the POI warheads in potential CCL2 targeting PROTACs. As the DKPs had shown to selectively target CCL2 (over CCL5 and CCL7) in previous work¹, it was proposed that these could be incorporated

into selective CCL2 PROTACs and provide a more effective route at targeting CCL2 than DKP small molecule inhibitors alone. Three CCL2 targeting PROTACs (**105** – **107**) were designed in which a DKP warhead was connected through either the tyrosine or hydroxyproline, to a flexible (PEG) thalidomide-linker conjugate (**Figure 6.3**).

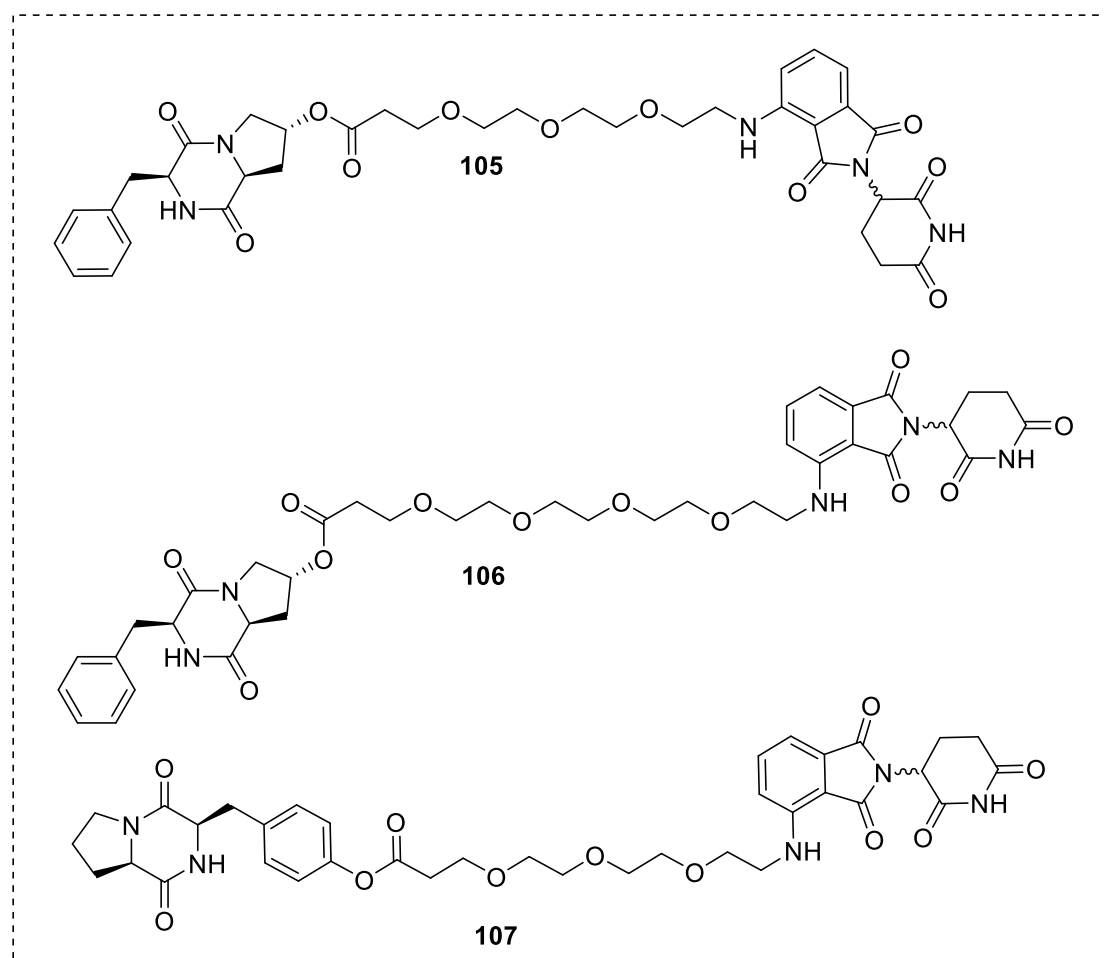


Figure 6.3 Chemical structures of potential CCL2-PROTACs (**105** – **107**) synthesised in this work.

A new assay was designed, in collaboration with the Ali group (Newcastle University), to analyse the CCL2 degradation potential of PROTACs **105** – **107** (Section 4.5.1). In this work, HMEC-1 cells were stimulated with cytokine TNF- α to produce controlled quantities of CCL2. The cells were co-treated with each PROTAC and subsequently incubated for 24 h, after which the secreted media was analysed using an ELISA to determine the CCL2 concentration. A preliminary experiment assessed two PROTAC concentrations: 10 μ M and 0.01 μ M. At 10 μ M, none of the PROTACs induced a reduction in secreted CCL2,

whereas at 0.01 μM a significant reduction was observed with PROTAC **107** (**Figure 4.4**). The lack of activity at 10 μM was attributed to the Hook effect (explained in **Chapter 1**) and therefore further repeats used 0.01 μM of each treatment. However, none of the PROTACs produced a statistically significant reduction in CCL2 (in comparison with stimulated only cells) (**Figure 4.5**) This was attributed to the lack of a consistent trend between repeats which was likely affected by inconsistent levels of stimulated CCL2. SPR analysis of btnCCL2 and the three PROTACs also supported previously obtained data from DKP-CCL2 SPR assays (**Chapter 3**) in which no CCL2 binding was observed.

Aspects of the assay design could be changed to produce more consistent results. For example, removing the additional error involved with the co-treatment of TNF- α by using cells that constitutively produce CCL2 (e.g. breast cancer cells). Additionally, a proteasome inhibitor such as Bortezomib could be incorporated to ensure that any changed levels in CCL2 did result from proteasomal degradation. However, based on the lack of binding inferred from the CCL2 SPR analysis (**Chapter 3**), this project was not taken further with the current DKP incorporating PROTACs (**105 – 107**).

Future work, however, could seek to incorporate the novel CCL2 binding ligands identified (**Chapter 3 – Table 3.1**) into new CCL2-PROTACs. For example, binder **80** has a small molecular weight (322 g/mol) and would enable the design of PROTACs that could fit within the bRO5 region. However, as explained previously, orthogonal biophysical assays would need to be undertaken to support the binding observed. Additionally, further optimisation should be undertaken to improve their binding affinity, as although a transient binding mode is required for PROTAC efficacy, the degrader still needs to effectively recruit the POI. Co-crystal structures or molecular docking could aid the design of new binders (based on those found in this work). This would also aid rational PROTAC design by highlighting solvent exposed regions in which to extend a linker. Alternatively, CCL2 targeting LYTACs could be designed, providing an alternative approach to targeted degradation. As explained in **Chapter 1**, LYTACs are used to pull extracellular targets into

the cell by high-jacking internalisation pathways. The small-molecule CCL2 binders shown in **Chapter 3**, or larger molecules such as peptides (e.g. evasin derived peptide BK1.3), could be used to pull CCL2 from the extracellular region into the cell for degradation.

Finally, the work in **Chapter 5** focused on the synthesis and subsequent biological testing of EBNA1-targeting PROTACs. In this work, 13 PROTACs were synthesised using either microwave assisted amide-coupling (**Figure 5.10**) or 1,2,3-triazole click chemistry (**Figure 5.11**). These incorporated linkers of different length and composition, as well as different points of attachment to the POI warhead. All PROTACs synthesised in **Chapter 5** were CRBN-targeting (by incorporating lenalidomide) and were included into a larger library (synthesised by Cobb group student Eleanor Taylor Newman) of PROTACs for EBNA1 degradation testing.

The 28 PROTAC library was assessed using a GFP-based degradation assay. In this assay, three PROTACs (**147**, **149** and **153**), that were synthesised in this thesis (**Figure 6.4**) were able to reduce the fluorescence of GFP-EBNA1 Δ GA transfected HEK293 cells, < 80%. However, these results were from one biological repeat therefore further testing would be required to reach a conclusion regarding PROTAC efficacy. In addition, ongoing work seeks to supplement this data by testing EBNA1-PROTACs in a more typical degradation assay. For this assay, LCL cells which constitutively express EBNA1, will be treated with each PROTAC. To determine degradation, the subsequent levels of EBNA1 after the PROTAC treatment, will be assessed using a western blot. Furthermore, it would be beneficial to incorporate an inactive, PROTAC control. This involves modifying the E3 ligand to disable E3 recruitment (for analogues of thalidomide this is achieved by imide methylation or the removal of an imide carbonyl group).⁹ The incorporation of this inactive control can help validate the mechanism of action by confirming the involvement of the proteasome in the observed degradation.

This work was part of an on-going collaborative project between the Cobb and Taylor group (University of Birmingham) that will continue to research the potential for EBNA1 proteasomal degradation. Biophysical studies are the main focus of future work, with the overexpression of EBNA1 currently being carried out in the Pohl and Cobb group. Following this, the ternary complex formation of EBNA1-PROTAC-CRBN will be assessed using the newly purchased Dianthus and/or SPR. Obtaining X-ray crystal structures of this ternary complex is an additional aim.

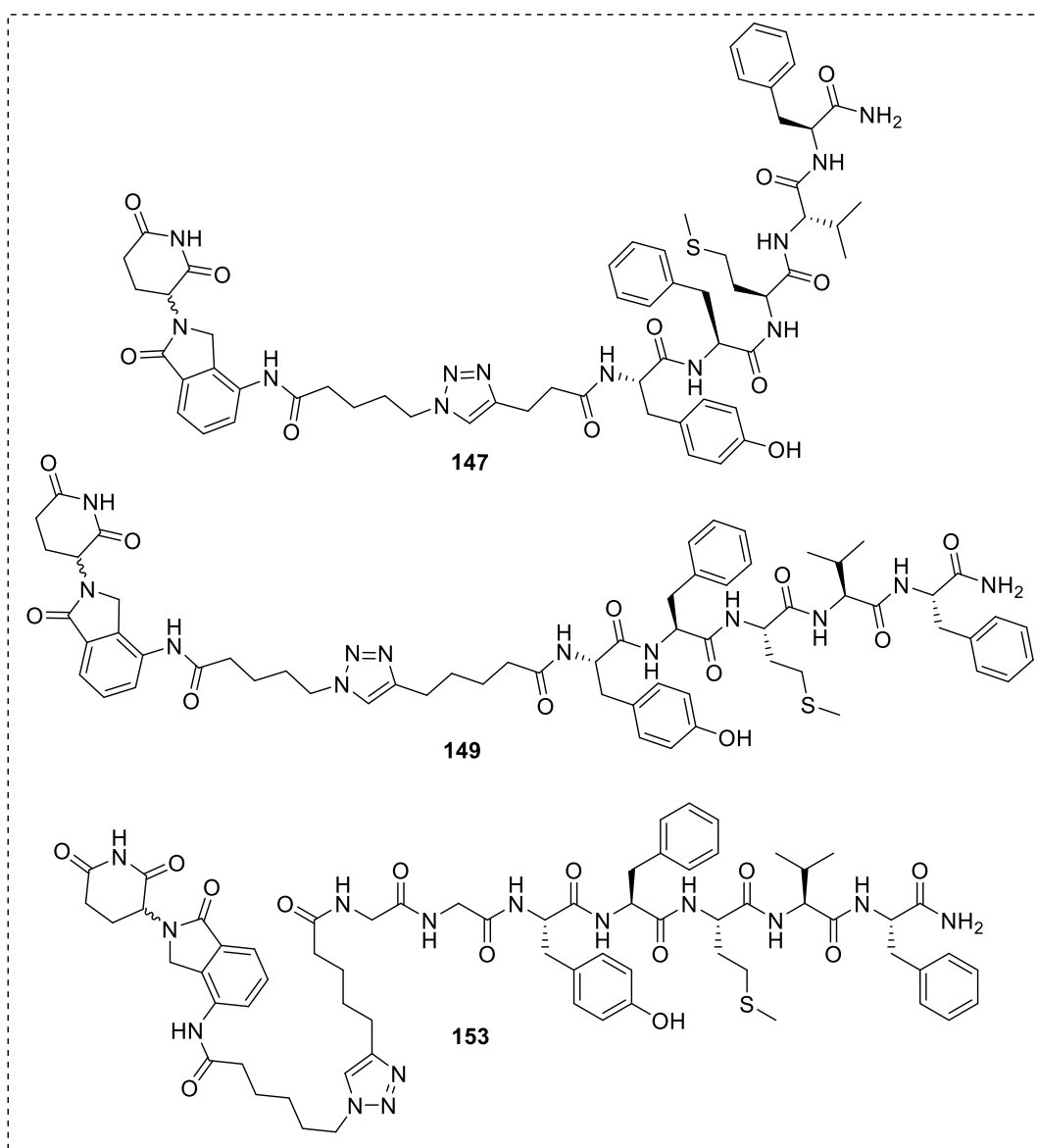


Figure 6.4 Chemical structures of EBNA1-PROTACs **147**, **149** and **153**, that showed promising initial results in EBNA1-degradation assays.

The first aim of this research was to further understand the mode of action of the DKP chemotaxis inhibitors as well as incorporate these as the POI warheads in potential CCL2-PROTACs. A new library of novel DKPs were synthesised in **Chapter 2**, with a new lead inhibitor (**43**) found. This and previous lead **27** were used in CCR2 internalisation assays, to rule out competitive antagonism as the mode of action. SPR assays demonstrated that the DKPS do not to bind directly to CCL2 leading to a new hypothesis that they act as allosteric CCR2 antagonists (**Chapter 3**). In addition, an in-house library of fluorinated fragments were screened in SPR assays which led to the discovery of novel small molecules that had the ability to directly bind CCL2. The DKPs were incorporated into three CCL2-targeting PROTACs (**Chapter 4**) however they showed no statistically significant reduction in CCL2, likely attributed to the lack of binding of the POI warhead (e.g. both the DKPs and the DKP-PROTACs were found not to bind CCL2 using SPR assays). The second key aim of the thesis was to incorporate analogues of pentapeptide YFMVF-NH₂ into potential EBNA1 targeting PROTACs. In **Chapter 5**, 13 PROTACs were successfully synthesised, to a high purity to carry forward for biological analysis. Initial testing has shown promising results with 3 out the of the 13 PROTACs reducing GFP-EBNA1ΔGA fluorescence by > 80%. This is an on-going project in the Cobb group and work towards understanding the biophysical properties of the PROTACs is a key aim.

6.1 References

1. M. Saleki, N. Colgin, J. A. Kirby, S. L. Cobb and S. Ali, *Med Chem Comm.*, 2013, **4**, 860–864.
2. S. Y. Kim, K. A. Song, E. Kieff and M. S. Kang, *Biochem. Biophys. Res. Commun.*, 2012, **424**, 251–256.
3. A. Hudson, PhD Thesis, Durham University, 2015 (available online via Durham University DRO).
4. P. Klausmeyer, O. M. Z. Howard, S. M. Shipley and T. G. McCloud, *J. Nat. Prod.*, 2009, **72**, 1–4.
5. T. R. Butt, S. C. Edavettal, J. P. Hall and M. R. Mattern, *Protein Expr. Purif.*, 2005, **43**, 1–9.
6. C. Auvynet, C. Baudesson De Chanville, P. Hermand, K. Dorgham, C. Piesse, C. Pouchy, L. Carlier, L. Poupel, S. Barthélémy, V. Felouzis, C. Lacombe, S. Sagan, B. Salomon, P. Deterre, F. Sennlaub and C. Combadière, *FASEB J.*, 2016, **30**, 2370–2381.
7. B. Darlot, J. R. O. Eaton, L. Geis-Asteggianti, G. K. Yakala, K. Karuppanan, G. Davies, C. V. Robinson, A. Kawamura and S. Bhattacharya, *J. Biol. Chem.*, 2020, **295**, 10926–10939.
8. C. Schulte, V. Khayenko, N. F. Nordblom, F. Tippel, V. Peck, A. J. Gupta and H. M. Maric, *iScience.*, 2021, **24**, 101898.
9. G. M. Burslem and C. M. Crews, *Cell*, 2020, **181**, 102–114.

7. Experimental

7.1 General procedures

Reactions were carried out in air using non-dried solvents and reagents (unless stated otherwise). Bond Elut (Agilent Technologies) solid phase extraction cartridges (20 mL polypropylene with two polypropylene frits) were used for peptide synthesis. Solvents were removed *in vacuo* using a Büchi Rotavapor R11 or R100. Aqueous solutions were lyophilised using a Christ Alpha 1-2 LD Plus freeze dryer. IR samples were run by Mr Lenny Lauchlan or Dr. Aileen Congreve. All reagents were obtained from commercial sources and used without further purification.

7.1.1 Nuclear Magnetic Resonance (NMR)

¹H NMR spectra were recorded at 400 MHz, 599 MHz or 700 MHz using Bruker Avance III, Varian VNMRS-600 or Varian VNMRS-700 spectrometers respectively. ¹³C NMR spectra were recorded at 101 or 151 MHz using Bruker Avance III or Varian VNMRS-600 spectrometers respectively. Chemical shifts are reported in parts per million (δ ppm) relative to residual solvent peaks; CHCl₃ (δ ¹H 7.26 ppm, δ ¹³C 77.0 ppm), DMSO (δ ¹H 2.50 ppm, δ ¹³C 39.52 ppm) and MeOD (δ ¹H 3.31 ppm, δ ¹³C 49.0 ppm). *J* couplings were measured in Hertz (Hz) and 2D NMR techniques (COSY, HSQC) were used to assign ¹H NMR spectra. Multiplicities are reported as: s = singlet, d = doublet, dd = doublet of doublets, ddd = doublet of doublet of doublets, m = multiplet, t = triplet, q = quartet, br = broad and app t = apparent triplet.

7.1.2 Mass Spectrometry (MS)

Liquid chromatography mass spectra (LCMS) were collected using a Waters SQD mass spectrometer. Samples were injected onto an Acquity UPLC BEH C18 column (1.7 μ m, 2.1 mm x 50 mm) and a linear gradient of 5 – 95 % of solvent B (MeCN) in solvent A (0.1% formic acid in H₂O) was applied at a flow rate of 0.6 ml/min over 3.8 min.

High resolution mass spectra (HRMS) were collected using a Waters QToF premier mass spectrometer. Samples were injected onto a an Acquity UPLC BEH C18 column (1.7 μm , 2.1 mm x 100 mm) and a linear gradient of 0 – 99 % of solvent B (MeCN) in solvent A (0.1 % formic acid in H_2O) was applied at a flow rate of 0.6 ml/min over 5 min.

7.1.3 Analytical HPLC

Analytical HPLC was used for the analysis of sample purity. Samples were dissolved in H_2O : MeCN to approximately 1 mg/mL and 75 μL or 150 μL was injected into a PerkinElmer Series 200 Autosampler onto an X-Bridge C18 column (5.3 μm , 4.6 x 100 mm) attached to a Perkin-Elmer 200 series LC system. A linear gradient of solvent 0 – 100% B (5: 95: 0.03 v/v% H_2O : MeCN: TFA) in solvent A (95: 5: 0.05 v/v% H_2O : MeCN: TFA) was applied at a flow rate of 1 mL/min over 60 min. Absorbance was collected at $\lambda = 220$ nm.

7.1.4 X-Ray Crystallography

DKPs were dissolved in a minimal amount of EtOAc or DCM. Hexane was added dropwise until a turbid solution was formed and this was cleared by adding the polar solvent dropwise. The solutions were left to form crystals by slow evaporation. Sample analysis and refinement were carried out by Dr Dmitri Yufit or Dr Toby J Blundell.

7.2 General procedures (Chapter 2)

7.2.1 Solid phase DKP synthesis

A peptide solution of Boc-protected amino acid (**AA**₁) (3.00 equiv.), DMAP (0.10 equiv.) and DIC (3.00 equiv.) in DCM (3 mL) was added to a preloaded MBHA-linker (**51**) (1.00 equiv.), and agitated at rt for 30 min. The resin was drained, and the coupling procedure was repeated. The resin was washed with DCM (5 x 3 mL) and drained. A deprotection solution of 40% TFA in DCM (3 mL) was added to the resin and agitated at rt for 10 min. The solution was drained, and this was repeated (2 x) before the resin was washed with DCM (5 x 3 mL) and drained. To the resin, a second peptide solution of Boc-protected amino acid (**AA**₂) (3.00 equiv.), DIPEA (5.00 equiv.) and PyBOP (3.00 equiv.) in DCM (3 mL) was added and agitated at rt for 1 h. The resin was drained, and coupling procedure was repeated. The resin was washed with DCM (5 x 3 mL) and if the mixture became difficult to drain, it was washed with DMF (2 x 3 mL) followed by DCM (5 x 3 mL). A deprotection solution of 40% TFA in DCM (3 mL) was added to the resin and agitated at rt for 10 min. The resin was drained and this was repeated (2 x). The resin was then washed with DCM (5 x 3 mL) and drained. Finally, 10% DIPEA in DCM (3 x 3 mL) was added to the resin and agitated at rt for 20 min, drained and collected. This was repeated (2 x). The resin was washed with DCM (2 x 3 mL), drained and collected. The combined filtrates were co-evaporated *in vacuo* with DCM (4 x 15 mL) followed by toluene (3 x 20 mL, 60 °C). The obtained residue was re-dissolved in DCM and 1 M aq. HCl was added until pH 3 was reached. The product was extracted into DCM (3 x 5 mL), dried over MgSO₄, filtered, and concentrated *in vacuo* to afford the DKP products.

7.2.2 Solution phase peptide coupling

OMe-protected amino acid (1.00 equiv.) and Cbz-protected amino acid (1.20 equiv.), HOBt.H₂O (1.50 equiv.), and DIPEA (1.50 equiv.) were stirred in DCM at 0 °C. EDC.HCl (1.50 equiv.) was added portion wise, and the mixture was stirred at rt for 24 h. The mixture

was washed with H₂O (3 x), brine (2 x) and extracted into DCM (2 x). The organic phases were combined and dried over Na₂SO₄, filtered, and concentrated *in vacuo*.

7.2.3 Solution phase DKP formation

CBZ-protected dipeptide (1.00 equiv.) was dissolved in dry MeOH and deoxygenated with N₂/Ar for 60 min. To this solution, 10% Pd/C (0.10 equiv.) was added under an inert atmosphere. NH₄HCO₂ (10.0 eq.) was added portion wise at 0 °C and the mixture was heated at reflux for 5 h. After this, the reaction mixture was cooled to rt, filtered through a bed of celite and washed with MeOH (3 x). The solution was concentrated *in vacuo* and the obtained solid was redissolved in MeOH and stirred under reflux for 24 h. After this time, the solution was concentrated *in vacuo*.

7.2.4 Formation of tetrafluoropyridyl (TFP) ethers

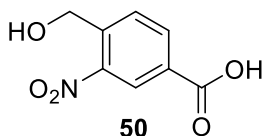
To a stirred solution of alcohol (1.00 equiv.) in MeCN, PFP (1.05 equiv.) and K₂CO₃ (1.05 equiv.) were added. This was stirred at rt for 16 h and after this time, the mixture was filtered, and the solution concentrated *in vacuo*.

7.2.5 Ester hydrolysis

To a solution of methyl ester (1.00 equiv.) in THF:H₂O (50:50 v/v), LiOH.H₂O (1.05 equiv.) was added and stirred at rt for 36 h. The mixture was concentrated *in vacuo* and the residue was acidified to pH 4 with citric acid (10% w/v), extracted into EtOAc (3 x), dried over MgSO₄ and concentrated *in vacuo*.

7.3 Chemical synthesis (Chapter 2)

7.3.1 Synthesis of 4-(hydroxymethyl)-3-nitrobenzoic acid (50)



4-Bromomethyl-3-nitrobenzoic acid (**49**) (2.75 g, 10.6 mmol, 1.00 equiv.) was dissolved in aq. NaHCO₃ (50%, 150 mL) and stirred under reflux for 2.5 h. The solution was filtered hot with water (50 mL) and acidified to pH 1 with 1 M aq. HCl (150 mL). The solution was

extracted into EtOAc (3 x 60 mL), and the organic fractions were combined. This was dried over MgSO₄, filtered, and concentrated *in vacuo*. Residual EtOAc was then co-evaporated with DCM (2 x 25 mL) to afford **50** as an orange solid (1.72 g, 83%).

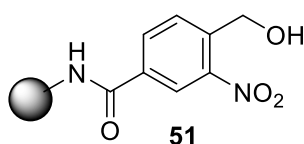
¹H NMR (400 MHz, MeOD) δ 5.00 (2H, s, CH₂), 7.99 (1H, d, *J* = 8.1 Hz, ArH), 8.30 (1H, dd, *J* = 8.1, 1.7 Hz, ArH), 8.61 (1H, d, *J* = 1.7 Hz, ArH).

¹³C NMR (101 MHz, MeOD) δ 60.5, 125.2, 128.4, 130.8, 133.8, 142.6, 147.1, 166.1.

m/z (ESI⁻) 196.1 [M-H]⁻

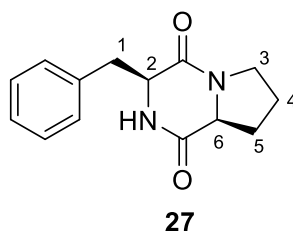
Physical and spectroscopic data obtained was consistent with the literature.¹

7.3.2 Synthesis of activated linker **51**



Rink amide-MHBA (4-Methylbenzhydrylamine hydrochloride) LL (low-loading) resin (**51**) was firstly swollen by agitation in DCM (3 mL) for 30 min. Acid **50** (5.00 equiv.) and DIC (5.00 equiv.) in DCM was added to the resin (1.00 equiv.) and agitated at rt for 18 h. The resin was washed with DCM (5 x 3 mL) before draining.

7.3.3 Synthesis of Cyclo (L-Phe-L-Pro) (**27**)



General procedure **7.2.1** was followed on a 0.20 mmol scale with Boc-Pro-OH (**AA₁**) and Boc-Phe-OH (**AA₂**). The crude was purified using an automated column chromatography CombiFlash (DCM: MeOH, 100:0 – 90:10) to afford DKP **27** as a pale-yellow solid (18.1 mg, 37%).

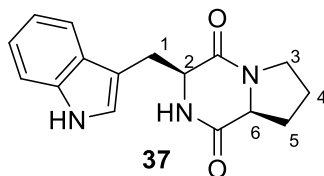
^1H NMR (599 MHz, CDCl_3) δ 1.81 – 1.92 (2H, m, H_4), 2.00 – 2.10 (1H, m, H_5), 2.31 – 2.39 (1H, m, H_5), 2.79 (1H, dd, $J = 14.5, 10.8$ Hz, H_1), 3.55 – 3.60 (1H, m, H_1), 3.60 – 3.64 (1H, m, H_3), 3.64 – 3.69 (1H, m, H_3), 4.10 (1H, t, $J = 7.6$ Hz, H_6), 4.27 (1H, dd, $J = 10.5, 2.8$ Hz, H_2), 5.65 (1H, br s, NH), 7.22 – 7.40 (5H, m, ArH).

^{13}C NMR (151 MHz, CDCl_3) δ 22.6, 28.4, 36.8, 45.5, 56.2, 59.1, 127.6, 129.1, 129.3, 135.9, 165.1, 169.5.

HRMS m/z (ESI $^+$) 245.1273 ($[\text{M}+\text{H}]^+$ $\text{C}_{14}\text{H}_{17}\text{N}_2\text{O}_2$ requires 245.1290).

Physical and spectroscopic data obtained was consistent with the literature.²

7.3.4 Synthesis of Cyclo(L-Trp-L-Pro) (**37**)



General procedure **7.2.1** was followed on a 0.20 mmol scale using Boc-Pro-OH (**AA**₁) and Boc-Trp-OH (**AA**₂). The crude was purified by column chromatography (DCM: MeOH, 100:0 – 97:3) to afford DKP **37** as an off-white solid (10.0 mg, 17%).

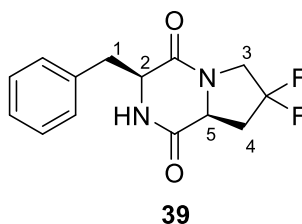
^1H NMR (400 MHz, CDCl_3) δ 1.79 – 1.99 (1H, m, H_5), 1.99 – 2.12 (2H, m, $\text{H}_5 + \text{H}_4$), 2.26 – 2.41 (1H, m, H_4), 2.99 (1H, dd, $J = 15.1, 10.8$ Hz, H_1), 3.57 – 3.73 (2H, m, H_3), 3.77 (1H, dd, $J = 15.0, 3.8$ Hz, H_1), 4.06 – 4.12 (1H, m, H_6), 4.37 – 4.40 (1H, m, H_2), 5.78 (1H, br s, NH), 7.15 – 7.05 (1H, m, ArH), 7.17 (1H, ddd, $J = 8.1, 7.1, 1.1$ Hz, ArH), 7.26 (1H, ddd, $J = 8.2, 7.0, 1.1$ Hz, ArH), 7.33 – 7.45 (1H, m, ArH), 7.48 – 7.60 (1H, m, ArH), 8.34 (1H, s, NH).

^{13}C NMR (101 MHz, CDCl_3) δ 22.6, 26.9, 28.3, 45.4, 54.6, 59.3, 109.9, 111.6, 118.5, 120.0, 122.8, 123.4, 126.7, 136.7, 165.6, 169.4.

HRMS m/z (ESI $^+$) 284.1381 ($[\text{M}+\text{H}]^+$ $\text{C}_{16}\text{H}_{18}\text{N}_3\text{O}_2$ requires 284.1399).

Physical and spectroscopic data obtained was consistent with the literature.²

7.3.5 Synthesis of Cyclo(L-Dfp-L-Phe) (**39**)



General procedure **7.2.1** was followed on a 0.20 mmol scale using Boc-Dfp-OH (**AA₁**) and Boc-Phe-OH (**AA₂**). The crude was purified by prep-TLC (DCM:MeOH, 95:5) to afford DKP **39** as a white solid (25.0 mg, 45%).

¹H NMR (599 MHz, CDCl₃) δ 2.45 – 2.56 (1H, m, H₄), 2.72 (1H, tdd, *J* = 14.0, 7.2, 3.2, Hz, H₄), 2.82 (1H, dd, *J* = 14.5, 10.3 Hz, H₁), 3.58 (1H, dd, *J* = 14.5, 3.8 Hz, H₁), 3.78 – 3.86 (1H, m, H₃), 4.03 (1H, ddd, *J* = 18.4, 13.6, 10.2 Hz, H₃), 4.26 – 4.31 (1H, m, H₂), 4.38 – 4.42 (1H, m, H₅), 5.70 (1H, s, NH), 7.21 (2H, dd, *J* = 7.3, 1.7 Hz, ArH), 7.28 – 7.33 (1H, m, ArH), 7.33 – 7.38 (2H, m, ArH).

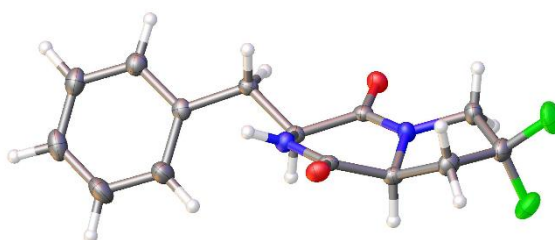
¹³C NMR (151 MHz, CDCl₃) δ 36.9, 37.6 (t, *J* = 25.6 Hz), 52.2 (t, *J* = 33.2 Hz), 55.7, 57.1 (d, *J* = 6.2), 125.4 (dd, *J* = 252.3, 245.4 Hz), 127.8, 129.1, 129.4, 135.2, 165.0, 167.0.

¹⁹F NMR (376 MHz, CDCl₃) δ -93.54 – -95.01 (1F, m), -102.88 (1F, dtdd, *J* = 237.4, 10.6, 6.0, 3.4 Hz)

¹⁹F{¹H} NMR (376 MHz, CDCl₃) δ -94.09 (1F, d, *J* = 238.2 Hz), -102.91 (1F, d, *J* = 238.2 Hz).

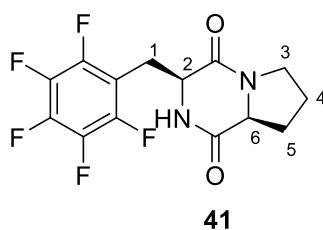
HRMS *m/z* (ESI⁺) 281.1096 ([M+H]⁺ C₁₄H₁₅F₂N₂O₂ requires 281.1102).

IR *V*_{max} (solid) / cm⁻¹ 1126 (s, C-F), 1641 (s, C=O), 2924 (w, C-H), 3207 (m, N-H).



Molecular structure showing 50% probability anisotropic displacement ellipsoids.

7.3.6 Synthesis of Cyclo(L-Pfp-L-Pro) (**41**)



General procedure **7.2.1** was followed on a 0.20 mmol scale using Boc-Pro-OH (**AA**₁) and Boc-Pfp-OH (**AA**₂). The crude was purified by prep-TLC (DCM:MeOH, 95:5) to afford DKP **41** as a white solid (8.50 mg, 13%).

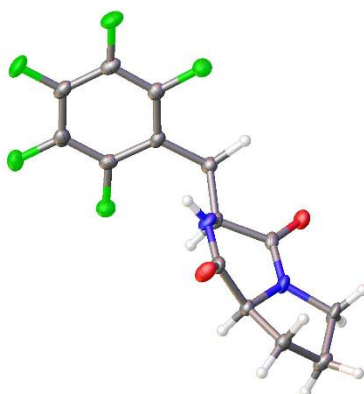
¹H NMR (599 MHz, CDCl₃) δ 1.85 – 1.95 (1H, m, H₄), 1.99 – 2.12 (2H, m, H₄, H₅), 2.23 – 2.33 (1H, m, H₅), 3.01 (1H, dd, *J* = 14.9, 9.8 Hz, H₁), 3.48 – 3.68 (3H, m, H₁, H₃), 4.04 (1H, t, *J* = 8.1 Hz, H₆), 4.33 (1H, dd, *J* = 9.8, 4.7 Hz, H₂), 6.71 (1H, s, NH).

¹³C NMR (151 MHz, CDCl₃) 22.7, 24.0, 28.1, 45.6, 54.0, 59.1, 109.8 – 110.21 (m), 135.9 – 138.6 (m), 140.0 – 141.7 (m), 144.3 – 147.1 (m), 164.3, 170.3.

¹⁹F NMR (376 MHz, CDCl₃) δ -141.25 – -141.45 (1F, m), -155.00 (1F, m), -161.06 – -161.92 (1F, m).

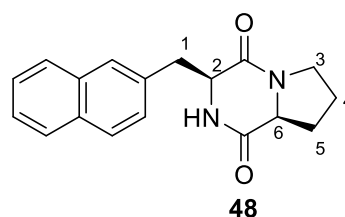
HRMS *m/z* (ESI⁺) 355.0809 ([M+H]⁺ C₁₄H₁₂F₅N₂O₂ requires 355.0819).

IR *V*_{max} (solid) / cm⁻¹ 1505 (s, C-F), 1664 (s, C=O), 2897 (w, C-H), 3211 (m, N-H).



Molecular structure showing 50% probability anisotropic displacement ellipsoids.

7.3.7 Synthesis of Cyclo(L-Phe-L-Nal) (48)



General procedure **7.2.1** was followed on a 0.20 mmol scale using Boc-2-Nal-OH (**AA**₁) and Boc-Phe-OH (**AA**₂). The crude was purified by prep-TLC (DCM:MeOH, 95:5) to afford DKP **48** as a white solid (16.3 mg, 27%).

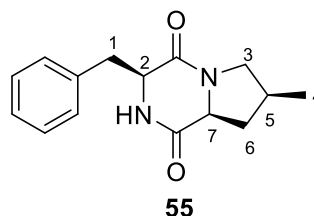
¹H NMR (599 MHz, CDCl₃) δ 1.76 – 1.87 (1H, m, H₄), 1.88 – 2.03 (2H, m, H₄, H₅), 2.19 – 2.34 (1H, m, H₅), 2.88 (1H, dd, *J* = 14.5, 10.6 Hz, H₁), 3.56 – 3.70 (2H, m, H₃), 3.71 (1H, dd, *J* = 14.5, 3.8 Hz, H₁), 4.00 (1H, app t, *J* = 7.3 Hz, H₆), 4.35 – 4.40 (1H, m, H₂), 5.65 (1H, s, NH), 7.27 (1H, dd, *J* = 8.4, 1.8 Hz, ArH), 7.36 – 7.49 (2H, m, ArH), 7.60 (1H, d, *J* = 1.8 Hz, ArH), 7.68 – 7.81 (1H, m, ArH), 7.82 – 7.86 (2H, m, ArH).

¹³C NMR (176 MHz, CDCl₃) δ 22.6, 28.3, 37.0, 45.5, 56.0, 59.2, 126.2, 126.6, 126.6, 127.6, 127.7, 128.1, 129.2, 132.7, 133.4, 133.6, 165.1, 169.4.

HRMS *m/z* (ESI⁺) 295.1447 ([M+H]⁺ C₁₈H₁₉N₂O₂ requires 295.1451).

IR *V*_{max} (solid) / cm⁻¹ 1680 (s, C=O), 2985 (m, C-H), 3202 (m, N-H).

7.3.8 Synthesis of Cyclo(L-4-Mep-L-Phe) (55)



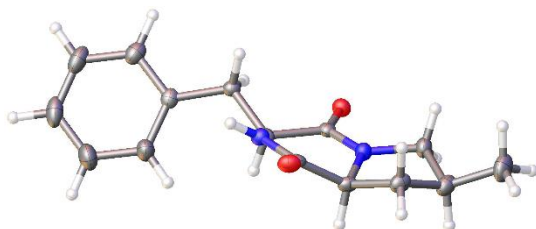
General procedure **7.2.1** was followed on a 0.20 mmol scale using Boc-4-Mep-OH (**AA**₁) and Boc-Phe-OH (**AA**₂). The crude was purified by prep-TLC (DCM:MeOH, 95:5) to afford DKP **55** as a white solid (11.1 mg, 24%).

^1H NMR (599 MHz, CDCl_3) δ 1.13 (3H, d, $J = 6.3$ Hz, H_4), 1.62 – 1.75 (1H, m, H_6), 2.26 – 2.47 (2H, m, H_5 , H_6), 2.79 (1H, dd, $J = 14.5$, 10.6 Hz, H_1), 3.05 – 3.19 (1H, m, H_3), 3.62 (1H, dd, $J = 14.5$, 3.7 Hz, H_1), 3.71 – 3.81 (1H, m, H_3), 4.06 – 4.10 (1H, m, H_7), 4.19 (1H, dd, $J = 10.6$, 3.7 Hz, H_2), 5.54 (1H, s, NH), 7.16 (2H, dd, $J = 7.1$, 1.7 Hz, ArH), 7.20 – 7.25 (2H, m, ArH), 7.25 – 7.31 (2H, m, ArH).

^{13}C NMR (151 MHz, CDCl_3) δ 17.7, 31.3, 36.5, 36.7, 52.3, 56.0, 59.7, 127.6, 129.1, 129.3, 136.0, 165.0, 169.5.

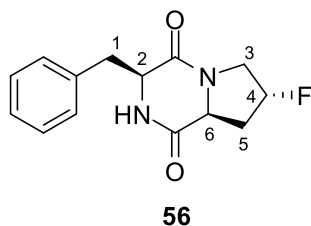
HRMS m/z (ESI $^+$) 259.1447 ($[\text{M}+\text{H}]^+$ $\text{C}_{15}\text{H}_{18}\text{N}_2\text{O}_2$ requires 259.1459).

IR V_{max} (solid) / cm^{-1} 1626 (s, C=O), 2871 (m, C-H), 2962 (m, C-H), 3253 (m, N-H).



Molecular structure showing 50% probability anisotropic displacement ellipsoids.

7.3.9 Synthesis of Cyclo(L-flp-L-Phe) (**56**)



General procedure **7.2.1** was followed on a 0.10 mmol scale using Boc-flp-OH (**AA**₁) and Boc-Phe-OH (**AA**₂). The crude was purified by column chromatography (DCM: MeOH, 100:0 – 97:3) to afford DKP **56** as a white solid (10.0 mg, 34%).

^1H NMR (599 MHz, CDCl_3) δ 2.54 (1H, dddd, $J = 33.0$, 15.1, 10.2, 4.9 Hz, H_5), 2.82 (1H, dd, $J = 14.6$, 10.8 Hz, H_1), 2.84 – 2.94 (1H, m, H_5), 3.43 (1H, ddd, $J = 33.0$, 12.1, 3.7 Hz, H_3), 3.67 (1H, dd, $J = 14.6$, 3.8 Hz, H_1), 4.23 (1H, dd, $J = 12.1$, 4.7 Hz, H_3), 4.29 – 4.43

(2H, m, H₆, H₂), 5.12 – 5.31 (1H, m, H₄), 5.69 (1H, s, NH), 7.21 – 7.24 (2H, m, ArH), 7.26 – 7.31 (1H, m, ArH), 7.32 – 7.38 (2H, m, ArH).

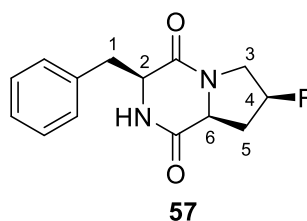
¹³C NMR (151 MHz, CDCl₃) δ 34.5 (d, *J* = 23.3 Hz), 36.3, 52.3 (d, *J* = 24.5), 56.0, 57.0, 89.8 (d, *J* = 180.5), 127.7, 129.1, 129.4, 135.7, 165.5, 168.8.

¹⁹F NMR (376 MHz, CDCl₃) δ -176.90 – -176.41 (1F, m).

¹⁹F{¹H} NMR (376 MHz, CDCl₃) δ -176.65 (1F, s)

HRMS *m/z* (ESI⁺) 263.1167 ([M+H]⁺ C₁₄H₁₆FN₂O₂ requires 263.1196).

7.3.10 Synthesis of Cyclo(L-Flp-L-Phe) (**57**)



General procedure **7.2.1** was followed on a 0.20 mmol scale using Boc-Flp-OH (**AA**₁) and Boc-Phe-OH (**AA**₂). The crude was purified by prep-TLC (DCM:MeOH, 95:5) to afford DKP **57** as a white solid (17.4 mg, 33%).

¹H NMR (599 MHz, CDCl₃) δ (1H, dddd, *J* = 41.4, 15.3, 11.5, 3.7 Hz, H₅), 2.64 (1H, td, *J* = 15.3, 6.2 Hz, H₅), 2.78 (1H, dd, *J* = 14.5, 10.5 Hz, H₁), 3.60 (1H, dd, *J* = 14.5, 3.9 Hz, 1H, H₁), 3.76 – 3.91 (2H, m, H₃), 4.32 (1H, dd, *J* = 10.5, 3.9 Hz, H₂), 4.41 (1H, dd, *J* = 11.5, 6.2 Hz, H₆), 5.29 (1H, dd, *J* = 51.9, 3.6 Hz, H₄), 5.69 (1H, s, NH), 7.20 – 7.23 (2H, m, ArH), 7.27 – 7.30 (1H, m, ArH), 7.33 – 7.37 (2H, m, ArH).

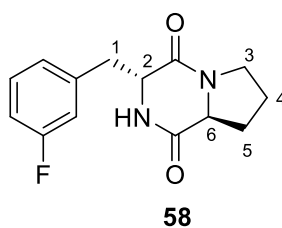
¹³C NMR (151 MHz, CDCl₃) δ 35.9 (d, *J* = 21.4 Hz), 36.7, 52.6 (d, *J* = 24.6 Hz), 56.1, 57.2, 90.1 (d, *J* = 176.7 Hz), 127.7, 129.1, 129.3, 135.6, 165.0, 168.7.

HRMS *m/z* (ESI⁺) 263.1194 ([M+H]⁺ C₁₄H₁₆FN₂O₂ requires 263.1196).

¹⁹F NMR (376 MHz, CDCl₃) δ -172.93 – -174.76 (1F, m).

$^{19}\text{F}\{\text{H}\}$ NMR (376 MHz, CDCl_3) δ -173.84 (1F, s).

7.3.11 Synthesis of Cyclo(d-3F-Phe-L-Pro) (58)



General procedure **7.2.1** was followed on a 0.20 mmol scale using Boc-Pro-OH (**AA**₁) and Boc-3F-d-Phe-OH (**AA**₂). The crude was purified by prep-TLC (DCM:MeOH, 95:5) to afford DKP **58** as a white solid (17.7 mg, 34 %).

^1H NMR (700 MHz, CDCl_3) δ 1.63 – 1.70 (1H, m, H₄), 1.71 – 1.78 (1H, m, H₅), 1.87 – 1.92 (1H, m, H₄), 2.12 – 2.17 (1H, m, H₅), 2.96 – 3.10 (3H, m, H₁, H₆), 3.35 (1H, ddd, $J = 12.2, 9.4, 2.9$ Hz, H₃), 3.51 – 3.61 (1H, m, H₃), 4.09 – 4.19 (1H, m, H₂), 6.73 – 7.00 (4H, m, ArH, NH), 7.18 – 7.29 (1H, m, ArH).

^{13}C NMR (176 MHz, CDCl_3) δ 20.7, 28.0, 39.1, 44.2, 56.8, 57.7, 113.42 (d, $J = 20.9$), 115.8 (d, $J = 21.1$ Hz), 124.6 (d, $J = 2.9$ Hz), 129.2 (d, $J = 8.3$ Hz), 136.9 (d, $J = 7.3$ Hz), 161.8 (d, $J = 247.2$ Hz), 163.6, 168.3.

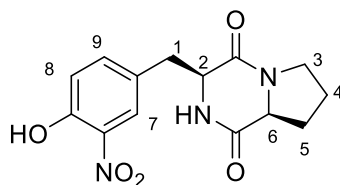
^{19}F NMR (376 MHz, CDCl_3) -112.23 – -112.33 (1F, m).

$^{19}\text{F}\{\text{H}\}$ NMR (376 MHz, CDCl_3) δ -112.27 (1F, s).

HRMS m/z (ESI⁺) 263.1204 ($[\text{M}+\text{H}]^+$ C₁₄H₁₆FN₂O₂ requires 263.1196) .

Molecular structure showing 50% probability anisotropic displacement ellipsoids.

7.3.12 Synthesis of Cyclo(L-Tyr(3-NO₂)-L-Pro) (**47**)



47

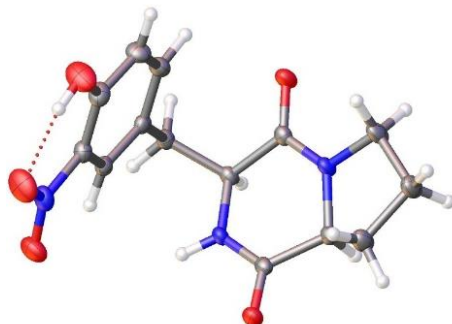
A peptide solution of Boc-Pro-OH (0.60 mmol, 3.00 equiv.) (**AA₁**), DMAP (0.02 mmol, 0.10 equiv.) and DIC (0.60 mmol, 3.00 equiv.) in DCM (3 mL) was added to a preloaded MBHA-linker (**51**) (0.20 mmol, 1.00 equiv.). This was agitated at rt for 30 min before the resin was drained, and the coupling procedure was repeated. The resin was washed with DCM (5 x 3 mL) and drained. A deprotection solution of 40% TFA in DCM (3 mL) was added to the resin and agitated at rt for 10 min. The solution was drained, and this was repeated (2 x). The resin was then washed with DCM (5 x 3 mL) and drained. To the resin, a second peptide solution of Fmoc-Tyr(3-NO₂)-OH (**AA₂**) (0.60 mmol, 3.00 equiv.), DIPEA (1.00 mmol, 5.00 equiv.) and PyBOP (0.60 mmol, 3.00 equiv.) in DCM (3 mL) was added. This was agitated at rt for 1 h before the resin was drained and the coupling procedure was repeated. The resin was washed with DCM (5 x 3 mL) followed by DMF (3 x 3 mL). A deprotection solution of 20% piperidine in DMF (3 mL) was then added to the resin and it was agitated at rt for 20 min, drained and collected. This was repeated (2 x). The resin was washed with DMF (3 mL) and the combined filtrates were co-evaporated with toluene at 60 °C. The obtained residue was purified by automated column chromatography CombiFlash (Hexane:EtOAc, 100:0 – 0:100) followed by prep-TLC (DCM:MeOH, 95:5) to afford **47** as a yellow solid (26.0 mg, 43%).

¹H NMR (599 MHz, CDCl₃) 1.82 – 2.06 (3H, m, H₄, H₅), 2.25 – 2.37 (1H, m, H₅), 3.08 (1H, dd, *J* = 14.7, 7.3 Hz, H₁), 3.35 (1H, dd, *J* = 14.7, 4.5 Hz, H₁), 3.49 – 3.65 (2H, m, H₃), 4.04 – 4.11 (1H, m, H₆), 4.28 – 4.33 (1H, m, H₂), 6.98 (1H, s, NH), 7.08 (1H, dd, *J* = 8.7, 0.8 Hz, H₈), 7.53 (1H, dd, *J* = 8.7, 2.2 Hz, H₉), 7.98 (1H, d, *J* = 2.2 Hz, H₇), 10.46 (1H, s, 1H, OH).

^{13}C NMR (151 MHz, CDCl_3) δ 22.5, 28.3, 35.0, 45.4, 56.0, 59.1, 120.4, 125.7, 128.4, 133.2, 139.1, 154.2, 164.4, 170.2.

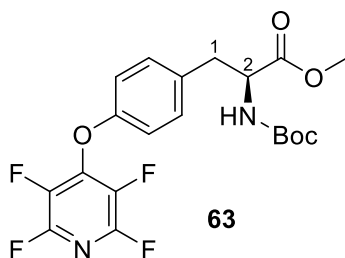
HRMS m/z (ESI $^+$) 306.1089 ($[\text{M}+\text{H}]^+$ $\text{C}_{14}\text{H}_{16}\text{N}_3\text{O}_5$ requires 306.1090).

Physical and spectroscopic data obtained was consistent with the literature.³



Molecular structure showing 50% probability anisotropic displacement ellipsoids.

7.3.13 Synthesis of Boc-TFP-Tyr-OMe (**63**)



General procedure **7.2.4** was followed using Boc-Tyr-OMe (4.00 g, 13.5 mmol, 1.00 equiv.). This afforded **63** as a white solid (5.64 g, 94%).

^1H NMR (599 MHz, CDCl_3) δ 1.43 (9H, s, *tert*-butyl), 3.10 (2H, m, H_1), 3.73 (3H, s, OMe), 4.57 – 4.64 (1H, m, H_2), 5.04 (1H, d, $J = 8.3$ Hz, NH), 7.01 (2H, d, $J = 8.6$ Hz, ArH), 7.17 (2H, d, $J = 8.7$ Hz, ArH).

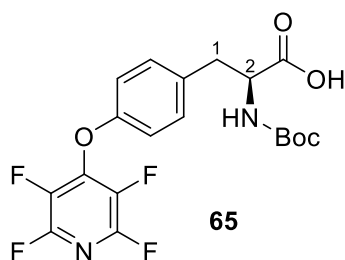
^{13}C NMR (151 MHz, CDCl_3) δ 28.3, 37.8, 52.3, 54.4, 80.1, 116.8, 131.0, 133.2, 134.3 – 138.3 (m), 141.7 – 146.3 (m), 144.1 – 144.6 (m), 154.8, 154.9, 172.1.

^{19}F NMR (376 MHz, CDCl_3) δ -83.46 – -91.87 (2F, m), -152.02 – -160.81 (2F, m).

IR V_{max} (solid) / cm^{-1} 972 (s, C-F), 1068 (s, C-F), 1505 (s, C-F), 1694 (s, C=O), 3000 (m, C-H), 3340 (m, N-H).

Physical and spectroscopic data obtained was consistent with the literature.⁴

7.3.14 Synthesis of Boc-TFP-Tyr-OH (**65**)



General procedure **7.2.5** was followed with Boc-TFP-Tyr-OMe (**63**) (2.00 g, 4.50 mmol, 1.00 equiv.) and LiOH.H₂O (0.19 g, 45.0 mmol, 1.00 equiv.) to afford acid **65** as a white solid (1.56 g, 80%).

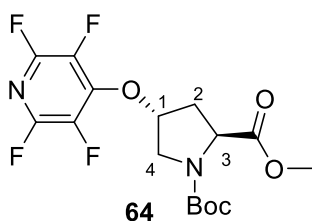
¹H NMR (400 MHz, MeOD) δ 1.43 (9H, s, *tert*-butyl), 2.99 – 3.19 (2H, m, H₁), 4.61 (1H, m, H₂), 7.01 (2H, d, *J* = 8.6 Hz, ArH), 7.17 (2H, dd, *J* = 8.8 Hz, ArH).

¹³C NMR (101 MHz, MeOD) δ 27.3, 36.6, 54.8, 79.2, 116.1, 130.7, 134.4, 134.5 – 138.3 (m), 142.0 – 146.0 (m), 144.2 – 144.5 (m), 155.0, 156.4, 173.8.

¹⁹F NMR (376 MHz, MeOD) δ -92.15 – -92.44 (2F, m), -155.94 – -158.07 (2F, m),

m/z (ESI-) 429.41.

7.3.15 Synthesis of Boc-TFP-Hyp-OMe (64)



General procedure **7.2.4** was followed with Boc-Hyp-OMe (3.10 g, 12.6 mmol, 1.00 equiv.). The crude was purified by column chromatography (Hexane: EtOAc, 7:3 – 0:10) to afford **64** as a white solid (2.48 g, 50%).*

**Mixture of rotamers 2:1; major product assigned.*

^1H NMR (400 MHz, CDCl_3) δ 1.47 (9H, s, *tert*-butyl), 2.25 – 2.34 (1H, m, H_4), 2.59 – 2.71 (1H, m, H_4), 3.77 (3H, s, OMe), 3.71 – 3.98 (2H, m, H_2), 4.45 – 4.52 (1H, m, H_2), 5.36 (1H, m, H_1).

^{13}C NMR (101 MHz, CDCl_3) δ * 28.2, 37.3, 52.3, 52.5, 57.6, 81.0, 81.6, 153.6, 172.8.*(Fluoro-pyridyl carbons not observed due to sample concentration and fast relaxation times).

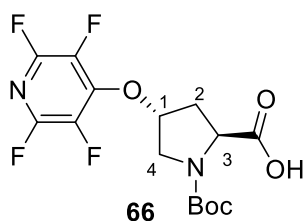
^{19}F NMR (376 MHz, CDCl_3) δ -89.26 – -89.61 (2F, m), -157.60 – -158.12 (2F, m).

HRMS m/z (ESI⁺)* 295.0685 ($[\text{M}-\text{Boc}+\text{H}]^+$ $\text{C}_{11}\text{H}_{10}\text{F}_4\text{N}_2\text{O}_3$ requires 295.0706).

*Please note MS observed -Boc due to column cleaning procedure.

Physical and spectroscopic data obtained was consistent with the literature.²

7.3.16 Synthesis of Boc-TFP-Hyp-OH (**66**)



General procedure **7.2.6** was followed with Boc-TFP-Pro-OMe (**66**) (0.83 g, 2.10 mmol, 1.00 equiv.) and LiOH.H₂O (0.09 g, 2.20 mmol, 1.05 equiv.) to afford acid **62** as an orange oil (0.53 g, 67 %).

Mixture of rotamers 2:1 – major product assigned.

¹H NMR (400 MHz, MeOD) δ 1.47 (9H, s, *tert*-butyl), 2.23 – 2.45 (1H, m, H₄), 2.63 – 2.84 (1H, m, H₄), 3.66 – 3.81 (1H, m, H₃), 3.80– 3.97 (1H, m, H₂), 4.33 – 4.50 (1H, m, H₂) 5.38 – 5.54 (1H, m, H₁).

¹³C NMR (101 MHz, MeOD) δ* 28.5, 38.1, 53.4, 59.1, 82.3, 83.7, 132.2 – 139.4 (m), 141.9 – 148.5 (m), 155.7, 175.8. *(Missing 1 fluoropyridyl peak).

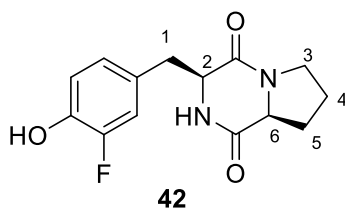
¹⁹F NMR (376 MHz, CDCl₃) δ -88.98 – -89.55 (m), -157.39 – -158.08 (m).

HRMS *m/z* (ESI⁺)* 281.0548 ([M-Boc+H]⁺ C₁₀H₉F₄N₂O₃ requires 281.0549).

*Please note MS observed -Boc due to column cleaning procedure.

IR V_{\max} (solid) / cm⁻¹ 973 (s, C-F), 1094 (s, C-F), 1478 (s, C-F), 1645 (s, C=O), 2987 (m, C-H).

7.3.17 Synthesis of Cyclo(L-3-Fluoro-Tyr-L-Pro) (**42**)



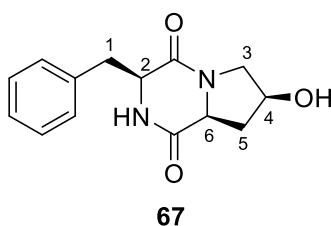
General procedure **7.2.1** was followed on a 0.20 mmol scale using (**AA**₁) Boc-Pro-OH and Boc-3-fluoro-Tyr-OH (**AA**₂). The crude was purified by prep-TLC (DCM:MeOH, 95:5) to afford DKP **42** as a colourless oil (~ 1 mg obtained) with trace amounts of DIPEA.

¹H NMR (400 MHz, CDCl₃) δ 1.81 – 2.11 (3H, m, H₄, H₅), 2.23 – 2.44 (1H, m, H₅), 2.78 (1H, dd, *J* = 14.6, 10.3 Hz, H₁), 3.48 (1H, dd, *J* = 14.6, 4.0 Hz, H₁), 3.55 – 3.66 (2H, m, H₃), 4.11 (ddd, *J* = 8.9, 6.4, 1.7 Hz, H₆), 4.24 (1H, dd, *J* = 10.3, 4.0 Hz, H₂), 5.89 (1H, s, NH), 6.82 – 6.91 (1H, m, ArH), 6.92 – 6.99 (2H, m, ArH).

¹⁹F NMR (376 MHz, CDCl₃) δ -137.61 (1F, dd, *J* = 11.5, 9.0 Hz).

HRMS *m/z* (ESI⁺) 279.1156 ([M+H]⁺ C₁₄H₁₆FN₂O₃ requires 279.1168).

7.3.18 Synthesis of Cyclo(L-CHP-L-Phe) (**67**)

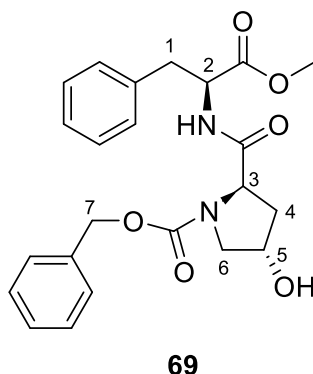


General procedure **7.2.1** was followed on a 0.20 mmol scale using Boc-CHP-OH (**AA**₁) and Boc-Phe-OH (**AA**₂). The crude was purified by prep-TLC (DCM:MeOH, 95:5) to afford DKP **67** as a colourless oil (~ 1 mg obtained) with trace amounts of DIPEA.

¹H NMR (400 MHz, CDCl₃) 2.44 – 2.52 (2H, m, H₅), 2.85 (1H, dd, *J* = 14.6, 10.7 Hz, H₁), 3.49 (1H, dd, *J* = 12.5, 4.8 Hz, H₃), 3.65 (1H, dd, *J* = 14.6, 3.9 Hz, H₁), 3.92 (1H, dd, *J* = 12.5, 2.7 Hz, H₃), 4.20 (1H, app t, *J* = 7.3 Hz, H₆), 4.32 (1H, dd, *J* = 10.7, 3.9 Hz, H₂), 4.55 (1H, ddt, *J* = 7.3, 4.7, 2.2 Hz, H₄), 5.82 (1H, s, NH), 7.20 – 7.43 (5H, m, ArH).

HRMS m/z (ESI⁺) 261.1230 ([M+H]⁺ C₁₄H₁₇N₂O₃ requires 261.1239).

7.3.19 Synthesis of Cbz-L-Hyp-L-Phe-OMe (69)



General procedure **7.2.2** was followed using L-Phe-OMe.HCl (2.00 g, 9.30 mmol, 1.00 equiv.) and Cbz-Hyp-OH (3.07g, 11.2 mmol, 1.20 equiv.). The crude was purified by column chromatography (DCM:MeOH, 100:0 – 93:7) to afford **69** as a white solid (3.05 g, 76%).

Mixture of rotamers 2:1. Major product assigned.

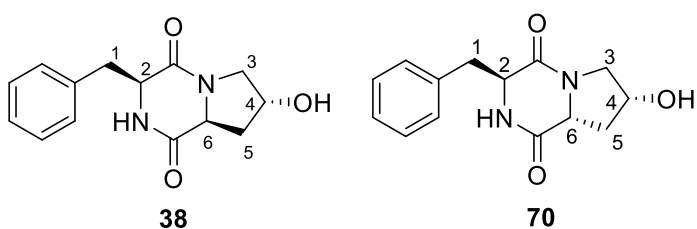
¹H NMR (400 MHz, MeOD) δ 1.84 – 2.02 (1H, m, H₄), 2.07 – 2.32 (1H, m, H₄), 2.81 – 3.19 (2H, m, H₁), 3.48 – 3.61 (2H, m, H₆), 3.62 (3H, s, OMe), 4.29 – 4.37 (1H, m, H₃), 4.40 – 4.50 (1H, m, H₅), 4.65 (1H, dd, $J = 8.6, 6.1$ Hz, H₂), 4.92 – 5.23 (2H, m, H₇) 7.06 – 7.41 (10H, m, ArH).

¹³C NMR (101 MHz, MeOD) δ 36.9, 39.3, 51.3, 53.7, 55.1, 58.8, 66.8, 68.6, 126.5, 127.3, 127.6, 128.1, 128.8, 129.0, 136.6, 136.7, 155.2, 171.9, 173.7.

HRMS m/z (ESI⁺) 427.1877 ([M+H]⁺ C₂₃H₂₇N₂O₆ 427.1869).

Physical and spectroscopic data obtained was consistent with the literature.⁵

7.3.20 Synthesis of Cyclo(L-Hyp-L-Phe) (38) and cyclo(D-Hyp-L-Phe) (70).



General procedure **7.2.3** was followed with dipeptide **69** (2.50 g, 5.90 mmol, 1.00 equiv.). The two stereoisomers were purified by column chromatography (DCM:MeOH, 100:0 – 93:7) to afford **70** as a white solid (0.25 g, 17%) and **38** as a white solid (0.67 g, 46%).

Minor product (desired product) (38)

^1H NMR (400 MHz, CDCl_3) δ 2.01 – 2.14 (1H, m, H_5), 2.39 (1H, dd, $J = 13.5, 6.3$ Hz, H_5), 2.80 (1H, dd, $J = 14.5, 10.8$ Hz, H_1), 3.57 – 3.70 (2H, m, H_1, H_3), 3.82 (1H, dd, $J = 13.3, 4.6$ Hz, H_3), 4.34 (1H, dd, $J = 10.8, 4.2$ Hz, H_2), 4.49 (1H, dd, $J = 11.2, 6.3$ Hz, H_6), 4.60 – 4.65 (1H, m, H_4), 5.63 (1H, s, NH), 7.17 – 7.54 (5H, m, ArH)

^{13}C NMR (101 MHz, CDCl_3) δ 36.7, 37.8, 54.4, 56.1, 57.4, 68.5, 127.7, 129.1, 129.4, 135.8, 165.1, 169.6.

HRMS m/z (ESI $^+$) 261.1233 ($[\text{M}+\text{H}]^+$ $\text{C}_{14}\text{H}_{17}\text{N}_2\text{O}_3$ requires 261.1239.)

Physical and spectroscopic data obtained was consistent with the literature.⁶

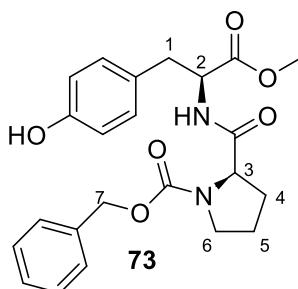
Major product (70)

^1H NMR (400 MHz, MeOD) δ 1.86 – 2.05 (1H, m, H_5), 2.25 (1H, ddd, $J = 13.2, 8.5, 5.9$ Hz, H_5), 2.77 – 2.87 (1H, m, H_6), 3.02 (1H, dd, $J = 13.7, 5.0$ Hz, H_1), 3.21 (1H, dd, $J = 13.6, 5.0$ Hz, H_1), 3.25 – 3.32 (1H, m, H_3), 3.57 – 3.67 (1H, m, H_2), 4.19 – 4.31 (2H, m, H_3, H_4), 7.17 – 7.24 (2H, m, ArH), 7.27 – 7.38 (3H, m, ArH).

^{13}C NMR (101 MHz, MeOD) δ 36.6, 39.5, 52.6, 55.8, 58.2, 67.1, 127.1, 128.3, 129.8, 135.4, 166.3, 169.6.

Physical and spectroscopic data obtained was consistent with the literature.⁷

7.3.21 Synthesis of Cbz-L-Pro-L-Tyr-OMe (**73**)



General procedure **7.2.2** was followed using L-Tyr-OMe.HCl (4.00 g, 17.4 mmol, 1.00 equiv.) and Cbz-Pro-OH (5.98 g, 24.6 mmol, 1.20 equiv.). The crude was purified by column chromatography (DCM:MeOH, 100:0 – 97:3) to afford **73** as a white powder (5.94 g, 80%).

Mixture of rotamer 3:2. Major product assigned.

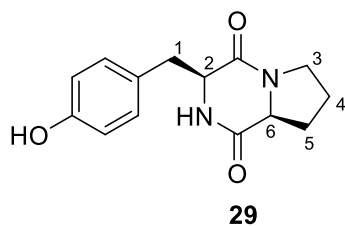
^1H NMR (400 MHz, MeOD) 1.77 – 1.98 (3H, m, H₄, H₆), 2.06 – 2.27 (1H, m, H₄), 2.74 – 3.09 (2H, m, H₁), 3.40 – 3.60 (2H, m, H₅), 3.66 (3H, s, OCH₃), 4.31 (1H, m, H₃), 4.56 – 4.67 (1H, m, H₂), 4.96 – 5.19 (2H, m, H₇), (2H, 6.70 (2H, m, ArH), 7.00 (2H, m, ArH), 7.24 – 7.43 (5H, m, Cbz).

^{13}C NMR (101 MHz, MeOD) δ 23.0, 31.0, 36.0, 47.0, 51.2, 54.0, 59.9, 66.8, 114.8, 127.2, 127.4, 127.6, 128.1, 129.8, 136.6, 155.0, 156.0, 172.0, 173.8.

m/z (ESI⁻) 427.4 [M+H]⁺.

Physical and spectroscopic data obtained was consistent with the literature.⁷

7.3.22 Synthesis of Cyclo(L-Pro-L-Tyr) (**29**)

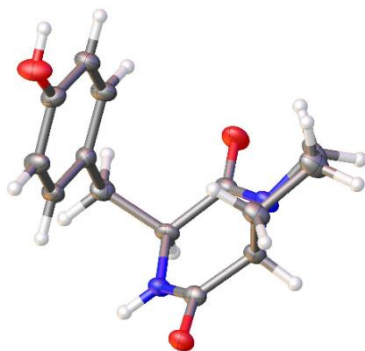


General procedure **7.2.3** was followed using dipeptide **73** (5.70 g, 13.3 mmol, 1.00 equiv.). The crude solid was purified by column chromatography (DCM:MeOH, 100:0 – 95:5) to afford DKP **29** as a white solid (1.48 g, 44% *yield over two steps*).

^1H NMR (400 MHz, CDCl_3) δ 1.13 – 1.34 (1H, m, H_5), 1.70 – 1.85 (2H, m, H_4), 2.02 – 2.15 (1H, m, H_5), 3.04 (2H, m, H_1), 3.27 – 3.41 (1H, m, H_3), 2.56 (1H, d, $J = 12.0, 8.3$ Hz, H_3), 4.05 (1H, dd, $J = 11.0, 6.3$ Hz, H_6), 4.37 (1H, m, H_2), 6.71 (2H, d, $J = 8.5$ Hz, ArH), 7.04 (2H, d, $J = 8.5$ Hz, ArH).

^{13}C NMR (101 MHz, CDCl_3) δ 21.4, 28.0, 36.3, 44.6, 56.5, 58.7, 114.8, 126.3, 130.7, 156.3, 165.6, 169.4.

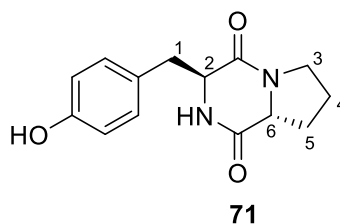
m/z (ESI $^+$) 261.4 [$\text{M}+\text{H}$] $^+$



Molecular structure showing 50% probability anisotropic displacement ellipsoids.

Physical and spectroscopic data obtained was consistent with the literature.⁸

7.3.23 Characterisation of diastereoisomer Cyclo(D-Pro-L-Tyr) (71)

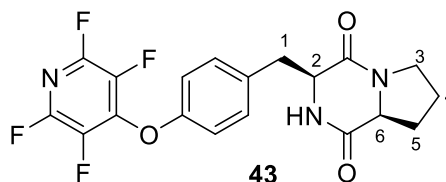


^1H NMR (400 MHz, MeOD) δ 1.53 – 1.75 (2H, m, H₄, H₅), 1.84 – 1.95 (1H, m, H₄), 2.03 – 2.11 (1H, m, H₅), 2.57 – 2.66 (1H, m, H₆), 2.89 (1H, dd, J = 13.8, 4.6 Hz, H₁), 3.13 (1H, dd, J = 13.8, 4.3 Hz, H₁), 3.26 – 3.40 (1H, m, H₃), 3.27 – 3.39 (1H, m, H₃), 4.16 (1H, t, J = 4.4 Hz, H₂), 6.74 – 6.69 (2H, d, J = 8.5 Hz, ArH), 6.95 – 6.99 (2H, d, J = 8.5 Hz, ArH).

^{13}C NMR (101 MHz, MeOD) δ 21.1, 28.5, 38.8, 44.7, 57.8, 58.5, 114.97, 125.5, 130.9, 156.9, 166.1, 170.0.

HRMS m/z (ESI⁺) 261.1236 ([M+H]⁺ C₁₄H₁₇N₂O₃ requires 261.1239).

7.3.24 Synthesis of Cyclo(L-TFP-Tyr-L-Pro) (43)



General procedure **7.2.4** was followed with cyclo(L-Tyr-L-Phe) (**29**) (0.10 g, 0.38 mmol, 1.00 equiv.) to afford **43** as a white solid (0.15 g, 98%).

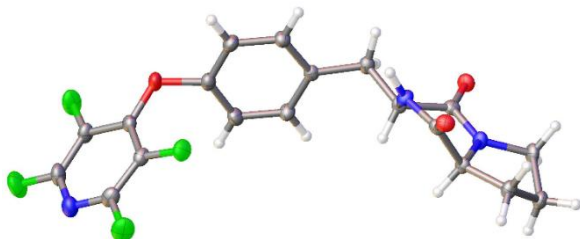
^1H NMR (599 MHz, CDCl₃) δ 1.82 – 2.05 (3H, m, H₅, H₄), 2.26 – 2.39 (1H, m, H₅), 2.87 (1H, dd, J = 14.6, 9.5 Hz, H₁), 3.50 – 3.54 (2H, m, H₁, H₃), 3.58 – 3.64 (1H, m, H₃), 4.02 – 4.09 (1H, m, H₆), 4.27 (1H, dd, J = 9.5, 4.3 Hz, H₂), 5.79 (1H, s, NH), 6.90 – 7.06 (2H, m, ArH), 7.22 – 7.28 (2H, m, ArH).

^{13}C NMR (151 MHz, CDCl₃) δ 22.5, 28.4, 36.1, 45.4, 56.2, 59.1, 117.3, 131.0, 133.0, 134.2 – 137.7 (m), 141.9 – 145.2 (m), 143.9 – 144.5 (m), 155.1, 164.7, 169.3.

^{19}F NMR (376 MHz, CDCl₃) δ -88.14 – -88.36 (2F, m), -153.94 – -154.14 (2F, m).

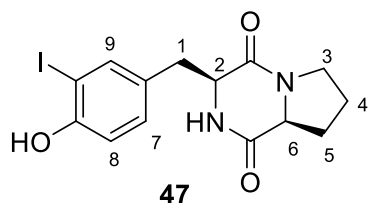
HRMS (m/z) (ESI⁺) 410.1131 ([M+H]⁺ C₁₉H₁₆F₄N₃O₃ requires 410.1128).

IR V_{\max} (solid) / cm⁻¹ 972 (s, C-F), 1073 (s, C-F), 1501 (s, C-F), 1687 (s, C=O), 2982 (m, C-H), 3358 (m, N-H).



Molecular structure showing 50% probability anisotropic displacement ellipsoids.

7.3.25 Synthesis of Cyclo(L-3-Iodo-Tyr-L-Pro) (**47**)



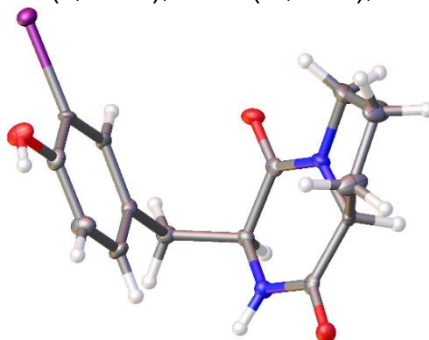
To a solution of cyclo(L-Tyr-L-Pro) (**29**) (0.10 g, 0.38 mmol, 1.00 equiv.) in TFA (1 mL), NIS (0.94 g, 0.42 mmol, 1.10 equiv.) was added and the solution was stirred at rt for 1 h. Following this, TFA was removed by concentration *in vacuo* and the residue was taken up in EtOAc (5 mL) and washed with 1 M sodium thiosulphate solution (2 x 5 mL). The organic phase was dried over MgSO₄ and concentrated *in vacuo* to afford **47** as a white crystalline solid (0.13 g, 94%).

¹H NMR (599 MHz, MeOD) 1.06 – 1.30 (1H, m, H₄), 1.75 – 1.96 (2H, m, Hz, H₅, H₄), 2.07 – 2.13 (1H, m, H₅), 2.98 (1H, dd, $J = 14.2, 4.7$ Hz, H₁), 3.14 (1H, dd, $J = 14.2, 4.6$ Hz, H₁), 3.32 – 3.46 (1H, m, H₃), 3.61 (1H, dt, $J = 12.0, 8.3$ Hz, H₃), 4.07 (1H, dd, $J = 10.9, 6.3$ Hz, H₆), 4.35 – 4.45 (1H, m, H₂), 6.76 (1H, d, $J = 8.2$ Hz, H₈), 7.06 (1H, dd, $J = 8.2, 2.2$ Hz, H₇), 7.58 (1H, d, $J = 2.2$ Hz, H₉).

¹³C NMR (151 MHz, MeOD) 25.3, 32.1, 39.7, 48.5, 60.4, 62.6, 87.0, 118.0, 132.4, 135.0, 144.1, 160.0, 169.3, 173.1.

HRMS m/z (ESI⁺) 387.0212 ([M+H]⁺ C₁₄H₁₆IN₂O₃ requires 387.0206)

IR V_{\max} (solid)/ cm⁻¹ 1605 (s, C=O), 3195 (br, O-H), 3463 (m, N-H).



Molecular structure showing 50% probability anisotropic displacement ellipsoids.

7.4 General procedures (Chapter 4)

7.4.1 Microwave synthesis of thalidomide analogues

A solution of 3-Boc-amino-2,6-dioxopiperadine (**94**) (1.00 equiv.) and corresponding anhydride (1.00 equiv.) in TFE was heated under microwave conditions at 150 °C for 2 h. After this time, the reaction mixture was cooled to rt and then to -20 °C for 2.5 h. EtOAc (4 drops) was added and the mixture was left for a further 4 h at -20 °C until a precipitate had formed. This was filtered and washed with cold EtOAc (2 x 10 mL) and the solid product was obtained.

7.4.2 Synthesis of thalidomide-linker conjugates

4-Fluorothalidomide (1.00 equiv.) (**96**), amino-PEG_n-*tert*-butyl ester (1.20 equiv.) and DIPEA (2.00 equiv.) were stirred in anhydrous DMF (10 mL) under N₂ at 90 °C for 20 h. After this time, the reaction was cooled to rt, washed with H₂O (2 x) and diluted with EtOAc. This was washed with brine and the organic phase was extracted into EtOAc (3 x 10 mL), dried over Na₂SO₄, filtered and concentrated *in vacuo*.

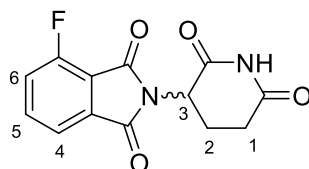
7.4.3 PROTAC Assembly via a Steglich Esterification

Thalidomide-linker conjugate (1.00 equiv.) and corresponding DKP (1.00 equiv.), DMAP (0.10 equiv.) and DIPEA (1.50 equiv.) were stirred in DCM (3 mL). At 0 °C, EDC.HCl (1.20 equiv.) was added portion wise. The solution was warmed to rt and stirred for 24 h. After

this time, the mixture was washed with H₂O (2 x 5 mL), acidified to pH 2 with 1 M aq.HCl and extracted in DCM (3 x 5 mL). The organic phases were combined and dried over Na₂SO₄, filtered, and concentrated *in vacuo*.

7.5 Chemical synthesis (Chapter 4)

7.5.1 Synthesis of 4-Fluorothalidomide (96)



96

General procedure **7.4.1** was followed using 4-fluoroisobenzofuran-1,3-dione (**95**) (0.40 g, 2.20 mmol, 1.00 equiv.) to afford **96** as a purple powder (0.41 g, 68%).

¹H NMR (599 MHz, DMSO) δ 2.00 – 2.12 (1H, m, H₂), 2.44 – 2.64 (2H, m, H₁, H₂), 2.84 - 2.95 (1H, m, H₁), 5.17 (1H, dd, *J* = 12.8, 5.4 Hz, H₃), 7.75 (1H, t, *J* = 8.7 Hz, H₆), 7.80 (1H, d, *J* = 7.3 Hz, H₄), 7.95 (ddd, *J* = 8.7, 7.3, 4.5 Hz, H₅), 11.17 (1H, s, NH).

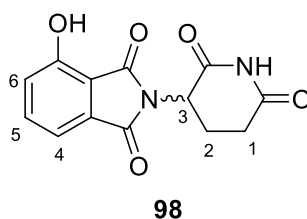
¹³C NMR (151 MHz, DMSO) δ 22.3, 31.4, 49.5, 117.5 (d, *J* = 12.5 Hz), 120.5 (d, *J* = 3.4 Hz), 123.5 (d, *J* = 19.6 Hz), 133.9, 138.5 (d, *J* = 7.9 Hz), 157.3 (d, *J* = 263.2 Hz), 164.4, 166.6, 170.2, 173.2.

¹⁹F NMR (376 MHz, DMSO) δ -114.68 (1F, dd, *J* = 9.5, 4.6 Hz).

HRMS *m/z* (ESI⁺) 277.0641 ([M+H]⁺ C₁₃H₁₀FN₂O₄ requires 277.0625).

Physical and Spectroscopic data obtained was consistent with the literature.⁹

7.5.2 Synthesis of 4-Hydroxythalidomide (**98**)



General procedure **7.4.1** was followed using 4-hydroxyisobenzofuran-1,3-dione (**97**) (0.40 g, 2.40 mmol, 1.00 equiv.) to afford **98** as a purple powder (0.58 g, 88%).

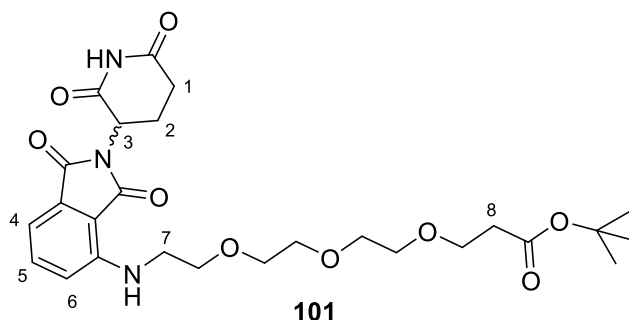
^1H NMR (599 MHz, DMSO) δ 1.91 – 2.09 (1H, m, H₂), 2.39 – 2.64 (1H, m, H₂), 2.77 – 2.95 (2H, m, H₁), 5.07 (1H, dd, J = 12.8, 5.4 Hz, H₃), 7.25 (1H, dd, J = 6.7 Hz, H₆), 7.32 (1H, d, J = 6.7 Hz, H₅), 7.65 (1H, dd, J = 8.4, 7.2 Hz, H₄), 11.10 (1H, s, NH).

^{13}C NMR (151 MHz, DMSO) δ 22.5, 31.4, 49.1, 114.8 (2 x) 124.0, 133.6, 136.9, 156.0, 166.3, 167.5, 170.5, 173.3.

HRMS m/z (ESI⁺) 275.0663 ([M+H]⁺ C₁₃H₁₁N₂O₅ requires 275.0668).

Physical and spectroscopic data obtained was consistent with the literature.⁹

7.5.3 Synthesis of *tert*-butyl 3-(2-(2-(2-((2-(2,6-dioxopiperidin-3-yl)-1,3-dioxoisindolin-4-yl)amino)ethoxy)ethoxy)ethoxy)propanoate (**101**)



General procedure **7.4.2** was followed using amino-PEG₃-*tert*-butyl ester (0.25 g, 0.77 mmol, 1.20 equiv.). The crude residue was purified by automated column chromatography CombiFlash (DCM:MeOH, 100:0 – 90:10) to afford **101** as a yellow oil (0.20 g, 49%).

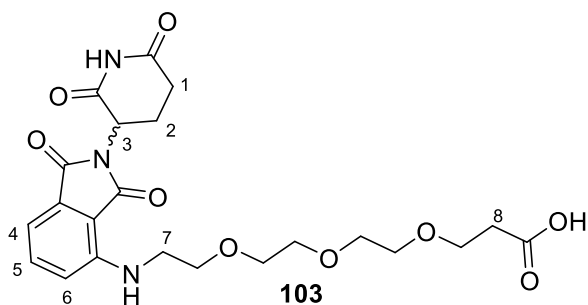
¹H NMR (400 MHz, CDCl₃) 1.45 (9H, s, *tert*-butyl), 2.09 – 2.17 (1H, m, H₂), 2.50 (2H, t, *J* = 6.6 Hz, H₈), 2.69 – 2.95 (3H, m, H₂, H₁), 3.48 (2H, t, *J* = 5.4 Hz, H₇), 3.60 – 3.76 (12H, m, PEG-H), 4.92 (1H, dd, *J* = 11.9, 5.4 Hz, H₃), 6.94 (1H, d, *J* = 8.6 Hz, H₄), 7.12 (1H, d, *J* = 6.6 Hz, H₆), 7.50 (1H, dd, *J* = 8.5, 7.1 Hz, H₅), 8.15 (1H, s, NH).

¹³C NMR (101 MHz, CDCl₃) 22.8, 28.1, 31.4, 36.3, 42.4, 48.9, 66.9, 69.5, 70.4, 70.6, 70.6, 70.8, 80.6, 110.3, 111.7, 116.8, 132.5, 136.0, 146.9, 167.7, 168.4, 169.3, 171.0, 171.2.

m/z (ESI⁺) [M-*tert*Bu+H]⁺ = 478.84

Physical and spectroscopic data obtained was consistent with the literature.¹⁰

7.5.4 Synthesis of 3-(2-(2-(2-(2-(2,6-dioxopiperidin-3-yl)-1,3-dioxoisindolin-4-yl)amino)ethoxy)ethoxy)ethoxy)propanoic acid (103)



Compound **101** (0.20 g, 0.38 mmol) was stirred in 50% TFA in DCM (4 mL) at rt for 16 h. After this time, the mixture was concentrated *in vacuo* with MeOH (3 x) to afford **103** as a yellow oil (0.18 g, quant)

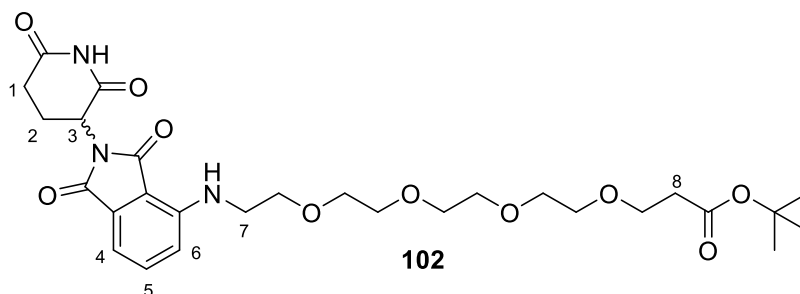
^1H NMR (400 MHz, CDCl_3) δ 1.99 – 2.13 (1H, m, H_2), 2.55 (2H, t, $J = 6.0$ Hz, H_8), 2.57 – 2.86 (3H, m, H_1 , H_2), 3.40 (2H, t, $J = 8.6$, 4.7 Hz, H_7), 3.48 – 3.78 (12H, m, PEG), 4.78 – 4.97 (1H, m, H_3), 6.85 (1H, d, $J = 8.6$ Hz, H_4), 7.03 (1H, d, $J = 7.1$ Hz, H_6), 7.42 (1H, dd, $J = 8.5$, 7.1 Hz, H_5), 8.89 (1H, s, NH).

^{13}C NMR (101 MHz, CDCl_3) δ 22.8, 31.3, 34.6, 42.3, 48.8, 66.4, 66.9, 70.3 (2x), 70.4, 70.6, 110.2, 111.8, 116.9, 132.4, 136.2, 146.8, 168.0, 169.3, 169.4, 172.2, 175.4.

LCMS m/z (ESI $^+$) $[\text{M}+\text{H}]^+ = 478.52$.

Physical and spectroscopic data obtained was consistent with the literature.¹⁰

7.5.5 Synthesis of *tert*-butyl 1-((2-(2,6-dioxopiperidin-3-yl)-1,3-dioxoisindolin-4-yl) amino)-3,6,9,12-tetraoxapentadecan-15-oate (**102**)



General procedure **7.4.2** was followed with amino-PEG₄-*tert*-butyl ester (0.15 g, 0.47 mmol, 1.20 equiv.). The crude residue was purified by column chromatography (DCM:MeOH, 100:0 – 97:3) to afford **102** as a yellow oil (0.095 g, 38%).

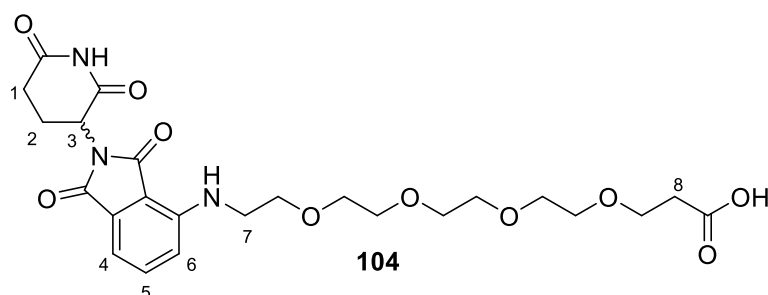
¹H NMR (400 MHz, CDCl₃) 1.44 (9H, s, *tert*-butyl), 2.08 – 2.19 (1H, m, H₂), 2.59 – 2.69 (2H, m, H₈), 2.74 – 2.93 (3H, m, H₂, H₁), 3.48 (2H, dd, *J* = 5.5 Hz, H₇), 3.59 – 3.86 (16 H, m, PEG), 4.92 (1H, dd, *J* = 12.1, 5.3 Hz, H₃), 6.49 (1H, m, NH) 6.93 (1H, dd, *J* = 7.7 Hz, H₄), 7.11 (1H, dd, *J* = 7.0 Hz, H₆), 7.45 – 7.55 (1H, m, H₅), 9.01 (1H, s, NH).

¹³C NMR (101 MHz, CDCl₃) δ 22.8, 28.1, 31.4, 36.2, 42.4, 48.9, 53.5, 66.9, 69.5, 70.3, 70.4, 70.6 (x2), 70.7, 80.6, 110.3, 111.6, 116.8, 132.5, 136.0, 146.9, 167.7, 168.5, 169.3, 171.0, 171.3.

HRMS *m/z* (ESI⁺) 578.2720 ([M+H]⁺ C₂₈H₄₀N₃O₁₀ requires 578.2714).

Physical and spectroscopic data obtained was consistent with the literature.¹⁰

7.5.6 1-((2-(2,6-dioxopiperidin-3-yl)-1,3-dioxoisindolin-4-yl)amino)-3,6,9,12-tetraoxapentadecan-15-oic acid (104)



Compound **102** (0.10 g, 0.18 mmol) was stirred in 50% TFA in DCM (4 mL) at rt for 16 h. After this time, the mixture was concentrated *in vacuo* with MeOH (3 x) to afford **104** as a yellow oil (0.09 mg, quant) .

^1H NMR (400 MHz, CDCl_3) δ 2.08 – 2.19 (1H, m, H_2), 2.59 – 2.69 (2H, m, H_8), 2.74 – 2.93 (3H, m, H_2 , H_1), 3.46 – 3.52 (2H, m, H_7), 3.59 – 3.86 (16H, m, PEG), 4.80 – 5.01 (1H, m, H_3), 6.93 (1H, dd, $J = 7.7$ Hz, H_4), 7.11 (1H, dd, $J = 7.0$ Hz, H_6), 7.45 – 7.55 (1H, m, H_5), 9.01 (1H, s, NH).

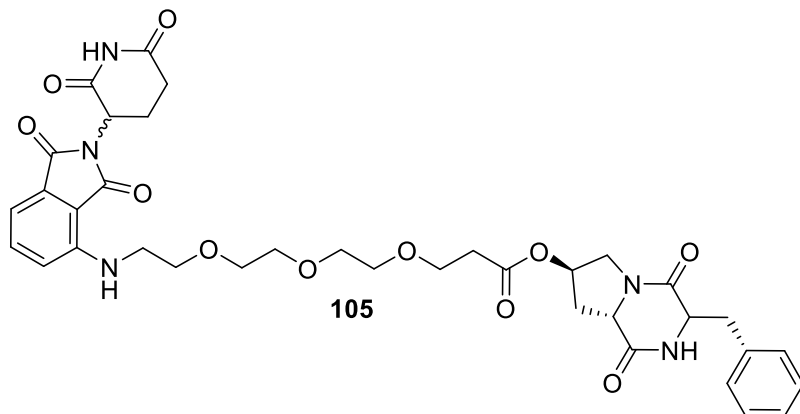
^{13}C NMR (101 MHz, CDCl_3) δ 22.8, 31.4, 34.8, 42.3, 48.8, 66.40, 69.4, 70.1, 70.5 (x 3), 70.6, 70.7, 110.3, 111.8, 116.9, 132.5, 136.1, 146.8, 167.7, 169.0, 169.3, 172.0, 175.3.

HRMS m/z (ESI $^+$) 522.2072 ([$\text{M}+\text{H}$] $^+$ $\text{C}_{24}\text{H}_{31}\text{N}_3\text{O}_{10}$ requires 522.2088).

Physical and spectroscopic data obtained was consistent with the literature.¹⁰

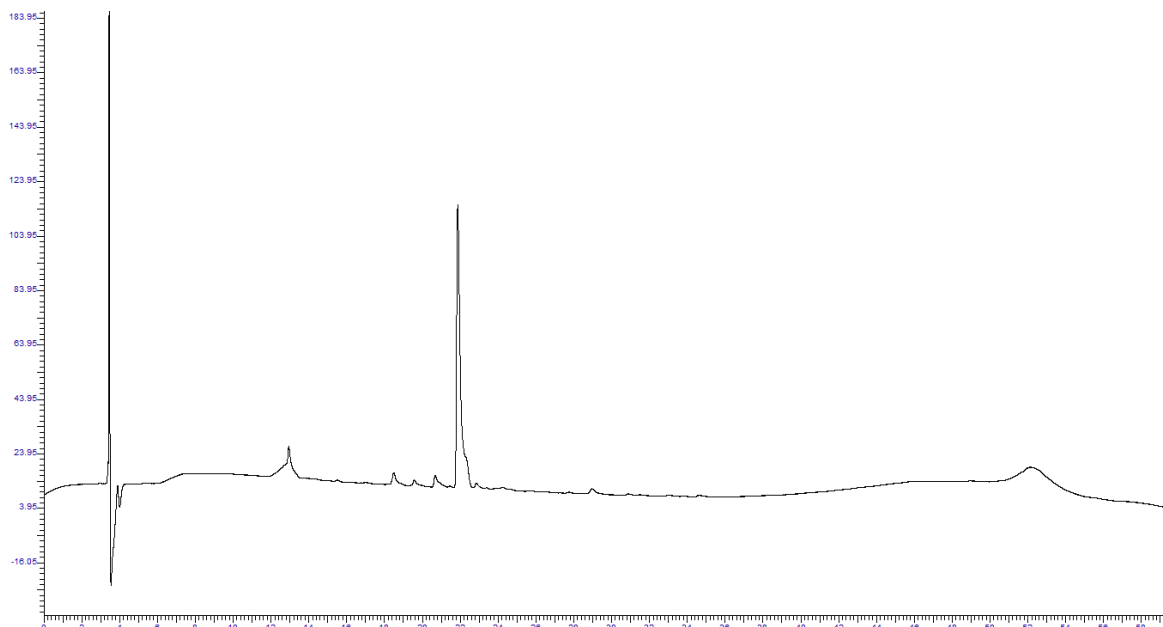
7.5.7 Synthesis of CCL2-PROTAC 105

General procedure 7.4.3 was followed using thalidomide-linker conjugate **103** (0.09 g, 0.19 mmol, 1.00 equiv.) and DKP **38** (0.05 g, 0.19 mmol, 1.00 equiv.). After this time, the reaction had not gone to completion, so the mixture was heated to reflux for 5 h. The resultant crude was purified by column chromatography (DCM:MeOH, 100:0 – 95:5) to afford **105** as a yellow oil (0.03 g, 22%). *Product present in a complex mixture.*

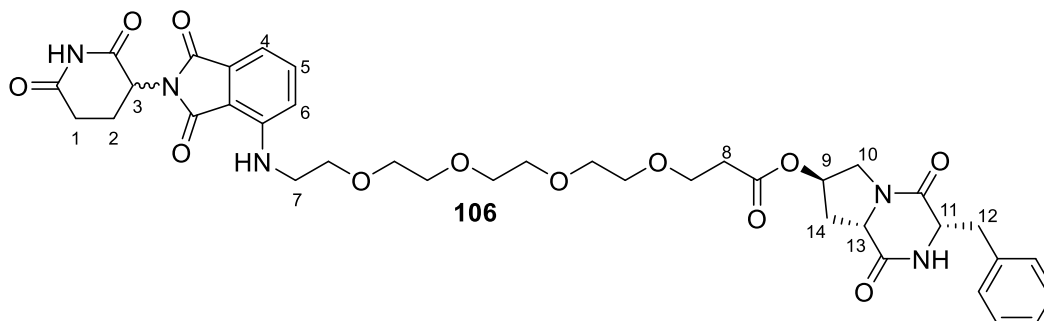


HRMS m/z (ESI⁺) 720.2898 ([M+H]⁺ C₃₆H₄₂N₅O₁₁ requires 720.2881).

Analytical HPLC R_t = 21.87 min.



7.5.8 Synthesis of CCL2-PROTAC 106



General procedure **7.4.3** was followed using thalidomide-linker conjugate **104** (0.04 g, 0.15 mmol, 1.00 equiv.) and DKP **38** (0.08 g, 0.15 mmol, 1.00 equiv.). The solution was warmed to rt and stirred for 24 h. The resultant crude was purified by column chromatography (DCM:MeOH, 100:0 – 98:2) to afford **106** as a yellow oil (0.02 g, 17%).

^1H NMR (599 MHz, CDCl_3) δ 1.99 – 2.12 (3H, m, H_{14} , H_2), 2.42 (1H, dd, $J = 14.1, 6.2$ Hz, H_{14}), 2.56 (2H, t, $J = 6.2$ Hz, H_8), 2.66 – 2.86 (4H, m, H_{12} , H_1), 3.44 (2H, t, $J = 5.1$ Hz, H_7), 3.51 – 3.76 (17H, m, H_{14} , PEG), 3.88 (1H, dd, $J = 14.0, 5.1$ Hz, H_{14}), 4.17 – 4.35 (2H, m, H_{11} , H_3), 4.84 – 4.91 (1H, m, H_{13}), 5.24 – 5.42 (1H, m, H_9), 5.83 (1H, s, NH), 6.90 (1H, dd, $J = 8.5, 2.6$ Hz, H_4), 7.08 (1H, dd, $J = 6.5, 2.6$ Hz, H_6), 7.15 – 7.34 (5H, m, ArH), 7.47 (1H, dd, $J = 8.5, 7.1$ Hz, H_5), 8.69 (1H, s, NH).

^{13}C NMR (151 MHz, CDCl_3) δ 22.9, 31.4, 35.1, 36.8, 42.4, 48.9, 52.0, 56.2, 57.5, 66.5, 69.4, 70.4 (x 2), 70.5, 70.6, 70.7, 70.9, 110.3, 111.6, 111.7, 116.8, 127.6, 129.3, 132.5, 135.7, 136.1, 146.8, 165.0, 167.7, 168.5, 168.6, 168.9, 169.2, 170.8, 171.3 (x 2).

HRMS m/z (ESI $^+$) 764.3133 ($[\text{M}+\text{H}]^+$ $\text{C}_{38}\text{H}_{46}\text{N}_5\text{O}_{12}$ requires 764.3143).

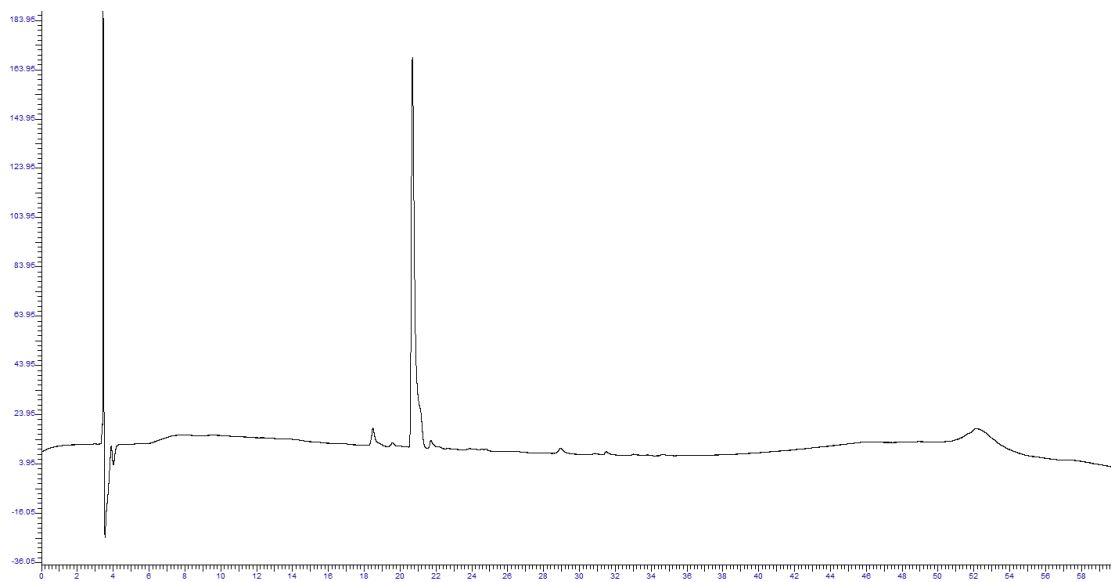
Analytical HPLC $R_t = 22.18$ min

were observed in the ^1H NMR. Given the chemical shifts it was assumed to be an NH proton. The reason for this “doubling” of the NH protons could not be rationalised.)

^{13}C NMR (151 MHz, CDCl_3)* 22.5, 22.8, 28.3, 30.9, 31.3, 35.3 (*d*), 36.1 (*d*), 42.4, 45.4, 48.9, 56.2 (*d*), 59.1 (*d*), 66.5, 69.4 (*d*), 70.6, 70.7, 110.29, 111.6, 116.7, 122.2 (*d*), 130.3 (*d*), 132.5, 133.5, 136.0, 146.8, 150.0 (*d*), 164.9 (*d*), 167.6 (*d*), 168.7, 168.9 (2 *x*), 169.2, 169.6, 170.2 (*d*), 171.4 (*d*).(*Several of the carbon signals appeared as doublets (*d*). The reason for the doubling of the carbon peaks could not be rationalised.)

Analytical HPLC $R_t = 20.69$ min

HRMS m/z (ESI $^+$) 720.2866 ($[\text{M}+\text{H}]^+$ $\text{C}_{36}\text{H}_{42}\text{N}_5\text{O}_{11}$ requires 720.2881).



7.6 General procedures (Chapter 5)

7.6.1 EDC mediated solution phase amide coupling

To a solution of lenalidomide (1.00 equiv.) and acid (1.00 equiv.) in DMF, DMAP (0.10 equiv.) was added followed by EDC.HCl (1.50 equiv.). The mixture was stirred at rt for 16 h. The crude mixture was concentrated *in vacuo* with toluene (3 x 20 mL) at 60 °C. The residue was taken up in EtOAc (20 mL) and washed with H₂O (3 x 20 mL). The precipitate was filtered and dried under high vacuum.

7.6.2 *tert*-butyl deprotection

A solution of *tert*-butyl ester in 50 % TFA in DCM was stirred at rt for 3 h. After this time, the solvent was concentrated *in vacuo* with MeOH (3 x). Where specified, the solid was dissolved in 50:50 MeCN/H₂O (50:50 v/v) and lyophilised.

7.6.3 Test cleavage

The peptide-resin was shrunk in Et₂O (3 x 5 mL) at rt for 20 min. A small spatula tip of resin was removed and 200 µL of cleavage cocktail (95% TFA, 2.5% H₂O and 2.5% TIPS) was added. After 15 min, MeCN (100 µL) was added and the beads were left to settle to the bottom of the solution. The MeCN layer was removed and analysed by LCMS.

7.6.4 Resin cleavage

The peptide-resin was transferred to a solid phase syringe and shrunk in Et₂O (3 x 7 mL) at rt for 2 min. To the resin, 3.15 mL of cleavage cocktail (2.85 mL TFA, 0.15 mL H₂O and 0.15 mL TIPS) was added, and the resin was agitated at rt for 4 h. The resin was drained into a falcon containing ice-cold Et₂O which allowed the peptide to precipitate out of solution. The falcons were centrifuged (4,000 rpm, 10 min) and the solute was discarded. This process was repeated. The remaining white solid was then dissolved in MeCN/H₂O to be purified by preparative HPLC (**Section 7.4.5**).

7.6.5 Preparative HPLC

Samples were dissolved in 1:1 MeCN: H₂O and 0.1% TFA to ~ 4 mg/mL, filtered (0.22 µm) and injected onto an XBridge C18 column (19 x 100 mm) attached to an Interchim Puriflash system. A linear gradient of 0 - 60% solvent B (A = H₂O, 0.1% formic acid; B = MeCN) over 10 min, followed by 60 - 95% B for 3 min, then a 95% B for 2 min at a flow rate of 17 mL/min was used. Absorbance was detected at λ = 220 or 254 nm.

7.6.6 Automated solid phase synthesis of peptides

All peptides in this chapter were synthesised by automated solid phase peptide synthesis using a Liberty Blue 2.0 microwave peptide synthesiser (CEM). Rink amide MBHA resin (0.351 mmol/g) was pre-swollen in DMF (5 mL) for 30 min before adding to the reaction vessel. All peptides were made on a 0.1 mmol scale, using Fmoc-amino acids (5.00 equiv.), DIC (10.0 equiv.), HOBT or OXYMA (5.00 equiv.) in DMF. Single coupling conditions were used (75 °C, 20 W, 10 min) and deprotection was achieved with 20% piperidine in DMF unless specified otherwise. After each coupling or deprotection, the resin was washed with DMF (5 x 4 mL). The peptide was retained on resin.

7.6.7 Automated solid phase functionalised peptide synthesis

Rink amide MBHA resin (0.351 mmol/g) was pre-swollen in DMF (30 min) before adding to the reaction vessel. All functionalised peptides were made on a 0.1 mmol scale unless stated otherwise, using Fmoc-amino acids (5.00 equiv.), DIC (10.0 equiv.) and HOBT or OXYMA (5.00 equiv.) in DMF. Single coupling conditions were used (at 75 °C, 20 W, 10 mins). Following peptide synthesis, functionalised carboxylic acid in DMF was coupled to the resin-peptide using DIC (10.0 equiv.) and HOBT (5.00 equiv.). Double coupling conditions were used for (75 °C, 20 W, 10 min). After each coupling the resin was washed with DMF (5 x 4 mL). No final deprotection conditions were used.

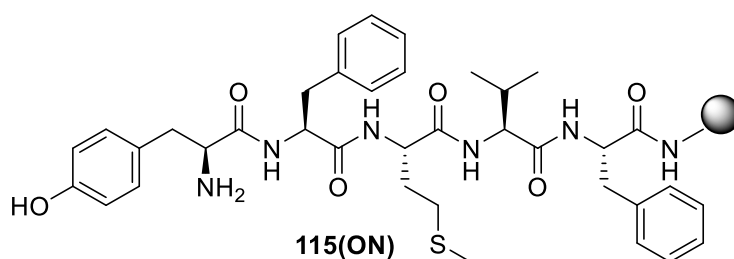
7.6.8 PROTAC assembly (click chemistry)

To a solution of the peptide coupled alkyne (1.00 equiv.) and azide coupled lenalidomide (1.00 equiv.) in DMF, a catalytic amount of CuSO₄ and sodium ascorbate was added to a

microwave vial. The mixture was pre stirred (5 s) and heated under microwave conditions (75 °C, 2 h). After this time, the mixture was cooled and filtered. The solute was concentrated *in vacuo* with toluene (3 x 20 mL, 60 °C). The remaining residue was dissolved in MeCN:H₂O (50:50 *v/v*) and purified following procedure **7.6.5**.

7.7 Chemical synthesis of Group 1 PROTACs (Chapter 5)

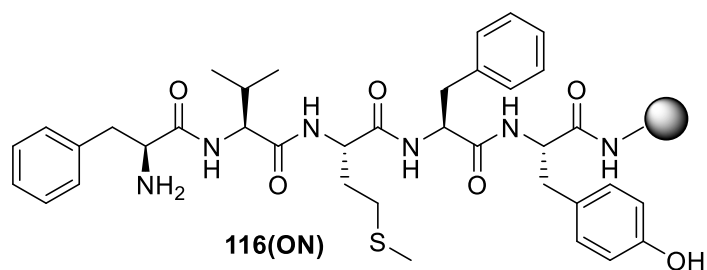
7.7.1 Synthesis of peptide 115(ON)



General procedure **7.6.6** was followed for the synthesis of peptide **115(ON)**. A test cleave was performed using conditions described in procedure **7.6.3** to confirm successful synthesis.

m/z (ESI⁺) [M+H]⁺ = 705.54

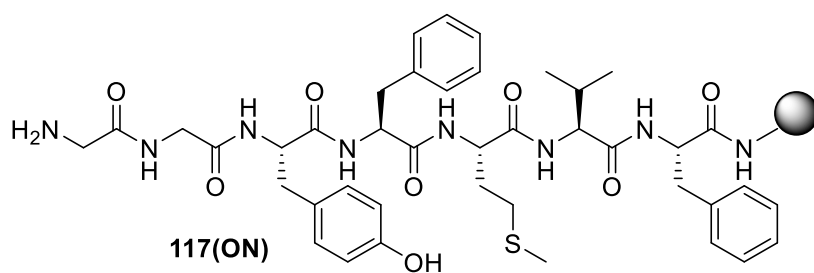
7.7.2 Synthesis of peptide 116(ON)



General procedure **7.6.6** was followed for the synthesis of peptide **116 (ON)**. A test cleave was performed using conditions described in procedure **7.6.3** to confirm successful synthesis.

m/z (ESI⁺) [M+H]⁺ = 705.50

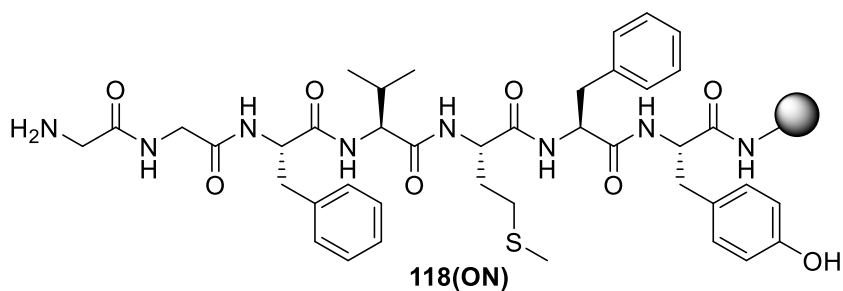
7.7.3 Synthesis of peptide 117(ON)



General procedure **7.6.6** was followed for the synthesis of peptide **117(ON)**. A test cleavage was performed using conditions described in general procedure **7.6.3** to confirm successful synthesis.

m/z (ESI⁺) [M+H]⁺ = 819.63

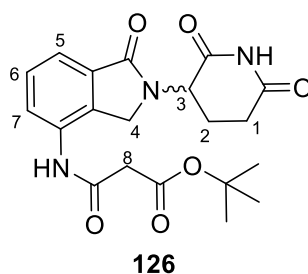
7.7.4 Synthesis of peptide 118(ON)



General procedure **7.6.6** was followed for the synthesis of peptide **118 (ON)**. A test cleave was performed using conditions described in procedure **7.6.3** to confirm successful synthesis.

m/z (ESI⁺) [M+H]⁺ = 819.68

7.7.5 Synthesis of *tert*-butyl 3-((2-(2,6-dioxopiperidin-3-yl)-1-oxoisindolin-4-yl)amino)-3-oxopropanoate (**126**)



General procedure **7.6.1** was followed using mono *tert*-butyl malonic acid (0.37 g, 2.31 mmol, 1.20 equiv.) to afford **126** as a white solid (0.61 mg, 79%).

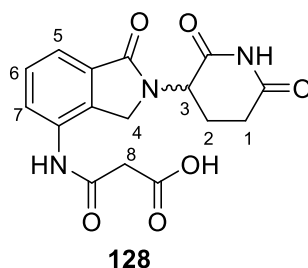
¹H NMR (400 MHz, DMSO) δ 1.43 (9H, s, *tert*-butyl), 2.00 – 2.08 (1H, m, H₂), 2.32 (1H, dd, J = 13.2, 4.8 Hz, H₂), 2.55 – 2.71 (1H, m, H₁), 2.87 – 3.00 (1H, m, H₁), 3.46 (2H, s, H₈), 4.33 (1H, d, J = 17.5 Hz, H₄), 4.42 (1H, d, J = 17.5 Hz, H₄), 5.16 (1H, dd, J = 13.3, 4.8 Hz, H₃), 7.48 – 7.56 (2H, m, H₆, H₇), 7.84 (1H, dd, J = 7.2, 1.8 Hz, H₅), 10.27 (1H, s, NH), 11.04 (1H, s, NH).

^{13}C NMR (101 MHz, DMSO) δ 23.2, 28.2, 31.7, 44.7, 47.0, 52.0, 81.3, 120.0, 125.6, 129.2, 133.2, 133.8, 134.0, 165.1, 167.3, 168.2, 171.6, 173.3.

IR V_{max} (solid) / cm^{-1} 1152 (s, C-O), 1680 (s, C=O), 2999 (m, C-H), 3092 (m, N-H), 3317 (m, N-H).

HRMS m/z (ESI⁺) 402.1660 ([M+H]⁺ C₂₀H₂₄N₃O₆ requires 402.1665).

7.7.6 Synthesis of 3-((2-(2,6-dioxopiperidin-3-yl)-1-oxoisindolin-4-yl)amino)-3-oxopropanoic acid (**128**)



General procedure **7.6.2** was followed using lenalidomide-conjugate **126** (0.82 g, 2.38 mmol, 1.00 equiv.). The product was dissolved in 15 mL MeCN:H₂O (50:50 v/v) and lyophilised to afford **128** as a white powder (0.81 g, quant).

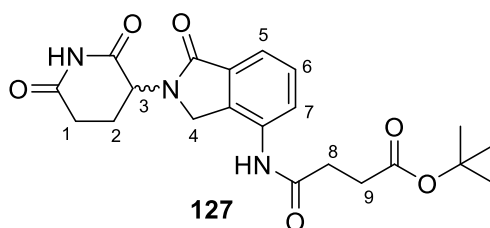
^1H NMR (400 MHz, DMSO) δ 1.97 – 2.09 (1H, m, H₂), 2.23 – 2.41 (1H, m, H₂), 2.57 – 2.65 (1H, m, H₁), 2.86 – 2.97 (1H, m, H₁), 3.42 (2H, s, H₈), 4.40 (1H, d, $J = 17.5$ Hz, H₄), 4.32 (1H, d, $J = 17.5$ Hz, H₄), 5.16 (1H, dd, $J = 13.3, 5.1$ Hz, H₃), 7.39 – 7.64 (2H, m, H₆, H₇), 7.87 (1H, dd, $J = 7.0, 2.1$ Hz, H₅), 10.02 (1H, s, NH), 11.04 (1H, s, NH).

^{13}C NMR (101 MHz, DMSO) δ 27.9, 36.4, 48.6, 51.6, 56.8, 124.5, 130.2, 134.0, 137.9, 138.6, 138.7, 170.0, 173.0, 174.4, 176.3, 178.1.

HRMS m/z (ESI⁺) 346.1031 ([M+H]⁺ C₁₆H₁₆N₃O₆ requires 346.1039).

IR V_{max} (solid) / cm^{-1} 1207 (s, O-H), 1692 (s, C=O), 3218 (m, N-H), 3338 (m, N-H).

7.7.7 Synthesis of tert-butyl 4-((2-(2,6-dioxopiperidin-3-yl)-1-oxoisindolin-4-yl)amino)-4-oxobutanoate (127)



General procedure **7.6.1** was followed using mono *tert*-butyl succinic acid (1.61 g, 9.24 mmol, 1.20 equiv.) to afford **127** as a white solid (2.70 g, 84%).

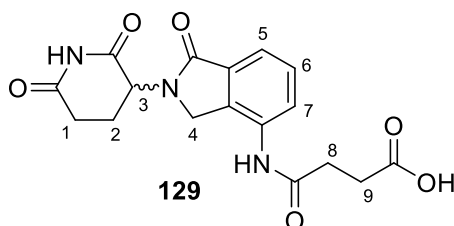
^1H NMR (400 MHz, DMSO) δ 1.39 (9H, s, *tert*-butyl), 1.99 – 2.07 (1H, m, H₂), 2.19 – 2.37 (1H, m, H₂), 2.51 – 2.65 (5H, m, H₁, H₈, H₉), 2.89 – 2.99 (1H, m, H₁), 4.29 (1H, dd, J = 17.6 Hz, H₄), 4.37 (1H, d, J = 17.6 Hz, H₄), 5.16 (1H, dd, J = 13.3, 5.1 Hz, H₃), 7.42 – 7.55 (2H, m, H₆, H₇), 7.78 (1H, dd, J = 7.0, 2.1 Hz, H₅), 9.90 (1H, s, NH), 11.04 (1H, s, NH).

^{13}C NMR (101 MHz, DMSO) δ 23.7, 28.7, 31.0, 32.0, 32.1, 47.3, 52.4, 80.7, 120.0, 126.0, 130.0, 133.6, 134.7 (x2), 168.8, 171.1, 172.0, 172.5, 173.8.

HRMS m/z (ESI⁺) 416.1836 ([M+H]⁺ C₂₁H₂₆N₃O₆ requires 416.1822).

IR V_{max} (solid) / cm⁻¹ 1154 (s, C-O), 1676 (s, C=O), 2992 (m, C-H), 3085 (m, N-H), 3350 (m, N-H).

7.7.8 Synthesis of 4-((2-(2,6-dioxopiperidin-3-yl)-1-oxoisindolin-4-yl) amino)-4-oxobutanoic acid (129)



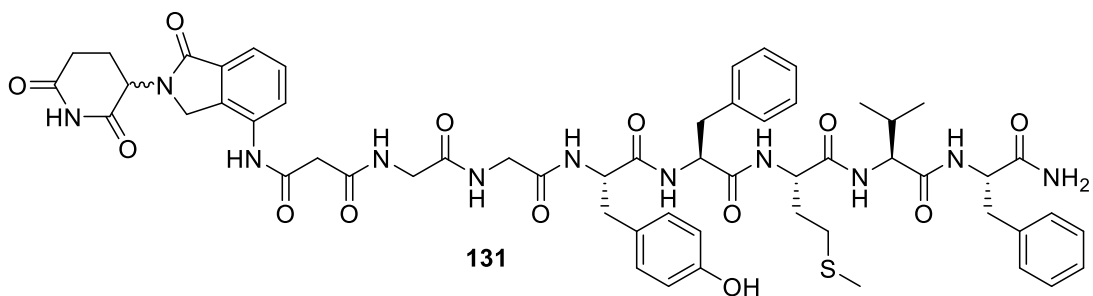
General procedure **7.6.2** was followed using lenalidomide-conjugate **127** (2.50 g, 6.02 mmol, 1.00 equiv.) The product was dissolved in 15 mL MeCN:H₂O (50:50 v/v) and lyophilised to afford acid **129** as an off-white solid (2.20 g, quant).

¹H NMR (400 MHz, DMSO) δ 2.00 – 2.08 (1H, m, H₂), 2.27 – 2.40 (1H, m, H₂), 2.53 – 2.71 (5H, m, H₁, H₈, H₉), 2.93 (1H, ddd, *J* = 17.2, 13.6, 5.4 Hz, H₂), H₄), 4.32 (1H, d, *J* = 17.5 Hz, H₄), 4.40 (1H, d, *J* = 17.5 Hz, H₄), 5.16 (1H, dd, *J* = 13.3, 5.1 Hz, H₃), 7.43 – 7.61 (2H, m, H₆, H₇), 7.82 (1H, dd, *J* = 6.9, 2.1 Hz, H₅), 9.88 (1H, s, NH), 11.04 (1H, s, NH).

¹³C NMR (101 MHz, DMSO) δ 23.1, 29.4, 31.1, 31.7, 46.9, 52.0, 119.4, 125.5, 129.1, 133.1, 134.1, 134.2, 168.3, 170.8, 171.6, 173.4, 174.3.

HRMS *m/z* (ESI⁺) 360.1202 ([M+H]⁺ C₁₇H₁₈N₃O₆ requires 360.1196).

7.7.9 Synthesis of PROTAC 131

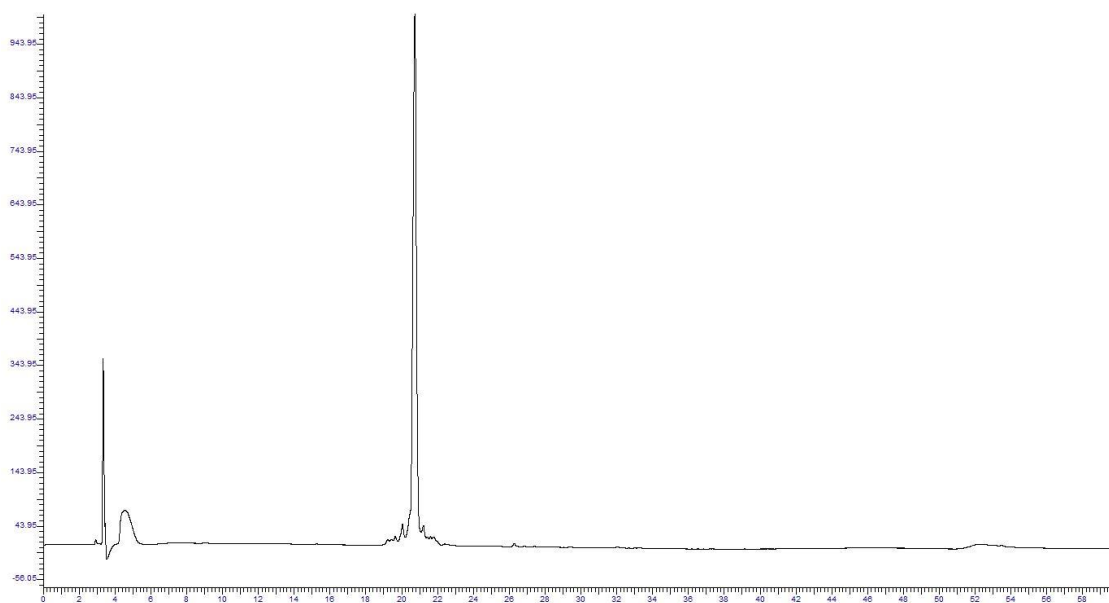


General procedure **7.6.7** was followed using peptide **117(ON)** and lenalidomide-acid conjugate **126** (3.00 equiv.). General procedure **7.6.4** was followed to afford crude PROTAC **131** (0.21 g) which was purified following general procedure **7.6.5** to afford PROTAC **131** as a white solid (20.4 mg).

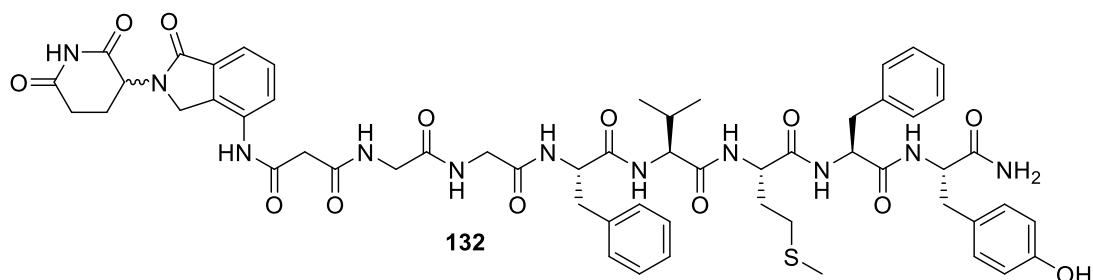
HRMS m/z (ESI+) 1146.4719 ($[M+H]^+$ $C_{57}H_{68}N_{11}O_{13}S$ requires 1146.4736).

HPLC R_t = 20.73, Purity = 92%.

*Purity corresponds to peak area determined by analytical HPLC following general procedure **7.1.3**.



7.7.10 Synthesis of PROTAC 132

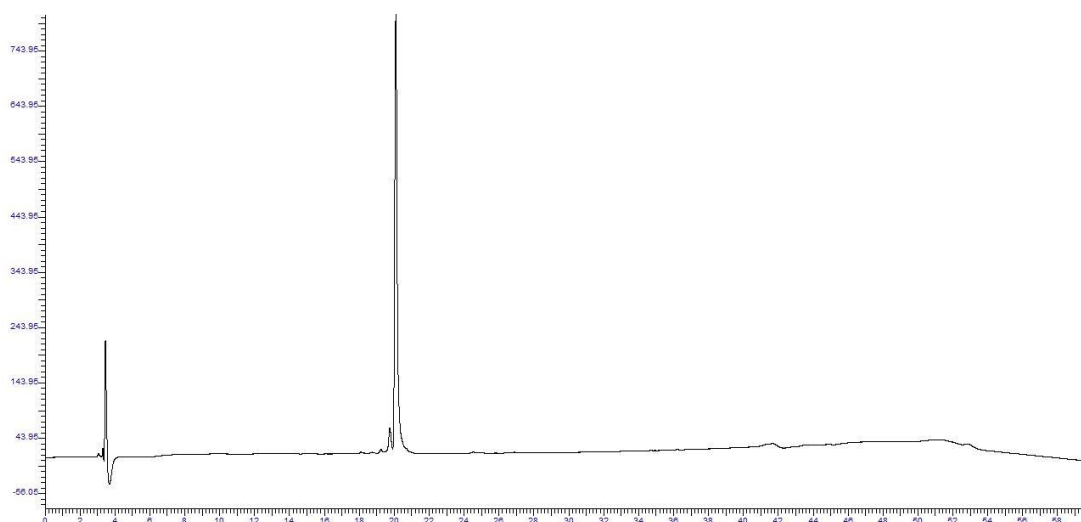


General procedure **7.6.7** was followed using on-resin peptide **118(ON)**, and lenalidomide-acid conjugate **128** (3.00 equiv.). General procedure **7.6.4** was followed to afford crude PROTAC **132** (0.110 g) of which (0.05 g) was purified following general procedure **7.6.5** to afford PROTAC **132** as a white solid (2.50 mg).

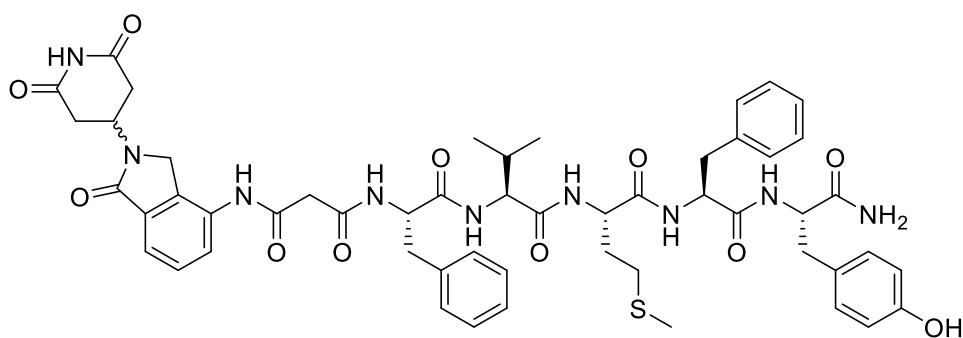
HRMS m/z (ESI⁺) 1146.4727 ([M+H]⁺ C₅₇H₆₈N₁₁O₁₃S requires 1146.4719).

HPLC R_t = 20.09 min. Purity = 95%.

*Purity corresponds to peak area determined by analytical HPLC following general procedure **7.1.3**.



7.7.12 Synthesis of PROTAC 134

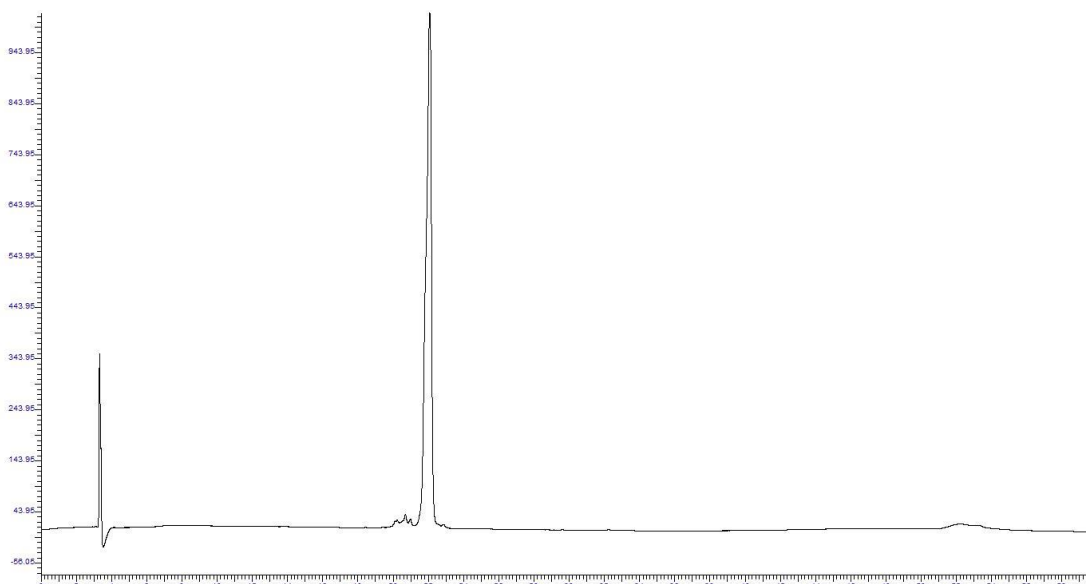


General procedure 7.6.7 was followed using peptide **118(ON)** and lenalidomide-acid conjugate **128** (3.00 equiv.). General procedure 7.6.4 was followed to afford crude PROTAC **134** (0.07 g) which was purified following general procedure 7.6.5 to afford PROTAC **134** as a white solid (17.0 mg).

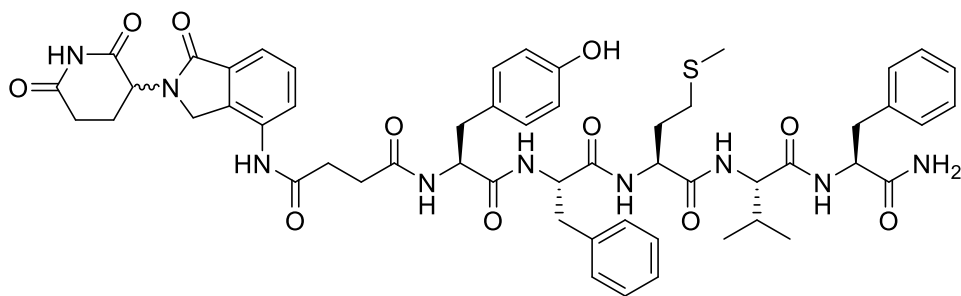
HRMS m/z (ESI⁺) 1032.4296 ([M+H]⁺ C₅₃H₆₂N₉O₁₁S requires 1032.4290).

HPLC R_t = 22.08, Purity = 99%.

*purity corresponds to peak area determined by analytical HPLC following general procedure 7.1.3.



7.7.13 Synthesis of PROTAC 135

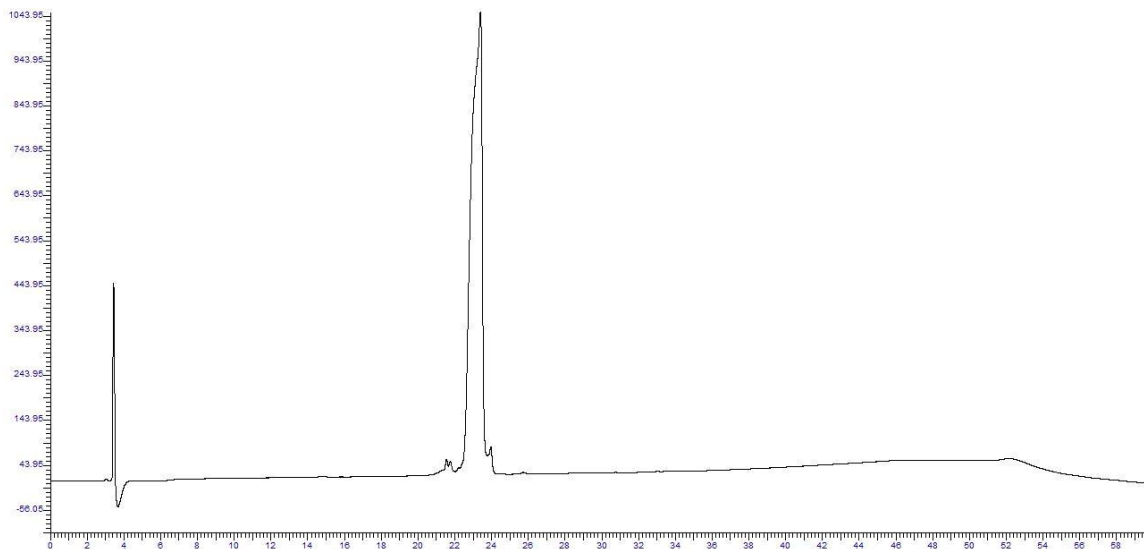


General procedure **7.6.7** was followed using peptide **116(ON)** and lenalidomide-acid conjugate **129** (3.00 equiv.). General procedure **7.6.4** was followed and 0.03 g of crude was purified following general procedure **7.6.5** to afford PROTAC **135** as a white solid (1.00 mg).

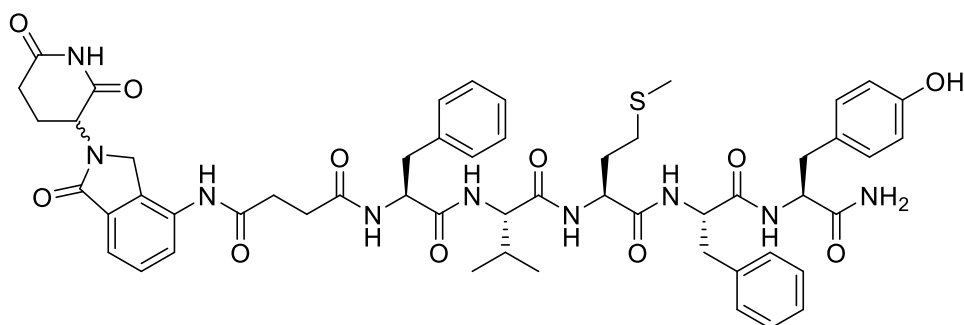
HRMS m/z (ESI⁺) 1046.4487 ([M+H]⁺ C₅₄H₆₃N₉O₁₁S requires 1046.4446).

HPLC R_t = 23.294, Purity = 97%.

*purity corresponds to peak area determined by analytical HPLC following general procedure **7.1.3**.



7.7.14 Synthesis of PROTAC 136

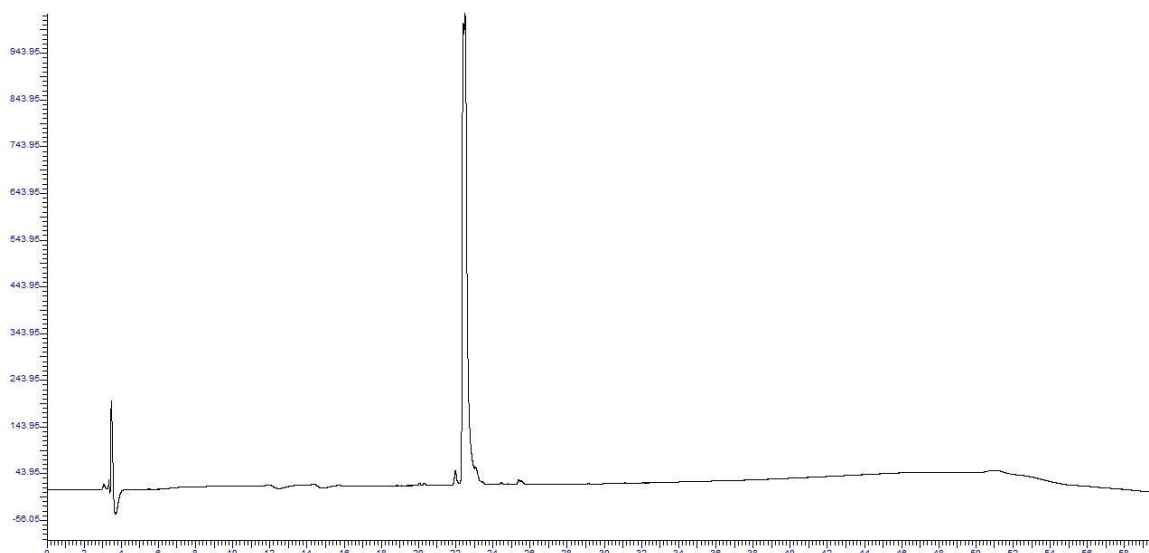


General procedure 7.6.7 was followed using peptide **116(ON)** and lenalidomide-acid conjugate **129** (3.00 equiv). General procedure 7.6.4 was used to afford crude PROTAC **136** (0.13 g) of which (0.05 g) was purified following general procedure 7.6.5 to afford PROTAC **136** as a white solid (6.30 mg).

HRMS m/z (ESI⁺) 1046.4447 ([M+H]⁺ C₅₄H₆₃N₉O₁₁S requires 1046.4446).

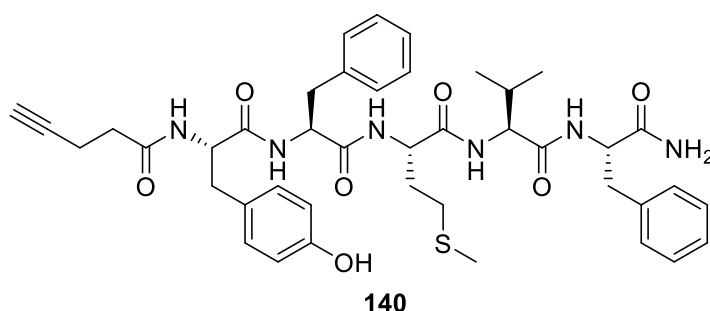
HPLC R_t = 22.50 (*note peak split in two).

*purity corresponds to peak area determined by analytical HPLC following general procedure 7.1.3.



7.8 Chemical synthesis of Group 2 PROTACs (Chapter 5)

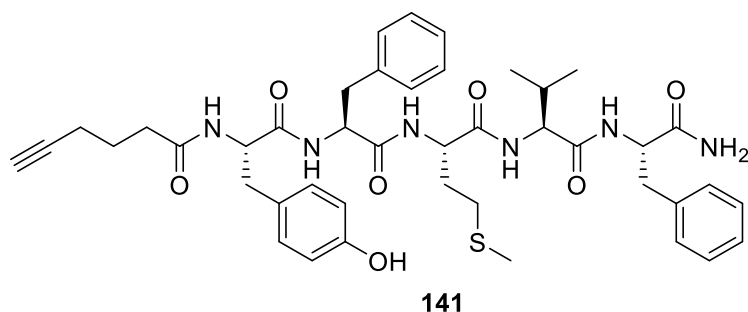
7.8.1 Synthesis of peptide 140



General procedure 7.6.7 was followed using 4-pentynoic acid (4.00 equiv.). General procedure 7.6.4 was used to afford peptide **140** as a crude beige solid (0.10 g). The product was deemed suitable by LCMS analysis to take onto the next step without purification.

m/z (ESI⁺) [M+H]⁺ = 785.62.

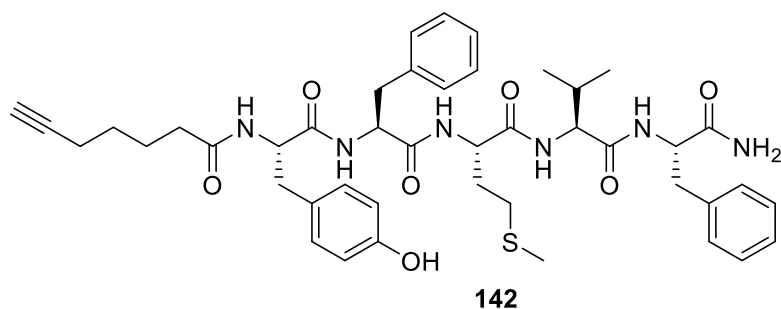
7.8.2 Synthesis of peptide 141



General procedure 7.6.7 was followed using 5-hexynoic acid (4.00 equiv.). General procedure 7.6.4 was used to afford peptide **141** as a crude beige solid (0.14 g). The product was deemed suitable by LCMS analysis to take onto the next step without purification.

m/z (ESI⁺) [M+H]⁺ = 799.64.

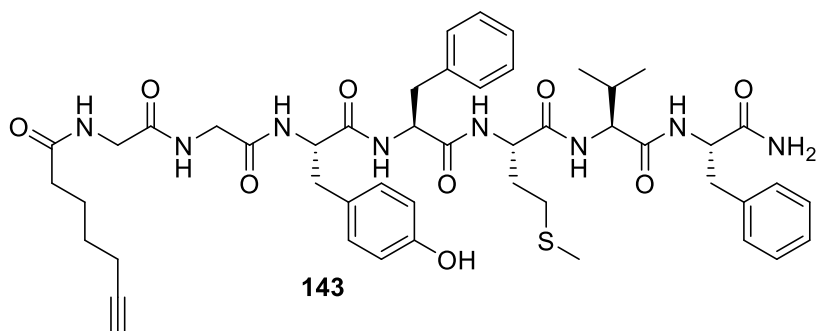
7.8.3 Synthesis of peptide 142



General procedure 7.6.7 was followed using 6-heptynoic acid (4.00 equiv.). General procedure 7.6.4 was used to afford peptide **142** as a crude beige solid (0.13 g). The product was deemed suitable by LCMS analysis to take onto the next step without purification.

m/z (ESI⁺) [M+H]⁺ = 813.66, R_t = 2.402

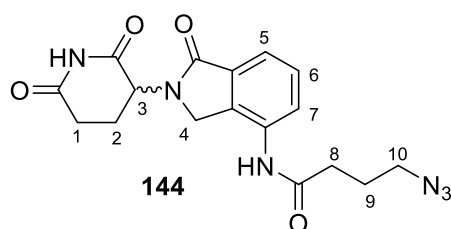
7.8.4 Synthesis of peptide 143



General procedure 7.6.7 was followed using 6-heptynoic acid (4.00 equiv.). General procedure 7.6.4 was used to afford peptide **143** as a crude beige solid (0.15 g). The product was deemed suitable by LCMS analysis to take onto the next step without purification.

m/z (ESI⁺) [M+H]⁺ = 927.675.

7.8.5 Synthesis of 4-azido-N-(2-(2,6-dioxopiperidin-3-yl)-1-oxoisindolin-4-yl)butanamide (144)



General procedure **7.6.1** was followed using 4-azido-butanoic acid (0.22 g, 1.71 mmol, 1.10 equiv.) to afford azide **144** as a white solid (0.35 g, 61%).

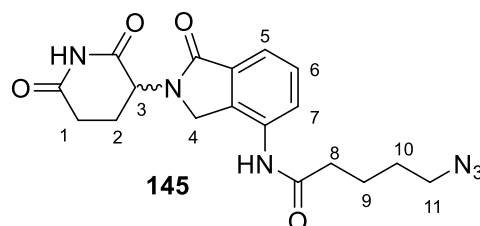
^1H NMR (400 MHz, DMSO) δ 1.87 (2H, p, $J = 7.0$ Hz, H_9), 1.98 – 2.08 (1H, m, H_2), 2.23 – 2.42 (1H, m, H_2), 2.47 (2H, t, $J = 7.3$ Hz, H_{10}), 2.55 – 2.68 (1H, m, H_1), 2.87 – 3.07 (1H, m, H_1), 3.40 -3.45 (2H, m, H_8), 4.34 (1H, d, $J = 17.5$ Hz, H_4), 4.41 (1H, d, $J = 17.5$, H_4), 5.15 (1H, dd, $J = 13.5$, 5.1 Hz, H_3), 7.44 – 7.60 (2H, m, H_6 , H_7), 7.82 (1H, dd, $J = 7.1$, 8.1 Hz, H_5), 9.88 (1H, s, NH), 11.04 (1H, s, NH).

^{13}C NMR (101 MHz, DMSO) δ 23.1, 24.8, 31.7, 33.2, 46.9, 50.8, 52.0, 119.6, 125.8, 129.1, 133.1, 134.1, 134.2, 168.3, 171.0, 171.5, 173.4.

HRMS m/z (ESI $^+$) 371.1467 ($[\text{M}+\text{H}]^+$ $\text{C}_{17}\text{H}_{19}\text{N}_6\text{O}_4$ requires 371.1468).

IR ν_{max} (solid) / cm^{-1} 1193 (s), 1675 (s, C=O), 2112 (s, N=N=N), 2977 (m, C-H), 3182 (m, N-H), 3338 (m, N-H).

7.8.6 Synthesis of 5-azido-N-(2-(2,6-dioxopiperidin-3-yl)-1-oxoisindolin-4-yl)pentanamide (145)



General procedure **7.6.1** was followed using 5-azido pentanoic acid (0.11 g, 0.77 mmol, 1.00 equiv.) to afford **145** as a white solid (0.11 g, 37%).

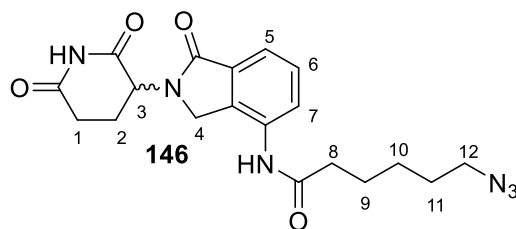
^1H NMR (400 MHz, DMSO) δ 1.48 – 1.79 (4H, m, H₉, H₁₀), 1.97 – 2.10 (1H, m, H₂), 2.29 – 2.43 (3H, m, H₂, H₁₁), 2.58 – 2.69 (1H, m, H₁), 2.92 (1H, ddd, J = 17.2, 13.6, 5.4 Hz, H₁), 3.22 – 3.49 (2H, m, H₈), 4.33 (1H, d, J = 17.5 Hz, H₄), 4.40 (1H, d, J = 17.5 Hz, H₄), 5.15 (1H, dd, J = 13.3, 5.1 Hz, H₃), 7.40 – 7.56 (2H, m, H₆, H₇), 7.81 (1H, dd, J = 7.1, 2.0 Hz, H₅), 9.82 (1H, s, NH), 11.04 (1H, s, NH).

^{13}C NMR (101 MHz, DMSO)* δ 27.5, 27.9, 33.0, 46.4, 40.4, 51.7, 56.0, 56.7, 124.3, 130.5, 133.9, 137.9, 138.9, 173.0, 176.2, 176.3, 178.1. (*missing ArC quaternary peak).

HRMS m/z (ESI⁺) 385.1632 ([M+H]⁺ C₁₈H₂₁N₆O₄ requires 385.1624).

IR ν_{max} (solid)/cm⁻¹ 1674 (s, C=O), 2092 (s, N=N=N), 3328 (m, N-H).

7.8.7 Synthesis 6-azido-N-(2-(2,6-dioxopiperidin-3-yl)-1-oxoisindolin-4-yl)hexanamide (146)



General procedure **7.6.1** was followed using 6-azido hexanoic acid (0.15 g, 0.92 mmol, 1.20 equiv.) to afford **146** as a white solid (0.14 g, 38%).

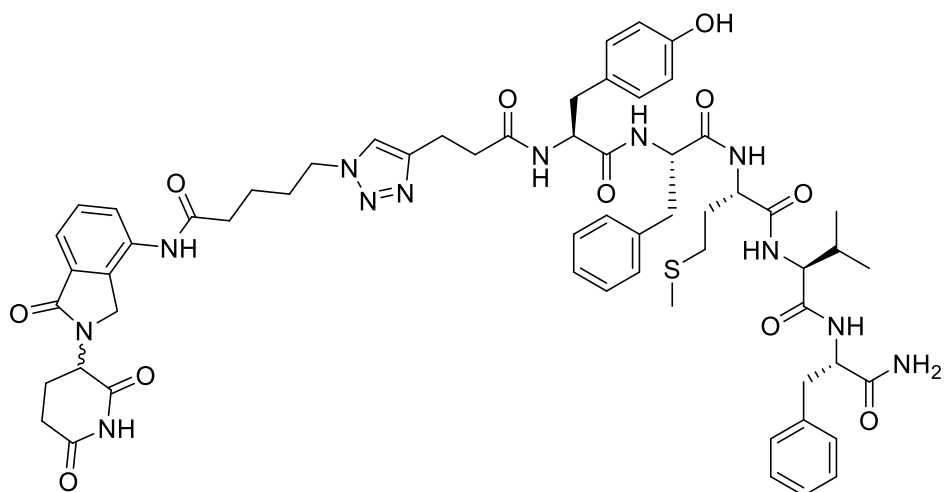
^1H NMR (400 MHz, DMSO) δ 1.34 – 1.42 (2H, m, H₁₁), 1.53 – 1.68 (4H, m, H₉, H₁₀), 1.99 – 2.19 (1H, m, H₂), 2.29 – 2.41 (1H, m, H₂), 2.38 (2H, t, J = 7.3 Hz, H₁₂), 2.54 – 2.68 (1H, m, H₁), 2.93 (1H, ddd, J = 17.3, 13.6, 5.4 Hz, H₁), 3.31 – 3.38 (2H, m, H₈), 4.34 (1H, d, J = 17.5 Hz, H₄), 4.40 (1H, d, J = 17.5 Hz, H₄), 5.16 (1H, dd, J = 13.3, 5.1 Hz, H₃), 7.37 – 7.57 (2H, m, H₆, H₇), 7.82 (1H, dd, J = 7.1, 1.9 Hz, H₅), 9.80 (1H, s, NH), 11.04 (1H, s, NH).

^{13}C NMR (101 MHz, DMSO) 23.1, 25.1, 28.5, 31.7, 36.1, 46.9, 51.0, 52.0, 119.5, 125.7, 129.1, 133.1, 134.2 (x 2), 134.3, 168.3, 171.6, 171.7, 173.3.

HRMS m/z (ESI⁺) 399.1794 ([M+H]⁺ C₁₉H₂₃N₆O₄ requires 399.1781).

IR ν_{max} (solid)/cm⁻¹ 1673 (s, C=O), 2092 (s, N=N=N), 3351 (m, N-H).

7.8.8 Synthesis of PROTAC 147

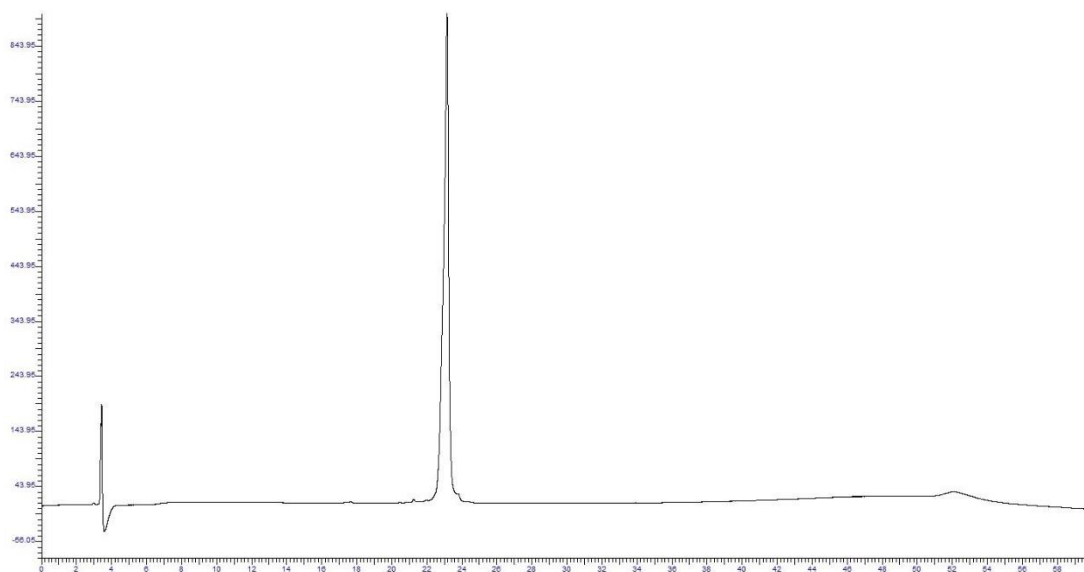


General procedure **7.6.7** was followed using peptide-alkyne conjugate **140** (0.05 g, 0.06 mmol, 1.00 equiv.) and lenalidomide-azide conjugate **145** (0.02 g, 0.06 mmol, 1.00 equiv.). This afforded crude PROTAC **147** (0.36 g) which was purified following general procedure **7.6.5** to afford PROTAC **147** as a white solid (4.3 mg).

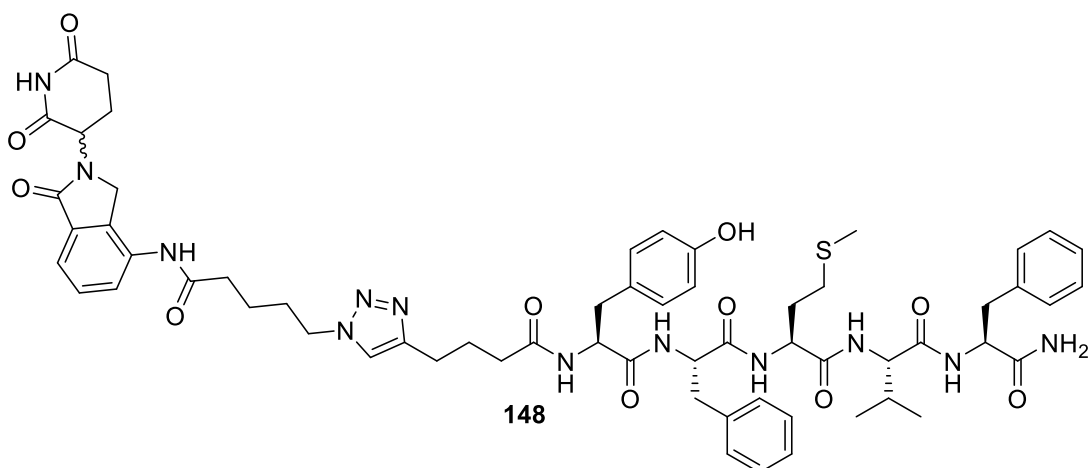
HRMS m/z (ESI⁺) 1169.5238 ([M+H]⁺ C₆₀H₇₃N₁₂O₁₁S requires 1169.5243).

HPLC R_t = 23.16 min, Purity = 100%.

*Purity corresponds to peak area determined by analytical HPLC following general procedure **7.1.3**



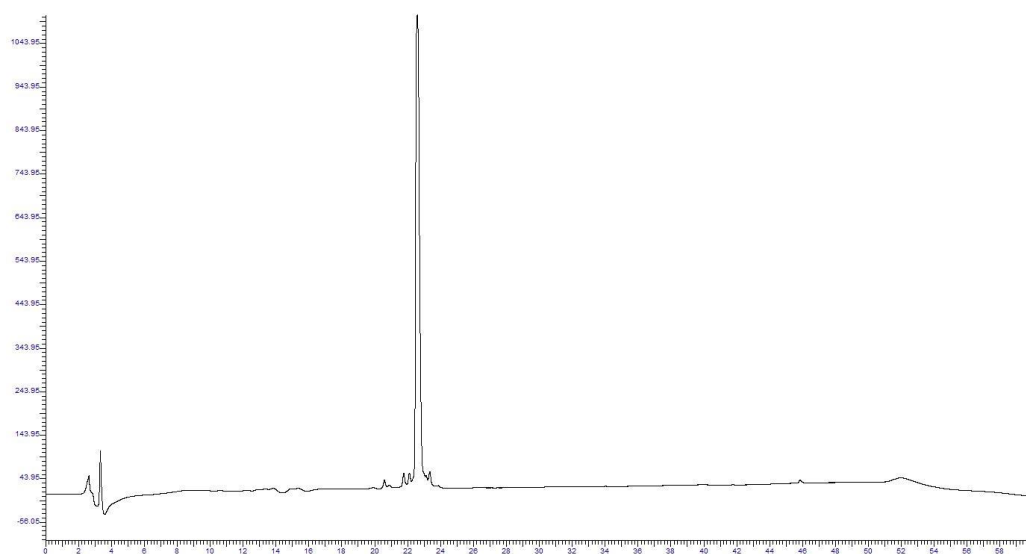
7.8.9 Synthesis of PROTAC 148



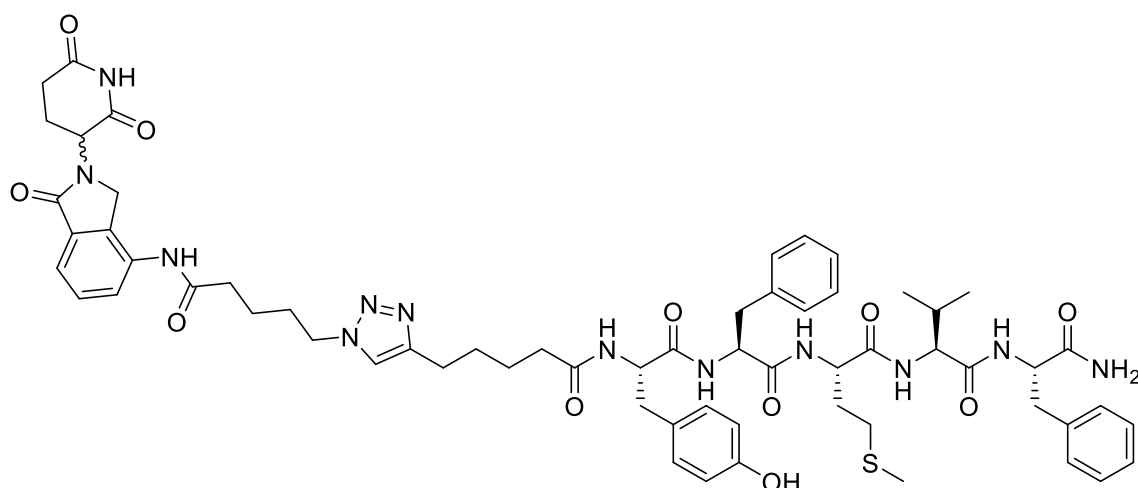
General procedure **7.6.7** was followed using peptide-alkyne conjugate **141** (0.07 g, 0.09 mmol, 1.00 equiv.) and lenalidomide-azide conjugate **145** (0.03 g, 0.09 mmol, 1.00 equiv.). This afforded crude PROTAC **148** of which 0.05 g was purified following general procedure **7.6.8** to afford PROTAC **148** as a white solid (14.0 mg).

HRMS m/z (ESI⁺) 1183.5408 ([M+H]⁺ C₆₁H₇₄N₁₂O₁₁S requires 1183.5399).

HPLC R_t = 22.59 min, Purity = 96%. *Purity corresponds to peak area determined by analytical HPLC following general procedure **7.1.3**



7.8.10 Synthesis of PROTAC 149

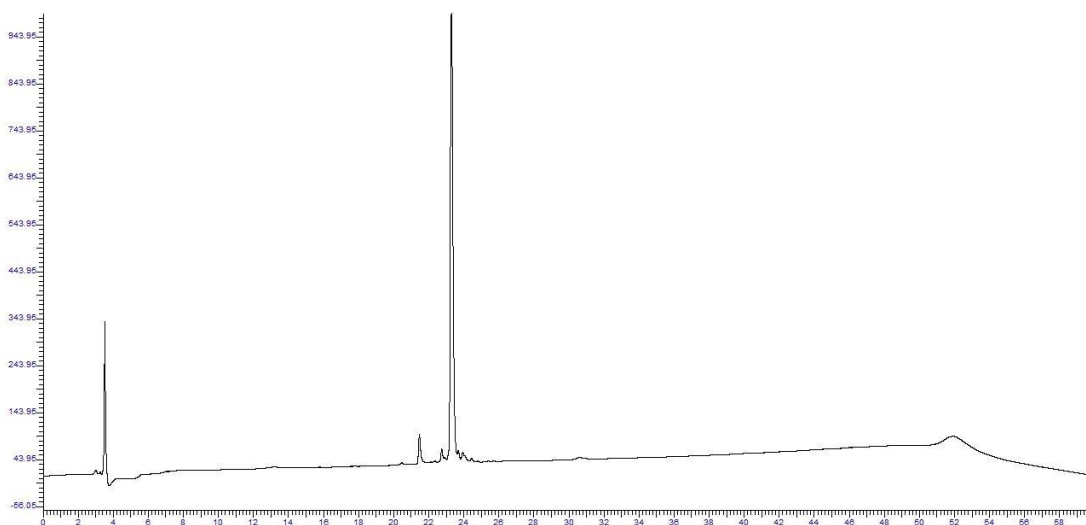


General procedure **7.6.8** was followed using peptide-alkyne conjugate **142** (0.05 g, 0.06 mmol, 1.00 equiv.) and lenalidomide-azide conjugate **145** (0.02 g, 0.06 mmol, 1.00 equiv.). This afforded 0.30 g of crude PROTAC **149** which was purified following general procedure **7.6.5** to afford PROTAC **149** as a white solid (2.30 mg).

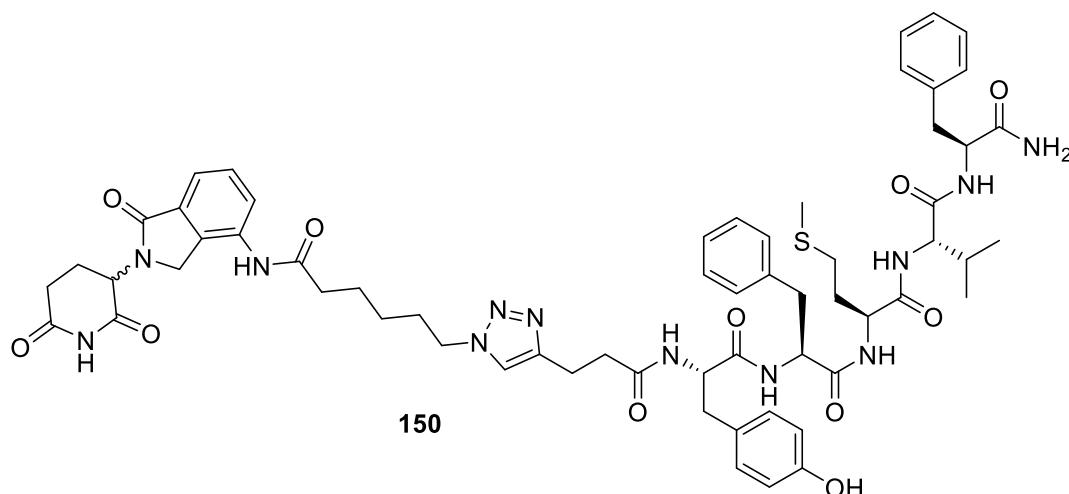
HRMS m/z (ESI⁺) 1197.5544 ($[M+H]^+$ C₆₂H₇₇N₁₂O₁₁S requires 1197.5555).

HPLC R_t = 23.30 min, Purity = 92%.

*Purity corresponds to peak area determined by analytical HPLC following general procedure **7.1.3**



7.8.11 Synthesis of PROTAC 150

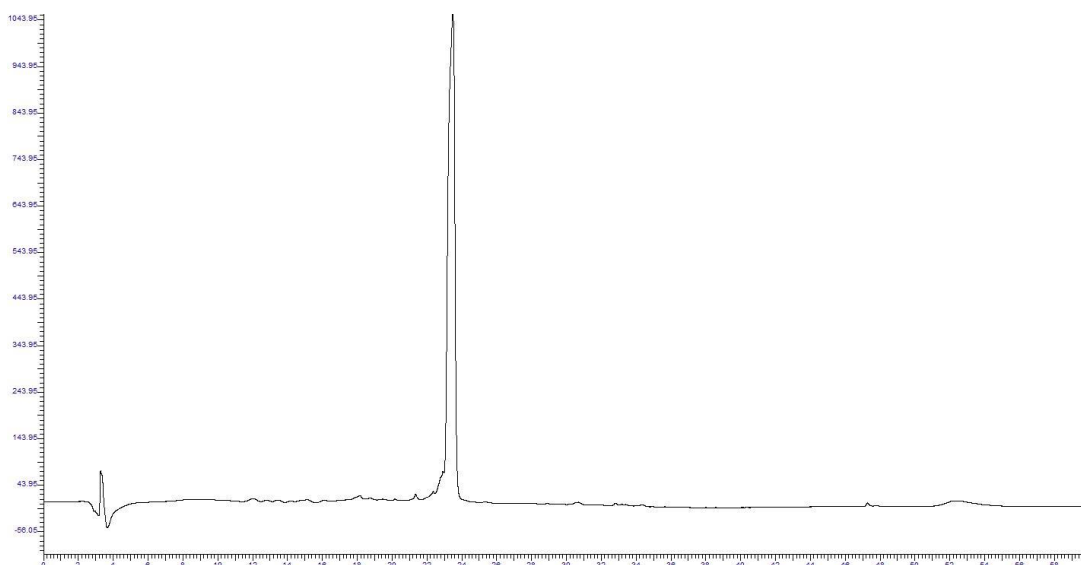


General procedure **7.6.8** was followed using peptide-alkyne conjugate **140** (0.05 g, 0.06 mmol, 1.00 equiv.) and lenalidomide-azide conjugate **146** (0.03 g, 0.09 mmol, 1.00 equiv.). The afforded crude PROTAC **150** (0.05 g) which was purified following general procedure **7.6.8** to afford PROTAC **150** as a white solid (4.40 mg).

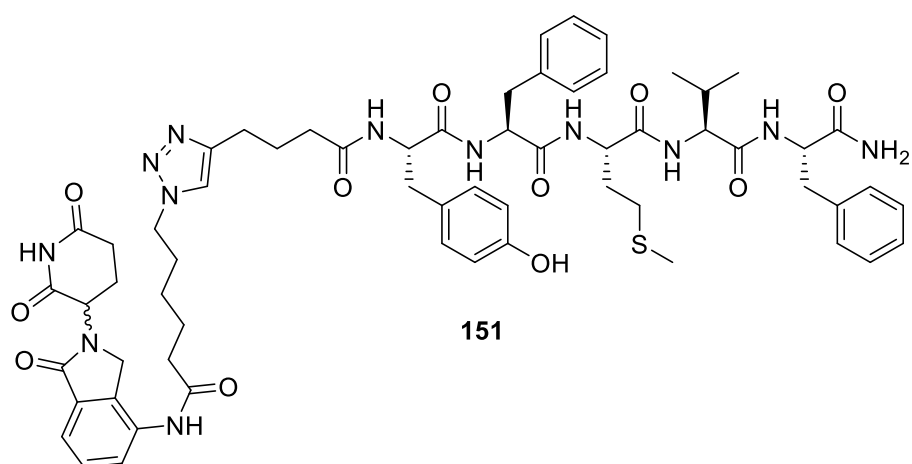
HRMS m/z (ESI⁺) 1183.5398 ([M+H]⁺ C₆₁H₇₅N₁₂O₁₁S requires 1183.5399).

HPLC R_t = 23.49 min, Purity = 95%.

*Purity corresponds to peak area determined by analytical HPLC following general procedure **7.1.3**.



7.8.12 Synthesis of PROTAC 151

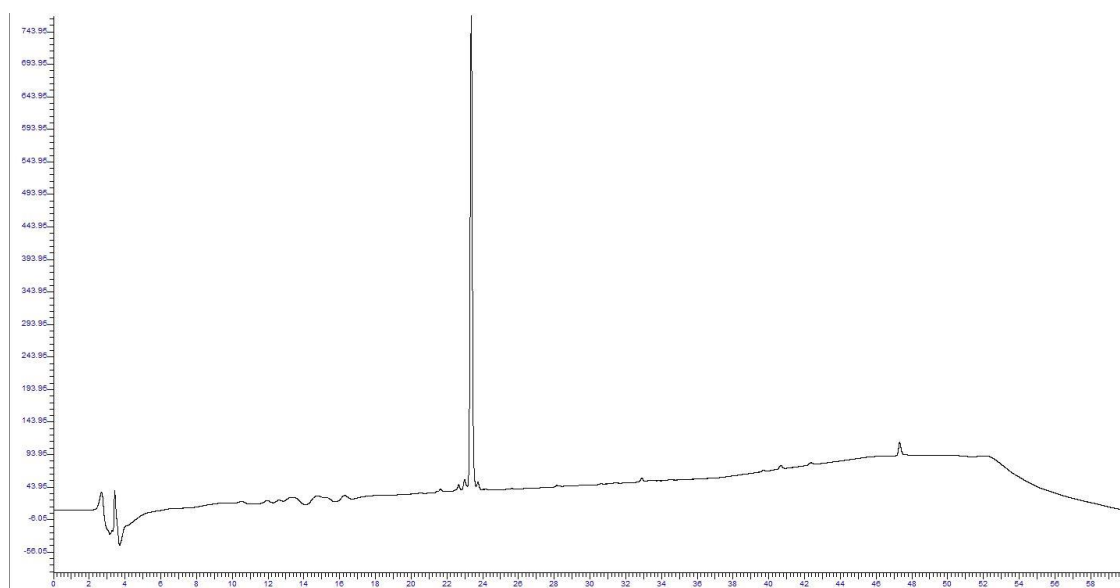


General procedure **7.6.8** was followed using peptide-alkyne conjugate **141** (0.07 g, 0.09 mmol, 1.00 equiv.) and lenalidomide-azide conjugate **146** (0.03 g, 0.09 mmol, 1.00 equiv.). This afforded crude PROTAC **151** (0.07 g) of which 0.03 g was purified following general procedure **7.6.5** to afford PROTAC **151** as a white solid (1.40 mg).

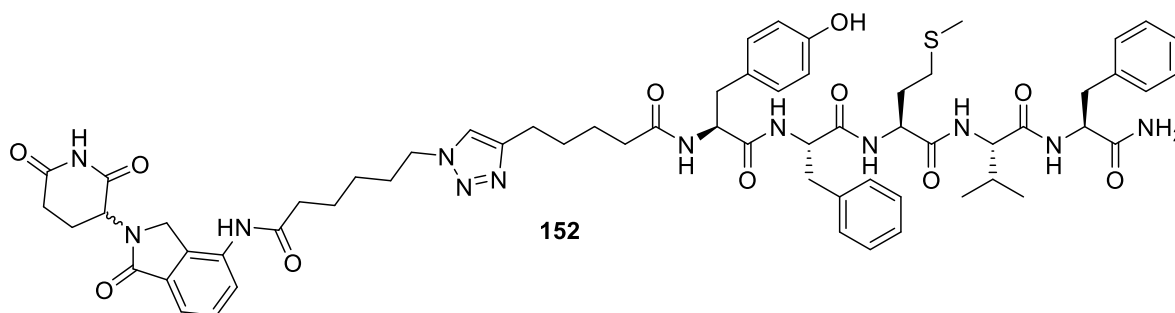
HRMS m/z (ESI⁺) 1197.5542 ([M+H]⁺ C₆₂H₇₇N₁₂O₁₁S requires 1197.5555).

HPLC R_t = 23.36, purity = 94%.

*Purity corresponds to peak area determined by analytical HPLC following general procedure **7.1.3**.



7.8.13 Synthesis of PROTAC 152

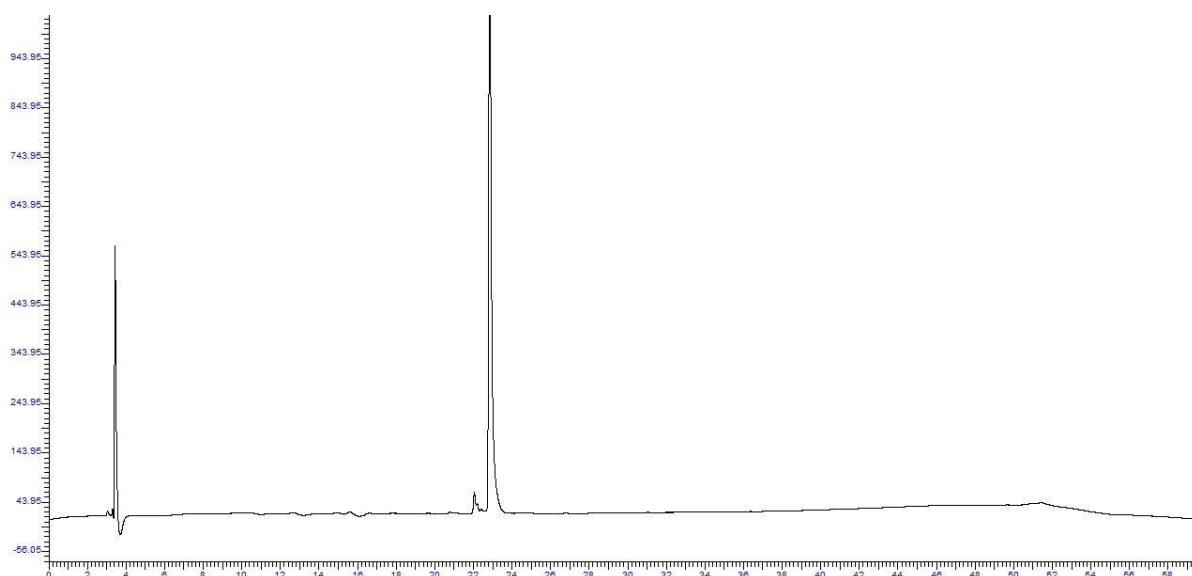


General procedure **7.6.8** was followed using peptide-alkyne conjugate **142** (0.11 g, 0.13 mmol, 1.00 equiv.) and lenalidomide-azide conjugate **146** (0.05 g, 0.13 mmol, 1.00 equiv.). This afforded crude PROTAC **152** (0.18 g) of which 0.05 g was purified following general procedure **7.6.5** to afford PROTAC **152** as a white solid (1.20 mg). (*Note* – in order to obtain pure material the HPLC purification had to be repeated).

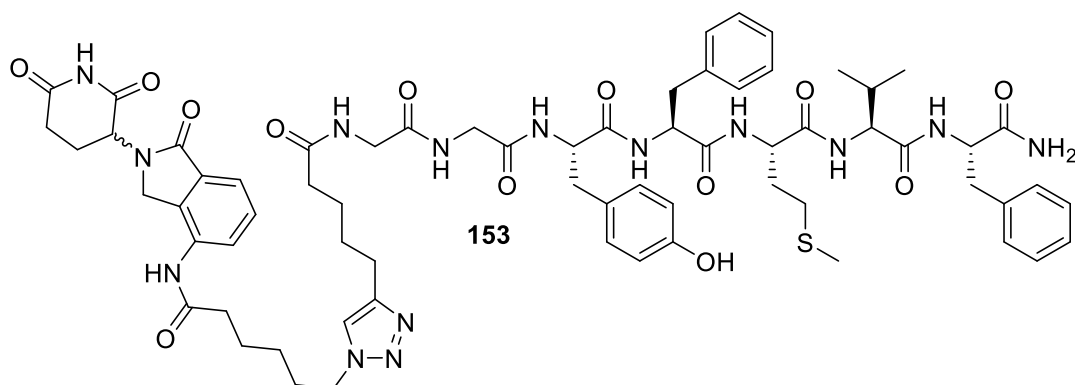
HRMS m/z (ESI⁺) 1211.5735 ([M+H]⁺ C₆₃H₇₈N₁₂O₁₁S requires 1211.5602).

HPLC R_t = 22.85 min, purity = 96%.

*Purity corresponds to peak area determined by analytical HPLC following general procedure **7.1.3**



7.8.14 Synthesis of PROTAC 153

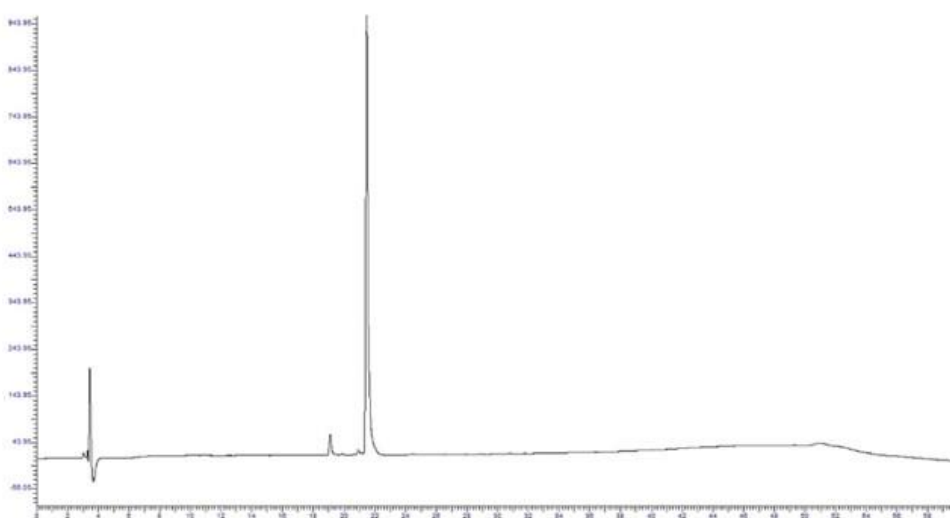


General procedure **7.6.8** was followed using peptide-alkyne conjugate **143** (0.07 g, 0.08 mmol, 1.00 equiv.) and lenalidomide-azide conjugate **146** (0.03 g, 0.08 mmol, 1.00 equiv.). This afforded crude PROTAC **153** (0.08 g) which was purified following general procedure **7.6.5** to afford PROTAC **153** as a white solid (2.70 mg).

HRMS m/z (ESI⁺) 1325.6133 ([M+H]⁺ C₆₇H₈₄N₁₄O₁₃S requires 1325.6141).

HPLC R_t = 24.46 min. Purity = 96%.

*Purity corresponds to peak area determined by analytical HPLC following general procedure **7.1.3**.



7.9 Biochemical methods (Chapter 3)

7.9.1 Plasmid Transformation

The *hsCCL2* plasmid was obtained from Genscript and was transformed into BL21(DE3) competent *E. coli* cells. The plasmid (4 µg) was spun (2000 g at 40 °C, 1 min) and reconstituted in MilliQ water (20 µL). The plasmid mixture (2 µL) was added to *E. coli* cells (50 µL) and placed onto ice (30 min). The cells were subjected to heat shock (10 min at 42 °C) and placed back onto ice (5 min). SOC media (950 µL) was added to the cells and the mixture was agitated (250 rpm, 37 °C, 1 h). The cells were mixed (inversion) and 100 µL was plated on LB agar (with 100 µg/mL ampicillin) and grown overnight (37 °C, 16 h).

7.9.2 Stock formation

Single colonies were selected from transformation plates and were used to inoculate 4 x 10 mL LB (20 g/L; 100 µg/mL ampicillin) which were grown overnight (37 °C, 150 rpm, 20 h). Glycerol stocks were made with these cultures using 50:50 v/v culture:glycerol (1 mL). These were stored long term at -80 °C.

7.9.3 Medium-scale protein expression

25 mL starter cultures (20 g/L LB; 100 µg/mL ampicillin) were generated from *hsCCL2* glycerol stocks and were grown overnight (37 °C, 150 rpm, 20 h). 6 x 1 L LB (20 g/L; 100 µg/mL ampicillin) were inoculated with the starter cultures (25 mL) and grown to OD₆₀₀ 0.4 – 0.6 (37 °C, 150 rpm, ~ 4 h). Overexpression was induced with IPTG (1 mM) followed by further agitation overnight (either 30 °C or 20 °C, 150 rpm, 20 h). The cell was harvested by centrifugation using a Beckmann Avanti Hi-Speed centrifuge (JLA-8.1000 rotor, 1300 g, 4 °C, 25 min). The supernatant was decanted and the cell pellet stored at -80°C until required for purification.

7.9.4 Large scale protein expression

25 mL starter cultures (20 g/L LB; 100 µg/mL ampicillin) were generated from *hsCCL2* glycerol stocks and were grown overnight (37 °C, 150 rpm, 20 h). 10 x 500 mL LB (20 g/L;

100 µg/mL ampicillin; 5 drops of antifoam) were inoculated with the starter cultures (25 mL) and grown to OD₆₀₀ 1.25 (38.5 °C, 6 h) using a Harbinger LEX™-48 Bioreactor. This was heated under constant air flow (< 10 PSI). Overexpression was induced with the addition of IPTG (1 mM final concentration), and the temperature was reduced (31.5 °C) and incubated overnight (20 h). The cell was harvested by centrifugation using a Beckmann Avanti Hi-Speed centrifuge (JLA-8.1000 rotor, 1300 g, 4 °C, 25 min). The supernatant was decanted, and the cell pellet stored at -80 °C until required for purification.

7.9.5 Immobilised metal ion affinity chromatography (IMAC)

The following buffers were used in this purification:

IMAC Binding buffer: 20 mM imidazole, 300 mM NaCl, 50 mM NaH₂PO₄, pH 7.5.

IMAC Elution buffer: 1M imidazole, 300 mM NaCl, 50 mM NaH₂PO₄, pH 7.5.

IMAC Dialysis buffer: 50 mM NaH₂PO₄

Cell pellets were thawed on ice and resuspended in 20 mL binding buffer with complete Mini EDTA-free Protease Inhibitor Cocktail (1 tablet). The suspension was sonicated on ice (50% power, 2 x 1 min) and the cell was harvested by centrifugation using a Beckmann Avanti Hi-Speed centrifuge (JA-25.50 rotor, 50,000 g, 4 °C, 50 min). The lysate was filtered (0.22 µm) and loaded onto a 1 mL HisTrap™ HP affinity column (Cytiva). The column was washed with 5 column volumes (CVs) of IMAC binding buffer on an AKTA Pure FPLC and the target protein was eluted in 0.5 or 1 mL fractions using a 20 CV linear imidazole gradient (20 mM – 50 mM). Absorbance was detected at λ = 280 nm. Fractions containing *hsCCL2* were combined and purified by IEX or SEC, or they were dialysed overnight and stored at -80 °C.

7.9.6 Ion exchange chromatography (IEX)

The following buffers were used in this purification:

IEC Binding buffer: 50 mM Tris base, pH 7.5.

IEC Elution buffer: 50 mM Tris-base, 1 M NaCl, pH 7.5.

IEC Dialysis buffer: 30 mM Tris-base, 300 NaCl, pH 7.5.

Protein elution volumes obtained from IMAC were concentrated to 5 mL using VivaSpin™ spin concentrators, MWCO; 3,000 Da. Concentrated protein (5 mL) was injected onto a Mono S 5/100 GL column (Cytiva) via a 5 mL injection loop on an AKTA Pure FPLC. Protein was eluted into 0.5 mL fractions and absorbance was detected at $\lambda = 280$ nm. The resulting fractions were stored at 4 °C until further required, or dialysed into dialysis buffer for further use.

7.9.7 Size Exclusion Chromatography

The following buffer was used in this purification:

SEC buffer: 50 mM NaH₂PO₄, pH 7.5.

Size exclusion chromatography (SEC) was performed using a 120 mL HiLoad 16/600 Superdex 75 pg column on an AKTA pure FPLC. The column was equilibrated with 1.5 CVs of SEC buffer. Protein elution volumes obtained from IMAC were concentrated to 5 mL using VivaSpin™ spin concentrators (Cytiva), MWCO; 3,000 Da. Concentrated protein sample (5 mL) was injected onto the column via a 5 mL loop. The protein was eluted in 1.5 mL fractions using two column volumes (CVs) of SEC buffer at a flow rate of 1 mL/min. Absorbance was detected at $\lambda = 280$ nm. The resulting protein fractions were stored at -80 °C until required.

7.9.8 SDS-PAGE

Following protein purification, fractions were assessed using SDS-PAGE. Novex™ Tris-Glycine protein gels (16%) were run at 200 V for 45 – 50 min. Gels were subsequently

stained with InstantBlue™ Coomassie stain and imaged using a BioRad Molecular Imager GelDoc™ XR + with ImageLab™ Software. Samples were run against 5 µL of a 10 – 180 kDa PageRuler™ Pre-stained Protein Ladder or 10 – 250 kDa PageRuler Plus™ Pre-stained Protein Ladder (Thermo Scientific).

7.9.9 Sample preparation (for SDS-PAGE)

SDS loading buffer (4 µL) was added to the sample (16 µL) and the mixture was heated at 96 °C for 10 min. 5 µL of sample was loaded onto the gel.

7.9.10 ES⁺ TOF MS

Protein samples were buffer exchanged into MilliQ water and concentrated to 0.5 – 1 mg/mL using a VivaSpin™ MWCO: 3000, spin concentrator (Cytiva). Samples were analysed by electrospray ionisation (ESI) mass spectrometry using a Quad Time-of-flight (QToF) Premier Spectrometer (Waters).

7.9.11 Trypsin digest MS

Trypsin digest tandem MS experiments were performed by Dr A. Brown at the Proteomics Facility, Durham University. SDS-PAGE protein bands were provided for analysis.

7.9.12 Circular Dichroism (CD)

CD spectra were recorded on a Jasco J-1500 spectrometer, filled with a Jasco MCB-100 mini circulation bath. All samples were recorded as the average of 10 accumulations using a QS high precision cell with 0.1 cm of path length from Hellma Analytics. 0.5 mg/mL *hsCCL2* was prepared (in 50 mM H₂PO₄) and for recorded spectra, the buffer baseline was subtracted.

7.9.13 Surface Plasmon Resonance (SPR)

SPR experiments were carried out using a Biacore S200 (GE Healthcare Life Sciences) on either a Sensor Chip SA (Cytiva) or a Sensor Chip NTA (Cytiva). Experiments were performed using single cycle kinetics, in which each compound was injected sequentially in order of increasing concentration over both immobilised protein and reference surfaces. Compound stocks were made to 10 mM in DMSO. For *hsCCL2* (NTA) 4 concentrations of compound: (0.1 μ M, 1 μ M, 10 μ M and 100 μ M) and *BtnCCL2* (SA) 6 concentrations of compound: (2.5 μ M, 5.0 μ M, 25 μ M and 50 μ M, 100 μ M and 200 μ M) were prepared in 20 mM HEPES, 150 mM NaCl, 0.01% Tween-20, 1% DMSO, pH 7.4 in series across all flow cells. All experiments were conducted in SPR running buffer (20 mM HEPES, 150 mM NaCl, 0.01% Tween-20, 1% DMSO, pH 7.4) and used an 8-point DMSO solvent correction to account for any bulk flow interactions. Responses were analysed using Biacore s200 Evaluation Software (GE Healthcare Life Sciences, Chicago, IL, USA) using affinity fit.

$$\textit{Theoretical } R(\text{max}) = \frac{MW(\textit{ligand})}{MW(\textit{CCL2})} \times \textit{Immobilised CCL2 (RU)}$$

7.9.14 Protein capture (NTA)

NTA chip surface was regenerated with EDTA (300 mM) before injection of NiCl_2 buffer (0.5 mM) followed by EDC-NHS (1:1). *HsCCL2* (approx. 1mg/ml) was diluted to 100 μ g/mL in sodium acetate buffer (10 mM, pH 5.0) and the protein was exposed to the surface for 23 min until saturation was achieved. The surface was then exposed to injections of ethanolamine buffer (1 M) followed by EDTA (300 mM).

7.9.15 Protein capture (SA)

The SA chip was stabilised with 3 injections of regeneration buffer (1 M NaCl, 50 mM NaOH). *BtnCCL2* (10 mg/mL) was diluted to 100 μ g/mL in DMSO free SPR buffer. The protein was exposed to the surface for 160 s.

7.10 Molecular biology methods (Chapter 2)

7.10.1 THP-1 cell culture

THP-1 is a human monocytic cell line derived from an acute monocytic leukaemia patient; ATCC TIB-202. THP-1 cells grow in suspension and were cultured in RPMI 1640 medium with 10% FBS and penicillin/ streptomycin (100 µg/mL). The cells were maintained at 1×10^5 cells/mL and were not allowed to exceed 1×10^6 cells/mL. They were split every 3 - 4 days at a 1:3 ratio.

7.10.2 THP-1 cell migration (chemotaxis) assays

The ability of compounds to inhibit the CCL2-mediated chemotaxis of THP-1 cells was assessed using a 24-transwell system formed by placing 3.0 µm pore polyester membrane inserts (Sardstedt) into 24-well culture plates. Firstly, the lower compartment was blocked with blocking buffer (1 mL, 2% BSA in PBS) for 1 h (minimum). This was removed before CCL2 (1 mg/mL) was diluted as required in chemotaxis buffer (0.2% BSA in serum free RPMI) and was added to the lower compartment (500 µL). The DKPs were dissolved in DMSO and were used at 50 µM. R5 504393 (Tocris) stock solution (5 mM in DMSO) was diluted in serum free RPMI for a final assay concentration of 330 nM. THP-1 cells (300,000) were resuspended in chemotaxis buffer (300 µL) and were added to the upper compartment. These were allowed to migrate through the membrane (37 °C, 5% CO₂, 3 h). After this, the cells were removed from the upper compartment and the compartment was washed with PBS (2 x 200 µL). The flow-through was removed and placed into flow-cytometry tubes and the lower compartment was washed with PBS (2 x 500 µL) and placed into the corresponding tubes. Accutase® (300 µL) was then added to the lower compartment and the plates were agitated (300 rpm, 37 °C, 5 min). The Accutase® solution was removed and added to the corresponding flow-cytometry tubes. Cell samples were resuspended in PFA buffer (200 µL, 4% paraformaldehyde in PBS) and incubated (rt, 15 min). The cells were washed with PBS (2 x 200 µL) and resuspended in FACs buffer (200 µL, 2% BSA in PBS). CountBright™ Absolute Counting Beads (20 µL) were added to

each sample and the number of cells were analysed using a Fortessa X20 Flow Cytometer, recording 2,000 events. The negative control used was the absence of CCL2. Assays were conducted in technical duplicate and biological triplicate. The absolute count (cells/ μL) was calculated using the following formula:

$$\text{Absolute cell count} \left(\frac{\text{cells}}{\mu\text{L}} \right) = \frac{(\text{Cell count} \times \text{counting bead vol})}{(\text{Counting bead count} \times \text{cell vol})} \times \text{Counting beads conc} \left(\frac{\text{beads}}{\mu\text{L}} \right)$$

7.10.3 Cell apoptosis assay

Dead and alive cells were determined using: Dead Cell Apoptosis Kit with Annexin V FITC and Propidium Iodide for Flow Cytometry (Invitrogen). In flow cytometry tubes, THP-1 cells (300,000) were suspended in serum free RPMI (500 μL) containing each DKP treatment (50 μM or 100 μM , 0.02 % DMSO) and were incubated (37 $^{\circ}\text{C}$, 5% CO_2 , 3 h). For the positive control, half a sample of untreated cells (250 μL , ~ 150,000 cells) were subjected to heat shock (65 $^{\circ}\text{C}$, 1 min). The cell sample was immediately placed on ice, before combining with the original sample. Following incubation, the cells were placed on ice and washed with ice cold FACs buffer (2 x 500 μL) before resuspension in binding buffer (200 μL). To each cell sample was added FITC Annexin V (5 μL of solution in 25 mM HEPES, 140 mM NaCl, 1 mM EDTA, pH 7.4, 0.1 % BSA) and PI (10 μL of 5 mM solution in deionised water). Samples were gently vortexed and incubated in the dark (rt, 15 min). 1 x Annexin V binding buffer (400 μL of 50 mM HEPES, 700 mM NaCl, 12.5 CaCl_2 , pH 7.4) was added to each tube. FACs was performed using a Fortessa X20 flow cytometer, recording at least 10,000 events. Assays were conducted in triplicate.

7.10.4 CCR2 internalisation assay

THP-1 cells (200,000) were resuspended in serum free RPMI (500 μL). The corresponding treatments were added: 100 nM CCL2, DKP compounds only, or CCL2 + DKP compounds and the cells were incubated (37 $^{\circ}\text{C}$, 5% CO_2 , 30 min). Cells were placed on ice and washed with ice-cold PBS (2 x 500 μL). Cells were resuspended in FACs buffer (100 μL) and an APC anti-human CD192 CCR2 antibody (2 μL , Biolegend) or APC Mouse IgG2a

isotype control antibody (2 μ L, Biolegend) was added. Cells were incubated in the dark (rt, 30 min) and washed with PBS (2 x 300 μ L). Following this, the cells were resuspended in PFA buffer (300 μ L) and incubated (rt, 15 min). Cells were washed again in PBS (2 x 300 μ L) and resuspended in FACs buffer (200 μ L). Flow cytometry was performed using a Fortessa X20 flow cytometer, recording at least 10,000 events. All assays were carried out in triplicate.

7.11 Molecular biology methods (Chapter 4)

7.11.1 HMEC-1 cell culture

HMEC-1 cells are a human microvascular endothelial cell line.¹¹ HMEC-1 cells grow adherently and were cultured in 75 cm³ flasks in MCDB131 medium, supplemented with 10% FBS, 1 μ g/mL hydrocortisone, 10 nM L-glutamine, penicillin/streptomycin (100 μ g/mL), 10 ng/mL epidermal growth factor in a humidified atmosphere at 37 °C with 5% CO₂.

7.11.2 Cell viability (HMEC-1 cells)

The cell viability of HMEC-1 cells with each PROTAC treatment was assessed using a Cell Proliferation Kit II (XTT) (Sigma Aldrich). HMEC-1 cells (10,000) in MCDB131 were seeded overnight in a 96-well plate. The media was removed and the cells were washed with PBS (2 x 100 μ L). 6 concentrations of PROTAC treatment (10 μ M, 1 μ M, 100 nM, 10 nM, 1 nM, 0.1 nM) were prepared in serum free MCDB131. These were added to the cells (100 μ L) and the plate was incubated (37 °C, 5% CO₂, 24 h). Next, the media was removed and the cells were washed with PBS (100 μ L). Fresh MCDB131 (100 μ L) and the XTT labelling mixture (50 μ L) were added and the cells were incubated (37 °C, 5% CO₂, 24 h). Absorbance was measured using a microplate (ELISA) reader. The experiments were carried out in technical and biological triplicate.

7.11.3 PROTAC degradation assay

Stock solutions of PROTAC (10 mM, DMSO) were diluted in serum free MCDB131 to the desired final concentration. HMEC-1 cells (200,000) were seeded in 6-well plates using serum free MCDB131 (1.5 mL) and were incubated (37 °C, 5% CO₂, 16 h). The media was removed from each well and the cells were washed with PBS (2 x 500 µL). The corresponding treatments (1.5 mL) were then added to the cells: media only (untreated), TNF-α (10 ng/mL) only, 0.01% DMSO vehicle control +TNF-α (10 ng/mL), or PROTAC + TNF-α (10 ng/mL) and the plate was incubated (37 °C, 5% CO₂, 24 h). The media was removed from each well, subjected to centrifugation at 300 G and stored at -20°C until further use. CCL2 levels were quantified using a Human CCL2/MCP-1 ELISA Kit (R&D systems) and the experiment was carried out in biological and technical triplicate.

7.11.4 Data processing

Data was processed as the mean ± SEM of replicates. *t*-tests and one-way ANOVA were performed using PRISM GraphPad to establish levels of significance in comparison to control values.

7.12 References

1. M. Teixidó, E. Zurita, R. Prades, T. Tarrago and E. Giralt, *Adv. Exp. Med. Biol.*, 2009, **611**, 227–228.
2. A. Hudson, PhD Thesis, Durham University, 2015 (available online via Durham University DRO).
3. M. M. Bobylev, L. I. Bobyleva and G. A. Strobel, *J. Agric. Food Chem.*, 1996, **44**, 3960-3964.
4. W. D. G. Brittain and S. L. Cobb, *J. Org. Chem.*, 2020, **85**, 6862–6871.
5. A. Obregón-Zúñiga and E. Juaristi, *Tetrahedron.*, 2017, **73**, 5373–5380.
6. M. Harizani, E. Katsini, P. Georgantea, V. Roussis and E. Ioannou, *Molecules.*, 2020, **25**, 13–17.
7. M. Cortes-Clerget, J. Y. Berthon, I. Krolkiewicz-Renimel, L. Chaisemartin and B. H. Lipshutz, *Green Chem.*, 2017, **19**, 4263–4267.
8. T. T. H. Dat, N. T. K. Cuc, P. V. Cuong, H. Smidt and D. Sipkema, *Mar. Drugs.*, 2021, **19**, 353.
9. G. M. Burslem, P. Ottis, S. Jaime-Figueroa, A. Morgan, P. M. Cromm, M. Toure and C. M. Crews, *ChemMedChem.*, 2018, **13**, 1508–1512.
10. *US Pat.*, WO2020/176983A1, 2020.
11. E. W Ades, F. J. Candal, R. A. Swerlick, V. G. George, S. Summers and D. C. Bosse, *J. Invest. Dermatol.*, 1992, **6**, 683–690.

8. Appendices

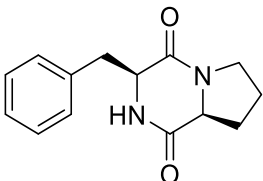
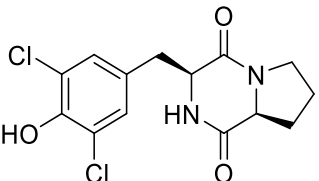
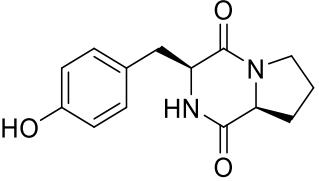
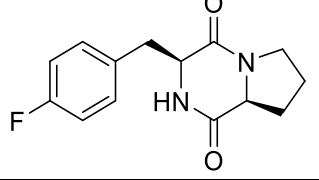
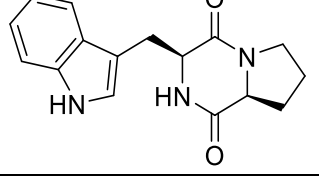
8.1 Trypsin digest for *hsCCL2* (Chapter 3, Section 3.7.1)

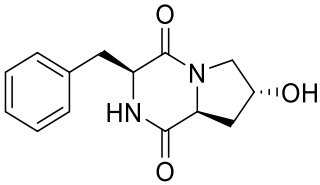
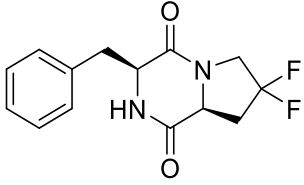
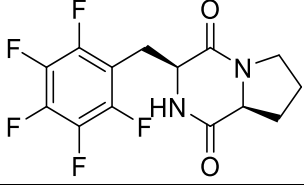
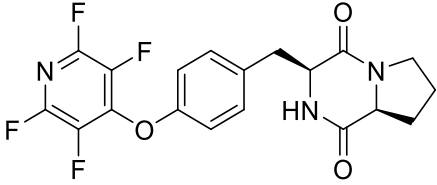
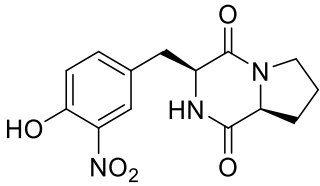
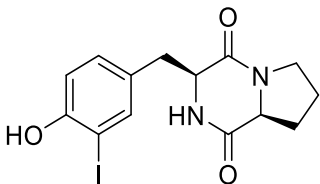
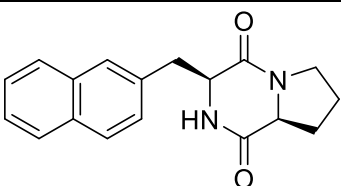
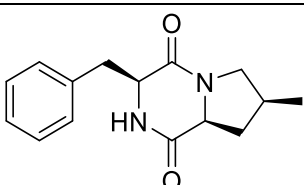
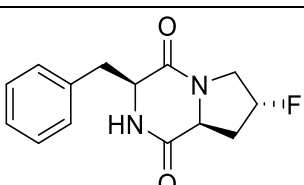
10 kDa - Protein coverage of database entry 'lzyy_seq_4-6-21'.

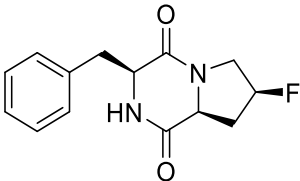
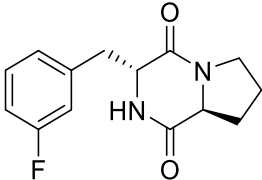
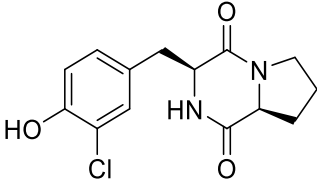
MGSSHHHHHHHSSGLVPRGSHMQPDAINAPVTCCYNFTNRKISVQRLASYRRITSSKCPKEAV
IFKTIVAKEICADPKQKWVQDSMDHLDKQTQTPKT

ProteinPilot database search engine output. Green are peptides identified with high confidence scores, yellow – medium confidence and red low.

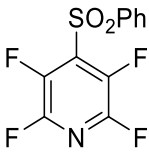
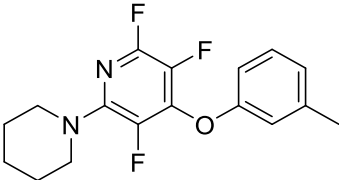
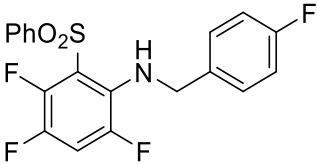
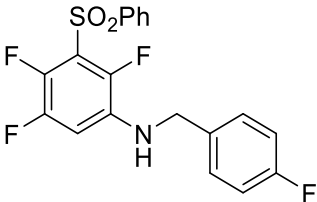
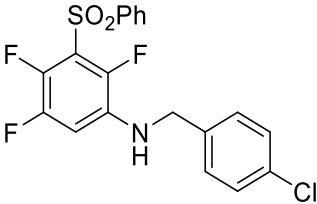
8.2 SPR DKP screen (Chapter 3, Section 3.8.2)

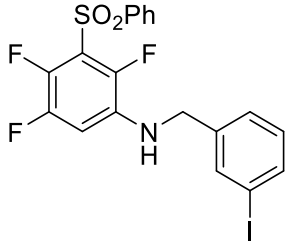
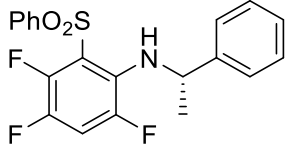
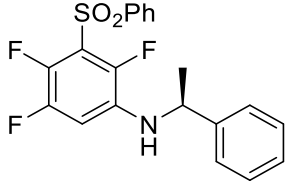
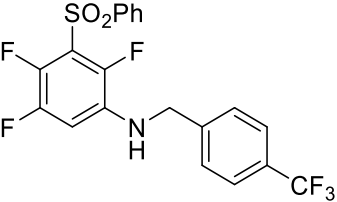
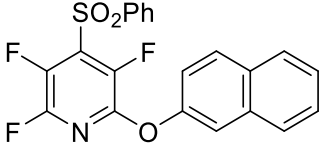
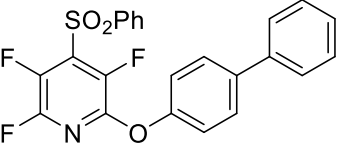
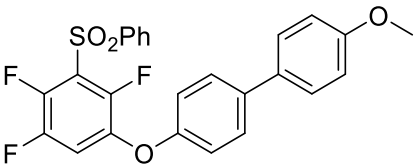
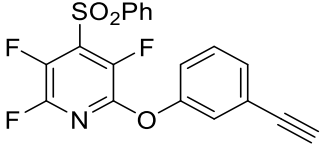
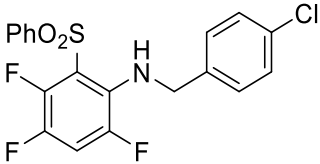
Compound Number	Structure
27	
28	
29	
36	
37	

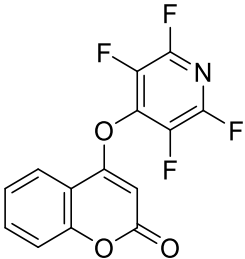
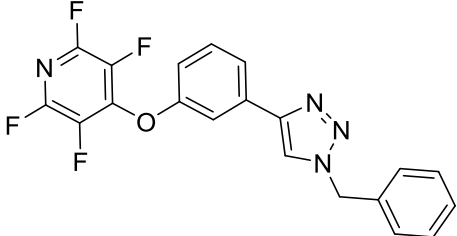
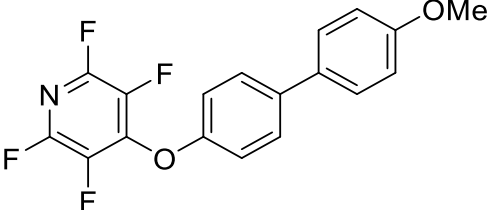
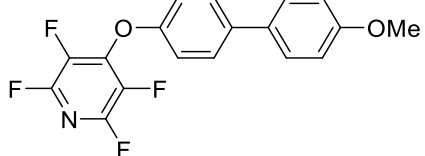
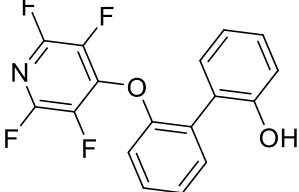
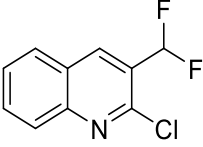
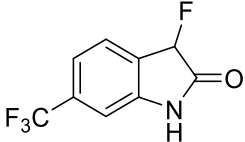
38	
39	
41	
43	
46	
47	
48	
55	
56	

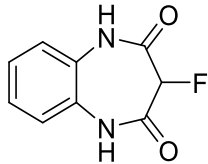
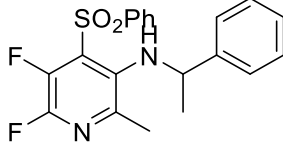
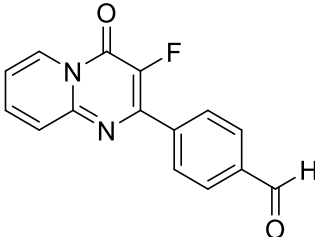
57	
58	
160	

8.3 SPR fragment screen - *hsCCL2* (Chapter 3, Section 3.9)

Compound Number	Structure
60	
80	
81	
82	
83	

84	
85	
86	
87	
88	
89	
90	
91	
161	

162	
163	
164	
165	
166	
167	
168	
169	

170	
171	
172	

8.4 HMEC-1 viability (Chapter 4).

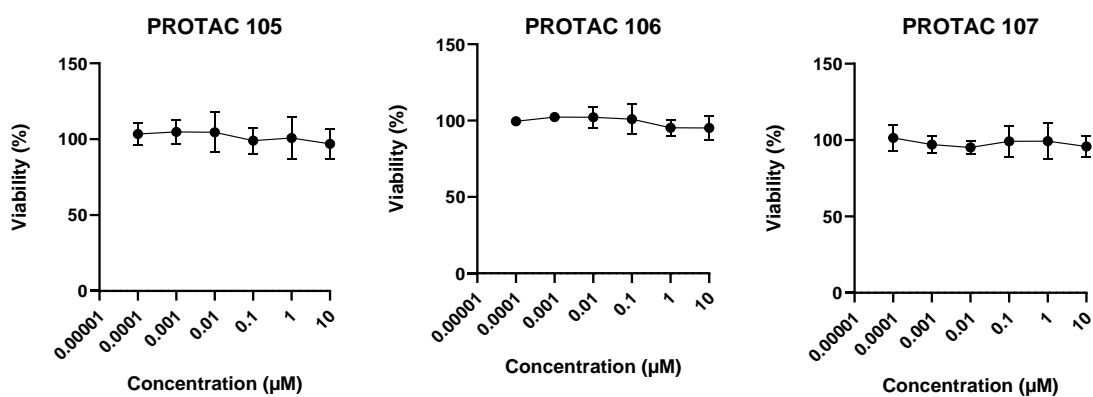


Figure 8.1 HMEC-1 viability screening with three PROTAC treatments (**105 – 107**). Compounds tested in a 10-fold dilution series from 10 µM to 0.1 nM. Assays were tested in biological and technical triplicate (n = 3)